POLITECNICO DI TORINO

MASTER's Degree in Energy and Nuclear Engineering

Politecnico di Torino

MASTER's Degree Thesis

Investigation of SFNM-04 Perovskite Supported Composite Oxides for Chemical Looping CO2 Dissociation

Supervisors

Prof. MASSIMO SANTARELLI

Dr. DOMENICO FERRERO

Dr. SALVATORE CANNONE

Candidate

ALBERTO GRIMALDI

October 2021

Abstract

The persistent increase of the average temperature of the Earth indicates that global warming is the main problem to be solved in the next years, since it affects both planet and human health. The global warming problem is strictly connected to rising greenhouse gas (GHG) emissions, pollution, and the resulting climate changes, causing irreversible alterations to the environment. For this reason, according to international agreements in limiting the rise in global average temperatures, mitigation actions against CO_2 emissions are becoming increasingly crucial. The principal cause of global warming is the continuous use of fossil fuel plants to satisfy the ever-increasing energy demand. One possible alternative to counteract global warming is to investigate CCUS (Carbon Capture Utilization and Storage) technologies for capturing CO_2 already generated by current fossil fuel energy systems and develop methods to convert CO_2 into useful chemicals or combustible gases. The role of CCUS is to act as interim solution to stabilize GHG emissions while still using fossil power plants: the future of the energy sector should be decarbonized, without using fossil fuels. To curb future CO_2 emissions, not only we should build low-carbon power plants (e.g., based on renewables), but we will have to retrofit existing power plants with carbon capture devices. Among the possible methods, one of the most promising is the renewable chemical looping process (R-CLR) for two-step thermochemical CO_2 splitting: heat at high temperature provided by a renewable energy system (typically a Concentrated Solar Power CSP system) is imposed on the looping material that alternates between a reduced and an oxidized state producing syngas ($CO + H_2$) as a useful product starting from CO_2 and H_2O.

The aim of this dissertation is to investigate the feasibility to perform chemical looping processes for syngas production using a new perovskite-based oxygen carrier for the conversion of the captured carbon dioxide CO_2 to carbon monoxide CO. The Master Thesis and Stage project is carried out at CO_2 *Circle Lab* inside the Environment Park located at Parco Dora, Turin, Italy in collaboration with University of Udine and Massachusetts Institute of Technology (M.I.T.), Boston, USA. More detailed, the material under investigation is $Sr_2FeNi_{0.4}Mo_{0.6}O_{6-\delta}$ (SFNM-04) and it was synthetized by University of Udine; its redox ability and stability is comprehensively analyzed performing microreactor tests. The ideal perovskite structure adopts a cubic symmetry, and the chemical formula is ABX_3, where A is a large alkaline or rare earth element (e.g. Calcium, Strontium), B is a smaller transition metal cation (Iron, Chromium) and X is the superoxide ion O^{2-} that bonds to both cations.

The A-site cation is responsible for the thermal resistance, while the B-site cation is responsible for the reactivity and catalytic activity in chemical looping reactions. As a result, the selection of the A and B-site cations is crucial in the design of promising perovskite-structure oxygen carriers. The SFNM-04 material under investigation presents a double perovskite structure, meaning that its chemical structure transits from a classical cubic structure to a layered Ruddlesden-Popper structure: this configuration is composed by a perovskite layer followed by rock-salt layer. As expressed by the stoichiometric coefficients of the chemical formula, there are two atoms of Strontium located at the A-site, one atom of Iron, 0.4 of Nickel and 0.6 of Molybdenum located at the B-site that can arrange in alternative way inside the oxygen octahedra.

In literature there are not present experimental analysis of this material for chemical looping, hence this makes the master thesis project even more fascinating. Thanks to iron (from Fe^{2+} to Fe^{3+})and molybdenum (from $Mo^{6+}$to Mo^{5+}) state of oxidation transition, this material has a high ionic conductivity, hence these redox couples non balanced inside the lattice allows the creation of many oxygen vacancies, the main driver of the chemical looping process. One of the most interesting property of this material is related on its capability to grow, throughout the Hydrogen reducing step, giving birth to an exsolution evolution, with the consequential appearance of spread Nickel-Iron alloy nanoparticles on the surface outer layer that enhance the catalytic activity of the perovskite surface. This alloy evolution is one of the crucial property useful to increase the stability of the material, becoming more resistant to sulphide and coke poisoning than a classical metallic material.

The experimental section of this Master Thesis project is focused on the CO production achieved during the oxidation reactions in which a gas mixture containing different concentrations of carbon dioxide reacts with the SFNM-04 sample. The chemical looping test bench is composed by a gas delivery system with three Bronkhorst mass flow controllers used to automatically send a certain gas flow mixture, a horizontal alumina reactor positioned inside a tubular furnace that guarantees an isothermal environment up to $1600\,°C$ and a real-time Emerson X-stream gas analyser (multichannel NDIR/UV/TCD) used to analyse the outlet gas composition.

The variables that change during the oxidation and reduction experimental procedures are the operating temperatures (from $550\,°C$ to $850\,°C$), gas mixture compositions (from $6\,\%$ to $100\,\%$) of CO_2 during the oxidation step and from $5\,\%$ to $100\,\%$ of H_2 during the reduction step in a N2-based gas mixture), and reaction times (from 15 to 120 minutes) in order to assess the perovskite response and the consequent CO global yield and CO maximum production rate in percentage and in $[\mu mol/g/s]$, and the CO_2 conversion evaluating the grams of oxygen exchanged with respect the grams of SFNM-04 used. The objective of this set of experiments is to find the optimal conditions that allow to the maximum CO production rate. Considering the operating temperatures variation, the main evident result is a negative impact on the redox ability of the sample when reducing the operating temperature of both oxidation and reduction. Each oxidation curve exhibits a fast-initial CO increase corresponding to the rapid oxygen vacancies ion incorporation followed by a sudden decrease. This behaviour demonstrates a strong temperature dependence of the CO rate profile, which becomes higher and wider at higher temperature due to the higher amount of available oxygen sites; $T = 850\,°C$ is the maximum temperature value imposed, furthermore, increasing it too much may be ineffective since one of the goals to be reached employing perovskite oxygen carrier is to obtain promising results at lower temperatures than those used for ceria or metal oxide chemical looping processes. Concerning the gas mixture compositions variation, as the concentrations increased a higher CO production was detected by the gas analyzer, so both the cases have been investigated separately, focusing first on the oxidation reaction conditions variation and then on the reduction ones. All the experimental results obtained are properly post-processed so as to deduce if the reactions are completed or not, trying to identify if there is a need for further operating conditions variations in order to obtain a completely oxidized or reduced sample.

In conclusion, it is useful to remark the aim of this master thesis project: it is a preliminary study useful to determine the reproducibility of redox cycles for SFNM-04 perovskite to produce CO starting from CO_2. The perovskite structure is very stable and it can accommodate a huge concentration of oxygen vacancies, which can allow highly productive redox cycles. On the other side, the ability of perovskite oxides to accommodate different chemical elements allows innumerable combinations of elements in stable solid solutions leaving a lot of space for improving existing materials. Further structural analysis of the sample after the thermochemical processes should be integrated to recognize the operating conditions effects on the material and to verify if the SNFM-04 sample is totally oxidized or reduced.

For instance, a XRD analysis can be useful to detect the eventual presence of different structural phases that may negatively impact on the redox performance, as the presence of carbonates ($SrCO_3$) and molybdate ($SrMoO_4$) that inhibits the re-oxidation of the sample.

To give a concrete application of this work, it is possible to assert that it points out the necessity of developing new CCUS technologies and materials aimed to successfully complete the energy transition path and to reach the sustainable goals evidenced by the United Nations and UE within the 2030.

Summary

List of Figures

List of Tables

Acronyms

GHG	Greenhouse Gas
UNFCC	United Nations Framework Convention on Climate Change
IEA	International Energy Agency
SDG	Sustainable Development Scenario
TFEC	Total Final Energy Consumption
TES	Transforming Energy Scenario
SDS	Sustainable Development Scenario
CCS	Carbon Capture & Sequestration
CCU	Carbon Capture & Utilization
DME	Dimethyl Ether
SMR	Steam Methane Reforming
CSP	Concentrated Solar Power
TR	Thermal Reduction
IGCC	Integrated Coal Gasification Combined Cycle

WGS	Water Gas Shift
MEA	Monoethanolamine
PSA	Pressure Swing Adsorption
CaL	Calcium Looping
ASU	Air Separation Unit
ITM	Ion Transport Membrane
EOR	Enhanced Oil Recovery
SOEC	Solid Oxide Electrolytic Cell
AEC	Alkaline Electrolytic Cell
PEMEC	Proton Exchange Membrane Electrolytic Cell
PEC	Photochemical Cell
HTGR	High-Temperature Gas Reactor
CDCL	Coal Direct Chemical Looping
CTSCL	Coal to Syngas Chemical Looping
FCC	Fluid Catalytic Crackers

PBR	Packed Bed Reactor
CLC	Chemical Looping Combustion
CLOU	Chemical Looping with Oxygen Uncoupling
WS	Water Splitting
CDS	Carbon Dioxide Splitting
CLR	Chemical Looping Reforming
MPSZ	MgO-partially Stabilized Zirconia
RPC	Reticulated Porous Ceramic
TGA	Thermogravimetric Analysis
BET	Braunauer-Emmet-Teller
SFNM	Strontium-Iron-Nickel-Molybdenum perovskite
MFC	Mass Flow Controller
UniUD	University of Udine
SCADA	Supervisory Control and Data Acquisition
TCD	Thermal Conductivity Detector

EDTA	Ethylenediaminetetracetic acid
SCS	Self-Combustion Synthesis
TPR	Temperature Programmed Reduction
XRD	X-ray Diffraction
RP	Ruddlesden-Popper
MIT	Massachusetts Institute of Technology
SEM	Scanning Electron Microscopy
TRL	Technology Readiness Level

Chapter 1

1. Introduction

1.1 – Energy Transition Path and COP26 Goals

The anthropogenic carbon dioxide (CO_2) emissions are primarily derived from burning fossil fuels, with about 34 Gt being emitted in 2020 [1]. Nevertheless, considerable investment and a significant decrease of renewable energy prices, fossil fuels continue to play a crucial role in the World's energy mix [2]. As discussed in a recent report by International Energy Agency [1], annual CO_2 emissions rebound quickly from the dip cause by the Covid-19 pandemic in 2020: they increase from 34 Gt in 2020 to 36 Gt in 2030 and they remain around this level until 2050. This aspect is depicted in *Figure 1.1* where it is illustrated the energy-related and industrial process CO_2 emissions by region (on the left) and by sector (on the right), in agreement to the IEA Stated Policies Scenario (STEPS) that illustrates the consequences of existing and stated policies for the energy sector. If this emissions trend grows along the same trajectory after 2050, the global average surface temperature rise would be around 2.7 $°C$ in 2100 (with a 50 % of probability).

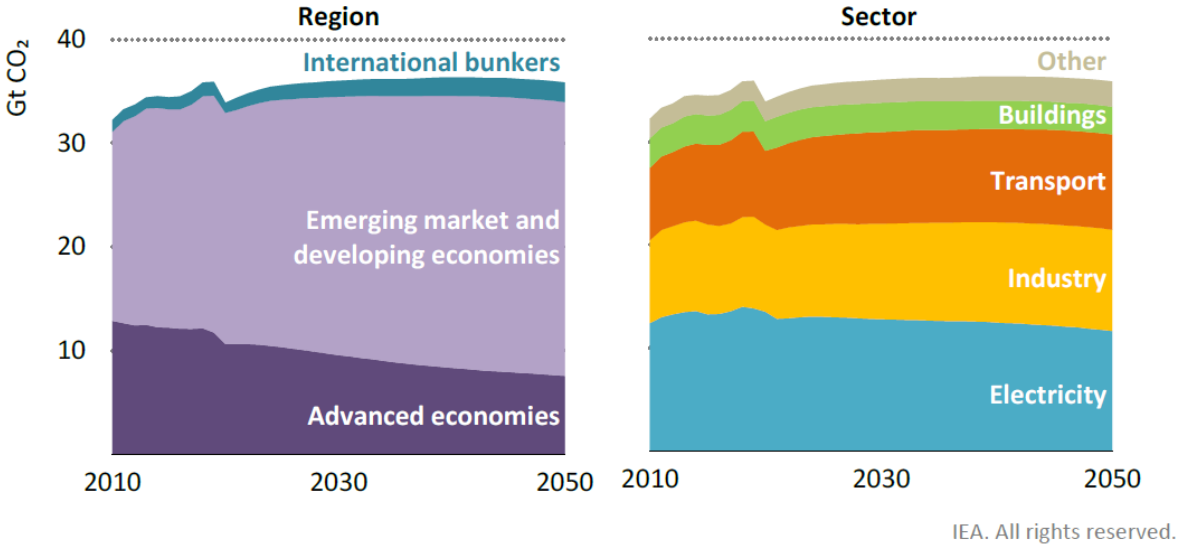

***Figure 1.1**: Energy-related and Industrial Process CO_2 emissions by Region and Sector in the STEPS [1].*

The projected trends in CO_2 emissions in the STEPS are mainly due to the changes in the amount of energy used and the mix of fuels and technologies adopted in each World's country. As represented by *Figure 1.2*, the Total Energy Supply (TES) increases over 30 % between 2020 and 2050. Without a projected annual average reduction of 2.2 % in energy intensity (energy intensity is defined by the ratio between energy use and Gross Domestic Product GDP), the TES in 2050 would be about 50 %. Concerning the World's fuel energy mix, the coal usage presents a peak in 2014, and then decreases by around 15 %. Differently, the oil demand after a significant fall in 2020 due to the pandemic, increases returning to the 2019 level of 98 million barrels per day $[mb/d]$ by 2023 and achieving a plateau of about 104 $[mb/d]$ after 2030. Considering the natural gas energy demand trend, it grows from 3900 billion cubic metres $[bcm]$ in 2020 to 4600 $[bcm]$ in 2030 and 5700 $[bcm]$ in 2050. Regarding the nuclear energy, it would increase by 15 % between 2020 and 2030 mainly due to the expansion of nuclear power plants in China. Finally, the traditional use of biomass presents a steady-state behaviour. The dashed blue line indicates the CO_2 intensity of TES and it could achieve a value lower than 45 gCO_2/MJ.

Hence to sum up, the coal use assumes a downward trend, the oil seems to reach a plateau, while the natural would significantly grow up to 2050.

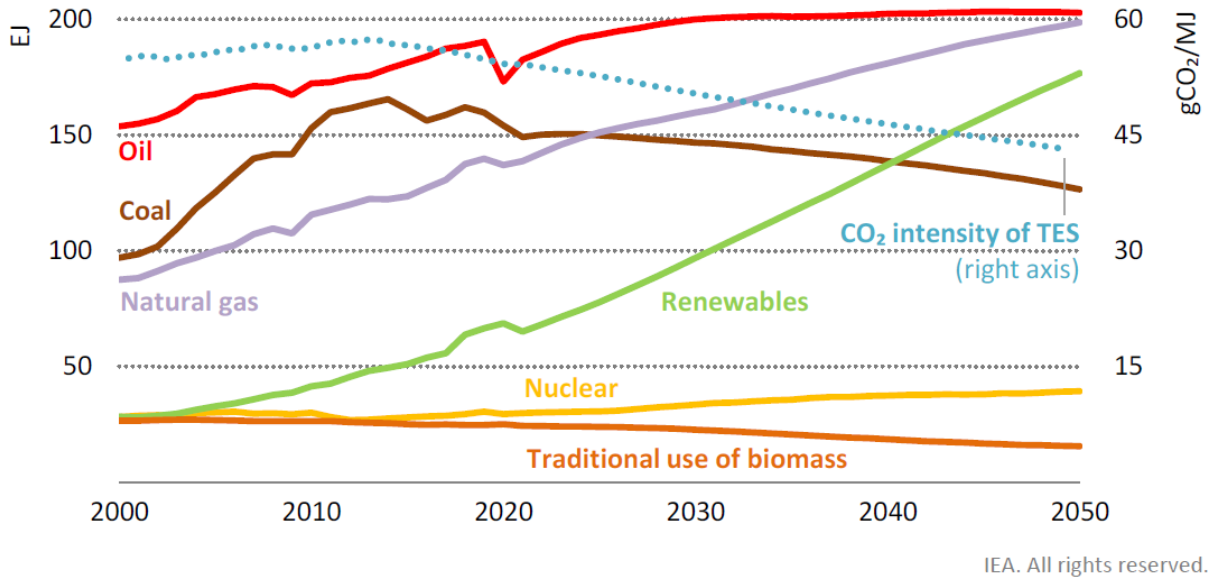

***Figure 1.2**: Total Energy Supply (TES) and CO_2 Emissions Intensity in the STEPS [1]. EJ = exajoule; MJ = megajoule.*

Another relevant parameter that provides a useful indication of the Worldwide energy Mix is the Total Final Energy Consumption (TFEC). As reported by the following *Figure 1.3*, according to STEPS, electricity and natural gas assume a predominant role. In fact, the global electricity demand raises by 80 % between 2020 and 2050 and more than 85 % of the growth in global electricity demand derives from emerging market and developing markets. Despite a significant growth in energy renewables, coal and oil continue to present the highest values in TFC, especially in industry and transport sector. Summarizing, the final energy consumption increases on average by 1 % per year between 2020 and 2050. To satisfy this progressive increase of TFC, electricity and natural gas use results crucial in the energy mix.

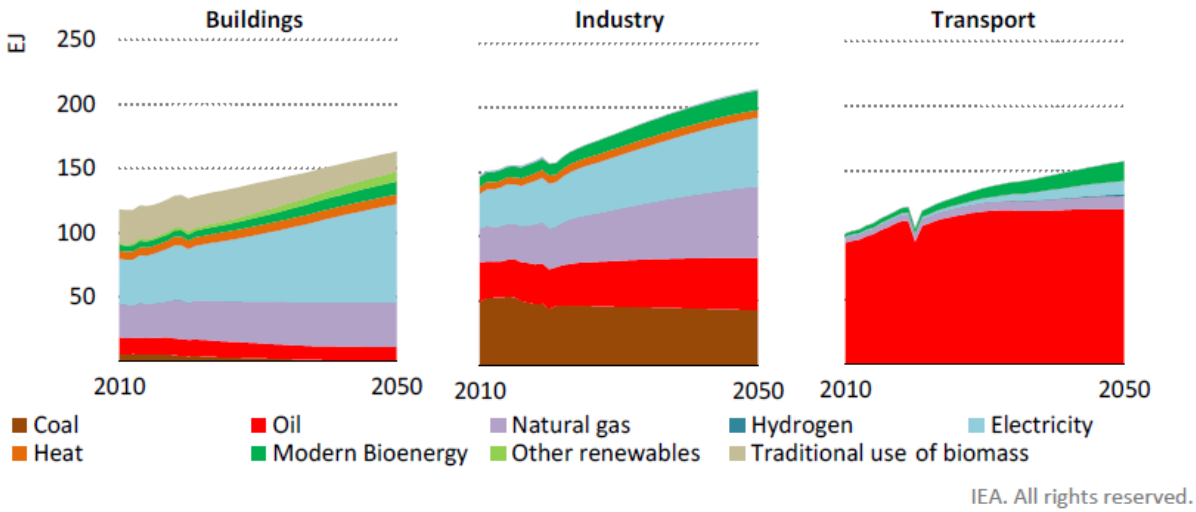

***Figure 1.3**: Total Final Consumption (TFEC) by Sector and Fuel in the STEPS [1].*

Finally, in the following *Figure 1.4* is represented the CO_2 emissions in $[Gt]$ terms from existing infrastructure by sector and region. In the energy sector are contained a large number of long-lived and capital-intensive assets as urban infrastructure, coal-fired power lants, heavy industrial facilities that can present technical and economic lifetimes of over 50 years. Concerning this aspect, if the energy infrastructure today already present operate until the end of the typical lifetime, IEA estimates that this would allow to cumulative energy-related and industrial process CO_2 emissions between 2020 and 2050 of about 650 $Gt\ CO_2$. This predicted value is around 30 % more than the remaining total CO_2 budget consistent with limiting global warming to 1.5 $°C$ with a probability of 50 %.

More precisely, about 50 % of the total emissions would derive from the electricity sector, 40 % of the total emissions would derive from coal-fired power plants and industry sector involving steel, cement chemicals and other industry accounting for about 30 % total emissions from existing assets. From this figure it is possible to deduce that the emerging market and developing economies account for three-quarters of cumulative emissions from existing infrastructure. In agreement with IEA Global Energy & CO_2 Status Report [3], the CO_2 emitted from coal combustion is responsible for over 0.3 $°C$ of the 1 $°C$ increase in the global average annual surface temperature above pre-industrial levels. This is clear signal of why the energy transition path is necessary, enhancing the share of renewable energy in TFEC and adopting clean power generation plants more and more efficient.

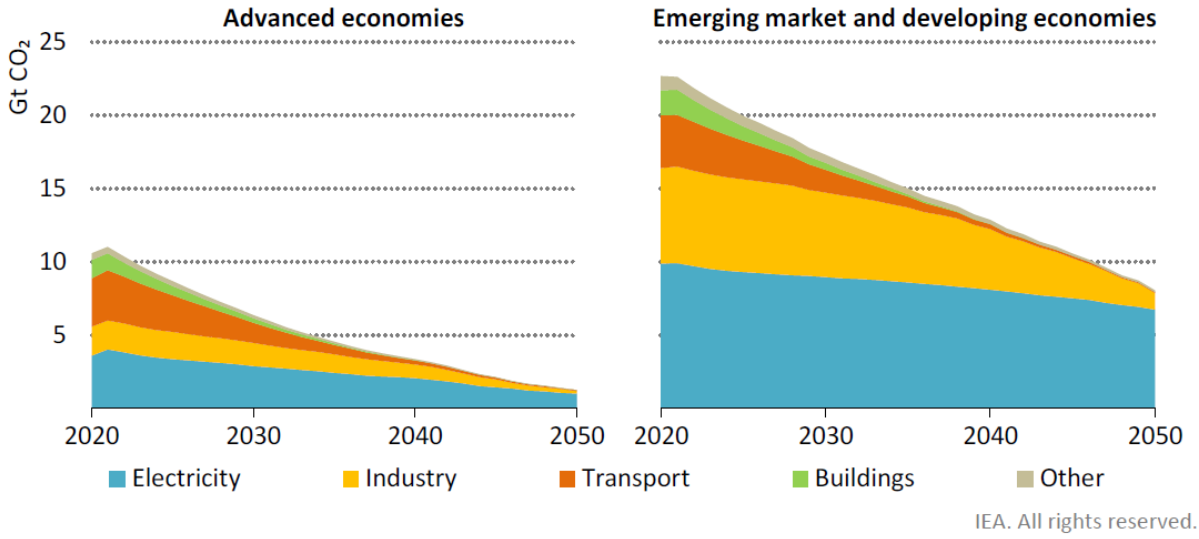

***Figure 1.4**: CO_2 emissions in $[Gt]$ from Existing Infrastructure by Sector and Region [1].*

To better understand why it is necessary to successfully complete the global decarbonization pathway to net-zero CO_2 emissions in 2050, it is crucial to know the dangerous effect of CO_2 molecules trapped into the atmosphere. Firstly, CO_2 is a long-lived greenhouse gas, hence it owns a persistent impact on radiative forcing and, being stable from a chemical point of view, it is able to remain hundreds of thousands of years in the atmosphere. According to IPCC report [4] and as shown in *Figure 1.5*, the cumulative presence of CO_2 into the atmosphere raises every year reaching an average value of $34\ Gt$ in 2020. More detailed, to give a concrete demonstration of why the CO_2 emissions are the first cause of the increase in global Earth mean temperature, in this plot it is noticed that level of warming is currently raising at a rate of $0.3 \div 0.7\ °C$ among 30 years.

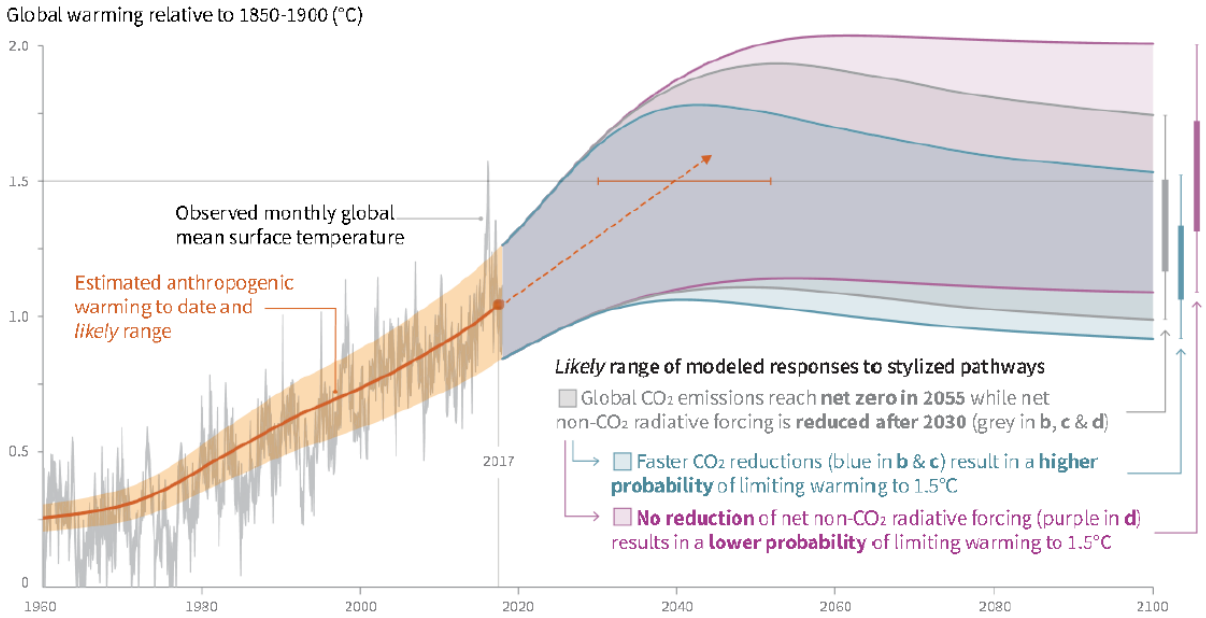

***Figure 1.5**: Current Global Temperature Change due to CO_2 emissions and Modelled Responses to Stylized Anthropogenic Emission and Forcing Pathways in agreement to IPCC report 2018 [4].*

In general, to give a physical explanation of the dangerous GHG effects, in the following *Figure 1.6* it is presented the spectral flux at the top of the atmosphere (light blue curve) and the ideal blackbody emission at $T = 294\,K$ (red curve) in $[mW/m^2 \cdot cm]$ terms as a function of the wavenumber in $[cm^{-1}]$. The first indicates the actual emission flux measured at the top of the atmosphere layer, while the second represents the radiative emission spectrum of the Earth's surface in the absence of atmosphere. As more GHGs are emitted and entrapped into the atmosphere, it is produced a shift towards a warmer Earth's surface. This is due because Earth is on a radiative equilibrium with respect to the Sun, hence, as much solar radiation (Short Wave SW emission) is received on average by Earth surface, the same quantity is emitted back by the Earth in infrared Long Wave (LW) radiation form. Therefore, in a perfect equilibrium configuration, the average Earth's surface temperature remains constant over the time. This does not happen because GHGs are transparent to SW radiation derived from the Sun, and at the same time they strongly interact and absorb the LW emissions emitted by the Earth. The actual emission flux measured at the top of the atmosphere layer (light blue curve) accounts for emission absorption at selected wavelengths corresponding to the absorption of GHGs gases like H_2O, CO_2, N_2O, CH_4, O_3. It is not very well known that H_2O is a strong GHG, notwithstanding it is not human derived as CO_2, N_2O and CH_4 that are emitted due to a direct responsibility of anthropogenic activities.

To conclude, as more GHGs are trapped into the atmosphere, the harder will be for Earth to evacuate LW radiation because of the selective trapping effect of GHG gases toward infrared radiation. Thence, to maintain the radiative equilibrium condition, the Earth's surface temperature is forced to rise.

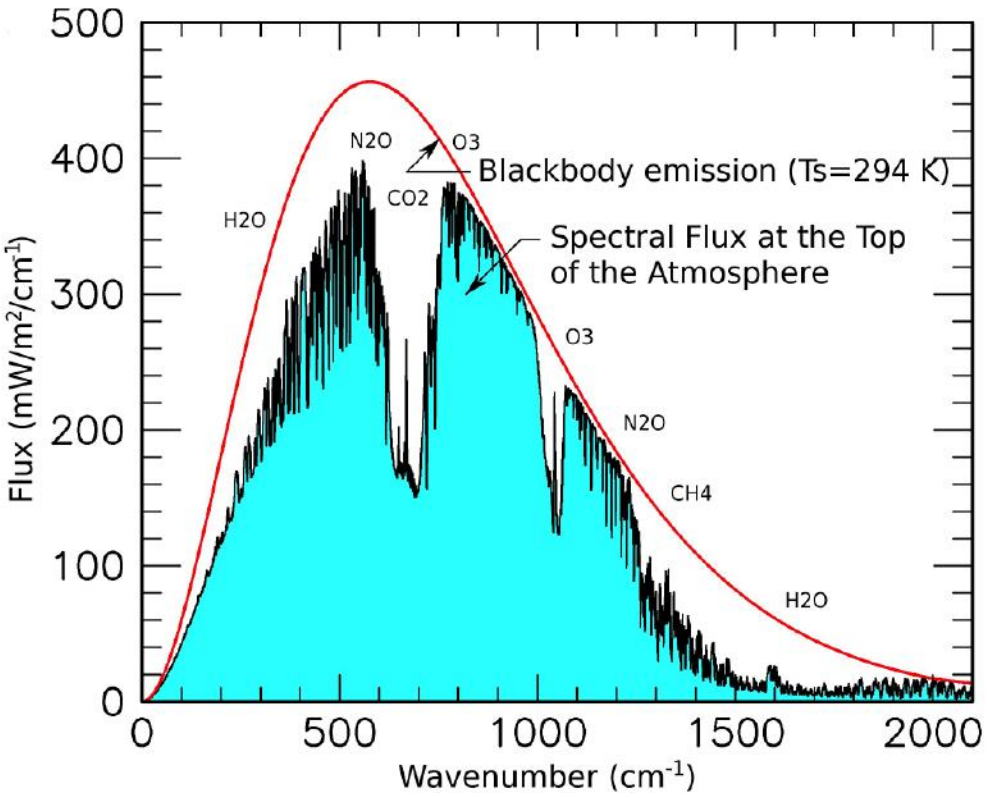

Figure 1.6: *Spectral flux at the top of the atmosphere (light blue curve) and the ideal blackbody emission at* $T = 294\ K$ *(red curve) in* $[mW/m^2 \cdot cm]$ *terms as a function of the wavenumber in* $[cm^{-1}]$.

Furthermore, to give a numerical evaluation of the impact of GHGs and other pollutants, in the following *Figure 1.*7 is quantified this impact in term of temperature increase/decrease after 20 years (left figure) and after 100 years (right figure) [4]. Hence, one pulse of emissions emitted today will produce a certain temperature impact 20 years and 100 years from now. It is crucial to detect this delayed impact instead of an immediate one, because the GHSs and pollutants present a certain lifetime in the atmosphere once emitted. It is noticed that CO_2 (red bar) assumes the predominant role in both cases because it is the longest living gas in the atmosphere among the various GHGs and other pollutants included in this IPCC simulation. The cumulated net impact is $40\ [mK/yr]$ after 20 years, and about $25 \div 30\ [mK/yr]$ after 100 years.

Assuming a constant emission rate every year, the previous values indicate that the net temperature increase would be 4 $°C$ over a period of 100 years, hence, the resulting cumulative emission for 100 years is 3000 Gt of CO_2. As discussed before, also in this case it is confirmed that the energy and industry are the most impacting sectors.

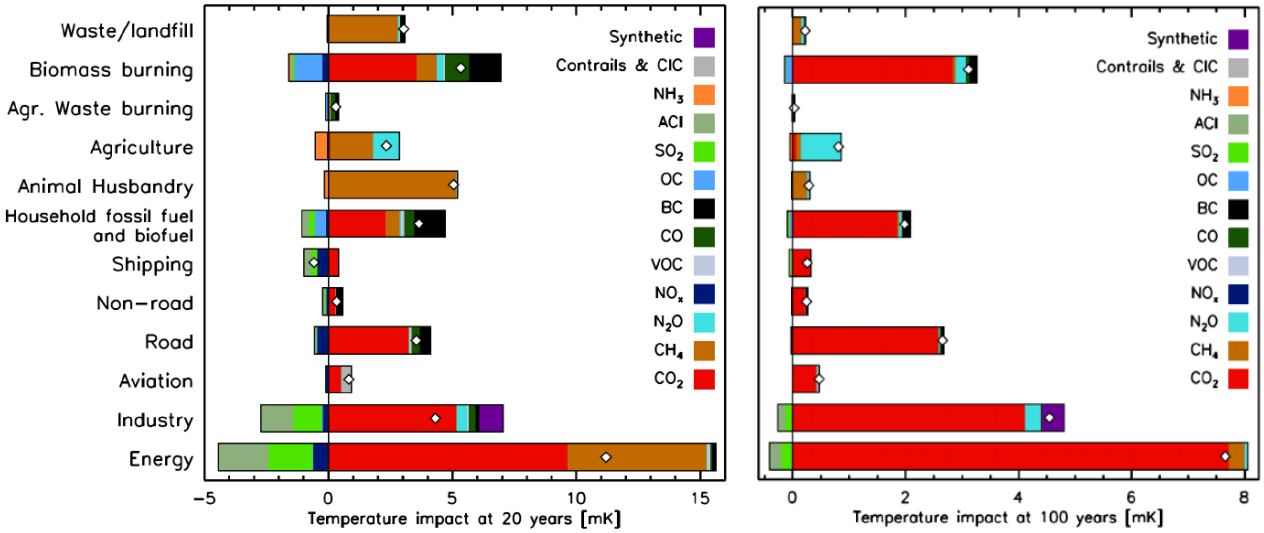

Figure 1.7: *Impact of GHGs and other pollutants in term of temperature increase/decrease after* 20 *years (left) and after* 100 *years (right) [4].*

Once the irreversible effects of GHGs emissions are described, in a report of 2019 of International Panel on Climate Change (IPCC) [5], the goal of restricting the global warming rise of 2 $°C$ to 1.5 $°C$ within by 2040 is posted mandatory. Since 1994, when it was negotiated the first international environmental treaty, namely UNFCCC (United Nations Framework Convention on Climate Change) a lot of energy policies have been announced aimed to mitigate the climate crisis. The *Figure 1.8* summarizes the most relevant ones issued during these years. Firstly, UNFCCC indicates as crucial objective to stabilize GHG concentrations into the atmosphere at a level that would have prevented harmful anthropogenic interference for the Earth's surface. After that, in 1997, the Kyoto Protocol gives a first numerical measure to reduce the pollutant emissions by no less than 8.65 % in the period between 2008-2012, and to reduce the CO_2 emission by 5 % with respect to the emissions recorded in 1990 (reference year). It also provides detailed methods and mechanisms for how the emission reductions can be achieved, measured and verified. Then, initially proposed in 2007 and adopted by 2009, the Climate and Energy Package is composed by a set of EU (European Union) legislative measures, designed to reach three main targets within 2020. It is also known as "20-20-20 by 2020" because the main designed goals are:

1. 20 % reduction of EU GHG emissions from 1990 levels.
2. 20 % increase in the share of EU energy consumption produced form renewable resources.
3. 20 % improvement in the EU's energy efficiency to reduce GHG emissions.

Then, in 2015 it is issued the Paris Agreement COP21 that effectively replaces the Kyoto Protocol and presents long-term objective to limit the increase of global Earth average temperature below 2 $°C$ threshold above pre-industrial levels and to limit this raise to 1.5 $°C$. Thanks to this COP21 agreement, for the first time every country around the world enter into a legally binding commitment to reduce emissions. It also set out ambitious goals on adaptation and on finance recognising that many people around the world already experiencing the impacts of changing climate.

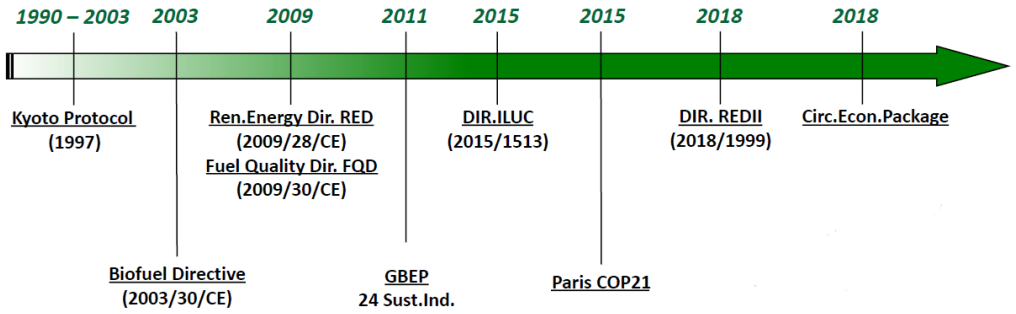

Figure 1.8: Climate Change Eenrgy Policies Pathway.

In conclusion, COP26 will take place in November 2021 at Glasgow. COP stands for Conference of the Parties and the parties are the signatories of the UNFCCC (today the parties are 196 countries). As reported by COP26 Explained [6], the principal goals that need to achieve at COP26 are:

1. Secure global net zero by mid-century and keep 1.5 $°C$ within reach. To achieve these targets the participating countries will need to accelerate the phase-out of coal, curtail the deforestation, speed up the switch to electrical vehicles and encourage investment in renewables.
2. Adapt to protect communities and natural habitats affected by climate change by protecting and restoring ecosystems, building defences, warning systems and resilient infrastructure and agriculture to avoid loss of homes, livelihoods and even lives.
3. An effective mobilise finance of at least \$ 100 bn in climate finance per year by 20202 to achieve the first two goals.

4. Finalise the Paris Rulebook, namely the detailed rules that make the Paris Agreement operational and promote accelerate actions to tackle the climate crisis through collaboration between governments, businesses, and civil society.

In summary, the most promising ways to successfully complete the energy transition path in order to decarbonize all the end-use sectors and mitigate the CO_2 emissions are:

1. Reduce the consumption of fossil fuels persecuting the transition towards renewable energy sources by adopting energy policies able to drive the deployment and technological competitiveness, with long-term solutions and investments
2. Improvement of energy conversion efficiency of all the energy systems.

In agreement to IEA's Sustainable Development Scenario (SDS) [7] depicted in *Figure 1.9*, the increase of the penetration of renewables in the energy mix allows to produce a reduction of CO_2 emissions of about 32 %, while the increase of energy conversion efficiency gives a contribution in terms of CO_2 emissions of about 37 %.

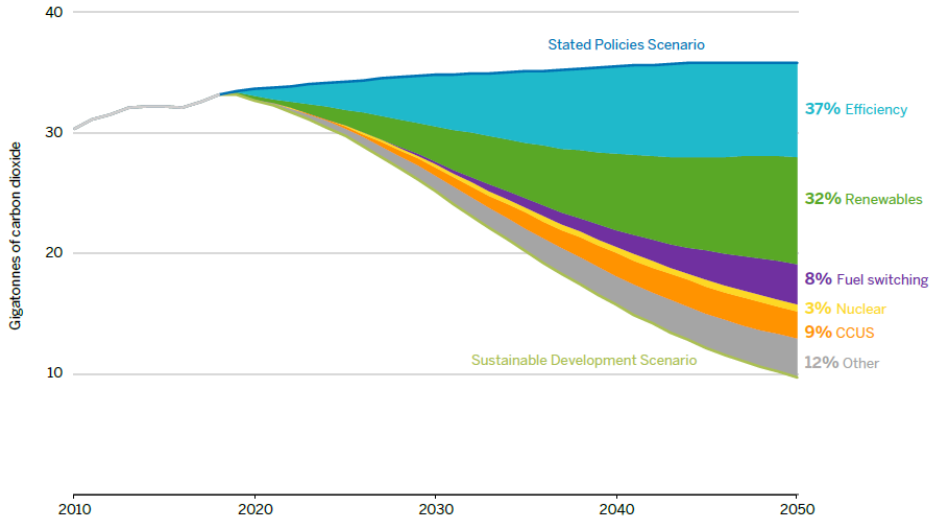

Source: IEA 2019a.
Note: Reduced thermal losses in power generation account for 15 percent of efficiency improvements.
CCUS = carbon capture, utilization, and storage.

Figure 1.9: *Methods to Reduce the CO_2 emissions according to IEA's Sustainable Development Scenario (SDS) [7].*

In addition, as represented by the orange curve of the previous figure, Carbon Capture Utilization & Storage (CCUS) technologies assume a crucial role to curb the CO_2 emissions. This dissertation is really focused on a particular CCUS technology already in development phase, for this reason in the next section are described the main reasons why CCUS technologies are crucial to successfully complete the energy transition path.

1.2 – Carbon Capture Utilization & Storage Technologies

The carbon capture process was introduced for the first time in the early 1970s, after the global crisis. At firs instance, this method is implemented to inject CO_2 in an oil field to boost its recovery [8]. In agreement to IEA Special Report on Carbon Capture Utilisation and Storage [9], CCUS will need to form a key pillar of efforts to put the world on the path to net-zero emissions assuming a major role alongside electrification, hydrogen, and sustainable bioenergy. A simple schematic of CCUS is depicted in *Figure 1.10.*

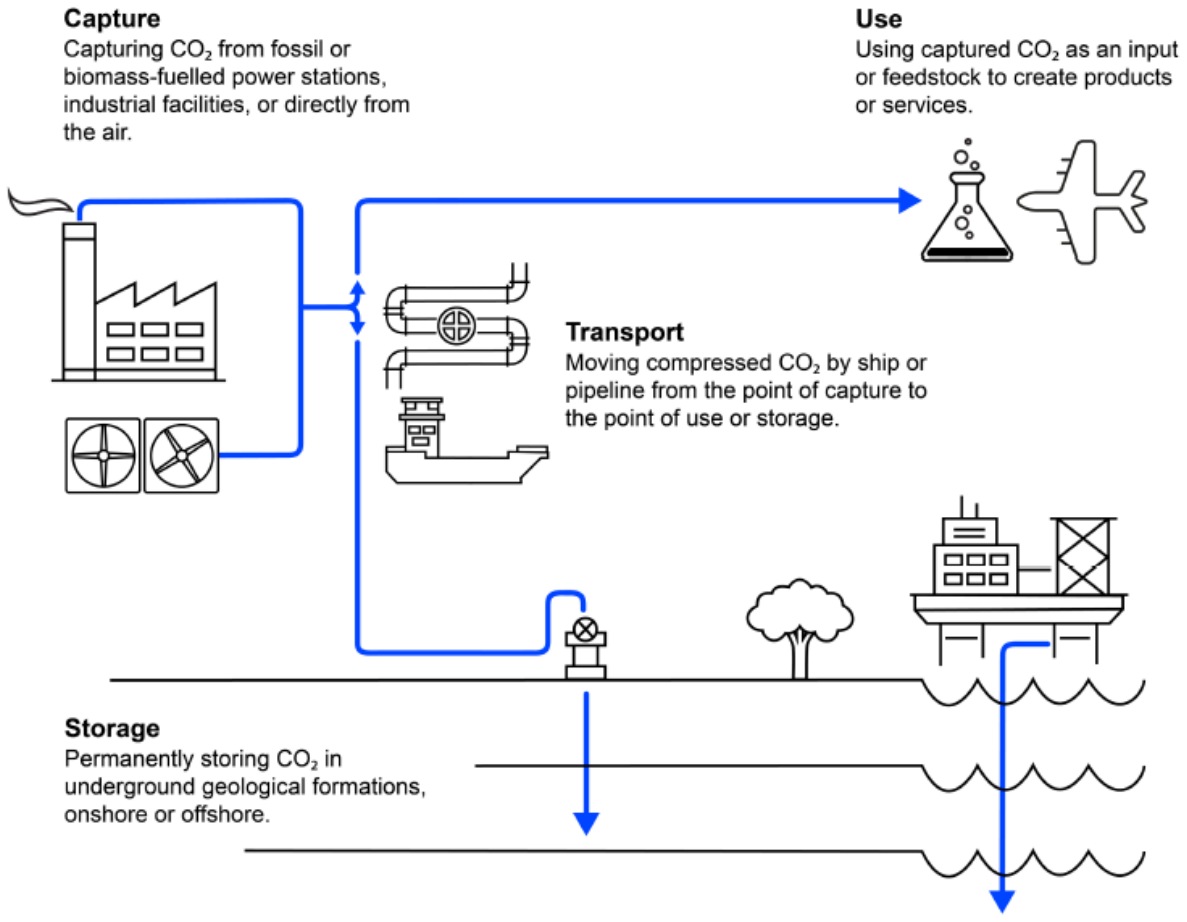

Figure 1.10: *Schematic of CCUS [9].*

The CO_2 captured can derive from a range of several sources, such as fossil or biomass power plants, industrial facilities or directly from the air. Then, there are different adopted terminology to indicate the pathway of the CO_2 captured implementing a CCUS technology:

1. Carbon Capture and Storage (CCS) involves all the applications in which the CO_2 is captured and permanently stored in underground geological formations, onshore or offshore and then transported by ship or pipeline.
2. Carbon Capture and Utilisation (CCU) corresponds to all the possible chemical, physical processes where the CO_2 captured is used to produce synthetic fuels and chemicals.
3. Carbon Capture, Utilisation and Storage (CCUS) includes both CCS and CCU, hence the CO_2 captured can be used and stored, for instance in EOR (Enhanced Oil Recovery) or in building materials.

Despite in the last decade its development has been slow due mainly to insufficient incentives, interest in CCUS is starting to grow with plans for more than 30 commercial facilities announced in the last three years with a potential investment of around $\$\ 27\ bn$, that more than double the investment planned in 2017. As shown in *Figure 1.11*, today there 21 operating CCUS facilities able to capture up to 40 $[Mt]$ of CO_2 per year. It is evident that the natural gas processing is the most effective pathway in terms of CO_2 captured; however, starting from 2020 it is noticed an increase of the diversification in CCUS technologies, especially for Hydrogen production (red bar).

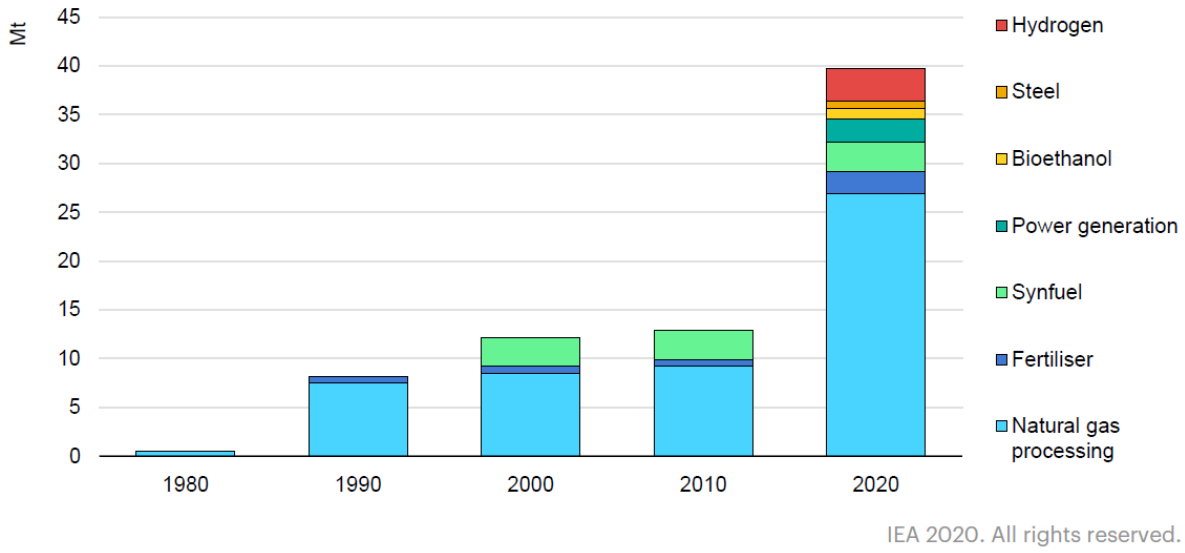

Figure 1.11: *Total CO_2 captured in $[Mt]$ terms at large-scale facilities by source [9]. Source: IEA analysis based on GCCSI (2020), Facilities Database, https://co2re.co/FacilityData.*

More precisely, CCUS technologies contribute to the energy transition path to net-zero emissions in different ways as described following.

1) Firstly, CCUS can be retrofitted to existing power and industrial plants that could emit 600 billion tonnes of CO_2 over the next five decades. This aspect can be better understood by observing *Figure 1.12* that show the future CO_2 emissions in $[Gt/yr]$ from committed (upper-left), realized and remaining (lower-left) and future (upper-left) energy infrastructures. The blue curve in the upper-right part of the graph indicates the historical trend of committed CO_2 emissions according to IEA.

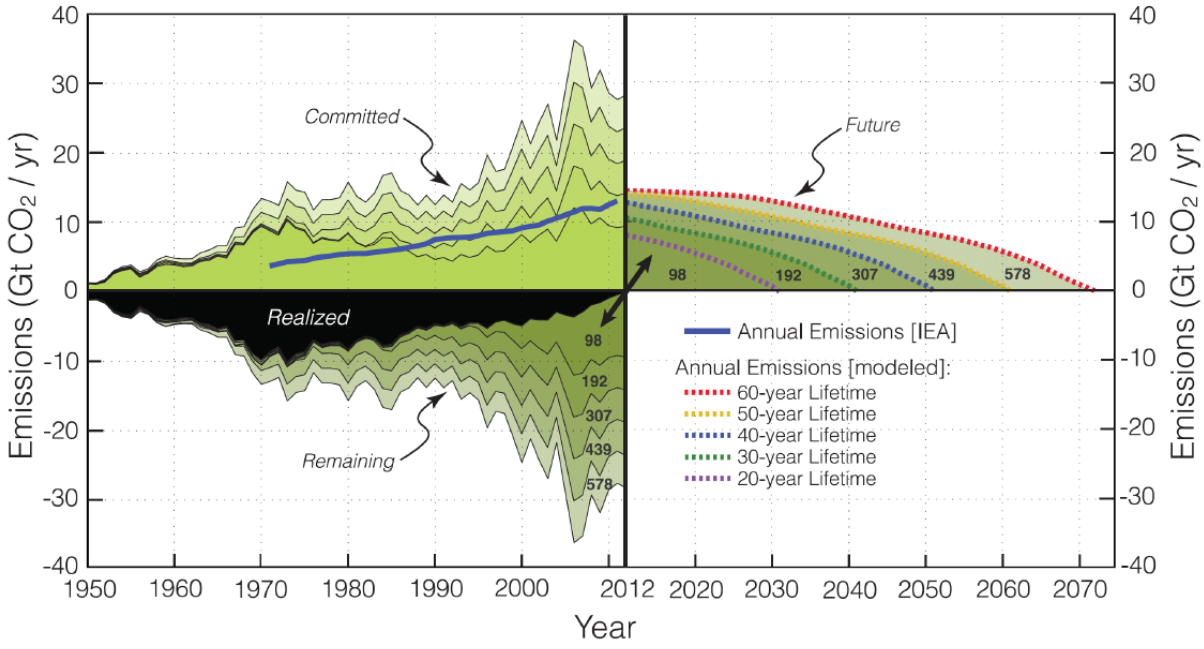

Figure 1.12: *Future CO_2 emissions from committed, realized, remaining and future energy infrastructures [10].*

The main aspect described in this graph is that almost half of the CO_2 emissions that have been committed so far by building fossil power plants worldwide have still to be realized. In fact, every year a certain amount of fossil power plants is being built, considering only the last decade there was installed a capacity of about 1400 $[GW]$. As depicted by the dashed lines in the upper-right of the graph, for each pant is associated an expected lifetime (on average $35 - 40\ yr$) and a specific emission factor evaluated in $[gCO_2\ eq./kWh_{el}]$ terms. Another useful parameter known is the average annual capacity factor defined considering the overall operating hours of the plant in 1 year divided by the total available hours. Hence, once the fossil plant has been built, it is possible to estimate the committed CO_2 emissions that are expected from that specific power plant.

Therefore, the committed emissions are all accounted for in the year in which the plant is effectively put online, and not as energy is produced. As reported by the upper-left part of the graph, more and more fossil power plants are being built since the trend of committed CO_2 emissions is progressively increasing. Concerning the bottom-left part of the graph, it is shown how much of the committed stock of CO_2 emissions has been already realized (black area) and how much is still remaining (green area). Once the committed emission are known, as well as how many of them have been realized and how many are still remaining, it is possible to extrapolate future CO_2 emissions resulting just from the actual fossil fuel plant infrastructure. This is represented by the dashed lines in the upper-right part of the graph, where a sensitivity analysis on the plant lifetime is performed, but, basically, $40\ yr$ of plant lifetime should be regarded as the reference curve. Summarizing, the crucial aspect outlined by this graph is that even if we would stop today to build new fossil power plants, the already existing infrastructure is entailed to a future with significant CO_2 emissions. Furthermore, in this plot are considered only the CO_2 emissions derived from the energy sector without considering other very pollutant sectors as the transport one, hence this again emphasizes the crucial role of CCUS technologies. To mitigate and curb future CO_2 emissions, not only it is necessary to build low-carbon power plants and persecuting the transition towards renewable energy sources, but it is also necessary to retrofit existing power plants with proper carbon capture devices. Thence, concerning new fossil power plants, they should include a carbon capture section as part of their original design.

To conclude this first argumentation, the future of the energy sector should be decarbonized without the implementation of fossil fuels. Nevertheless, there is a large and even growing fossil infrastructure already in place. Hence, the role of CCUS technologies is to act as interim solution to stabilize GHGs emissions while still using fossil power plants.

2) Secondly, CCUS technologies are an effective solution for decarbonize heavy industries, like iron, steel, and chemicals manufacturing where other technology options are limited. In fact, nowadays, CCUS is virtually the only technology able to reduce the emissions from cement production. Furthermore, CCUS can be implemented to produce synthetic fuels for long-distance transport, such as in the aviation field. Concerning this aspect, in the following *Figure 1.13* are represented the main possible pathways that the captured CO_2 from power plants, biomass production or air capture can tread [11]: besides the possibility to directly use the captured CO_2, it can be converted into synthetics fuels and chemicals, and through mineralization into inorganic carbonates.

Others attractive possibilities are the hydrogenation process that allows to methanol production and the production of syngas, namely a fuel composed by a mixture of CO and H_2.

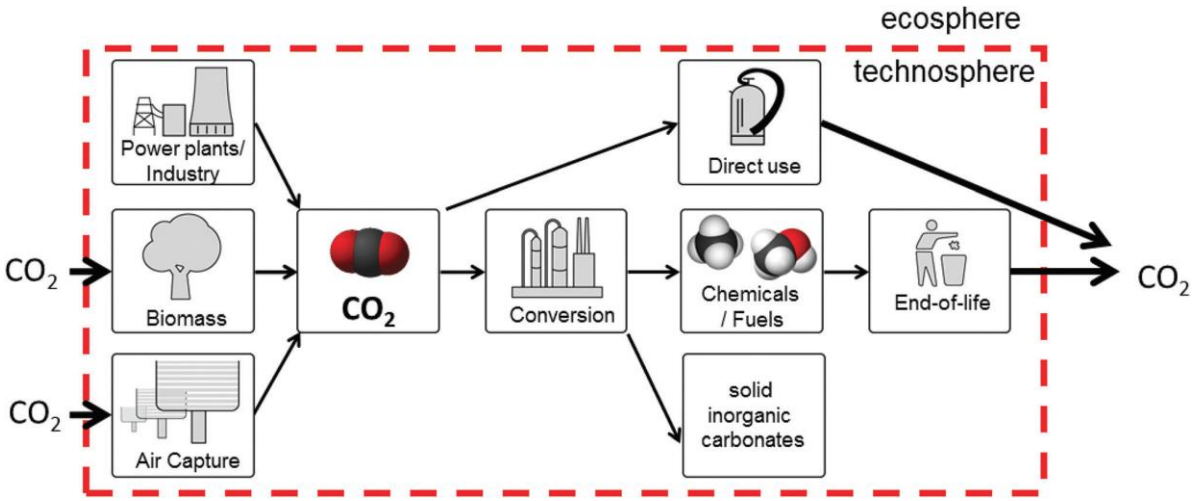

***Figure 1.13**: Possible Pathways of CO_2 captured [11].*

3) Moreover, CCUS can contribute to reach net-zero energy transition because it is a cost-effective pathway for low-carbon hydrogen production. Hydrogen is a versatile energy vector that is crucial to support the decarbonisation in several sectors, as transport, industry, power and buildings. Generally, CCUS can make more simpler the production of clean hydrogen from natural gas and coal in a cost-effective way. In fact, the cost associated to these processes is around half that of producing hydrogen through electrolysis (water splitting reaction to produce hydrogen and oxygen) driven by renewables. Hence, CCUS can facilitate the decarbonise hydrogen production both by reducing emissions from existing hydrogen plant (around 75 $[Mt]$ of H_2 is currently produced for industrial use with more than 800 $[Mt]$ of CO_2 emitted) and by providing a less-expensive pathway to scale up new hydrogen production facilities.

4) In conclusion, another promising application of CCUS is focused on removing CO_2, or more in general carbon compounds, directly from the atmosphere. This kind of processes can facilitate the ambitious climate goals issued by the IPCC previously described. Nevertheless, today the technologies able to directly capture carbon from the atmosphere are technologically challenging and prohibitively expensive.

As discussed before in *Figure 1.10*, the CCUS technologies are based on several steps: CO_2 capture, utilisation and conditioning, transport and storing. Concerning the first step of the chain, namely the CO_2 capture, it is possible to distinguish three different pathways as shown in *Figure 1.14*: the most relevant CO_2 capture technologies are: post combustion carbon capture, pre-combustion and oxyfuel combustion.

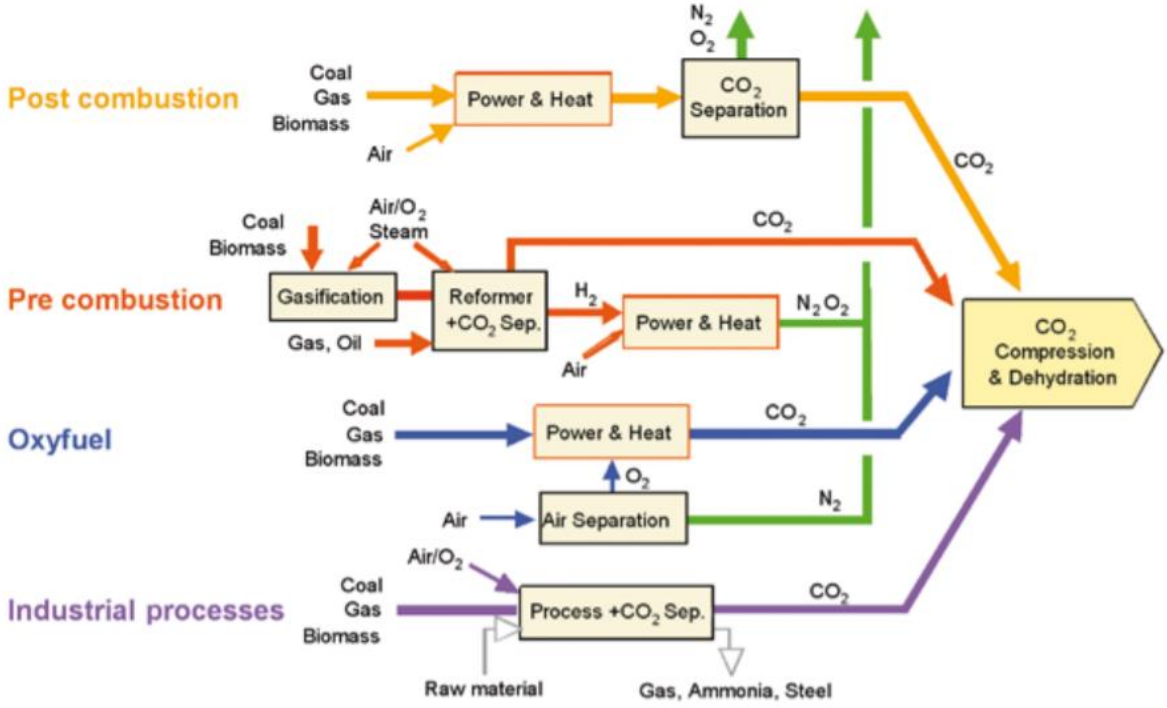

Figure 1.14: *CO_2 Capture Processes [12].*

Considering the first pathway, during post-combustion processes the flue gas containing CO_2 is treated with a chemical solvent to extract selectively CO_2 from nitrogen and water vapour after the combustion phase. The CO_2 separation can be performed through chemical and/or physical absorption. The chemical absorption of CO_2 is based on the reaction between CO_2 and a chemical solvent, as compounds of ethanolamine. As depicted in *Figure 1.15*, typically, this process is carried out using two columns, one for adsorption (scrubber column) and the other operating at higher temperature aimed to release CO_2 and to regenerate the chemical solvent for further operations (regeneration column). This kind of process, namely the chemical absorption using amine-based solvents is the most advanced CO_2 separation technique (Technology Readiness Level TRL 9-11).

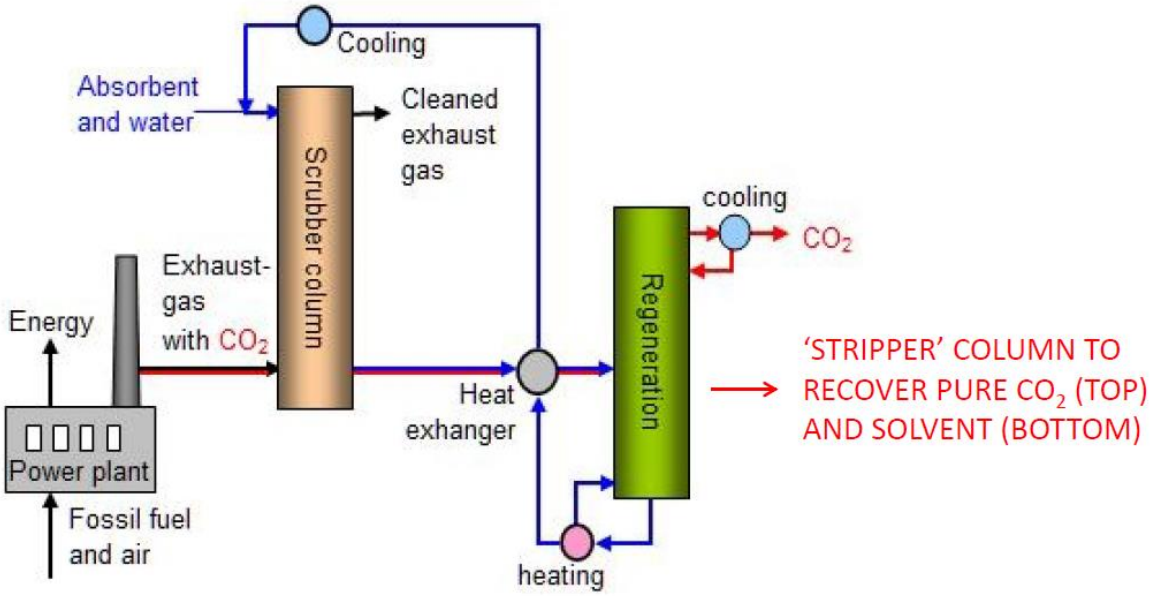

***Figure 1.15**: Post Combustion Process example. Pulvirized Coal Plant with Post-Combustion CCS based on Chemcial Absorbtion using a Monoethanolamine-based Solvent [13].*

The exhaust gas containing diluted CO_2, deriving from a fossil fuel power plant, enters at the bottom of the scrubber column and flows in counter-current with respect to the chemical solvent fed from the top of the column and composed by a solution of Monoethanolamide (MEA) and water. This solvent solution is chilled before entering the scrubber to enhance the chemical absorption process. In this way, at the top of the scrubber column is obtained an almost CO_2-free exhaust gas. At the bottom, in order to start a new absorption cycle with CO_2-free solvent, the CO_2-rich solvent is regenerated into the regeneration column using medium-pressure (MP) steam and high operating temperature. Also the concentrated CO_2 steam is recovered to feed it to the compression train for pipeline transportation. Inside the regeneration column, also named stripper, the CO_2 is stripped off from the solvent; this process is enhanced by the bottom reboiler that helps the separation of the absorbed CO_2 from the amines solution by increasing the temperature level. At the same time, a top re-condenser is used to increment the purity of the recovered CO_2. A heat-exchanger is located between the two columns to recover the thermal energy. In fact, the energy consumption during this process is due to the medium pressure steam for the re-boiler that typically is extracted from the MP stage of the Rankine cycle to reduce its net electricity production, and to the chiller units where the electricity is necessary to drive the refrigeration cycles. A possible option to reduce the energy consumed by the re-boiler is to increase the operating pressure of the stripper column, but simultaneously the cost related to the compression stage increases. A good compromise is to operate with a pressure $p = 2\ [bar]$.

Differently, concerning the second pathway, namely the pre-combustion CCS, CO_2 is removed before combustion takes place. It is typically based on physical CO_2 separation processes and employed in gasification cycles. In turn, physical separation of CO_2 is carried out through either absorption, adsorption, cryogenic separation, or dehydration and compression. Physical absorption implements liquid solvents, like Selexol or Rectisol, on the other hand, physical adsorption a solid surface, such as activated carbon, zeolites alumina. A simple schematic of poly-generation with pre-combustion CO_2 capture is presented in the following *Figure 1.16.*

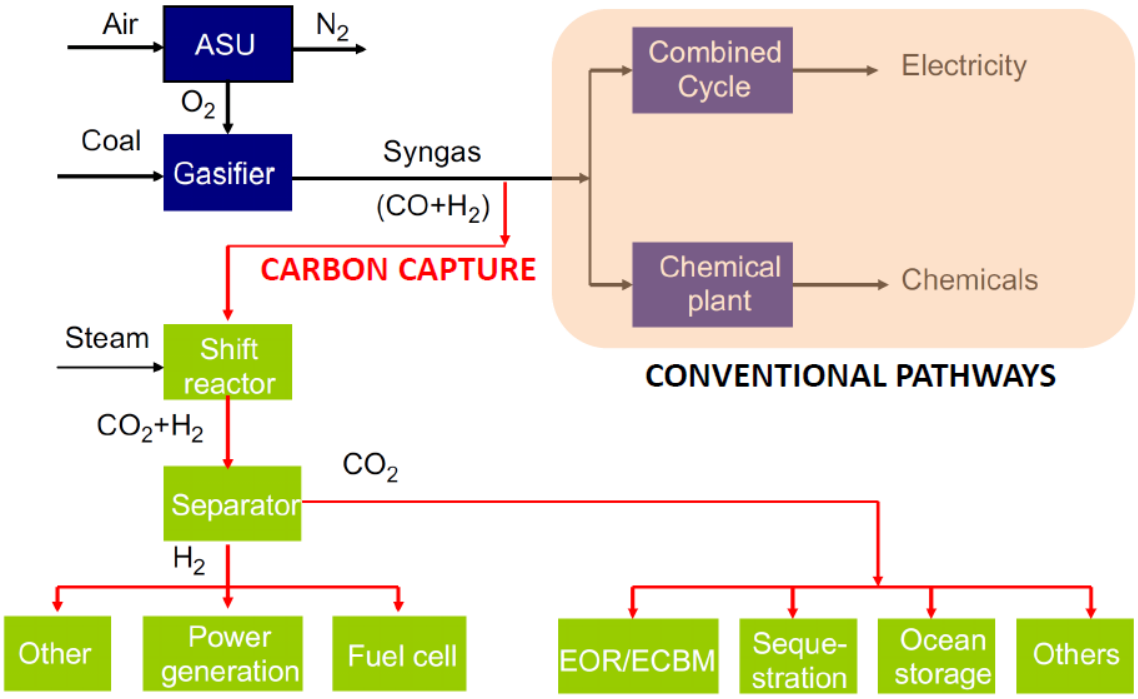

Figure 1.16: *Schematic of Poly-generation with Pre-Combustion CO_2 capture.*

Firstly, in the Air Separation Unit (ASU) air is separated into N_2 and O_2, where the latter becomes the blast for the coal gasifier. Concerning the CCS scenario, the clean syngas ($CO + H_2$) obtained by coal gasification is shifted by means of the exothermic (released heat energy) Water Gas Shift (WGS) reaction to produce a H_2/CO_2 stream:

$$(WGS) \quad CO + H_2O_{(g)} \leftrightarrow H_2 + CO_2 \qquad \Delta\bar{H} = -41 \ [MJ/kmol]$$

Then the separator is used to extract CO_2 from H_2 that can be both consequently implemented in other processes. This separation process can be done via physical/chemical absorption or using a membrane [14] [15].

More precisely, the resulting H_2-rich syngas is used for power generation in a combined cycle adopting H_2-fired turbine or in a more advanced fuel cell cycle, while the recovered CO_2 can be transported to a geological sequestration site or used for EOR or other destinations. A similar process is followed in the case of natural gas processing: in this configuration it is firstly performed the endothermic (external heat source is required) Steam Methane Reforming (SMR) reaction:

$$(SMR) \quad CH_4 + H_2O \leftrightarrow 3H_2 + CO \qquad \Delta\overline{H} = +206\ [MJ/kmol]$$

Then, it is again carried out the WGS reaction to produce CO_2 and enhance the H_2 content [16]. Today physical separation is mainly used in natural gas processing and ethanol, methanol and hydrogen production with nine large plants in operation (TRL 9-11). But the post-combustion CCS remains the predominant process because there are three main issues related to the pre-combustion CCS in connection with an integrated coal gasifier plant:

1. The WGS reaction inside the shift reactor used to convert all the carbon C and carbon monoxide CO into CO_2 molecules is a highly energy intensive process as medium pressure steam is required. More detailed, the WGS reaction is obtained by the combination between the Boudouard (B) reaction and the Water Gas (WG) endothermic reaction, respectively defined as:

$$(B) \qquad C + CO_2 \leftrightarrow 2CO \qquad \Delta\overline{H} = +172\ [MJ/kmol]$$

$$(WG) \qquad C + H_2O_{(g)} \leftrightarrow CO + H_2 \qquad \Delta\overline{H} = +131\ [MJ/kmol]$$

The WGS reaction is precisely the difference between the Boudouard and the Water Gas reaction:

$$(WGS) \quad CO + H_2O_{(g)} \leftrightarrow H_2 + CO_2 \qquad \Delta\overline{H} = -41\ [MJ/kmol]$$

Generally, at the inlet of the shift reactor it is required a $H_2O_{(g)}/CO$ molar ratio equal to 2. Since typically this reactor is designed adiabatic and the WGS reaction is exothermic, more than one reactor is necessary to convert all the CO into CO_2 and an intercooling phase between two subsequent reactors is also needed to re-establish a favorable thermodynamic equilibrium condition before each reactor stage.

2. Another issue is related to the complex design of H_2-fired turbines of the combined cycle needed to accommodate the H_2-rich syngas. Since H_2 is a very calorific fuel, it is quite challenging to perform a pure-H_2 combustion.
3. The third issue is economic-related, in fact there are still high investment costs associated with Integrated Coal Gasification Combined Cycle (IGCC) with a CCS section.

In conclusion, concerning the third possible pathway of CO_2 capture process, during oxyfuel CCS, the fossil fuel is directly burnt with oxygen instead of air obtaining in this way a resulting flue gas without N_2, making the CO_2 separation process simpler. Since an almost stoichiometric oxycombustion is performed, the residual concentration of O_2 in the resulting flue gas is essentially negligible. Thence, this oxicombustion process allows to produce a flue gas that effectively contains only CO_2 and H_2O. Consequentially, by cooling down the flue gas through a proper condenser, the water molecules can be easily condensed out to obtain a stream composed by almost pure CO_2.The energy intensive step related to the CO_2 separation step from the flue gas is avoided, nevertheless the burden in now on the air separation process to extract pure oxygen from atmospheric air. In the following *Figure 1.17* is represented the comparison of CO_2 recovery processes for Integrated Coal Combined Cycle (IGCC): the upper scheme (a) corresponds to a pre-combustion configuration previously explained, while the lower scheme (b) represents the oxyfuel configuration [17].

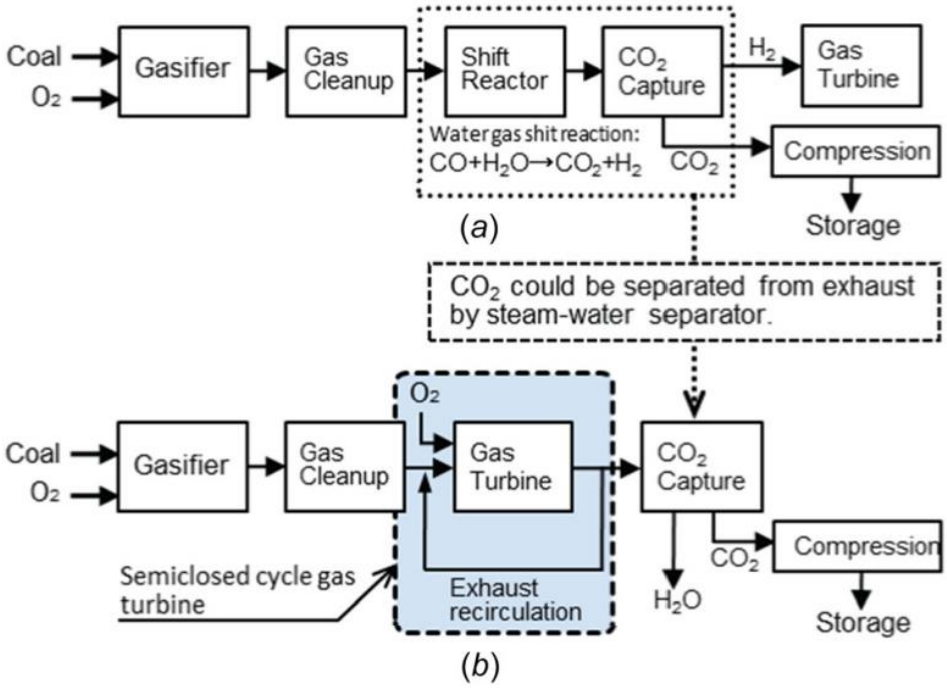

Figure 1.17: *CO_2 recovery processes for IGCCs: (a) pre-combustion configuration; (b) oxyfuel combustion configuration [17].*

The oxyfuel carbon capture technology is currently at the large prototype or pre-demonstration stage (TRL 5-7) and the key factors to reduce the capture costs are focused on lowering the energy consumption of the low-temperature air separation unit, that represents the highest energy-intensive process.

To conclude, another CO_2 capture method investigated in this dissertation and detailed explained in the next chapter is the so-called chemical looping carbon capture process. It is a novel technology that involves CO_2 capture at high temperature using two main reactors: in the first one small particles of metals are used to bind oxygen from the air to form a metal oxide, that is then transported to the second reactor where it reacts with fuel, generating energy and a concentrated stream of CO_2 by regenerating the reduced form of the metal. Finally, the metal is looped back to the first reactor. Nowadays, chemical looping technologies have been developed by academia and research organisations (as in our case where a prototype of chemical looping reactor is located at CO_2 Circle Lab in environment Park Spa, Turin). There are around 35 pilot projects with a capacity up to 3 $[MW]$ for coal, gas, oil, biomass combustion and concerning the TRL, it is still in prototype pre-demonstration stage (TRL 4-6).

Chapter 2

2. Literature Review

2.1 – Chemical Looping Process

As discussed in chapter 1, fossil, liquid hydrocarbon fuels are currently the most implemented ones to satisfy the ever-increasing world energy demand and they will be used in the next years due their demand in transportation and the extensive existing infrastructures. A promising non-fossil alternative are the so-called Synthetic Fuel (Synfuel): this term refers to a liquid fuel produced at commercial scale from low energy content carbonaceous sources, like coal, natural gas, oil shale and other biomass, that are upgraded at the expense of additional energy [18]. In this perspective the most used Synfuel is the Syngas, namely a gas mixture containing CO and H_2, whose exothermic conversion to fuels has been commercially developed several years ago, via the Fischer-Tropsch (FT) technology [19]. This synfuel can be also implemented as a source of pure hydrogen and carbon monoxide [20], in fact hydrogen and syngas basically are the raw energy vectors to produce Synthetic Liquid Fuels (SLF) and other chemicals through established industrial processes. Moreover, these processes can be considered more attractive from an environment point of view if combined with renewables, for instancy by exploiting solar energy [21]. In this case, employing solar energy to produce raw materials for the synthesis of SLF, these fuels can be named Solar Fuels. Generally, there are three main pathways to produce syngas starting as input the solar energy: photochemical (or photobiological) process, thermochemical and electrochemical process [22] [23] [24]. Considering the thermochemical path, typically the renewable systems used as driver of the process are the Concentrated Solar Power (CSP) systems that provide solar thermal energy at high temperature in order to perform various high-temperature reactions aimed to produce syngas through the conversion of fossil and non-fossil fuels. In this dissertation it is investigated the CSP-aided syngas production via Water Splitting (WS)/Carbon Dioxide Splitting (CDS) thermochemical chemical looping processes, especially the set of experimental tests presented in chapter 4 are aimed to investigate the most relevant parameters related to the Carbon Monoxide CO production through CDS reaction exploiting the chemical looping method.

To better visualize the high number of syngas applications, in the following *Figure 2.1* are shown the most relevant multiple processes where the syngas is used for either chemical, fuel and power generation.

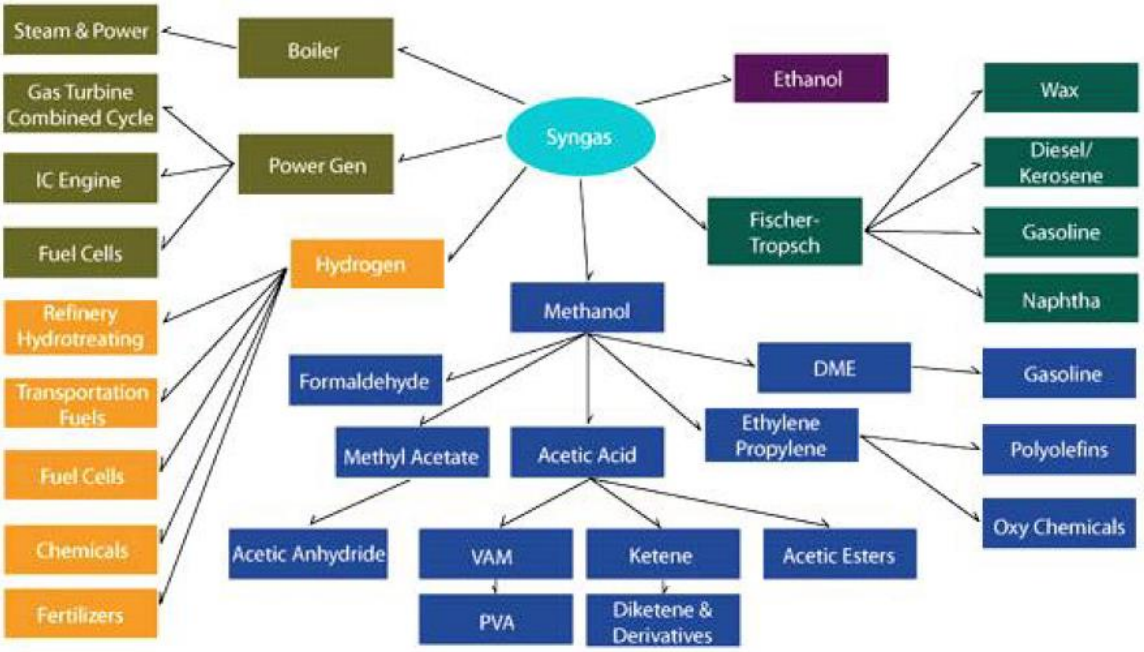

Figure 2.1: *Utilisation Pathways of Syngas in the industrial sector.*

Thermochemical conversions of CO_2 can be performed basically in two methods, namely direct dissociation of CO_2 and chemical looping. The first requires extremely high temperatures in the range between $T = 1900 \div 2400\ °C$ and presents a conversion efficiency of about 6 % of CO_2 transformed into CO, as discussed by Traynor et al. [25]. Nevertheless, due to the high temperature levels and high energy-intensive quenching process, direct dissociation of CO_2 is considered a complex method and unprofitable. Differently, chemical looping method requires lower temperature ($T = 600 \div 1300\ °C$) and it is based on a set of chemical redox reactions occurring inside multiple reactors, where one of the reactants (that is an oxygen carrier) continuously circulates between reactors creating a closed loop as shown in *Figure 2.2.* The oxygen carrier (often a metal oxide) is subjected to oxidation and reduction reactions and, by recirculating inside the loop, it is re-generated and alternated between different oxidation states.

The reactors inside which the redox reactions occur can be two or three units. In the following figure is showed the three-steps configuration.

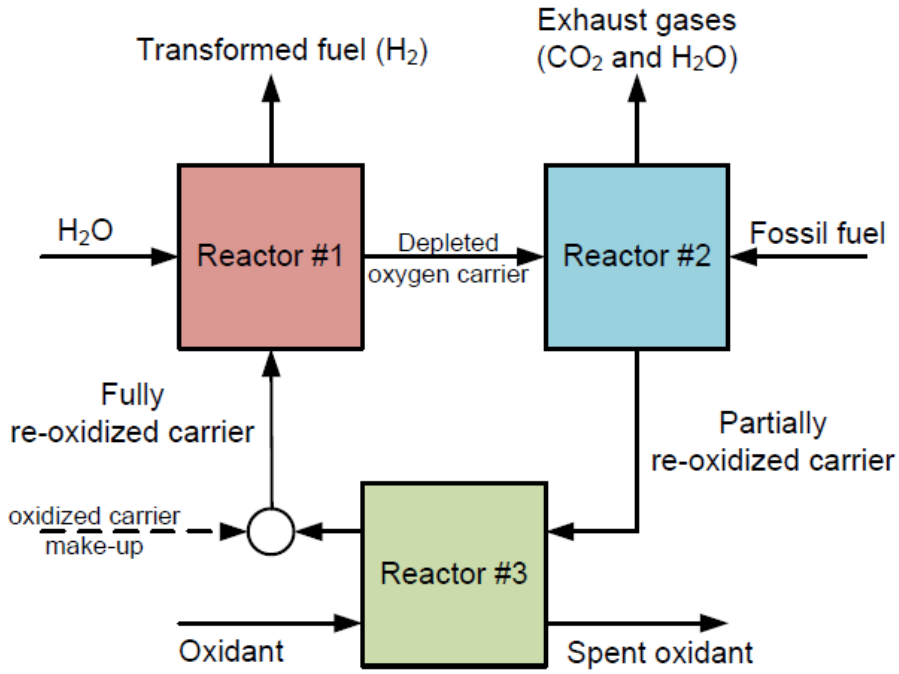

Figure 2.2: *Three reactors set up Chemical Looping scheme.*

To provide a more practical example, in the *Figure 2.3* is described the previous three reactors configuration with a different arrangement using CH_4 as fossil fuel and an iron-based oxygen carrier (Fe_2O_3) as the reactant inside the loop. Inside the Fuel Reactor the fuel CH_4 is converted into CO_2 and H_2O (exhaust gas), while the oxygen carrier Fe_2O_3 is reduced into FeO. Consequently, inside the Steam Reactor the reduced oxygen carrier FeO reacts with steam producing H_2, H_2O and Fe_3O_4 that is converted again into Fe_2O_3 performing an oxidation reaction with the oxygen contained in the air inside the Air Reactor. As indicated by the dashed line in the previous *Figure 2.2*, it is needed a make-up of the reactant into the closed-loop system because, as the number of the looping cycles increases, the iron-based oxygen carrier loss more and more integrity producing leakages inside the system. Typically, the make-up section is located upstream the Steam Reactor. This kind of configuration and oxygen carrier is generally implemented in syngas chemical looping process. More detailed, for capturing CO_2, the Fuel Reactor is a counter-current moving bed reactor, the same for the Steam Reactor able to regenerate the oxygen carrier. Instead, the Air Reactor, responsible of hydrogen production, is normally used a dense fluidized bed air reactor, useful to hydrogen production [26].

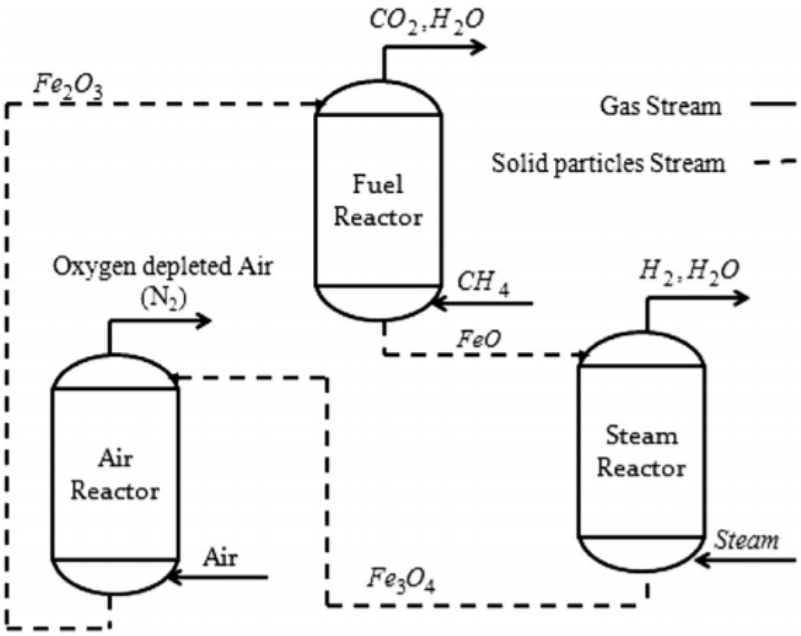

Figure 2.3: *Three reactors set up Chemical Looping scheme using an Iron-based Oxygen Carrier* Fe_2O_3 *and* CH_4 *as fuel [27].*

The three-steps configuration presents several issues related to the temperature swings between the reactors that often are higher than $\Delta T = 100\ °C$ and to the simultaneous occurrence of different redox reactions at different temperature levels; for this reason, regenerative heat exchangers are frequently inserted into the system. A promising alternative is the two-step configuration where the oxidation and reduction reactions occur in two different proper reactors, respectively. Normally, once the reduction is an endothermic reaction ($\Delta\overline{H} > 0$), it requires higher temperature levels compared to the oxidation reaction that is exothermic ($\Delta\overline{H} < 0$), generating a temperature difference between the two reactors. But in some circumstances, it is possible to operate in isothermal conditions that, often are more energetically convenient with respect to the non-isothermal ones. Hence, chemical looping process can be performed in several ways depending on the typology of oxygen carrier, of the reactors implemented and on the operating conditions imposed. A possible option very similar to the oxycombustion CO_2 capture method previously explained, is the Coal Direct Chemical Looping (CDCL) process. The advantage of this method, compared to oxycombustion, is that it is not required a pure steam of oxygen to perform the combustion and so the challenging design of the Air Separation Unit (ASU) is not more needed [28]. CDCL implements a counter-current moving bed fuel reactor, at the contrary, the Coal To Syngas Chemical Looping (CTSCL) process involves a co-current moving bed fuel reactor.

Other options, illustrated in *Figure2.4*, using a Packed Bed Reactor (PBR), are the Chemical Looping Combustion (CLC) and the Chemical Looping with Oxygen Uncoupling (CLOU). The main difference compared to the moving bed fuel reactor applications. Is that in this case the redox oxygen carrier material does not move into the closed loop cycle, but it remains stationary inside the PBRs. Concerning the CLC process, the oxygen used during the combustion step is not more injected though an extern air or oxygen steam, but it is transported by the oxidized oxygen carrier. Hence, inside the PBR the oxygen carrier is firstly oxidized using air and then reduced in the fuel reactor by the fossil fuel stream. Theoretically, CLC is quite similar compared to the chemical looping process investigated in this work and, as usual, the goal of this process is to decarbonize the fossil fuel generating CO_2 and consequentially separated it form the exhaust gases [29]. Considering the CLOU process, the only difference with respect to CLC is that in this case the oxygen transported by the oxygen carrier is released inside the fuel reactor and then used inside to perform the combustion reaction.

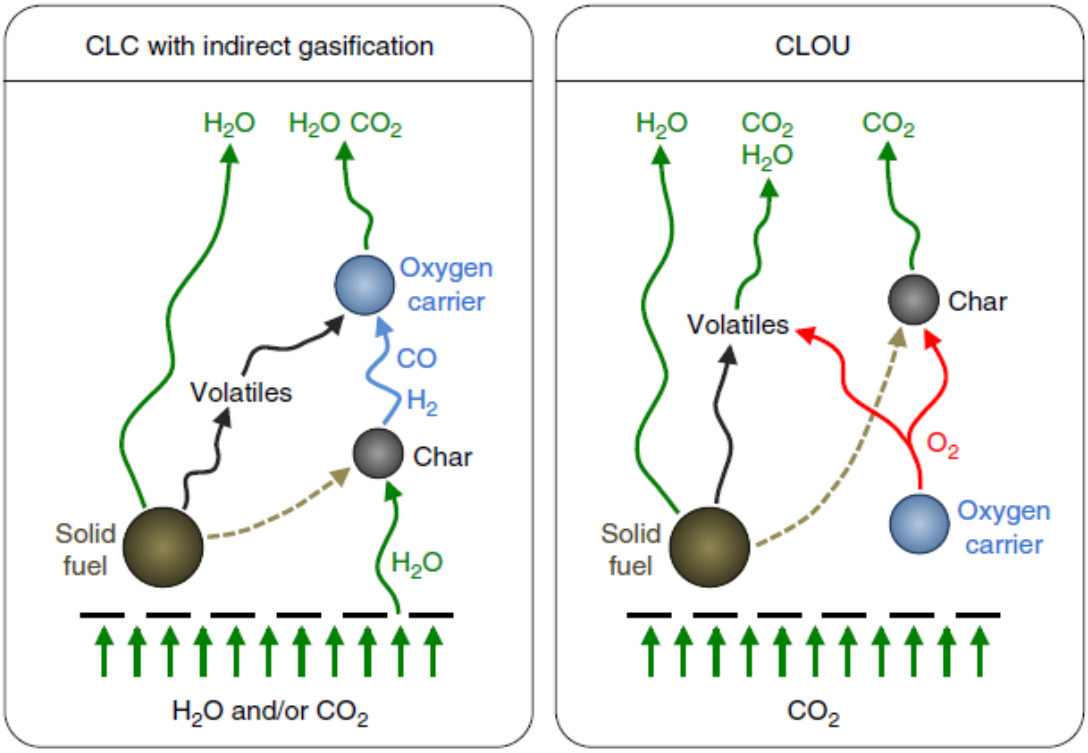

Figure 2.4: *CLC and CLOU process scheme [30].*

2.2 – Chemical Looping for CO_2 and H_2O Splitting

In this section it is more deeply investigated the chemical looping process presented in this dissertation. The goal of Chemical Looping (CL) novel method is to produce syngas ($CO + H_2$) by splitting CO_2 and H_2O to produce CO and H_2, respectively. The most common configuration consists of a circulating closed loop composed by two interconnected reactors (reduction and oxidation reactor) that contain metal oxides particles, subjected alternatively to reduction and oxidation step. The main driver of this process is the spontaneous release of oxygen molecules by the metal oxide's crystalline lattice generated during the thermal reduction reaction at high temperature level (above $T = 1300\ °C$) or through the fuel reduction reaction. Thanks to the oxygen release, a large amount of oxygen vacancies is created inside the lattice of metal oxide. After the reduction step, the reduced metal oxide is re-oxidized in the low temperature oxidation reactor at around $T \cong 1000\ °C$, using water and/or carbon dioxide. This is the main advantage of CL process, compared to other thermochemical cycles it is possible to perform simultaneously the WS and CDS reaction. In addition, as shown in *Figure 2.5*, since the thermal reduction reaction requires heat at high temperature, the CL process integrated with a CSP system is extensively promising to split CO_2 and H_2O.

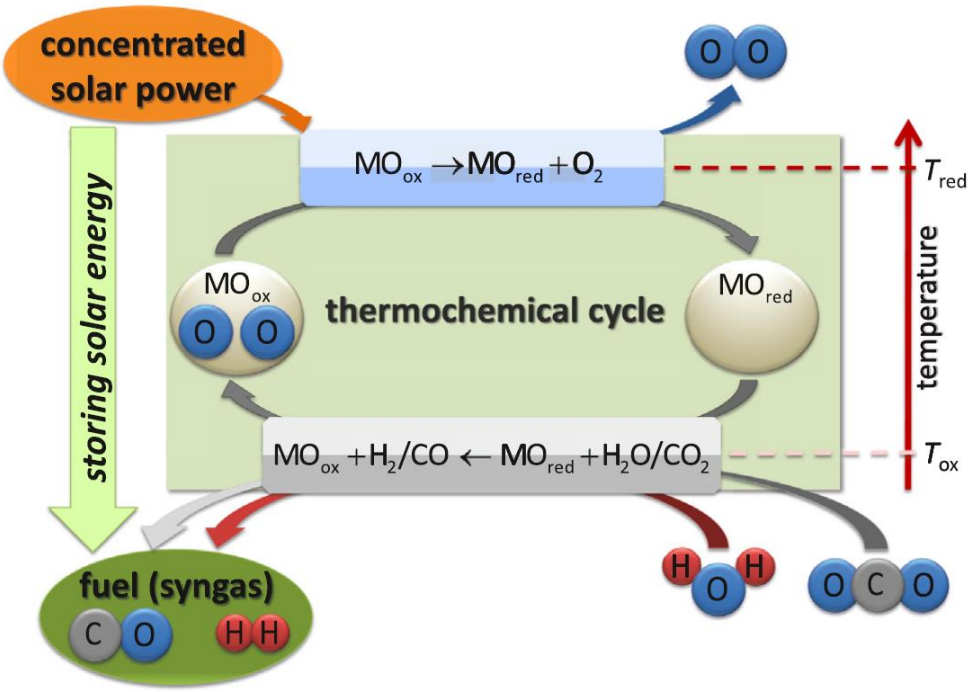

Figure 2.5: *General schematic of the CSP-aided, two-step, redox-pair-base, water and/or carbon dioxide splitting chemical looping process [31].*

The reactions above mentioned are listed below:

$$Thermal\ reduction\ (TR):\ MeO_x\ \rightarrow\ MeO_{x-\delta} + \frac{1}{2}O_2$$

$$Water - splitting\ (WS):\ MeO_{x-\delta} + \delta H_2O\ \rightarrow\ MeO_x + \delta H_2$$

$$CO_2 - splitting\ (CDS):\ MeO_{x-\delta} + \delta CO_2\ \rightarrow\ MeO_x + \delta CO$$

Concerning the TR reaction, it useful to mention that it is favoured at high operating temperature (above $T = 1300\ °C$) and with a very low oxygen partial pressure (vacuum pressures); otherwise, the WS/CDS reaction is promoted at low temperature levels ($T \cong 1000\ °C$) and with high oxygen partial pressure. Thence, in the two-step CL process typically it is present a pressure and temperature difference between the two interconnected reactors. Anyway, it is also possible to operate in isothermal conditions in the case of a reducing fuel, and at pressure levels near to the atmospheric ones in the case of a strongly reducing environment. In fact, by increasing the reducing rate, it is possible to lower the reduction temperature until reaching the oxidation temperature level.

Nevertheless, a promising method useful to reduce the temperature level of the process, is to combine the redox cycle with the methane reforming [32] [33]. This method, called Chemical Looping Methane Reforming (CLMR), is composed by a first step aimed to convert methane CH_4 into syngas ($CO + H_2$) using a suitable oxygen carrier (typically metal oxides) at a temperature range of about $T = 800 \div 1000\ °C$, in agreement to the following reaction:

$$MeO_x + \delta CH_4\ \rightarrow\ MeO_{x-\delta} + \delta(CO + 2H_2)$$

Then, during the second step, it is generally performed the CDS/WS reaction using water and carbon dioxide, as previously described. Hence, $Me_{x-\delta}$ reacts with incoming CO_2 and H_2O producing respectively CO and H_2 by re-incorporating oxygen molecules into the lattice. The two schemes proposed, CL and CLMR, and their differences, are represented in *Figure 2.6*.

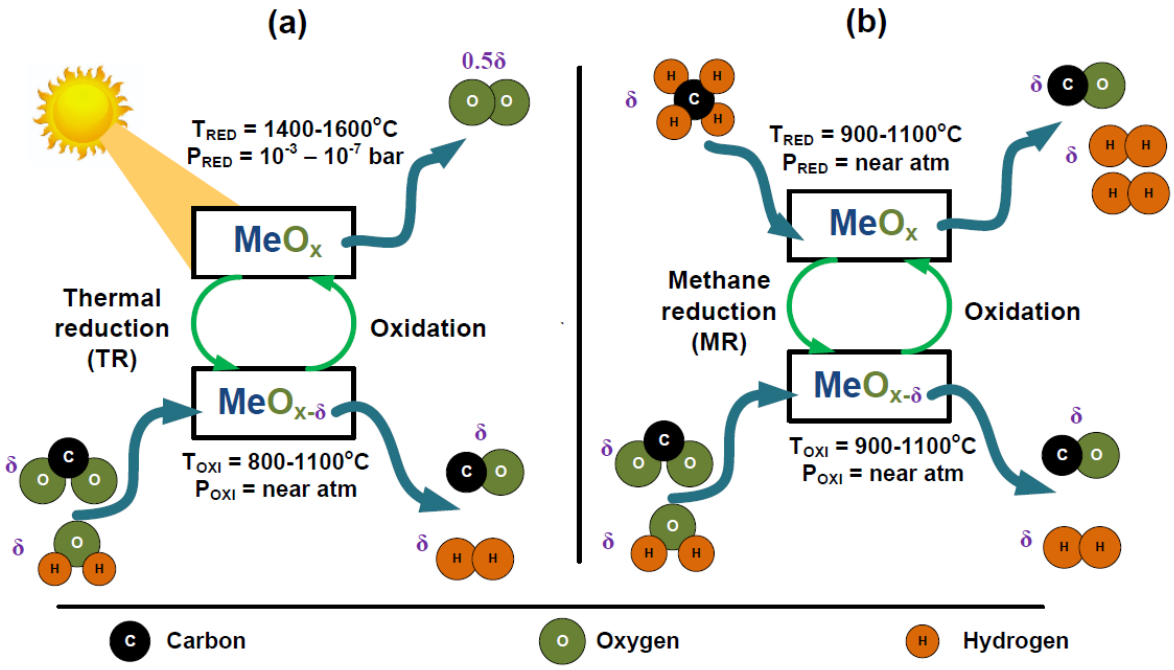

Figure 2.6: *(a) CL and (c) CLMR processes schemes [32] [33].*

In the two configurations, the oxygen carrier during both the Thermal Reduction (TR) and Methane Reduction (MR) reaction is often reduced to a non-stoichiometric extent δ. More precisely, this means that 0.5δ moles of oxygen are released during the thermal reduction step from the oxygen carrier. This release causes the creation of oxygen vacancies that, during the consequent oxidation step, are occupied by water/carbon dioxide molecules. In this way, it is produced hydrogen/carbon monoxide, and this indicates that the creation of oxygen vacancies is the driver of both CL and CLMR process. In this perspective, one of the crucial requirements that the oxygen carrier (looping material) should have, is the ability of generating oxygen vacancies and this property strictly depends on the crystalline lattice structure of the oxygen carrier. Furthermore, the CLMR method presents some advantages compared to CL. Firstly, CLMR represents a promising alternative to the current high energy-intensive industrial process of Steam Methane Reforming (SMR) for syngas production. In addition, since the Methane Reduction (MR) needed pressure levels near to the atmospheric ones and fuel reduction, it is possible to reduce the oxygen carrier at atmospheric pressures, hence thanks to this benefit, it can avoid the pressure swing across the two-step interconnected reactors.

At the contrary, one of the most relevant drawback of CLMR process, or more in general in the processes related to carbonaceous fuels, is the carbon deposition phenomenon. It consists on the creation of carbon solid particles deposited on the surface causing a decrease in the redox performance. More precisely, this phenomenon occurs during the reduction steps via two different reactions, namely the Boudouard (B) and the Methane Dissociation (MD) reaction:

$$(B) \qquad 2CO \quad \leftrightarrow \quad C_{(s)} + CO_2$$

$$(MD) \qquad CH_4 \quad \leftrightarrow \quad C_{(s)} + 2H_2$$

The carbon $C_{(s)}$ produced can be transported by the oxygen carrier and reacts also inside the oxidation reactor with CO_2 and H_2O as follows:

$$C_{(s)} + H_2O \rightarrow CO + H_2$$

$$C_{(s)} + CO_2 \rightarrow 2CO$$

In both reactions are produced syngas components, hence concurring with the oxidation step of the reduced oxygen carrier, its ability in terms of redox performance is strongly negatively affected.

In this dissertation it is investigated the Chemical Looping (CL) method, evaluating the redox performance of a double perovskite oxygen carrier considering a two-step thermochemical cycle for CO_2 dissociation producing CO. Therefore, it considered only the CDS reaction, and not the WGS reaction. In the next chapter 3 and 4 are described the experimental procedures and the results obtained by the experimental tests, respectively.

2.3 – Looping Materials as Oxygen Carriers

The key to success for chemical looping is the choice of the looping material. The fundamental phenomenon that governs the feasibility of these processes and consequently their convenience or not, is the creation of oxygen vacancies within the material matrix during the reduction step. In fact, the looping materials are called oxygen carriers due to their ability to exchange and transport oxygen molecules assuming different state of oxidation. This fundamental property is defined as the usable oxygen in the oxygen carrier during one redox cycle which determines the fuel conversion and the circulation rate. This crucial characteristic not only depend on the thermodynamic conditions (operating temperature and partial pressure of the chemical species), but also on diffusion phenomena and reaction kinetic based on the component chemical structure as well as texture properties such as particle size, porosity and specific surface area. A suitable perovskite used as oxygen carrier presents the following characteristics:

- It requires an excellent oxygen transport capacity with a large range of oxygen non-stoichiometry ions.
- Then, a good oxygen carrier should present high reactivity at high temperature, but this temperature must be below and far their melting point.
- The looping material should have a sufficient stability in the sense that it withstands multiple cycles without large loss in the integrity of physicochemical properties.
- Finally, it obviously must me cost-effective especially for industrial application and environmentally friendly to keep the whole process green without GHG emissions.

Several redox pairs used as oxygen carrier for WS/CDS thermochemical cycles are deeply investigated in literature [34] [35] One of the most relevant classification of the materials for chemical looping regards how they change their chemical structure through the various steps of the redox cycle. Hence, they can be divided into volatile and non-volatile in agreement to whether the oxygen carrier containing chemical species changes its state during the whole process or remains in condensed state, correspondingly. Concerning the volatile oxygen carrier, since the temperature level required by the thermal reduction reaction is high, the reduced chemical species can exhibit a solid-to-gas transition of the other-than-oxygen product (both the metal or the lower valence oxide) during the reduction step. Differently, the non-volatile oxygen carriers present the same solid phase during both reduction and oxidation state.

2.3.1 – Volatile Oxygen Carriers

The most common volatile oxygen carriers include Zinc, Cadmium, Germanium and Tin Oxides. As discussed before, this kind of oxygen carrier can be subjected to a solid-to-gas phase transition during the reduction step. This phenomenon is strictly related to the high temperature level reached during the thermal decomposition reaction, in fact the volatile oxygen carriers often exceed the boiling temperature of the reduced contained chemical species. This eventual phase transition is a positive aspect from a thermodynamic point of view because, in this way, it is obtained a high entropy gain. Notwithstanding, this phase transition process introduces several issues mainly related to the recombination of the other-than-oxygen product of the decomposition reaction with oxygen back to the initial reactant in the gas stream produced; therefore, the principal issue of volatile cycles is how to avoid the recombination of the decomposition products back to the oxidized state of the oxide. In the next section is presented a briefly description of the most common volatile cycles, even if in this dissertation it is investigated a non-volatile perovskite oxygen carrier.

The Zinc Oxide ZnO/Zn Cycle

The ZnO/Zn cycle is characterized by a combination of favourable thermodynamic properties because the zinc element is sufficiently non-precious to react with water and presents a low atomic weight and consequentially a high energy content per mass being attractive as a transportable energy vector [36]. Nevertheless, the thermal reduction decomposition of ZnO requires a temperature of about $T = 2300\ K$, and Zn has a melting point at $T = 692\ K$, and a boiling point at $T = 1180\ K$. This type of oxygen carrier has been extensively studied by a research group at Swiss Federal Institute of Technology [37], mainly focusing on the thermal reduction aspects and obtaining a solar-to-chemical energy conversion of about 39 %. At first instance, the primarily application of ZnO/Zn cycle is for WS reaction to produce hydrogen, but in recent years it is investigated also the CDS reaction for carbon monoxide production. An example of WS/CDS thermochemical cycle using ZnO/Zn is represented in *Figure 2.7*. The first step corresponds to the zinc oxide thermal reduction (TR) decomposition and it is based on the following reaction that presents a high endothermicity:

$$(TR) \qquad ZnO \rightarrow Zn + \frac{1}{2}O_2$$

The second step of the cycle corresponds to the WS/CDS exothermic reaction, producing H_2 and CO, that normally occurs at temperature levels lower than $T = 1400\ K$.

$$(WS) \qquad Zn + H_2O \rightarrow ZnO + H_2$$

$$(CDS) \qquad Zn + CO_2 \rightarrow ZnO + CO$$

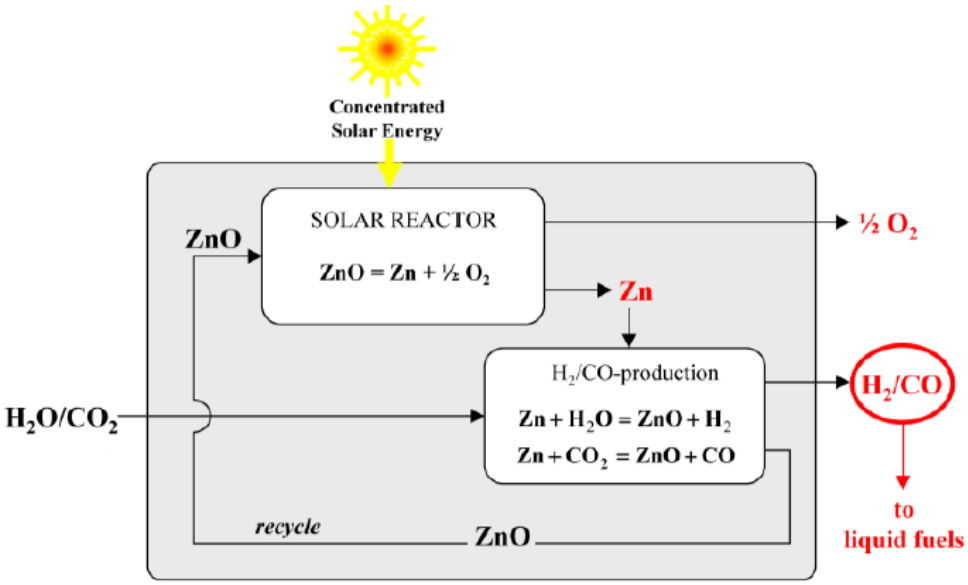

Figure 2.7: *ZnO/Zn two-step WS/CDS thermochemical cycle [38].*

As discussed before, ZnO/Zn cycle is thermodynamically favourable, however it is often subjected to the issue related to the recombination of oxygen decomposition products back to the oxidized state of the oxide.

The Zinc Oxide CdO/Cd Cycle

The CdO/Cd cycle is one the first one analysed in the early '80s [39]. The cadmium oxide thermal decomposition occurs at a temperature range $T = 1423 \div 1723\,K$ following this reaction:

$$CdO \rightarrow Cd + \frac{1}{2}O_2$$

As usual, also in this case it is needed a energy-intensive quenching process to avoid the recombination of Cd with O_2. During the second oxidation step, it occurs the hydrolysis of Cd producing hydrogen from molten Cd. Typically, a fluidized bed reactor integrated with a CSP systems is designed for this kind of cycle. However, due to the high toxicity of Cd, there are not so many recent studies for real-world applications.

Generally, the first drawback is that these volatile oxygen carriers exhibit a solid-to-gas phase transition during the reduction step, for this reason these alterations render their utilization in a cyclic process to be challenging because of the ever-changing physical properties over time and difficulty in preventing reverse reactions when cooling. Then another drawback is the high endothermicity of the Thermal Reduction corresponding to high temperature values (for instance considering the Zinc oxide cycle, the reduction temperature required is about 1900 °C). So, to ensure thermal integrity these materials are very expensive. However, at this high temperature, the main problem is the recombination of the reduced volatile metals with the released oxygen. As consequence, a high energy intensity quenching process to fast cool the metal is an indispensable step to remove oxygen from metal vapours. Nevertheless, during the quenching process, a certain amount of oxygen recombines with the metal oxide reducing the overall effectiveness and efficiency of the cycle. Finally, the most relevant benefit of the use of volatile materials is that these looping materials typically perform stoichiometric redox reactions, this means that all the Oxygen released during the reduction step is taken back during the oxidation step. Given these disadvantages, the study of these materials has recently been left out, giving more space on non-volatile materials that don't require strong post-reduction removal.

2.3.2 – Non-Volatile Oxygen Carriers

The most popular non-volatile oxygen carriers for WS/CDS thermochemical cycles are ferrites, ceria, hercynite and perovskite cycles. Firstly, these looping materials remain condensed, solid during the whole process and require lower endothermicity and so lower temperature values during the Thermal Reduction (in some cases the temperature is below 900 °C). As a consequence, the recombination issue is avoided and since they remain in the solid state throughout the process their physicochemical characteristics such as surface area, particle size, intra-particle porosity, are maintained constant during the operating conditions. Another direct consequence of the lower temperature is the needed of a rapid and low energy intensity quenching process. In conclusion, a drawback is the non-stoichiometric condition of the redox reactions corresponding to a lower oxygen storage capacity than volatile oxygen conveyors.

The Ferrites' Cycle

The ferrites cycles are initially investigated only for WS thermochemical cycle, but recently, these studies are extended to include CDS, both separately or simultaneously with WS [40]. The thermal decomposition reaction occurs at still high temperature ($T = 1600 \div 1700\ K$). An example of ferrite cycle is the magnetite/wustite cycle, studied for the first time by Nakamura [41]. As usual, this cycle is composed by a reduction and an oxidation step following these reactions, respectively:

$$Fe_3O_4 \rightarrow 3FeO + \frac{1}{2}O_2$$

$$3FeO + H_2O \rightarrow Fe_3O_4 + H_2$$

This kind of iron oxides are implemented in several applications, as the CLC process, but in this case, it is mainly adopted a three reactors configuration. Nevertheless, the recent studies are not so focused on these cycles due to the strong limitation related to the still high temperature level during the reduction step. The main cause of the required high temperature is the sintering of the oxide resulting in smaller particles size negatively affecting the redox performance. In fact, with smaller oxide particles size, the H_2/CO production rate obtained by WS/CDS reaction significantly decreases.

The Ceria Cycle

Among all studied non-volatile oxygen carriers, the ceria oxygen carrier CeO_2 is established as the state-of-art redox material due to its promising thermodynamic and physical-chemical properties, such as the slight effect of sintering at high temperature, rapid reaction kinetics, sufficient mechanical strength and structural stability. As discussed by Abanades et al. [42], due the extreme temperature level (above $T = 2300\,K$) required by the stoichiometric reduction from Ce^{4+} to Ce^{3+}, the studies are mainly focused on a non-stoichiometric thermal reduction that occurs at about $T = 1500\,°C$ though the following reactions:

$$2CeO_2 \rightarrow Ce_2O_3 + 0.5O_2$$

$$CeO_{2-\delta_{ox}} \rightarrow CeO_{2-\delta_{red}} + \left(\frac{\delta_{red} - \delta_{ox}}{2}\right) O_2$$

Then, as usual, the following step consists of WS/CDS at a lower temperature level ($T = 600 \div 1000\,°C$) as follows:

$$(WS) \quad CeO_{2-\delta_{red}} + (\delta_{red} - \delta_{ox})H_2O \rightarrow CeO_{2-\delta_{ox}} + (\delta_{red} - \delta_{ox})H_2$$

$$(CDS) \quad CeO_{2-\delta_{red}} + (\delta_{red} - \delta_{ox})CO_2 \rightarrow CeO_{2-\delta_{ox}} + (\delta_{red} - \delta_{ox})CO$$

In these reactions the terms δ_{red} and δ_{ox} indicate the non-stoichiometry content after the reduction and oxidation reaction, respectively. Their difference provides an evaluation of the amount of fuel that can produced per mols of CeO_2 reacted. As discussed by Chueh et al. [43], the ceria oxide CeO_2 is considered a ste-of-art redox material due to its very high diffusion coefficient and a considerable entropy gain (a parameter strictly related to the ability to exchange oxygen molecules). As a result, CeO_2 is able to release a remarkable amount of oxygen molecules and, at the same time, thanks to its thermodynamic properties, it is generally possible to reduce the temperature swing between the reduction and oxidation step. A schematic example of two-step thermochemical ceria oxide-based cycle is depicted in *Figure 2.8*.

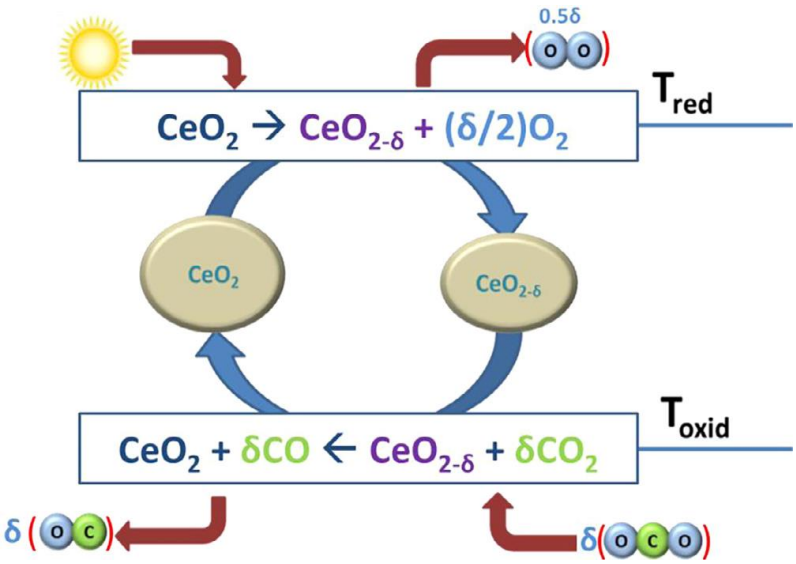

Figure 2.8: *Two-step solar energy-aid ceria-based thermochemical cycle [44].*

To conclude, in the following *Table 1* are summarized the redox temperature range for the most implemented oxygen carriers in chemical looping processes, both volatile and non-volatile. In detailed, the first three rows correspond to volatile oxygen carriers, while the last four rows the non-volatile oxygen carriers.

Table 1: *Redox temperature ranges for the most common oxygen carriers.*

Material cycle	Temperature range (ºC)
Tin cycle	600-1600
GeO_2/GeO cycle	1400-1800
CdO/Cd cycle*	1150-14-1723
Ferrite cycle	927-1327
Zinc cycle	1127-1727
Ceria	700-1600
Perovskites	1000-1600

*Cd is toxic and has very few studies

2.3.3 – Perovskite Oxygen Carriers

Perovskite oxides has been extensively studied in recent years as promising alternative to other materials in several energy applications. They are broadly implemented in fuel cells [45] and in oxygen permeable membranes [46] for their reversibility in releasing and picking up oxygen molecules at high temperatures. They are currently a confirmed alternative to the ceria oxides [47]. The main reason that perovskite oxides have been receive fast-growing interest for WS/CDS chemical looping thermochemical cycle is because they satisfy many looping materials requirements:

- They present an excellent oxygen exchange capacity thanks to the lattice defects.
- Perovskite oxides are energetically stable and very versatile material class being able to structurally accommodate a large variety of elements of the periodic table.
- In contrast to materials which decompose or change their phase during thermochemical redox cycles, perovskites are supposed to retain a single phase under reducing and oxidizing conditions for long-term durability assuming also the role of reagent during the oxidation step.
- Finally, they present environmentally favourable characteristics, and they can be reproduced on a large scale and at competitive costs for the future.

In the *Figure 2.9* is represented the ideal perovskite structure that adopts a cubic symmetry and crystallize in the space group $Pm\bar{3}m$: P means Primitive lattice type (unit cell that contains one and only one lattice point that is the position in the unit cell where the probability of finding an atom or ion is the highest), and $Pm\bar{3}m$ symbol refers to a cubic space group with the threefold symmetry of the body diagonals. The chemical formula is ABX_3, where A is a large alkaline or rare earth cation 12-fold coordination (as for example Calcium, Strontium), B is a smaller transition metal cation with octahedral, 6-fold coordination (Iron, Chromium) and X is the superoxide ion O_2^- that bond to both cations [48]. The A-site cation is responsible for the thermal resistance, while the B-site cation is responsible for the reactivity and catalytic activity in chemical looping reactions [49]. As a result, the selection of the B-site cations is crucial in the design of promising perovskite-structure oxygen carriers. In addition, the interaction between the A and B cations can affect the reactivity during redox reactions as well as the stability of the structure.

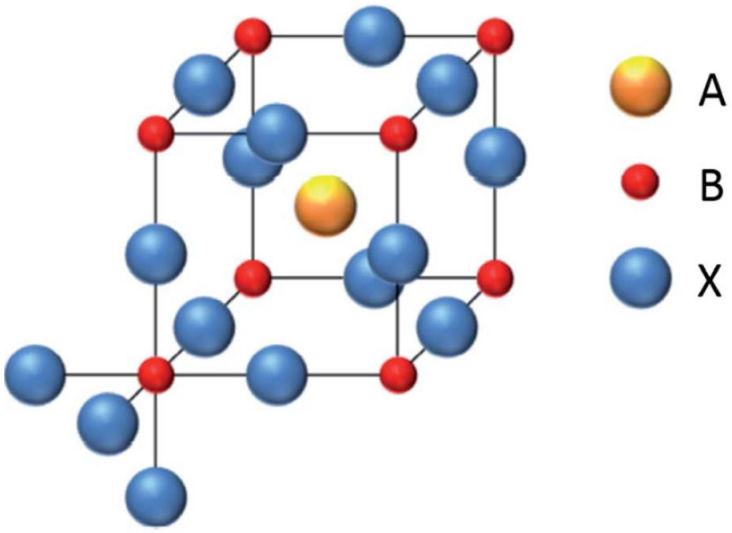

Figure 2.9: *Ideal cubic $Pm\bar{3}m$ structure of ABX_3 perovskite [50].*

As depicted by the previous figure, the A cations are located at the center of the perovskite chemical structure that contains corner-shared BO_6 octahedra sites composed by oxygen anions O_2^- inside which a B cation is enclosed. Thanks to this lattice arrangement, it is possible to adopt doping process to enhance magnetic, ionic and electronic properties basing on the radius size of the dopant element incorporated. This is mainly due to the size mismatch between the $A-X$ and $B-X$ chemical bonds, in fact the radius size of A cation is often higher than that of B cation. Therefore, a break from the ideal cubic $Pm\bar{3}m$ symmetry is regularly observed depending on the ABX_3 elements selected for the structure. The large variety of electronic, ionic or magnetic that can be achieved with perovskites is a consequence of the large number of chemical elements and different cations that can successfully be incorporated on the A- or B-sites in the crystal lattice. This structural flexibility to stabilize several different distorted lattices can be analysed considering the *Goldschmidt tolerance factor* t that defines the relationship between the structural geometry and the ionic bonds length:

$$t = \frac{r_A + r_O}{\sqrt{2}(r_B + r_O)}$$

This tolerance factor is based on the ionic radii r_A, r_B and r_O of A, B and O elements, respectively. The ideal cubic structure is verified if $t = 1$, at the contrary higher or lower deviations from $t = 1$ demonstrate an increased tendency for structural distortion in the lattice. For instance, a rhombohedral structure is obtained if $t > 1.02$ and an orthorhombic or tetragonal structure if $t < 1$. The deviations can be induced both on the perovskite chemical species and on the operating conditions; the most relevant examples are the double perovskite structures ($A_2B_2O_{5+\delta}$) and the Ruddlesden-Popper phase ($A_{n+1}B_nO_{3n+1}$) [51], and anti-perovskites where A and B are anions sites.

Concerning the two-step thermochemical cycles, the perovskite as oxygen carriers for CO_2/H_2O splitting has received fast growing interest thanks to their ability to accommodate a large number of oxygen non-stoichiometry and a well-fitting enthalpy of formation. For this reason, it is enhanced the oxygen vacancies generation during the reduction step, the main driver of the chemical looping process. As generally explained before, the thermochemical production of syngas consists of a series of endothermic and exothermic reaction steps during which the perovskite metal oxide is reduced by solar thermal energy and then the reduced metal is oxidized by either water and carbon dioxide to produce syngas, hence hydrogen and carbon monoxide. More detailed, as described by the following reactions, the perovskite-based two-step CO_2/H_2O splitting thermochemical cycle is composed by a high temperature reduction step during which the perovskite oxide is thermally reduced, and by a consequent oxidation step during which CO and H_2 are produced by splitting CO_2 and H_2O:

$$ABO_{3-\delta_{ox}} \rightarrow ABO_{3-\delta_{red}} + \left(\frac{\delta_{red} - \delta_{ox}}{2}\right) O_2$$

$$ABO_{3-\delta_{red}} + (\delta_{red} - \delta_{ox})H_2O \rightarrow ABO_{3-\delta_{ox}} + (\delta_{red} - \delta_{ox})H_2$$

$$ABO_{3-\delta_{red}} + (\delta_{red} - \delta_{ox})CO_2 \rightarrow ABO_{3-\delta_{ox}} + (\delta_{red} - \delta_{ox})CO$$

In *Figure 2.10,* it is depicted a simple scheme of perovskite-based two-step chemical looping process.

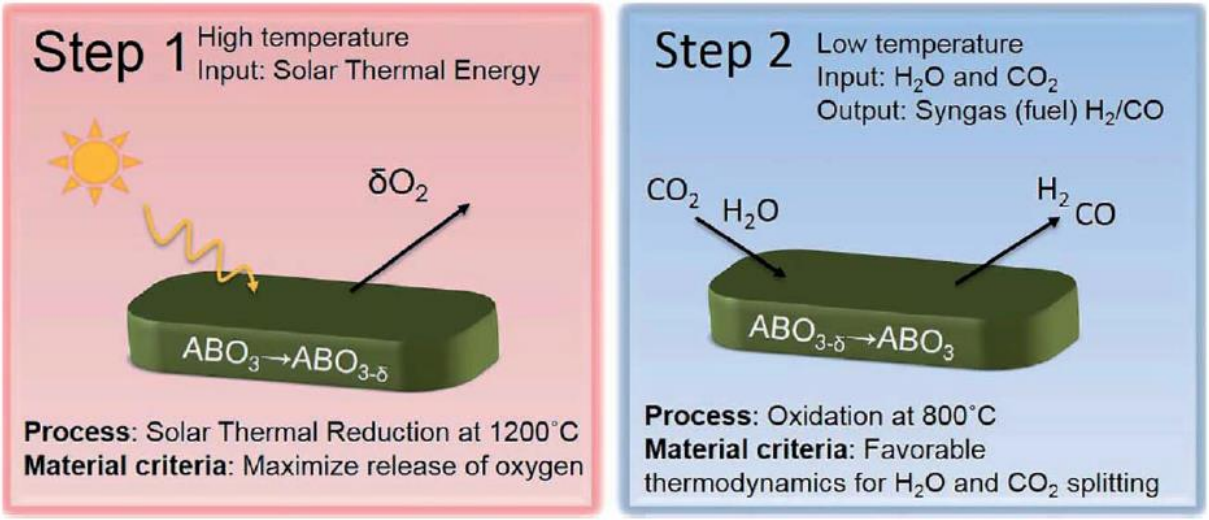

Figure 2.10: *Scheme of the two-step CO_2/H_2O splitting thermochemical cycle using as oxygen carrier a non-stoichiometric perovskite oxide [50].*

As reported in this scheme, after the oxidation step and the consequent release of oxygen molecules, in the perovskite $ABO_{3-\delta_{ox}}$ the highest oxidized state is reached at $\delta_{red} = 0$; while after the reducing step and the incorporation of oxygen molecules, the highest reduced state is reached at about$\delta_{ox} = 0.5$. These oxygen non-stoichiometry limits are given by the stability of the crystal structure and phase transformations.

Thermodynamic

In this section it is presented a briefly thermodynamic analysis of the spontaneous reactions occurred during the thermochemical cycles. The thermodynamic variables that drive these spontaneous reactions are the operating temperature and the pressure level. Since the reactions involved are spontaneous, the standard Gibbs free energy $\Delta G°$ presents a negative value. In order to reach this thermodynamic condition, the follows criteria must be satisfied:

$$\Delta G°_{TR}\left(P_{O_2,red}, T_{red}\right) < 0$$

$$\Delta G°_{WS}\left(P_{O_2,ox}, T_{ox}\right) < -\Delta G°_{H_2O}\left(P_{O_2,ox}, T_{ox}\right)$$

$$\Delta G^{\circ}{}_{CDS}\left(P_{O_2,ox}, T_{ox}\right) < -\Delta G^{\circ}{}_{CO_2}\left(P_{O_2,ox}, T_{ox}\right)$$

The subscript TR, WS, CDS, ox, red indicate thermal reduction, water splitting, carbon dioxide splitting, oxidation step, and reduction step, correspondingly. As presented by Kubicek et al. [50], in the following *Figure 2.11* is the Gibbs free energy change of reduction $\Delta G°$ as a function of temperature for several perovskites at a certain oxygen non-stoichiometry after the thermal reduction step $\delta = 0.1$. Furthermore, the blue line represents the Gibbs free energy change of carbon dioxide splitting reaction, while the red line indicates the water splitting reaction. In this perspective, it is noticed that for a certain range of temperature the red line is above the blue one, while increasing the temperature, the red line is below the blue one. The physical meaning of this is that, at lower temperature range when the red line is above the blue line, the water splitting reaction is more thermodynamically favorable with respect the carbon dioxide splitting reaction, and vice versa.

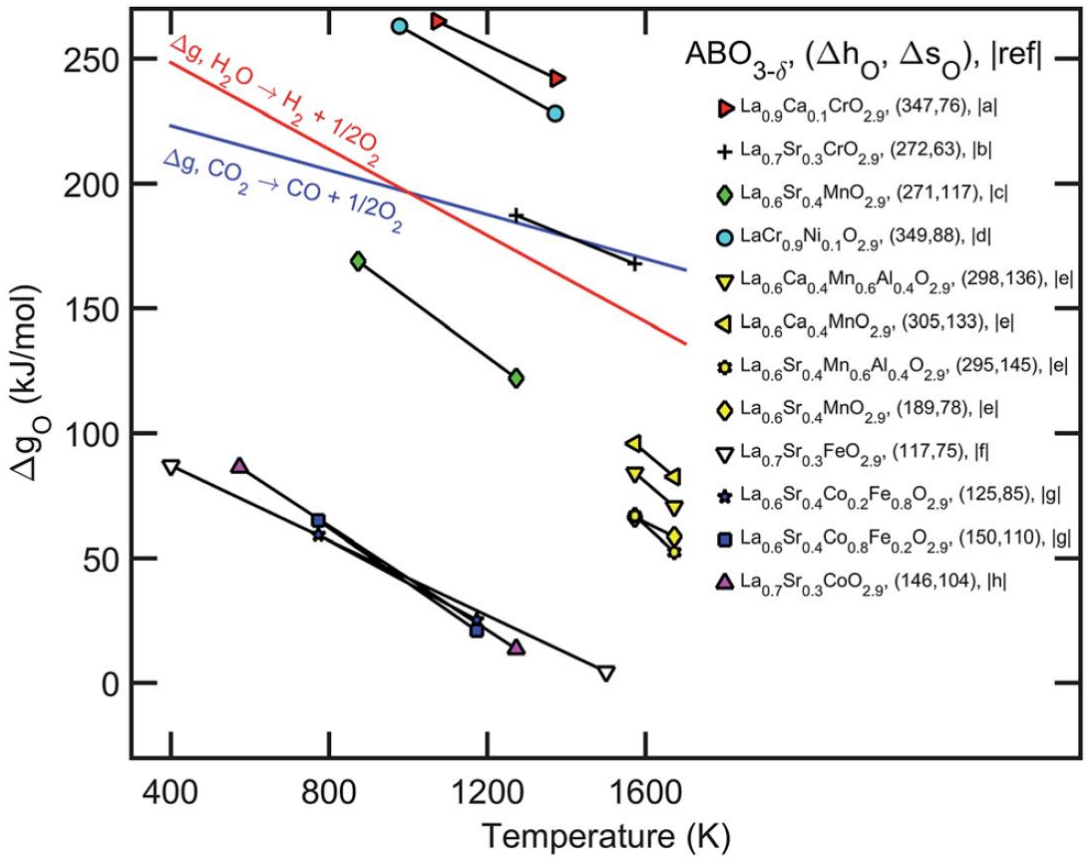

Figure 2.11: *Scheme of the two-step CO_2/H_2O splitting thermochemical cycle using as oxygen carrier a non-stoichiometric perovskite oxide [50].*

As reported in the bottom, lattice defects in the perovskite chemical structure control the Thermodynamic equilibrium and the kinetics of the thermochemical redox cycles. The most relevant are the point defects because they react in their thermodynamic equilibrium to external drivers such as temperature or oxygen partial pressure. Three types of point defects exist in perovskite oxides: electronic defects, cationic defects and ionic defects.

- Electronic defects (electrons or electron holes in the lattice structure) are responsible to enable charge transfer at the surface reaction (both oxygen incorporation or release).

- Oxygen ionic defects (typically are oxygen vacancies) are the most relevant because these vacancies are necessary to incorporate (during oxidation) and release (during reduction) oxygen. The difference of oxygen vacancies in the perovskite under reducing and oxidizing conditions determine the maximum convertible mass in each thermochemical cycle.

2.3.4 – SFNM04 Looping Material Description

The material tested in this dissertation is a double perovskite with the following chemical formula: $Sr_2FeNi_{0.4}Mo_{0.6}O_{6-\delta}$; the set of experimental tests are aimed to analyze the redox stability of this material during the two-step chemical looping CO_2 splitting process by evaluating the CO production rate that occurs in the oxidation step. Before starting the description of the experimental tests, in this paragraph it is done a brief review on the most relevant properties of SFMN-04.

Firstly, the synthetization process is done by University of Udine starting from $Sr_2Fe_{1.5}Mo_{0.5}O_{6-\delta}$ and then a Ni-doping process is performed to improve the oxygen storage capacity of the material. The reference project is "PRIN17 – Direct Biopower" [52], where a detailed electrocatalytic analysis is presented. Basing to current knowledge, the crystalline structures of perovskite family material are classified as ABO_3 (simple perovskite), $A_2(BB')O_6$ (double perovskite composed by $B'O_6$ and $B''O_6$ octahedrons), $AA'B_2O_5$ (layered perovskite), and A_2BO_4 (Ruddlesden-Popper-type perovskite). In this work it is considered a double perovskite $A_2(BB')O_6$, where:

- A site indicates an alkaline earth atom, in this case is Strontium Sr (other typical examples are Barium Ba, Calcium Ca and Lanthanum La).

- B and B' site corresponds to transitional metallic atoms that in this case are Iron Fe and Molybdenum Mo (other typical examples are Yttrium Y, Chromium Cr, Copper Cu, Manganese Mn, Cobalt Co and Nickel Ni).

The atomic arrangement, depicted in *Figure 2.12*, shows that Sr atoms are placed in the hallow site between the alternating $FeO_{6/2}$ and $MoO_{6/2}$ corner-shared octahedra along the three cubic axes creating a cubic symmetry crystallizing in the space group $Fm\bar{3}m$.

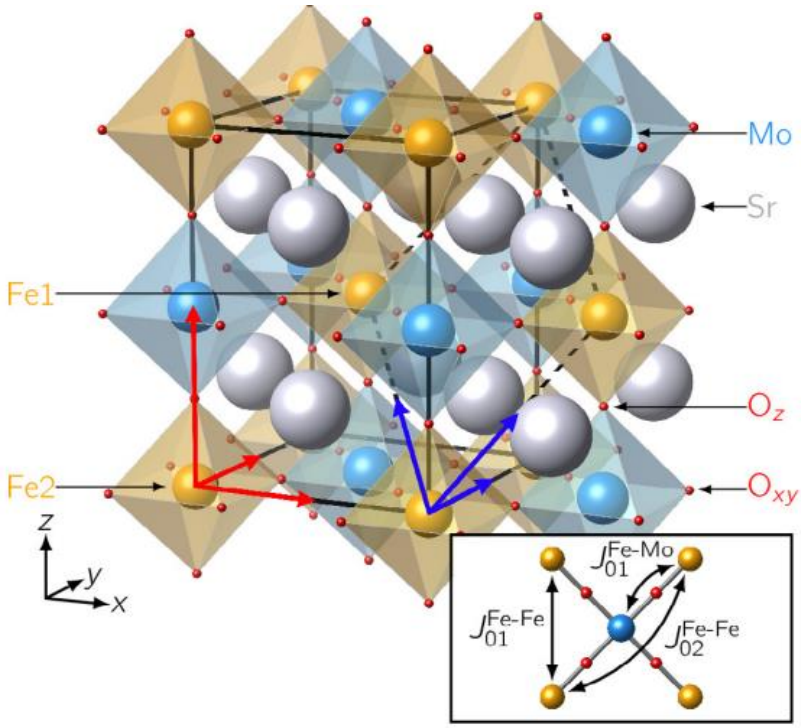

Figure 2.12: *$Sr_2Fe_{1.5}Mo_{0.5}O_{6-\delta}$ double perovskite crystalline structure. The colored polyhedra correspond to the octahedral surroundings of the Fe and Mo atoms (orange and blue respectively). Two different oxygen positions (O_{xy} and O_z) appear according to the tetragonal symmetry. The black solid lines and the red arrows indicate the tetragonal supercell that contains two functional units with two Fe sites ($Fe1$ and $Fe2$); while the primitive unit cell is represented by the black dashed lines and the blue arrows [53].*

The most relevant properties of the SFMO double perovskite material class are:

- High electronic conductivity and electrocatalytic activity mainly due to the combined presence of mixed redox species with a transitional state of oxidation (Iron from Fe^{2+} to Fe^{3+} and Molybdenum from $Mo^{6+}$to Mo^{5+}).
- High ionic conductivity thanks to these unbalanced redox couples that allow the creation of many oxygen vacancies due to weak $Fe-O$ bonds. This ability to generate high concentrations of oxygen vacancies is one of the crucial requirements for looping materials.

- Structural stability at high temperatures under reducing and oxidizing atmospheres.
- Excellent thermal properties, for instance its thermal expansion coefficient (TEC) value is about $13{,}9 \times 10^{-6}\, K^{-1}$, a value very close to the materials used as electrolytes in SOFC. Consequently, the SFMO can be a promising material as electrode for SOFCs due to its mixed ion-electronic structure, high catalytic activity and the ability to create high concentrations of oxygen vacancies as discussed in [54] and [55].
- Elevated tolerance to carbon formation and sulfur poisoning enabling to process Hydrogen with good structural stability and thermodynamics [56].
- High magnetoresistance [57] and high transition temperature.

The most common method to synthetize these perovskites is the solid-state reaction, where the precursor phases are usually $SrMoO_4$ and $SrFeO_{3-\delta}$ oxides, while the initial reagents are Fe_2O_3, $SrCO_3$ and MoO_3. Alvarado-Flores et al. [58] investigate the possibility to implement a mechanical ball milling synthetizing method, instead of a solid-solution reaction, to avoid the negative effect of the sublimation of the initial reagent MoO_3. In this paper, to synthetize the Sr_2FeMoO_6 double perovskite, mechanical milling, calcination, reduction in H_2/Ar is performed in a thermogravimetric analyzer demonstrating that the fabrication process has significant effects on the physical properties of double perovskites. In literature several synthetization methods are implemented: one-step combustion method with glycine $C_2H_5NO_2$ and citric acid $C_6H_8O_7$, citric nitrate $C_6H_7NO_9$ combustion method [59], solution route with citric acid and ethylenediaminetetraacetic acid $C_{10}H_{16}N_2O_8$ (EDTA) [60],microwave-assisted combustion method [61]. In this dissertation, UniUD perform the synthetization process via Self-Combustion Synthesis (SCS) with citric acid; after this, to create a cubic structure, the obtained powders are subjected to calcination process at more than $T = 1100\ °C$. More in general considering the various step of the synthetization process described in literature, there is a report where the powders are calcined at $T = 900\ °C$, followed by grinding, compacting and, finally, reduced in $5\ \%\ H_2/Ar$ [62]. In another experiment, the powders are ground, compacted in pellets, calcined at $T = 900\ °C$, ground again, compacted at a pressure $p = 450\ MPa$; then, they are reduced in an atmosphere of $6\ \%\ H_2/Ar$ at $T = 1200\ °C$, ground in a high-energy mill in an Argon atmosphere and, finally, compacted again at $p = 450\ MPa$ [63]. In conclusion, in another work, the precursors are mixed, ground, and heated up at $T = 900\ °C$ for a time of $10\ h$ in an air atmosphere; then they are compacted in pellets for synthesis at $T = 1280\ °C$ in $5\ \%\ H_2/Ar$ for $5\ h$ with a temperature increase rate of $5\ °C/min$. This phase is followed by grinding compacting and synthetization for $25\ h$ [64].All these examples remark

the crucial role of the synthetization process for fabricating double perovskites: by changing the application of mechanical alloying and the synthesis operating conditions, the performance of these looping materials during two-step CO_2 splitting process vary and the aim is to find the most efficient method that allows to the maximum CO production rate.

After the synthetization process, it is useful to describe the Ni doping process aimed to promote the oxygen storage capacity. The doping process involves the Ni^{2+} cations insertion within the double perovskite lattice structure by substituting some of the Fe^{2+}cations already present; consequently, the amount of Fe^{3+} cations is higher compared to Fe^{2+} enhancing the electronic conduction mechanism of Nickel. As discussed by Alvarado-Flores et al. [58], after the mechanical alloying and calcination process, the $SrMoO_4$ phase can appear accordingly to the following chemical reaction between the initial reagents of the synthetization process:

$$SrCO_3 + MoO_3 \rightarrow SrMoO_4 + CO_2$$

The segregation of this new $SrMoO_4$ phase is a negative phenomenon decreasing the electronic conductivity of the material due to its insulant property. This aspect is taken into account also by UniUd during the Ni doping process starting form the undoped reference double perovskite sample $Sr_2Fe_{1.5}Mo_{0.5}O_{6-\delta}$. As represented by *Figure 2.13,* UniUD compares different Ni content implementing an X-Ray Diffraction analysis (XRD) finding a Ni solubility upper limit of $x = 0.5$ in the lattice.

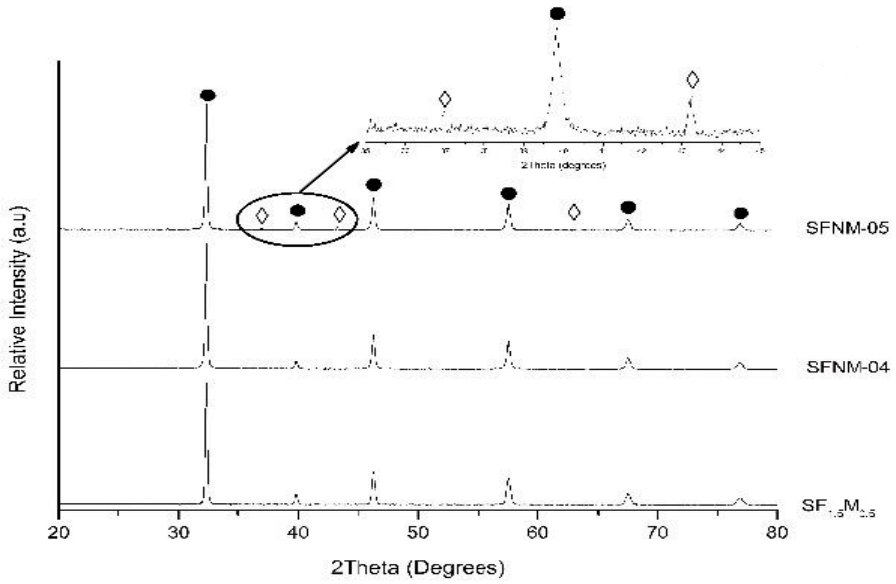

***Figure 2.13*:** XRD Analysis of SFNM-05 (up) and SFNM-04 (down) double perovskite sample.

This means that for $x = 0.5$ the double perovskite $Sr_2Fe_{1.5}Ni_{0.5}Mo_{0.5}O_{6-\delta}$ (SFNM-05) presents a NiO segregation on the surface reducing the amount of Ni^{2+} cations inserted within the lattice, at the contrary, for $x = 0.4$ the double perovskite $Sr_2Fe_{1.5}Ni_{0.4}Mo_{0.5}O_{6-\delta}$ (SFNM-04) is not more subjected to NiO segregation on the surface.

This XRD patterns confirm the existence of a Ni solubility upper limit of $x = 0.5$. Once the upper limit is determined, Du et al. [65] investigate the phenomenon of $SrMoO_4$ phase segregation for low Ni content considering as undoped reference double perovskite sample $Sr_2FeMo_{0.65}O_{6-\delta}$. As shown in *Figure 2.14(a)*, when the Ni doping content x is between 0.25 and 0.30, a slight amount of $SrMoO_4$ phase still remains into the double perovskite lattice, while when the doping level increases until reaching $x = 0.35$, the characteristic peak of $SrMoO_4$ diminish and the two weak peaks at 19° and 38° represented in *Figure 2.14(*b) indicate he $Sr_2FeMo_{0.65}Ni_{0.35}O_{6-\delta}$ double perovskite structure.

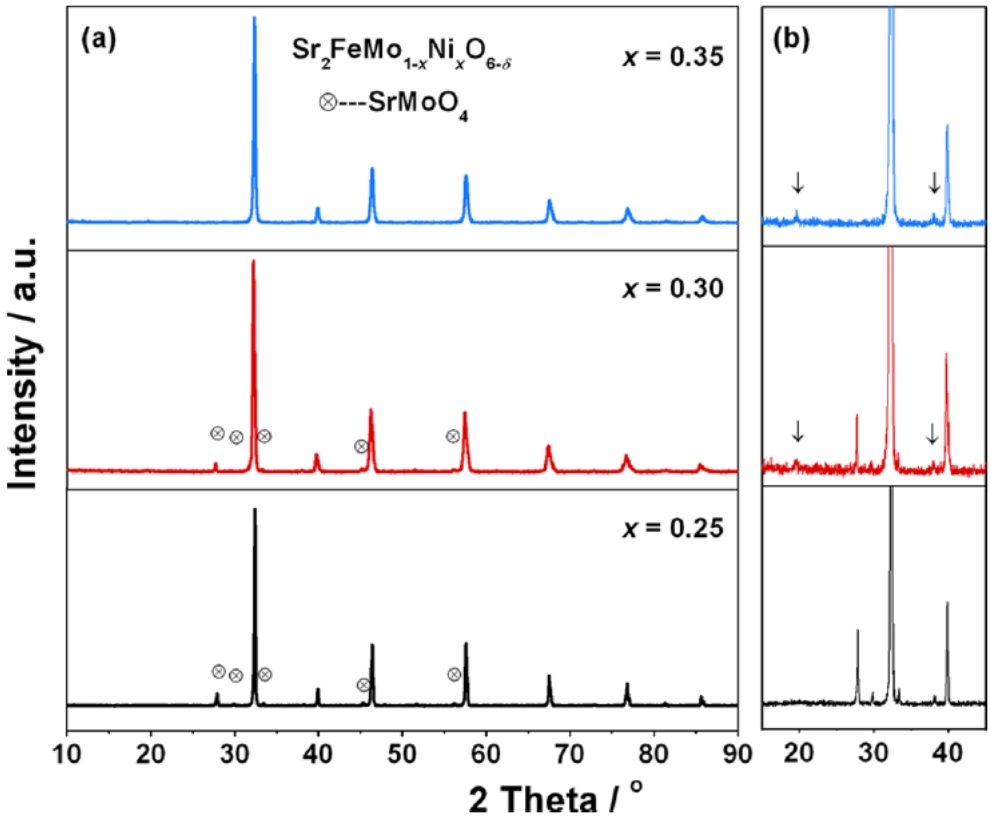

Figure 2.14: *XRD patterns at room-temperature of* $Sr_2FeMo_{1-x}Ni_xO_{6-\delta}$ *calcined at* $T = 1100\ °C$ *for* $10\ h$ *in air for different* Ni *doping content values* ($x = 0.25, 0.30, 0.35$)*: (a) XRD patterns for* $2\ Theta$ *between* $10°$ *and* $90°$*; (b) XRD patterns for* $2\ Theta$ *between* $17.5°$ *and* $45°$ *[65]* .

In conclusion, it is possible to assert that the upper Ni solubility upper limit is $x = 0.5$ while the lower limit is $x = 0.35$; for this reason, UniUD decide to synthetized the undoped reference double perovskite $Sr_2FeMo_{0.6}O_{6-\delta}$ sample with a Ni content of $x = 0.4$ obtaining the SFNM-04 $Sr_2FeNi_{0.4}Mo_{0.6}O_{6-\delta}$ under investigation in this dissertation.

To better understand the effect of the doping process in terms of CO production rate, D. Sastre et al investigate the role of Sr^{2+}doping using $La_{1-x}Sr_xFeO_3$ as perovskite for coupling Chemical Looping Methane Reforming (CLMR) with CO_2-splitting reactions using a fixed-bed, continuous-flow reactor operating isothermally at $T = 850°C$. As for SFNM perovskites, also LSF perovskites present attractive redox capacities due to Sr^{2+} incorporation, which allows the formation [66] of large amount of oxygen vacancies that can favour oxygen exchange increasing the Oxygen Storage Capacity (OSC): partial substitution of La^{3+} by Sr^{2+} cations involves changes in the crystalline structure due to the difference in the ionic radii ($0.136\ nm$ for La^{3+} and $0.144\ nm$ for Sr^{2+}) and, mainly due to the difference in the oxidation state; to maintain the electroneutrality of the lattice both formation of oxygen vacancies and partial oxidation of Fe^{3+} to Fe^{4+} occur. In this work [66], a modified Pechini method is used for the synthesis of perovskites with composition $La_{1-x}Sr_xFeO_3$ with different Sr doping content x. More detailed:

- the name LF perovskite indicates a null Sr doping content ($x = 0$)
- L9S1F corresponds to a Sr doping content equal to $x = 0.1$
- L7S3F to $x = 0.3$
- L5S5F to $x = 0.5$
- L3S7F to $x = 0.7$
- L1S9F to $x = 0.9$
- SF to $x = 1$

In order to assess the effect of Sr^{2+}doping on CO production (more in general on syngas production), all the LSF samples are subjected to five redox cycles at $T = 850\ °C$, swinging the gas composition between 5 % CH_4 and 5 % CO_2 in Ar atmosphere. As depicted in *Figure 2.15*, significant differences of samples with high and low Sr content are visible in terms of CO production during both the CH_4 and CO_2 gas feeding stages: samples with high Sr- doping (SF, L1S9F, L3S7F, L5S5F) show a sharp peak of CO generation only for few minutes after introducing CO_2, in fact after about $5\ min$ the CO profile drops to zero.

On the other hand, LSF perovskites with $x \leq 0.3$ (L7S3F, L9S1F, LF) not only produces a higher amount of CO, but also highlight a significant reactivity for longer periods.

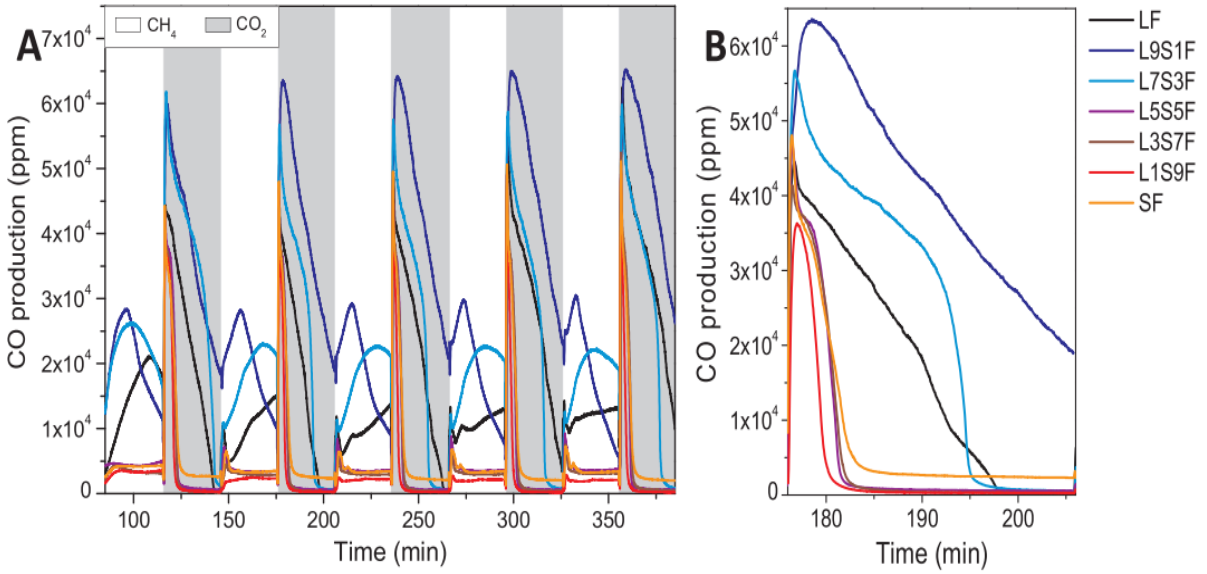

Figure 2.15: *(A) CO production in [ppm] during the 5-cycles redox at $T = 850°C$ alternating CH_4 and CO_2 for the LSF perovskite samples. (B) Zoom-detail of the second cycle of oxidation in 5 % CO_2 stream [66].*

Thus, this analysis demonstrates the higher activity of L7S3F, L9S1F and LF for coupling CLMR and CO_2-splitting process underlighting the crucial role of selecting the proper value of doping content x according to the specific thermochemical process under investigation.

In addition to the Ni-doping process of SFNM previously explained, the Ni and Fe cations inside the double perovskite lattice are responsible to the so-called exsolution phenomenon during which both Ni and Fe from the bulk rises up to the surface creating a new $Fe - Ni$ alloy nanoparticles that enhance the catalytic activity and the stability of the material. This is one of the most interesting features of SFNM perovskites and for this reason it is better described subsequently in paragraph 5.2.

Once the synthetization and doping processes are performed, to further analyze the material cyclical redox stability and repeatability under subsequent oxidation-reduction cycles, a Temperature Programmed Reduction (TPR) is carried out by UniUD for SFNM-04. The procedure is composed by the following steps:

1. Thermal pre-treatment up to $T = 500\ °C$ with a temperature increase rate of $10\ °C/min$ in air atmosphere useful to remove eventual impurities and other

species that may be created within the bulk; this step is performed to re-oxidize the sample after each reduction reaction.

2. Isothermal step at $T = 500\ °C$ extended for $1\ h$.
3. TPR step composed by a first temperature ramp from $T = 500\ °C$ to $T = 900\ °C$ with the same rate of $10\ °C/min$ in a reductive atmosphere 4.5 % H_2/N_2 with a continuous volumetric gas flow rate of $Q = 35\ mL/min$.
4. Cool down step from $T = 900\ °C$ to the ambient temperature through a ramp with the same temperature decrease rate of $10\ °C/min$ in N_2 atmosphere.
5. Sample re-oxidation step from room-temperature to $T = 500\ °C$ in air ambient as described at point 1.

The following *Figure 2.16* shows the results obtained by the four TPR cycles by plotting the raw TCD signal of the H_2 consumed in each reduction step as a function of the operating temperature. It is evident the marked difference of the H_2 consumption trend during the first reduction (black curve) compared to the other reductions (red, blue and violet curves). This difference may be attributed to the occurrence of a transition phase that reduces the redox ability of the SFNM-04 material; the existence of this new transition phase is more precisely described in the following paragraph.

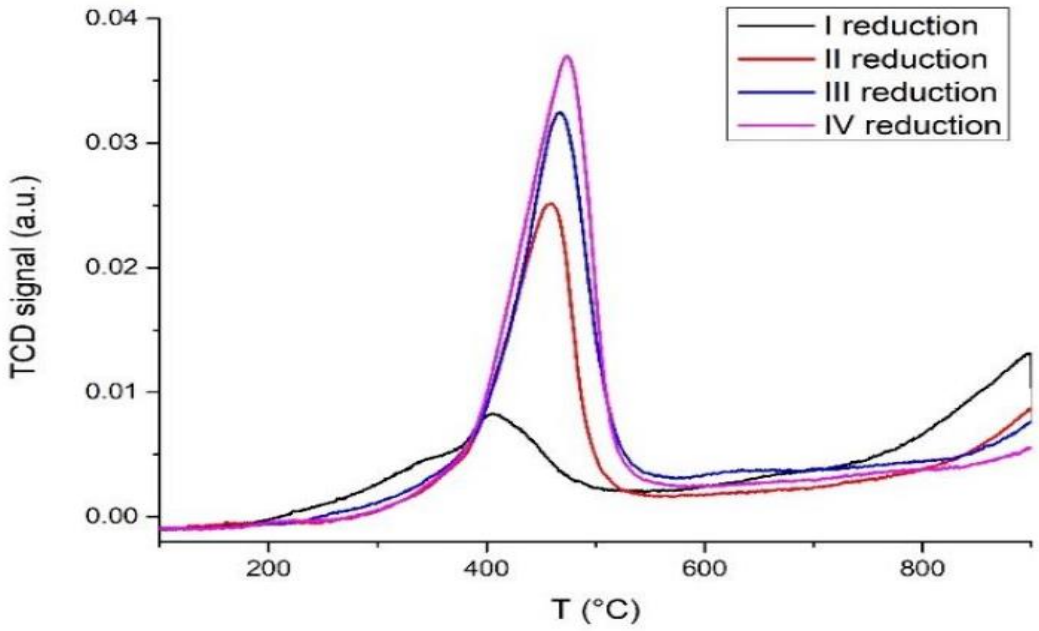

Figure 2.16: *TPR test of SFNM-04 for 4 subsequent reduction steps in* 4.5 % H_2/N_2 *[52].*

After the first reduction, the TPR test highlights the cyclic stability of the material by enhancing the H_2 consumption steps after steps, in fact from the second reduction onwards, the red, blue and violet curves present the same profile corresponding that a higher redox stability of SFNM-04 is reached with a TCD peak signal of about $0.025 \div 0.035\ [a.u.]$ at $T \cong 500°C$. At the contrary, the black curve corresponding to the first reduction exhibits a TCD peak signal value of about $0.01\ [a.u.]$ at $T \cong 400°C$.

The transition phase that reduces the redox ability and explains the marked difference between the first reduction (black curve) and the other ones, is a Ruddlesden-Popper (RP) phase presenting the following chemical formula $Sr_3FeMoO_{6.5}$. To better understand this aspect, further XRD analysis of SFNM-04 are carried out confirming the presence of this RP transition phase. More detailed, from the XRD analysis, it is deduced that this is not an absolute transition because both RP and double perovskite phase are detected, hence they are present at the same time in the global perovskite chemical structure. As depicted in *Figure 2.17*, the general formula for RP-type perovskites is $A_{n+1}B_nX_{3n+1}$, composed by n layers of ABX_3 perovskite blocks with corner-shared BX_6 octahedra and alternated AX rock salt layers distributed along the c axis.

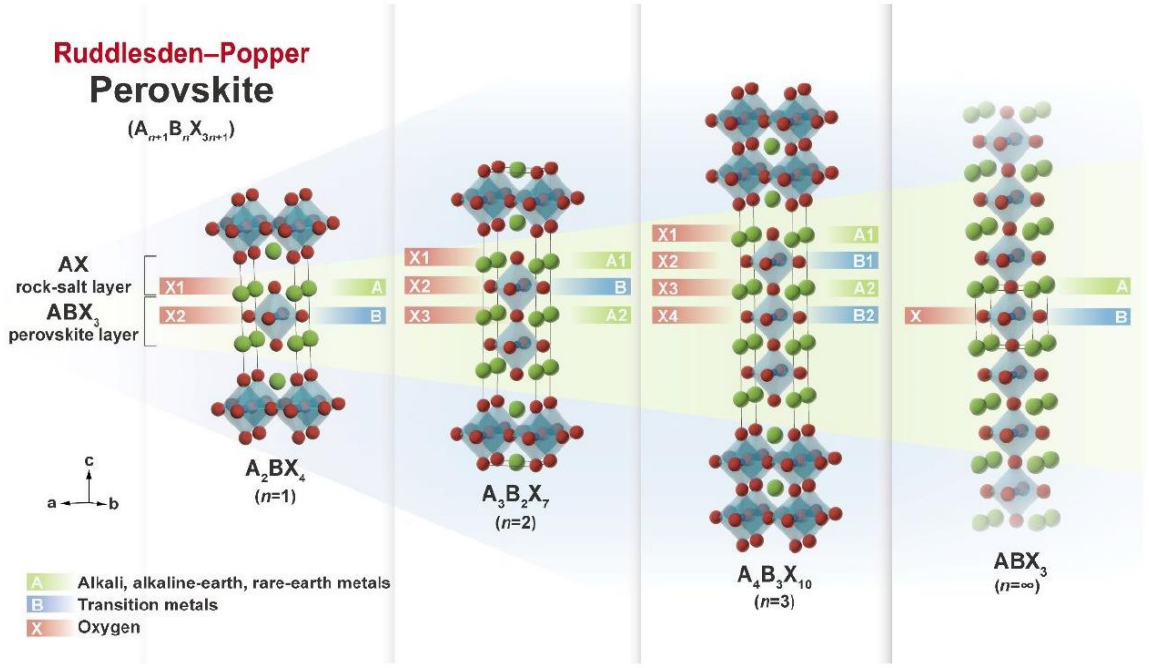

Figure 2.17: *Ideal tetragonal crystal structure of the Ruddlesden-Popper perovskite $A_{n+1}B_nX_{3n+1}$ (space group: I4/mmm) with different numbers of ABX_3 cubic layer $(n = 1,2,3 \ldots \infty)$. The ideal cubic crystal structure of the simple perovskite ABX_3 (space group: Pmm3) corresponds to the case of Ruddlesden-Popper perovskite with $n = \infty$ [67].*

The A-site is generally occupied by an alkaline, alkaline-earth, rare-earth metals, the B-site is a transition metal element (Fe, Cu, Mn, Ni). This type of perovskites has attracted increasing interests because of their excellent photocatalytic activity, visible light response, and unique optical and electronic properties and as discussed by Xiao et al. [68], one of the most promising application is for photocatalysis-based water splitting and wastewater treatment. Considering the SFNM-04 material under investigation, it presents a double perovskite structure composed by Fe and Mo cations that can arrange in alternative way inside the oxygen octahedra.

Concerning in detail the SFNM-04 XRD patterns displayed in *Figure 2.18*, beyond the coexistence of the double perovskite SFNM-04 and the RP $Sr_3FeMoO_{6.5}$ phase, it is also detected the formation of the $FeNi_3$ alloy on the SFNM-04 surface. As represented by the magnification of *Figure 2.18* below, the $FeNi_3$ alloy peak signal located at $2Theta = 44.5\,°$ is a clear consequence of the exsolution evolution phenomenon occurring during the Hydrogen reducing step, where both $Fe^{2+}$and Ni^{3+}cations move towards the surface creating a $FeNi_3$ metallic alloy. Another relevant aspect visible in the magnification of *Figure 2.18* is that the area below the $FeNi_3$ alloy XRD pattern tends to expand as the number of cycles increases, at the contrary the area below the RP $Sr_3FeMoO_{6.5}$ XRD pattern tends to decrease.

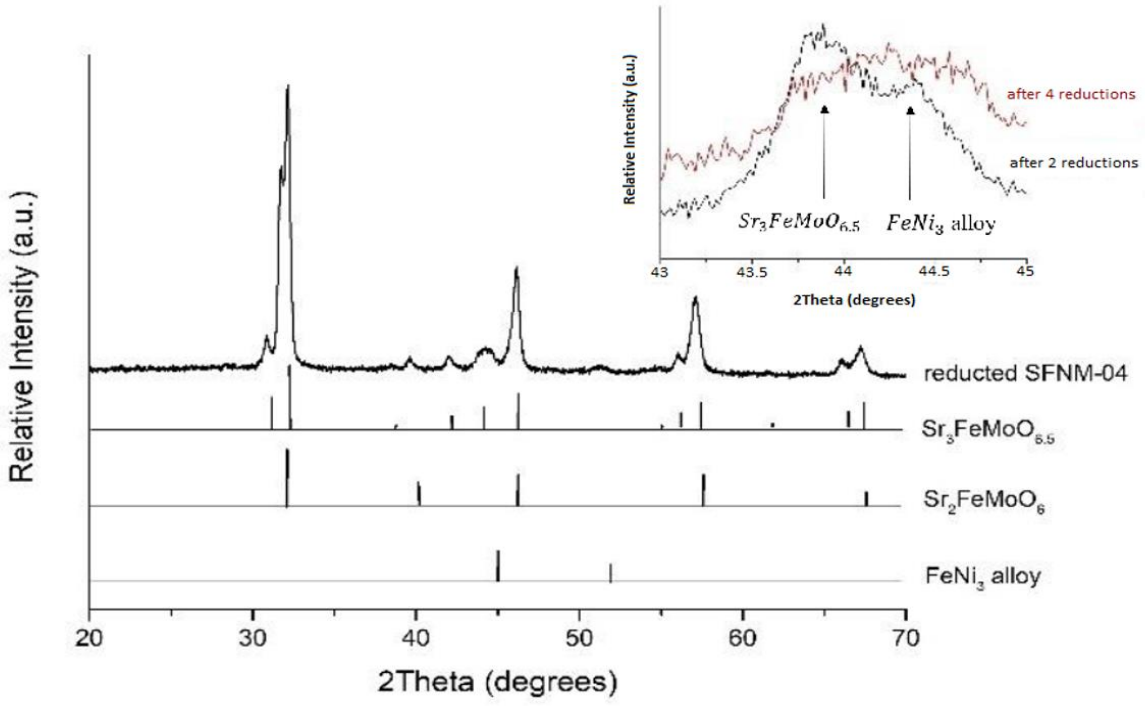

Figure 2.18: *XRD patterns of reducted SFNM-04 double perovskite phase, RP* $Sr_3FeMoO_{6.5}$ *phase and* $FeNi_3$ *alloy phase after 4 reduction steps. In the upper right there is a magnification of RP and* $FeNi_3$ *alloy phase XRD patterns in the range between* $43\,° \div 45\,°$ *after 2 reductions (black curve) and after 4 reductions (red curve).*

In fact, the black curve corresponding to the XRD signal after two subsequent reduction steps, presents a $Sr_3FeMoO_{6.5}$ peak located at about $2Theta = 43.8\,°$ indicating that the RP phase overestimates the metallic alloy, while the red curve corresponding to the XRD signal after four reductions, indicates that the predominant phase is the $FeNi_3$ metallic alloy with a peak located at $2Theta = 44.5\,°$. This behaviour demonstrates that the exsolution evolution is a phenomenon that progressively grows up during the H_2 reducing steps. In this way it is possible to assert that the TCD signal peaks of the H_2 consumed in each reduction step located at $T \cong 500°C$, depicted in *Figure 2.16*, are strictly correlated to both the $FeNi_3$ alloy reduction and the $Fe^{3+}$and Mo^{6+}reduction inside the RP phase structure.

Moreover, after the reduction stability assessment, the CO_2 oxidizing environment is tested via XRD analysis of two SFNM-04 samples differently treated. In detail before the XRD test, the first sample was subjected to a degradation process in a CO_2 oxidizing environment at room temperature for 1 year, while the second one (named SFNM-04-PROP) was treated in a 30 % C_3H_8/N_2 hydrocarbon environment at $T = 800\,°C$ for 2 hours.

The main result pointed out from the XRD test is that, for both the samples, the Ni presence in the SFM double perovskite structure promotes the formation of $SrCO_3$ carbonate due to the reaction of CO_2 with SrO and, furthermore, this process allows to the stabilization of the insulant phase $SrMoO_4$. Hence, this indicates the instability of the SFNM-04 when it is oxidized in hydrocarbon environment, because it degrades only after 2 hours creating the insulant phase $SrMoO_4$ and the carbonate $SrCO_3$ thanks to the presence of Ni that acts as catalyst for the hydrocarbon cracking reaction with the consequent release of CO_2.

As represented by the following *Figure 2.19*, this cracking process can be also detected through a TGA (Thermogravimetric Analysis) applied to two samples: SFNM-04 (blue curve) corresponds to the untreated sample, while the SFNM-04-PROP (black curve) corresponds to the sample treated in a 30 % C_3H_8/N_2 hydrocarbon environment at $T = 800\,°C$ for 2 hours.

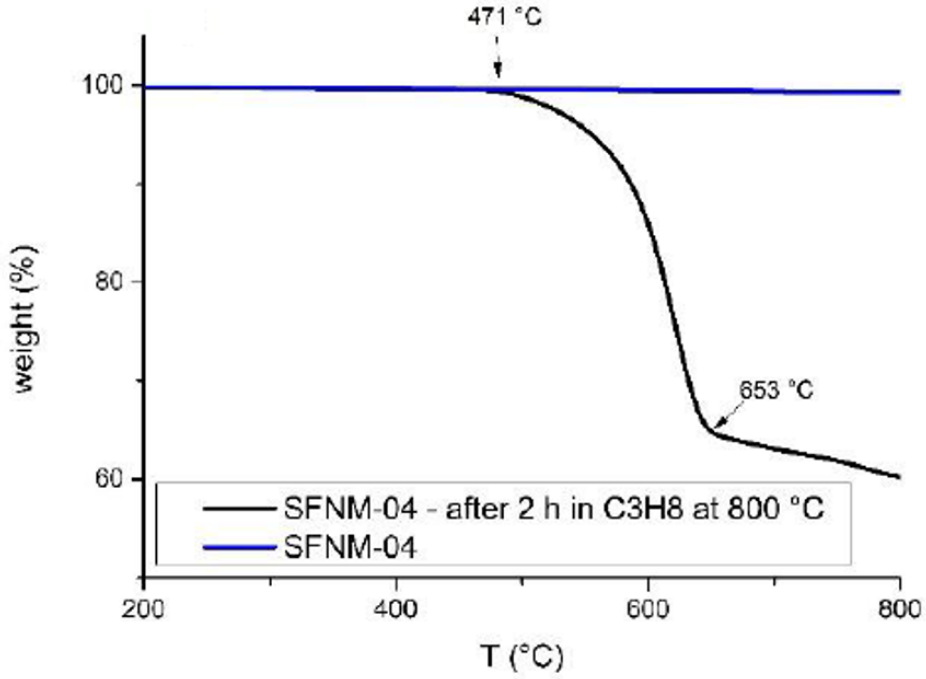

Figure 2.19: *TGA test applied to untreated SFNM-04 sample (blue curve) and to SFNM-04-PROP sample treated in a* $30\ \%\ C_3H_8/N_2$ *environment at* $T = 800\ °C$ *for* 2 *hours (black curve).*

It is evident that while the untreated SFNM-04 sample remains intact without any weight loss throughout the temperature range, considering the SFNM-04-PROP sample it is visible a significant weight loss from $100\ \%$ to about $60\ \%$ due to the carbonate decomposition occurring in the temperature range $T = 471\ °C \div 653\ °C$.

Nevertheless, another thermal treatment test in $100\ \%\ N_2$ oxidizing environment at $T = 800\ °C$ reveals that the carbonate compound $SrCO_3$ disappears and the insulant phase $SrMoO_4$ progressively decreases. Moreover, after this thermal treatment, a further calcination process in air environment at $T = 900\ °C$ is useful to re-generate the original phase of SFNM-04 through a re-absorption of the cubic phase $SrMoO_4$ inside the double perovskite lattice. In conclusion, oxy-dry reforming (ODR) catalytic tests are carried out involving a SFNM-04 sample of $80\ mg$ and an oxidizing gas flow with the following composition $CH_4 : CO_2 = 3 : 2$. The sample is pre-treated in H_2 reducing atmosphere at $T = 800\ °C$ for 1 hour, and then maintained always in reducing environment for 12 hours selecting as temperature set point $T = 700\ °C$, where the ODR reaction starts. The main results are that the CO_2 conversion presents an inflection between $T = 550\ °C \div 600\ °C$, at the contrary an increase of the CH_4 conversion is detected because of the direct combustion of methane with oxygen.

Chapter 3

3. Experimental Setup

3.1 – Chemical Looping Test Bench Description

The chemical looping test bench, where are carried out all the experimental tests focused on the investigation of redox performance of SFNM-04 double perovskite sample, is located at CO_2 *Circle Lab* inside the Environment Park centre in Turin, Italy. The scheme of the experimental bench is depicted in *Figure 3.1*.

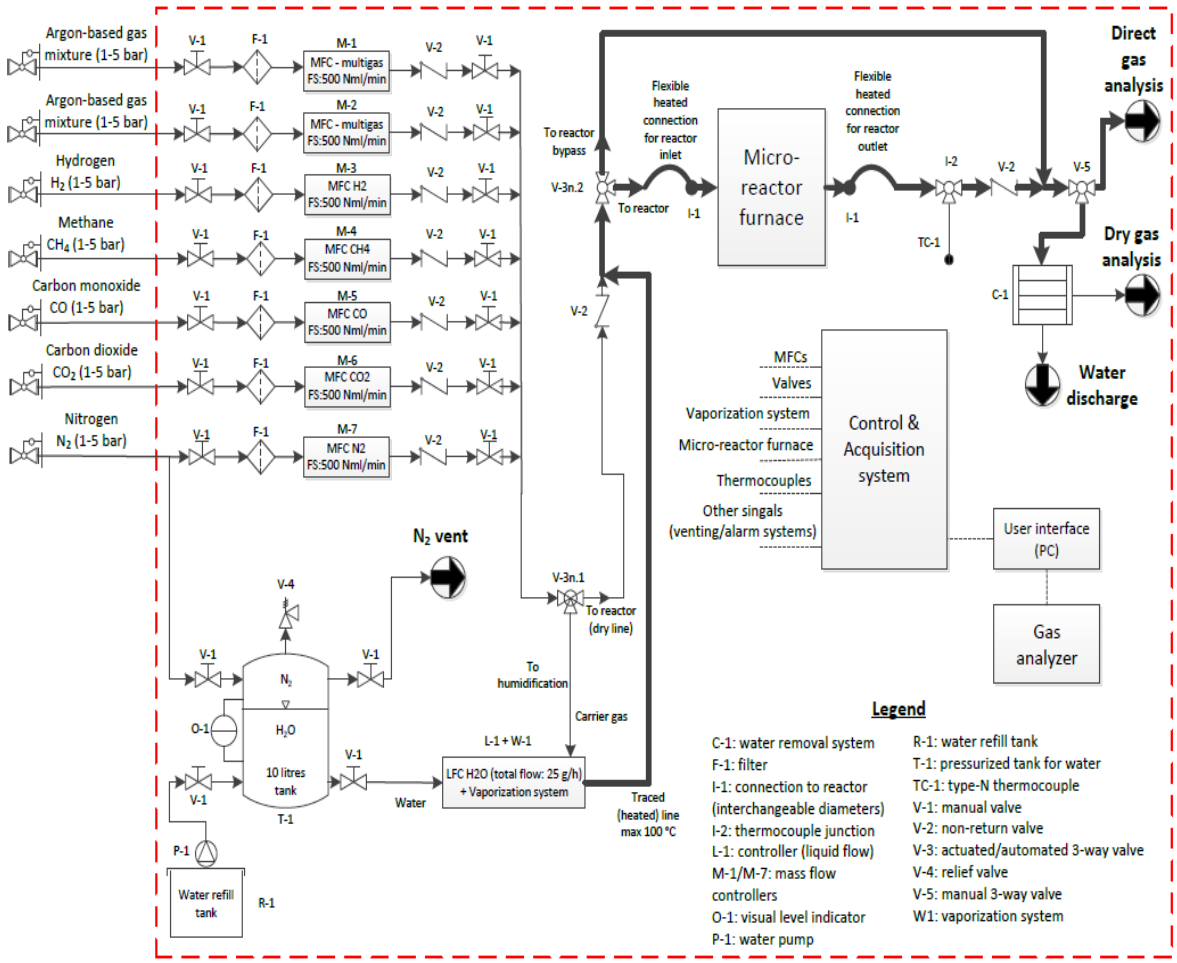

Figure 3.1: *Scheme of the Chemical Looping test bench implemented to perform all the experimental tests in this work.*

Starting from the left-up of the figure, Bronkhorst EL-FLOW mass flow controllers (MFCs) are used to automatically send a certain gas flow mixture. More precisely, the feeding system is composed by 7 gas lines and a water vapour generation unit. The different gas streams supplied are N_2, CH_4, CO, CO_2, H_2 and these 5 gas lines are directly connected to the laboratory lines using pressure reducers installed on the wall. Differently, the other two lines are connected to cylinders that are equipped by pressure reducers directly installed on them and activated at the moment in which they are connected to the experimental bench, hence during the operating conditions. In the section downstream the pressure reducers (valves V-1), there installed MFCs through which the gas streams flow by means of steel connection pipes (in the case of the 7 gas lines connected to the laboratory lines) and by means of Teflon connection pipes (in the case of the remaining 2 lines connected to cylinders). In this perspective, the gases contained in the two connected cylinders are normally Ar-H_2 (5 % max), Ar-CH_4 (5 % max), Ar-CO_2 (5 % max), Ar-O_2 (5 % max), and air. In all the gas lines it is imposed a pressure of $p = 2.5\ [bar]$, apart for the nitrogen gas line where a pressure of $= 3.5 \div 5\ [bar]$ is imposed because this line can be also implemented to pressurize the demineralized water tank. The aim of the Bronkhorst EL-FLOW MFCs is to regulate and measure the flow rate of the gases. After MFCs, all the gas lines converge into the dry mix line directly connected with the subsequent microreactor by means of a three-way valve (V-3n.1). In this section it is possible bot to send the dry mixture inside the microreactor, or also humidify it before entering. In this last case it occurs the mixing between the dry flow and the vaporized water obtaining a wet mixture that is as first heated, and then joined within the dry line. However, in this dissertation all the experimental tests performed use only dry lines. After that, it is present a second three-way valve (V-3n.2) useful to select two different ways: the first line is used to sent the gas mixture inside the microreactor, alternatively, the upper line can be used to bypass the microreactor. In this work the bypass line is used during the calibration procedures of the gas analyser.

After the feeding system, it is present the core of the system, namely the tubular microreactor made of alumina positioned inside a tubular furnace that guarantees an isothermal environment up to 1600 °C. The electric furnace (Carbolite Gero, Germany) is aimed to heat up the ceramic tube of the microreactor until an imposed temperature level, in accordance with the experimental test. The connection between the reactor and the gas lines is ensured implementing flanges sealed O-rings. Hence, the gas mixture flow pass through the inner tube where the SFNM-04 sample is placed in the centre, and inside this inner tube the redox reactions, reduction, and oxidation, occur.

At the outlet of the microreactor, the reconnection between the main and the bypass line occurs by using a manual valve (V-5), thanks which it is possible to impose the direction of the gas flow that can move towards the condenser or towards the outlet line where it is placed the gas analyser system the proper.

Finally, a real-time Emerson X-stream gas analyser (multichannel NDIR/UV/TCD) is used to analyse the outlet gas composition. This gas analyser measures the concentration of various gases (CO_2, H_2, CH_4, O_2, and CO) composing the outlet gas mixture exiting from the microreactor section. As usual, to avoid the release of gases inside the laboratory, the gas stream at the outlet of the gas analyser is conveyed to vent.

3.1.1 – Microreactor and Furnace Section

The microreactor and the furnace station are the core of the chemical looping test bench. Generally, most of the studies concerning to evaluate the redox performance of perovskite, or more in general, of looping materials subjected to a two-step WS/CDS thermochemical cycle, implements an experimental setup based on Thermogravimetric analysis (TGA). Nevertheless, in this work it is preferred to use a microreactor experimental setup because this configuration compared to TGA present several advantages [69]:

- The heat and mass transfer mechanism are enhanced.
- Microreactor setup is more flexible in terms of gas mixing, operating conditions control (temperature and volumetric flow rates can be controlled more efficiently).
- It allows to a higher products quality.
- Thanks to the microreactor setup it is possible to analyse the redox performance of the SFNM-04 sample that is closer to large-scale currently in commerce compared to TGA. In fact, using a TGA experimental setup a sample of about $10 \div 15$ $[mg]$ is generally used, while with a microreactor setup the SFNM-04 sample analysed in this work presents a mass of 200 $[mg]$.
- The TGA evaluates the mass variation of the sample adopting a balance mechanism, but this weight variation can be eventually induced both by the actual redox reactions performed, and by the formation of unwanted chemical species as carbonates, or other contaminants derived by the carbon deposition phenomenon.

Instead, using a microreactor setup, it is possible to directly evaluates the CO production during the two-step thermochemical redox cycle produced during the oxide step where it occurs the carbon dioxide splitting reaction.

In conclusion, it is right to assert that these two different experimental setups are complementary, and the data measured from both are in the same way correctly to point out the perovskite redox performance and its thermochemical properties.

Now, once the reasons why it is chosen a microreactor instead of a TGA setup are listed, in the next section it is provided a more detailed description of the microreactor and furnace station.

The microreactor employed in this dissertation is the Carbolite Gero working tube [70] positioned inside the tubular electric furnace system as depicted in *Figure 3.2.* In addition, the power supply unit guarantees the supply of electricity to the resistances allowing to reach the expected isothermal environment at the selected temperature level.

Figure 3.2: *Carbolite Gero microreactor positioned inside the tubular electric furnace [70].*

The power supply and conditioning unit, depicted in *Figure 3.3*, is used to manage and control the temperature program.

***Figure 3.3**: Power Conditioning Unit (PCU).*

In fact, the electric furnace is automatically controlled by an Eurotherm PID (Schneider Electric, France). Hence, it is possible to remotely impose step by a step a pre-fixed temperature program thorough the Eurotherm iTools [71]. Generally, the temperature program imposed is composed by several isothermal steps during which it is kept constant a certain temperature level, and proper ramp-up, or ramp-down steps to reach different temperature levels during the experimental test. In this perspective, when it is imposed an isothermal step it is necessary to specify the time duration, while using ramps, it is needed to select the proper set-point temperature values and the incre/decrease rate of progression in$[K/min]$ terms.

Considering the Carbolite Gero microreactor, is a continuous flow reactor composed by a 1-meter length horizontal tube of alumina (Al_2O_3) having an internal diameter of 32 mm inside which flows the gas mixture. In addition, several insulation layers are placed between the inner cylindrical tube and the outer layer to limit the eventual heat and flow leakages that negatively affect the process, and to provide a thermal flux barrier avoiding heat dispersion. As shown in *Figure 3.*4, at the center of the reactor it is located the SFNM-04 200 $[mg]$ powder sample contained in an alumina crucible.

***Figure 3.4**: SFNM-04 powder sample contained in an alumina crucible.*

The 200 $[mg]$ SFNM-04 powder mass is measured by means of an analytical balance represented in *Figure 3.5*. This balance has a high level of accuracy and a resolution of 0.1 $[mg]$, in fact it is equipped with a transparent container that enables the measurement of the sample mass without any undesired influences induced by air currents that can distort the measure.

***Figure 3.5:** Analytical balance implemented to measure the* 200 $[mg]$ *SFNM-04 powder.*

Now, once the SFNM-04 sample is ready to be inserted into the tubular microreactor, and once the temperature program is properly set, then it is needed to select the desired gas flow mixture compositions in accordance with the oxidation and reduction step. The gas mixture compositions are selected using a different software compared to the previous one used to impose the temperature level of the electric furnace. For this reason, the gas flows sequences are synchronized with the temperature program: when the microreactor reach the imposed temperature level using the power conditioning unit, the reducing gas is simultaneously sent into the inner cylindrical tube of the microreactor. The same concept is exploited during the oxidation step and for all the other steps of the thermochemical redox cycle. More precisely, the gas mixture compositions and the different sequences are remotely imposed by using a dedicated software running on a local PC connected to the data acquisition and control system of the test bench. The main interface of this software is represented in *Figure 3.6*, and in this interface it is also reported a simple scheme of the chemical looping test bench and all the 7 gas lines. Thanks to this software, it possible to select manually the value in percentage terms of the various chemical species composing the gas mixture sent to the microreactor, or alternatively it is possible to generate the desired sequence of operations that will be automatically executed. Furthermore, it is possible to decide to send the gas mixture not into the microreactor, but using the bypass line, directly to the outlet gas analyser system. Therefore, this software can be considered as a SCADA (Supervisory Control And Data Acquisition) [72] system, because it permits to control and supervise the whole process.

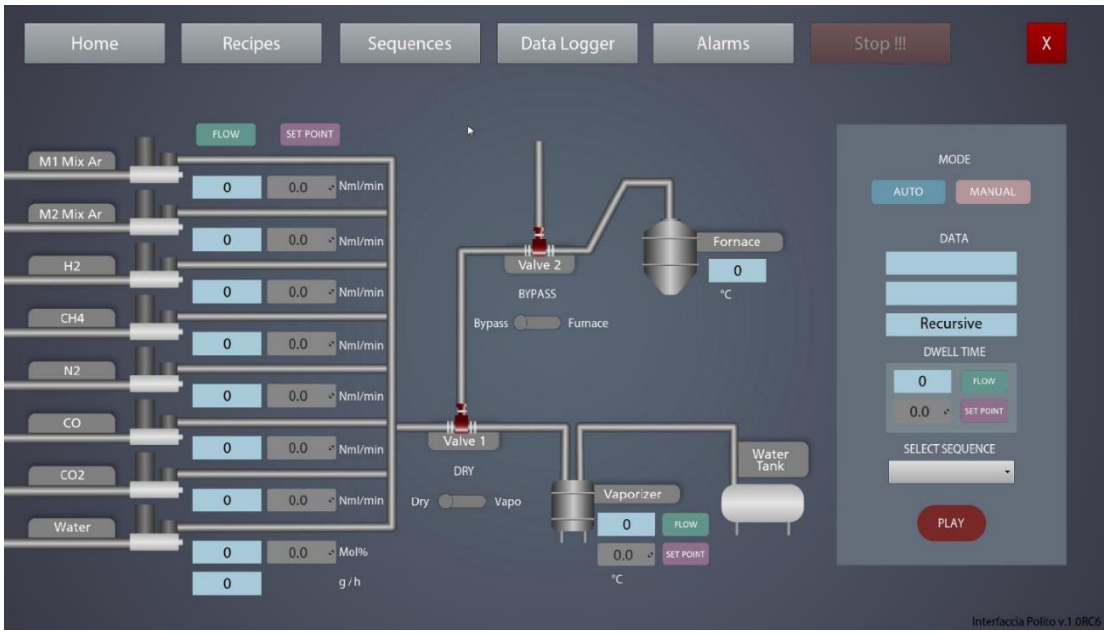

Figure 3.6: *Interface of the control system API-MIoT [72].*

3.1.2 – Gas Analyser System

The gas analyser system is the Emerson Rosemount X-Stream XE gas analyser. It operates with only conditioned gas mixtures, hence the gas flows before entering must be dry, dust-free, and free of other eventual contaminants that can damage the instrument. This the reason why upstream the gas analyser section there is a condenser used to remove moisture from the gas flows entering into the microreactor. The physical principle exploited by this system to measure the continuous gas flows composition is based on two different kind of detection technology: Thermal Conductivity Detector (TCD) and Infrared Detector (IRD). This diversification permits to expand the correct functioning of the instrument in several cases implementing different mixtures and compositions. The Emerson Rosemount X-Stream XE (multichannel NDIR/UV/TCD)) gas analyser allows to measure five distinct chemical species: CO_2, H_2, CH_4, O_2, and CO, one for each channel.

As investigated by Liu et al. [73] and represented in *Figure 3.7*, the gas sensing technologies can be mainly subdivided in two macro-areas: the first one based on electrical variation, the others on different typologies of variation. The most common performance indicators useful to compare these different sensing methods are: response time, sensitivity, selectivity, reversibility, adsorptive capacity, energy consumption, and fabrication cost,

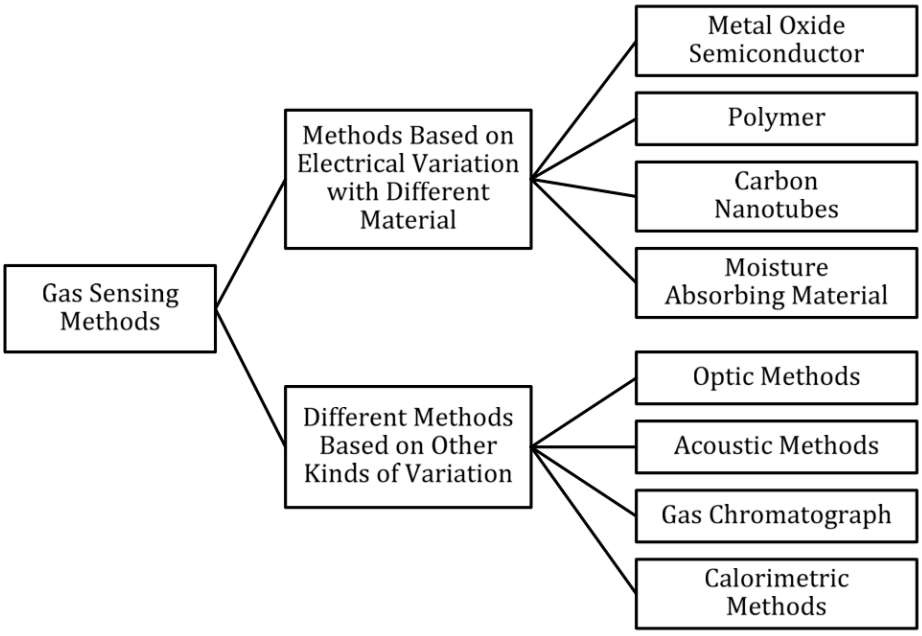

Figure 3.7: *Schematic classification of different gas sensing methods [73].*

Concerning one the two detections technology implemented in the Emerson X-Stream gas analyzer, the Infrared Detection (IRD) exploits the light absorption of the gas flow to distinguish the various chemical species of the mixture. Hence, irradiating a gas stream with IR light, as a result there are obtained different wavelengths that can pass though, or alternatively they can be absorbed. In this latter case, wavelengths absorption means that these wavelengths are equal to the vibrational frequencies of the gas mixture components. From a microscopic point of view, the atoms composing each molecule are able to vibrate only with characteristic frequencies, therefore, in this way it is possible to detect various chemical species by detecting the specific absorption band in which it is visible the characteristic frequency of the correspondent chemical compound. More precisely, to detect the presence of a single component in a gas mixture, the absorption intensity of its bands must be determined. This phenomenon is discussed by Twiss et al. [74] and represented in the *Figure 3.8*. The infrared analyser is composed by two infrared sources, a compensating cell containing air in parallel connection with another cell containing the same under investigation, and two sensitized cells. The IR radiation passes through the two cells: in the compensating cell the radiation is totally absorbed by the downstream sensitized cell because there is only air an not hydrocarbons; at the contrary, in the sample cell only a portion of IR radiation is absorbed, while the remaining part is absorbed by the other down-right sensitized cell. As a final result, the down-left sensitized cell will exhibit a higher temperature compared to the down-right sensitized cell due to the higher rate of IR absorption. Then, this temperature difference causes a deflection of the gold leaf diaphragm located at the centre, and the further conversion of this deflection allows to determine the precise hydrocarbon content in the sample cell.

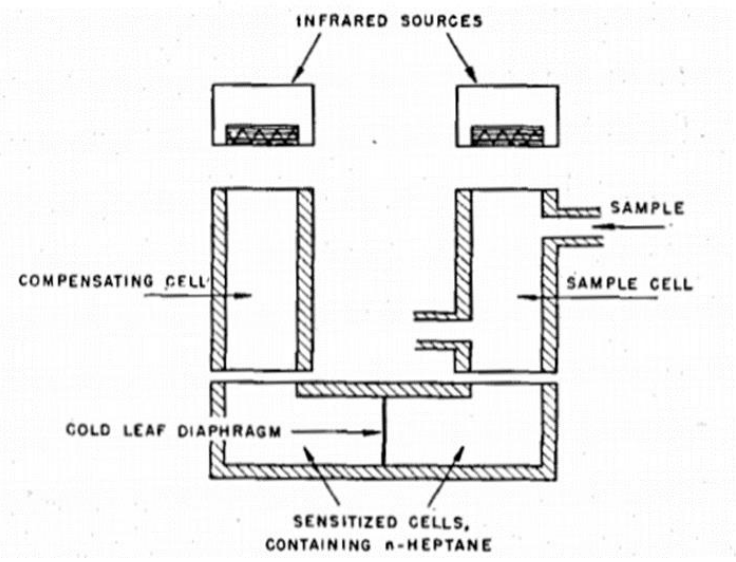

Figure 3.8: *Non-dispersive infrared analyser example [74].*

Moreover, considering the other detection technology exploited in the Emerson X-Stream gas analyzer, the Thermal Conductivity Detector (TDC) is based on the property of the material under investigation to conduct heat. More detailed, the thermal conductivity of a material can be evaluated by means of a Wheatstone Bridge, depicted in *Figure 3.9*. It is composed by 4 temperature sensitive resistors: the sensor R_S is collocated in the sample gas stream, while the second sensor R_R in a reference gas stream following a distinct path compared to the sample one. In the case no gas is flushing, the bridge signal U_{Br} (voltage difference) is equal to zero. The resistors are heated up by providing electrical energy, and then this heat is absorbed by the two gases flowing through the bridge. As a consequence, an electrical signal proportional to the heat absorbed (hence proportional to the thermal conductivity of the gas stream) is generated. In this way, two different electrical signals are generated due to the different amount of heat absorbed by the ample and by the reference gas stream. In conclusion, it is possible to traduce this electrical signal into the molar concentration of the chemical species in the sample gas stream.

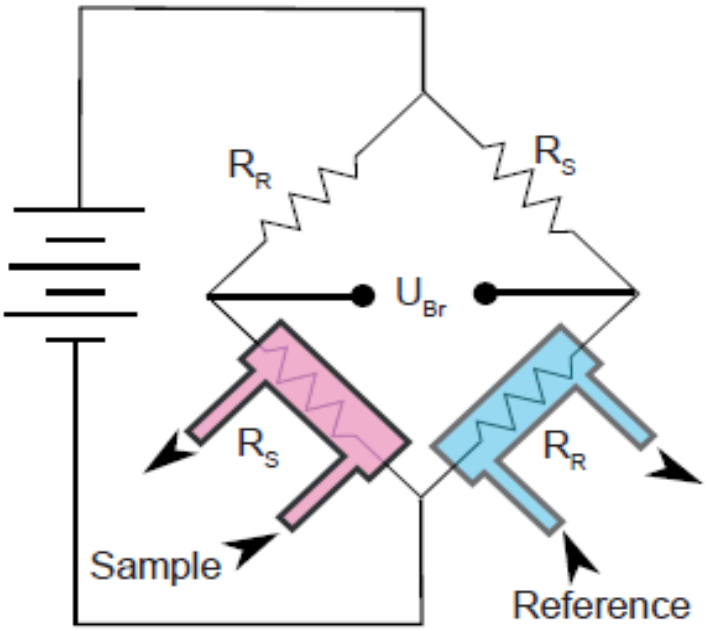

Figure 3.9: *Wheatstone Bridge schematic example [75].*

3.2 – Preliminary Experimental Procedures

In this section are described the preliminary experimental procedures adopted before starting the set of experimental tests described in the following chapter. Firstly, the microreactor is charged by inserting the SFNM-04 sample at the middle of the inner cylindrical tube. Before performing this operation and opening the reactor by removing the flanges, all the gas lines must be close, and the reactor has been previously purged by flowing a nitrogen or argon stream for a few minutes. Similarly, also the power conditioning unit must be switched off and the reactor is maintained at ambient temperature. After that, the SFNM-04 sample is weighted and placed inside the microreactor. Consequentially, the flanges of the charge reactor are re-closed and leak test is performed by automatically sending a certain gas mixture: if the flowmeters measure values lower than 10 % compared to the expected values, it means that the leakages occurring in the circuit can be considered acceptable. Then, the Emerson X-Stream analyser is connected to the outlet gas lines and the temperature program and the gas composition sequences are imposed. After this step, the last one consists to perform a calibration procedure of the gas analyser system in order to obtain measurements as reliable as possible. Hence, each channel range is modified in accordance with the expected reading concentrations, and the zero and maximum range value are verified by sending in the gas line the correspondent gas flow concentrations. Finally, the software programs and the gas analyser data reading are run, and the experimental tests can be properly carried out.

Chapter 4

4. Tests and Results

4.1 – Experimental tests

In this section are described all the experimental tests performed at CO_2 *Circle Lab* inside the Environment Park centre located in Turin, Italy. The CO production rate of SFNM-04 is evaluated considering different operating conditions:

- Operating oxidation and reduction temperatures from $T = 550\ °C$ to $T = 850\ °C$.
- Gas mixture compositions from 6 % to 100 % of CO_2 during the oxidation step and from 5 % to 100 % of H_2during the reduction step in a N_2-based gas mixture.
- Reduction and oxidation reaction time from 15 to 25 minutes.

The experimental analysis is performed in two different stages, the first one focused on the oxidation reaction parameters and the second one on the reduction reaction parameters. Before each test it is done a calibration procedure exploiting the by-pass line of the system to obtain the most possible dependable measurements; in detail, to read flat signals from the real-time Emerson X-stream gas analyser, the zero value for all the gas analyser channels is set while flowing in the gas lines an inert N_2 flow. At the same time for each channel, the maximum value is selected in agreement with the specific test; for instance, if the test is performed with a constant CO_2 flow composition of 20 % in a N_2-based gas mixture, the maximum value of CO_2 is set to 20 %, instead, if during another test the CO_2 flow composition varies from 6 % to 100 %, the maximum value of CO_2 measured by the specific channel is set to 100 %. The same concept is used during the reduction step but instead of a CO_2/N_2 gas mixture, it is sent a H_2/N_2 gas mixture. In this way, the instrument response to these variables change is correctly detected. The fixed variables maintained constant during the whole set of experiments are the SFNM-04 sample mass of $200\ mg$ and the volumetric gas mixture flow rate of $200\ NmL/min$. All the experimental tests are detailed described in the following sections and summarized schematically in *Table 2.*

Table 2: *Set of Experimental Tests of SFNM-04 CO_2 Splitting Reactions.*

TEST	OXI/RED TEMPERATURE T_{OXI} [°C] T_{RED} [°C]	OXI/RED GAS COMPOSITION	N° CYCLES	OXI/RED REACTIONS TIME
TEST (I)	Isothermal $T_{OXI} = 850\ °C$ $T_{RED} = 850\ °C$	Oxi: 20 % CO_2/N_2 Red: 10 % H_2/N_2	5	Oxi: 90 min Red: 60 min
TEST (II)	Non-Isothermal $T_{OXI} = 550, 650, 750, 850\ °C$ $T_{RED} = 850\ °C$	Oxi: 20 % CO_2/N_2 Red: 10 % H_2/N_2	5	Oxi: 30 min Red: 60 min
TEST (III)	Isothermal $T_{OXI/RED} = 750\ °C$ (3 cycles) $T_{OXI/RED} = 850\ °C$ (3 cycles)	Oxi: $20 - 40$ % CO_2/N_2 Red: 10 % H_2/N_2	$3 + 3$	Oxi: 30 min Red: 60 min
TEST (IV)	Isothermal $T_{OXI/RED} = 750\ °C$ (10 cycles) $T_{OXI/RED} = 850\ °C$ (10 cycles)	Oxi: $6 - 100$ % CO_2/N_2 Red: 10 % H_2/N_2	$10 + 10$	Oxi: 30 min Red: 60 min
TEST (V)	Non-Isothermal $T_{OXI} = 750\ °C$ $T_{RED} = 850\ °C$	Oxi: $6 - 100$ % CO_2/N_2 Red: 10 % H_2/N_2	10	Oxi: 30 min Red: 60 min

TEST	OXI/RED TEMPERATURE T_{OXI} [°C] T_{RED} [°C]	OXI/RED GAS COMPOSITION	N° CYCLES	OXI/RED REACTIONS TIME
TEST (VI)	Non-Isothermal $T_{OXI} = 850\ °C$ $T_{RED} = 550, 650, 750, 850\ °C$	Oxi: 20 % CO_2/N_2 Red: 10 % H_2/N_2	5	Oxi: 30 min Red: 60 min
TEST (VII)	Isothermal $T_{OXI/RED} = 850\ °C$ (9 cycles) $T_{OXI/RED} = 750\ °C$ (9 cycles)	Oxi: 20% CO_2/N_2 Red: 5 − 100 % H_2/N_2	9 + 9	Oxi: 30 min Red: 60 min
TEST (VIII)	Non-Isothermal $T_{OXI} = 750\ °C$ $T_{RED} = 850\ °C$	Oxi: 20% CO_2/N_2 Red: 5 − 100 % H_2/N_2	9	Oxi: 30 min Red: 60 min
TEST (IX)	Isothermal $T_{OXI} = 850\ °C$ $T_{RED} = 850\ °C$	Oxi: 20 % CO_2/N_2 Red: 10 % H_2/N_2	6	Oxi: 30 min Red:15, 30, 45, 60, 90, 120 min
TEST (X)	Isothermal $T_{OXI} = 850\ °C$ $T_{RED} = 850\ °C$	Oxi: 20 % CO_2/N_2 Red: 100 % H_2/N_2	1	Oxi: 7 $hours$ Red: 2 $hours$

4.1.1 – TEST (I): 5 Isothermal Redox Cycles at $T = 850\ °C$

This first test is considered the reference one consisting of 5 isothermal cycles at $T = 850\ °C$ with a gas mixture of 20 % CO_2/N_2 during the oxidation step and 10 % H_2/N_2 during the reduction step. The goal of this first test is to analyse the SFNM-04 sample cyclic stability performing 5 identical cycles with the same operating conditions. Before starting with the first redox cycle, it is carried out a pre-treatment step in air at $T = 500\ °C$ to delete any kind of contaminants and to operate with a sample fully oxidized. After that, using the temperature sequences controller, it is imposed a temperature increase from $T = 500\ °C$ to $T = 850\ °C$ with a ramp presenting a rate of $10\ °C/min$. More detailed, a single redox isothermal cycle is composed by the following sequences:

- Purging step in N_2 atmosphere for 5 min.
- Reduction step with a gas mixture composed by 10 % H_2/N_2 for 60 min.
- Purging step in N_2 atmosphere for 5 min.
- Oxidation step with a gas mixture composed by 20 % CO_2/N_2 for 90 min.

All the experimental tests are aimed to evaluate the CO production rate in $[\mu mol/g \cdot s]$. To obtain this unit of measurement, it is necessary to convert the CO production expressed in $[ppm]$ terms measured by the rate real-time gas analyser system. The conversion procedure consists of:

1. Firstly, according to the $[ppm]$ definition, the measured values are divided by 10^6 to obtain a dimensionless quantity [/].

2. Then, these dimensionless values are multiplied by the volumetric flow rate $Q = 200\ [mL/min]$ and divided by $60\ [s/min]$ to obtain the measured values expressed in $[NmL/s]$, where N indicates the NTP (Normal Temperature and Pressure) operating conditions ($T = 293.15\ K$, $p = 1\ atm$). Summarizing, the performed calculations are:

$$[/] \cdot 200\ \left[\frac{NmL}{min}\right] \cdot \frac{1}{60}\left[\frac{min}{s}\right] = \left[\frac{NmL}{s}\right]$$

3. After that, in agreement to the Ideal Gas Law, the molar volume of an ideal gas is equal to $22.4\ L$. In this way, the litres $[L]$ are converted to moles $[mol]$ and finally these values are multiplied by 10^3 to convert the $[mL]$ into $[\mu L]$. To sum up, this is the procedure:

$$\left[\frac{NmL}{s}\right] \cdot 10^3 \left[\frac{\mu L}{mL}\right] \cdot \frac{1}{22.4}\left[\frac{mol}{L}\right] = \left[\frac{\mu mol}{s}\right]$$

4. In conclusion, these values are divided by the SFNM-04 sample mass of $200\ mg$ achieving the desired unit of measurement:

$$\left[\frac{\mu mol}{s}\right] \cdot \frac{1}{200\ [mg]} \cdot 10^3 \left[\frac{mg}{g}\right] = \left[\frac{\mu mol}{g \cdot s}\right]$$

Once the CO production rate in $[\mu mol/g \cdot s]$ is evaluated second by second (as explained in the previous chapter the Emerson Rosemount X-Stream XE gas analyser provides the concentration values of all the five detectable chemical species in $[ppm]$ with a time discretization step of $1\ s$), another useful parameter is the CO production yield expressed in $[\mu mol/g]$. To obtain the yield, it is necessary to implement an integration method able to sum all the proper values below the oxidation curve. As shown in *Figure 4.1*, once the oxidation curve is plotted considering the CO production values in $[ppm]$ second by second during the oxidation step, it is evident that the tail of the curve never reaches the zero values observed before the peak, but it stabilizes at around $1400\ [ppm]$. For this reason, to avoid the negative tail effect summing very similar and low values obtaining a non-reliable CO yield, it was decided to exploit the first derivative and set as breaking point to calculate the yield the value in which the first derivative tends to be between a fixed tolerance having a maximum value of $0.05\ \%$ and a minimum value of $-0.05\ \%$. This procedure, represented in *Figure 4.2*, is quite conservative, but at the same time, it can be a good approximation of the CO yield because when the first derivative variation between one average value and the next one is lower than $0.05\ \%$ means that the tail has reached a constant value.

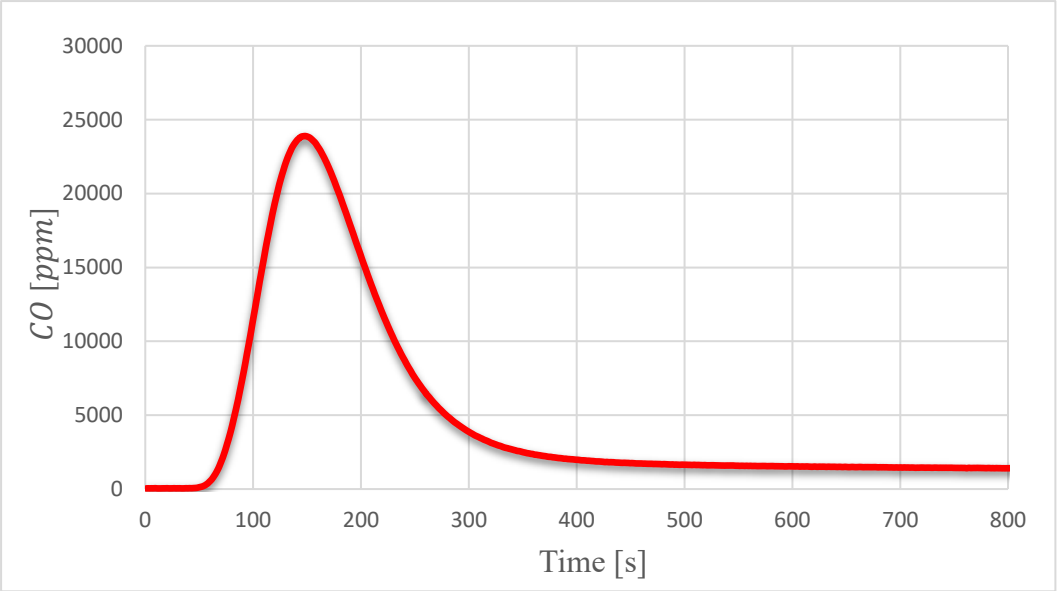

Figure 4.1: *CO production rate in* $[ppm]$ *during the oxidation step with* $20\ \%\ CO_2/N_2$.

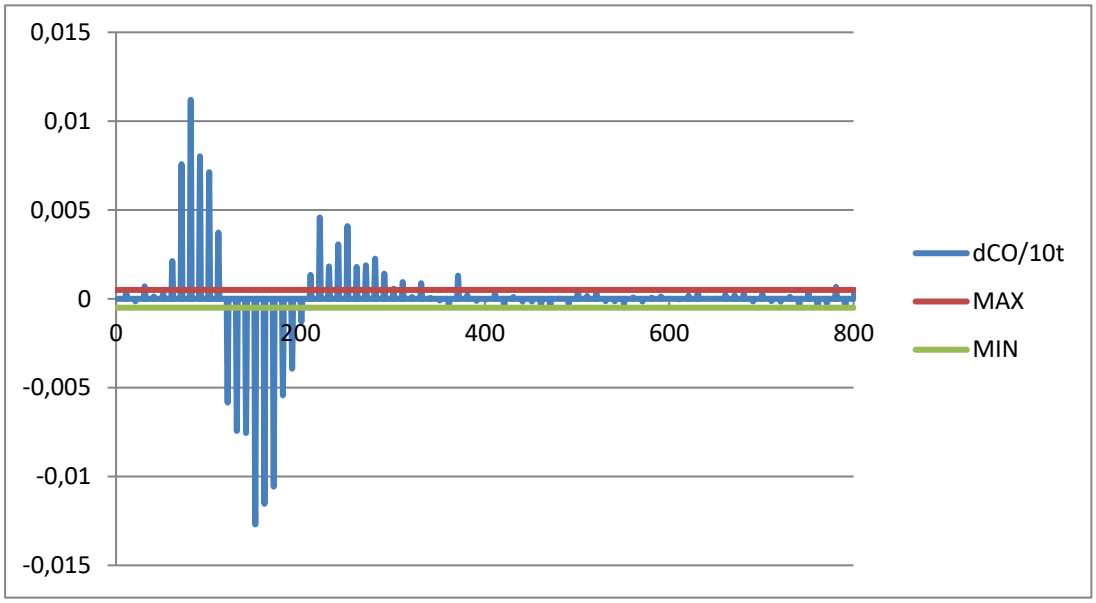

Figure 4.2: *First Derivative of* CO *production rate considering* 10 *subsequent time steps (blue lines). Maximum (red line) and minimum (green line) tolerance.*

In this case the time instant at which the oxidation curve can be considered concluded and stabilized is $t = 450\ s$. Therefore, once the breaking point to calculate the CO yield is set, it is possible to draw a straight line and evaluate the difference between the values of the CO production curve and the values of the straight line obtaining in this way a CO net production. This method is depicted by the following *Figure 4.3 (a)-(b).*

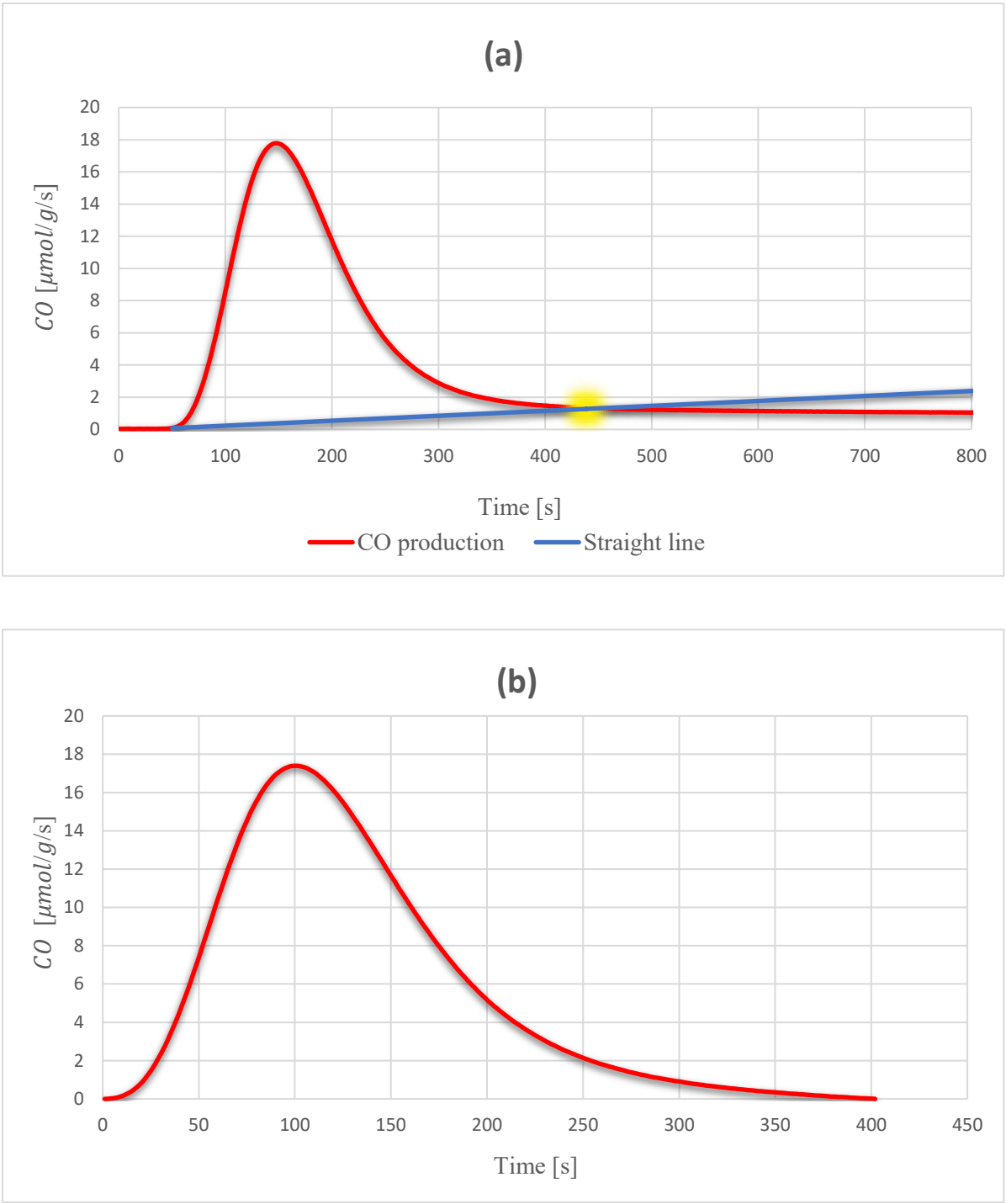

***Figure 4.3* (a)-(b):** *(a) CO production (red curve) cut by the straight line (blue line) at $t = 450\ s$. (b) Net CO production evaluated subtracting the values of the CO production curve to the values of the straight line.*

This integration method is implemented for all the experimental tests, and as discussed later in chapter 5, the choice of the integration method is crucial to obtain values of CO production rate for SFNM-04 comparable with other looping materials tested in literature.

Now that all the preliminary procedures are described, the oxidation curves obtained from TEST (I) are depicted by *Figure 4.4*, where the left vertical axis indicates the CO production rate in $[\mu mol/g \cdot s]$, while the left axis always the CO production rate but expressed in [%] terms.

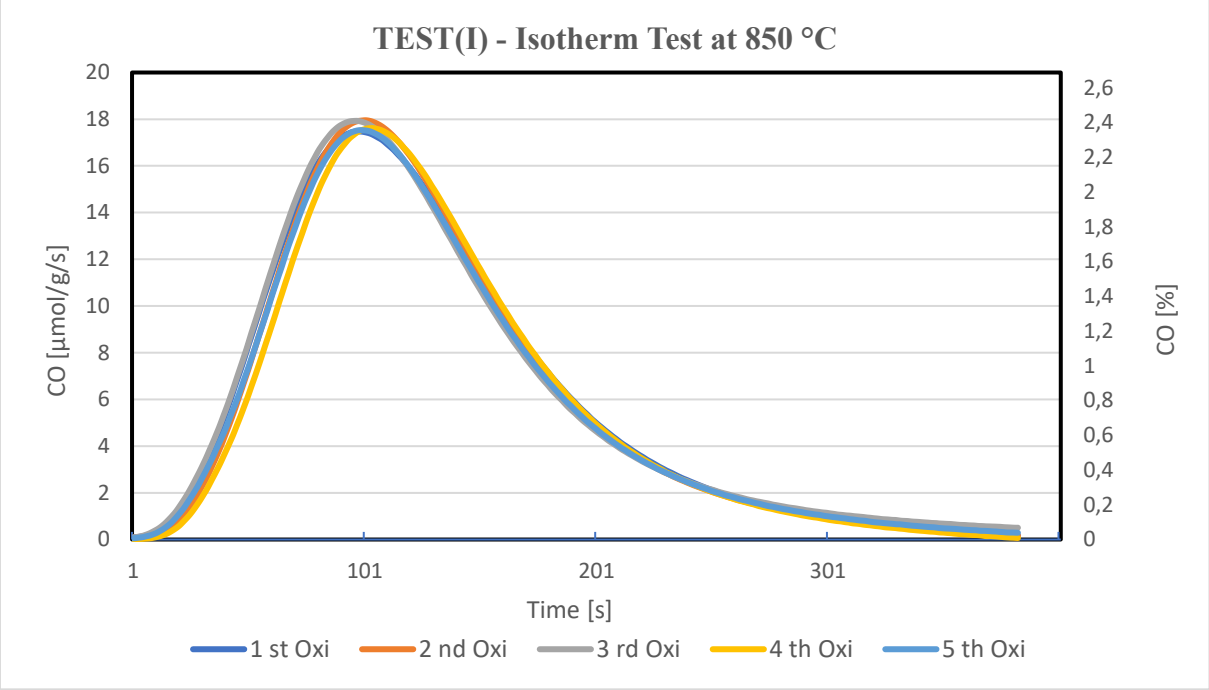

***Figure 4.4*:** *CO Production of TEST (I) in $[\mu mol/g \cdot s]$ and in [%] terms.*

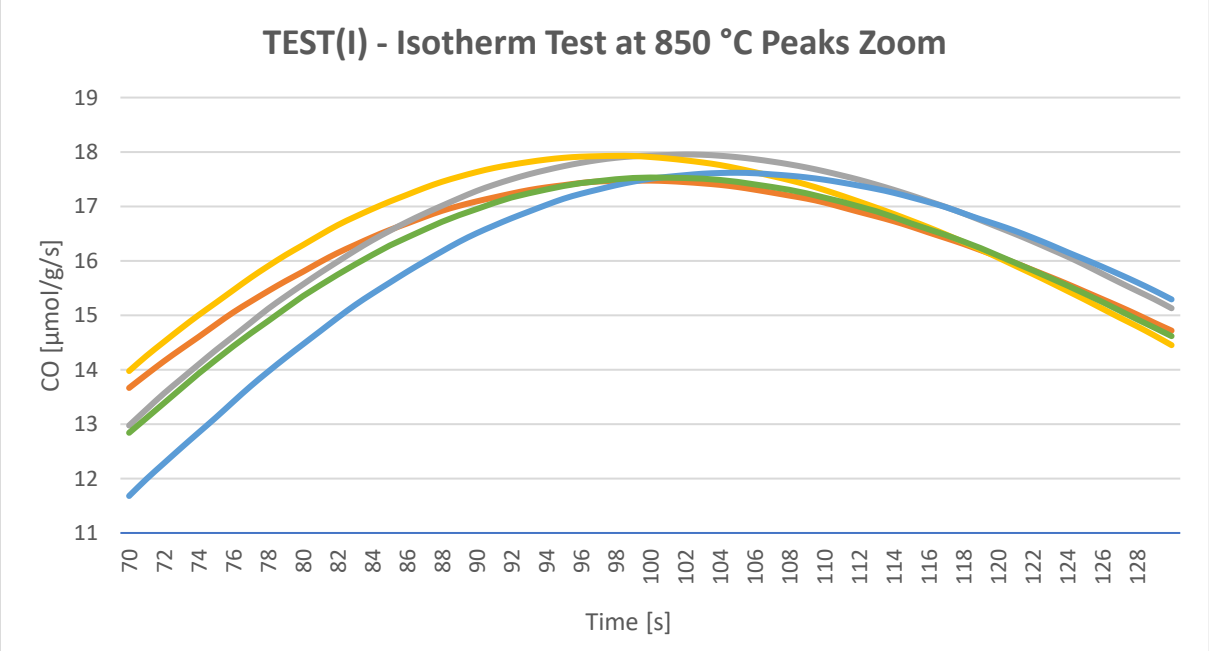

***Figure 4.5*:** Peaks Zoom of the Oxidation Curves during the TEST (I).

As expected, the SFNM-04 response during the five redox cycles remains the same indicating a good stability and repeatability throughout the whole process. Each oxidation curve exhibits a fast-initial CO increase corresponding to the rapid oxygen vacancies ion incorporation followed by a sudden decrease. The maximum CO yield reached is about 18 $[\mu mol/g \cdot s]$ corresponding to a maximum of CO percentage in the outlet mixture of about 2.4 %. For each redox cycle, the CO peak is considered concluded after $t = 375\ s$, hence from the start of the oxidation step when the gas mixture composed by 20 % CO_2/N_2 enters in the microreactor and laps the SFNM-04 sample. As shown in *Figure 4.5*, this almost identical trend of the five oxidation curves demonstrates that the kinetic of the redox reactions is comparable in all the five cycles. More detailed, in *Table 3* are summarized the most relevant results calculated for each cycle:

- The first column corresponds to the CO yield expressed in $[\mu mol/g]$ and evaluated in agreement with the integration method previously explained.
- The second column indicates the maximum CO yield in [%] terms reached during the oxidation step.
- The third column represents the CO_2 conversion in [%] terms calculated by dividing the maximum CO yield in [%] with respect to the initial CO_2 content in the gas mixture; hence, in this case the calculation is:

$$\frac{CO\ yield\ [\%]}{\frac{CO_2\ [\%]}{100}\ [/]} = CO_2\ converted\ [\%]$$

This term provides a numerical evaluation of the moles of CO_2 entering inside the microreactor converted into CO moles during the oxidation step, while the 20 % CO_2/N_2 gas mixture lapping the SFNM-04 sample.

- The fourth and fifth column express the mass exchanged during the oxidation step in grams terms of Oxygen and CO respectively with respect to the SFNM-04 sample mass. In this calculation it is assumed a molar ratio $1:1$ during the CO_2-splitting reaction of both O and CO; therefore, starting from the CO yield in $[\mu mol/g]$ and knowing the molar mass of O $(16\ g/mol)$ and of CO $(28\ g/mol)$, the ratio is evaluated as:

$$CO\ yield\ \left[\frac{\mu mol}{g_{SFNM}}\right] \cdot 16\ \left[\frac{g_O}{mol}\right] \cdot 10^{-6} \left[\frac{mol}{\mu mol}\right] = \frac{g\ (O)}{g\ (SFNM)}\ \left[\frac{g_O}{g_{SFNM}}\right]$$

$$CO\ yield\ \left[\frac{\mu mol}{g_{SFNM}}\right] \cdot 28\ \left[\frac{g_{CO}}{mol}\right] \cdot 10^{-6}\left[\frac{mol}{\mu mol}\right] = \frac{g\ (CO)}{g\ (SFNM)}\ \left[\frac{g_{CO}}{g_{SFNM}}\right]$$

Table 3: *Results for each redox cycle of TEST (I):* CO *yield in* $[\mu mol/g]$*, maximum* CO *yield in* [%]*,* CO_2 *conversion rate in* [%]*,* $g(O)/g(SFNM)$ *and* $g(CO)/g(SFNM)$*.*

N° Cycle	$\boldsymbol{CO}$ ***yield*** $[\boldsymbol{\mu mol/g}]$	***Max*** $\boldsymbol{CO}$ ***[%]***	$\boldsymbol{CO_2}$ ***conversion [%]***	$\boldsymbol{g(O)/g(SFNM)}$ $[\boldsymbol{g_O/g_{SFNM}}] \cdot \boldsymbol{10^{-2}}$	$\boldsymbol{g(CO)/g(SFNM)}$ $[\boldsymbol{g_{CO}/g_{SFNM}}]$ $\cdot \boldsymbol{10^{-2}}$
1	2278	2.35	11.75	3.65	6.38
2	2239	2.41	12.05	3.58	6.27
3	2286	2.41	12.05	3.66	6.40
4	2173	2.37	11.85	3.48	6.08
5	2212	2.36	11.80	3.54	6.19

As before analysing the graphical results, also these very similar numerical evaluations confirm the cyclic ability of SFNM-04 during the five redox cycles. The average CO yield reached is about $2238\ [\mu mol/g]$ with an average CO_2 conversion of 11.9 %. The last two columns of *Table 3* indicate that, starting from a SFNM-04 sample mass of $200\ mg = 0.2\ g$, the grams of oxygen exchanged are about $0.036\ g$, while the grams of CO exchanged are about $0.063\ g$. As better explained later in chapter 5, the sample mass of the material under investigation implemented during the microreactor tests is another crucial parameter useful to compare the performance of other looping materials tested in terms of CO production.

4.1.2 – TEST (II): 5 Redox Cycles at Different Oxidation Temperatures

As anticipated before and summarized in *Table 2*, the experimental analysis is primarily focused on the oxidation parameters (from TEST (II) to TEST (V)) and secondly on the reduction parameters (from TEST (VI) to TEST (X)). In fact, the goal of this TEST (II) is to investigate the CO production profile during the oxidation step by varying the oxidation temperature, by keeping the same reduction temperature of $T_{RED} = 850\ °C$, the same gas mixture composition of the previous reference TEST (I). More detailed, the first and the last cycles are performed at $T_{OXI} = 850\ °C$, while the other three oxidation steps respectively at $T_{OXI} = 550\ °C - 650\ °C - 750°C$. As usual, the first step consists of a pre-treatment in air at $T = 500\ °C$, then, while a $100\ \%\ N_2$ flow is flushing inside the microreactor, it is imposed a ramp with a temperature increase rate of $10\ °C/min$ in order to reach $T = 850\ °C$. The other following steps are listed below:

- Reduction step at $T_{RED} = 850\ °C$ with a gas mixture composed by $10\ \%\ H_2/N_2$ for $60\ min$.
- Purging step in N_2 atmosphere for $10\ min$ (cycle 1), cooling down step to $T_{OXI} = 550\ °C$ (cycle 2), to $T_{OXI} = 650\ °C$ (cycle 3), to $T_{OXI} = 750\ °C$ (cycle 4). Then another purge in N_2 for $10\ min$ (cycle 5).
- Oxidation step with a gas mixture composed by $20\ \%\ CO_2/N_2$ for $30\ min$ perfomed at $T_{OXI} = 850\ °C$ (cycle 1), at $T_{OXI} = 550\ °C$ (cycle 2), at $T_{OXI} = 650\ °C$ (cycle 3), at $T_{OXI} = 750\ °C$ (cycle 4) and finally again at $T_{OXI} = 850\ °C$ (cycle 5).
- Purging step in N_2 atmosphere for $10\ min$ (cycle 1), then heating back to $T_{OXI} = 850\ °C$ (cycle $2, 3, 4$), ramp-down up to room-temperature in N_2 (cycle 5 – end of the test).

The graphical and numerical results of TEST (II) are shown respectively in *Figure 4.6* and *Table 4*. At first view, it is again confirmed a well cyclic repeatability of SFNM-04 because the first and last cycle (red and blue curves), performed with the same operating conditions of the previous reference TEST (I), present an almost identical trend both graphically and numerically. The graph of *Figure 4.6* illustrates the CO peaks occurring during the oxidation reaction: the x-axis represents the time, the left axis shows the CO production rate in terms of $[\mu mol/g \cdot s]$, while the right axis in terms of volume percentage. It is evident that the CO production rate increases at high temperature levels with a maximum value equal to 18 $[\mu mol/g \cdot s]$ at $T_{OXI} = 850\ °C$. Each oxidation curve exhibits a fast-initial CO increase corresponding to the rapid oxygen vacancies ion incorporation followed by a sudden decrease.

This behaviour demonstrates strong temperature dependence of the CO rate profile, which becomes higher and wider at higher temperature due to the higher amount of available oxygen sites.

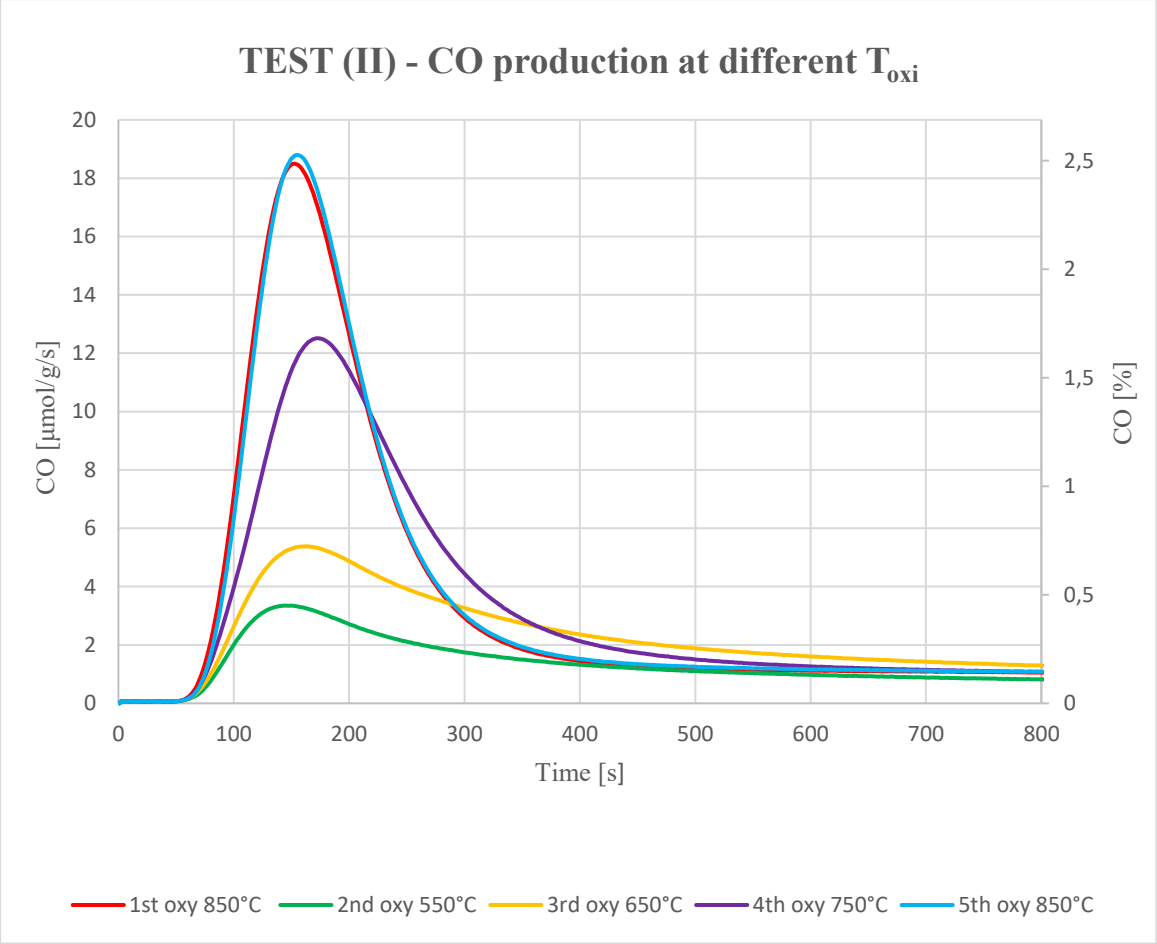

Figure 4.6: *CO Production of TEST (II) at different Oxidation Temperatures $T_{OXI} = 850\ °C - 550\ °C - 650 - 750 - 850\ °C$ expressed in $[\mu mol/g \cdot s]$ and in $[\%]$ terms.*

An increase from $T_{OXI} = 750\ °C$ to $T_{OXI} = 850\ °C$ shows significant enhancement of peak production rates, at the contrary from $T_{OXI} = 550\ °C$ to $T_{OXI} = 850\ °C$ the peak growth is less marked. This aspect can be explained observing that, at lower oxidation temperatures, the curves exhibit a slower trend suggesting that the oxidation temperature decrease allows to a slower reaction kinetics implying a lower CO yield. Finally, the fifth oxidation curve occurring again at $T_{OXI} = 850\ °C$ indicates that the material does not show a loss of reactivity performance after the cycles performed at lower temperature, in fact the two oxidation curves of the first and fifth cycles are almost identical. All these aspects are confirmed by the numerical results summarized in *Table 4*.

Table 4: *Results for each redox cycle of TEST (II): CO yield in $[\mu mol/g]$, maximum CO yield in $[\%]$, CO_2 conversion rate in $[\%]$, $g(O)/g(SFNM)$ and $g(CO)/g(SFNM)$.*

N° Cycle	T_{OXI} $[°C]$	*CO yield* $[\mu mol/g]$	*Max CO [%]*	CO_2 *conversion [%]*	$g(O)/g(SFNM)$ $[g_O/g_{SFNM}] \cdot 10^{-2}$	$g(CO)/g(SFNM)$ $[g_{CO}/g_{SFNM}]$ $\cdot 10^{-2}$
1	850	2276	2.49	12.43	3.64	6.37
2	550	825	0.45	2.25	1.32	2.31
3	650	1534	0.72	3.62	2.45	4.30
4	750	1864	1.68	8.41	2.98	5.22
5	850	2274	2.53	12.63	3.64	6.37

From these numerical results it is demonstrated that higher oxidation temperatures allow to obtain better performance, in fact at $T_{OXI} = 850\ °C$ the global CO yield is about three time higher than that at $T_{OXI} = 550\ °C$ and the CO_2 converted at $T_{OXI} = 850\ °C$ is six and four times higher than that at $T_{OXI} = 550\ °C$ and at $T_{OXI} = 650\ °C$, respectively. Notwithstanding, the recent studies on perovskite material as oxygen carrier for thermochemical redox cycles are aimed to reduce the operating temperature of the whole process. In fact, there are already looping materials tested for this kind of process able to outperform perovskite-base oxygen carrier, as for instance Ceria with typical operating temperatures of the order $T = 1000 - 1500\ °C$. Therefore, it is more relevant to investigate lower temperature ranges in order to test new promising oxygen-carrier materials because, in general, lower is the operating temperature, simpler will be the integration with the renewable energy system used to provide the thermal energy as input for the Renewable Chemical Looping Reforming (R-CLR) process. But at the same time, if the oxidation/reduction temperature is too low, especially the oxidation step during which occurring the effective CO production, beyond the poor performance, another problem strictly enhanced by the low temperatures is the formation of carbonates compound through the CO_2 adsorption on Sr atoms. This issue significantly affects the CO production and the CO_2 conversion because the CO_2 molecules, instead of splitting and converting into CO, actively participate to the creation of carbonate compounds like $SrCO_3$. In conclusion, the results of TEST (II) confirm that the oxidation temperature significantly affects the redox performance and catalytic activity of the SFNM-04 sample, especially its reaction kinetics.

4.1.3 – TEST (III): 6 Isothermal Cycles with CO_2 Content (20 ÷ 40 %)

Once the oxidation temperature variation is investigated, the goal of TEST (III) is to analyse the redox performance of SFNM-04 by varying the CO_2 content during the oxidation step. This test is composed by six redox cycles: the first three are performed at $T_{OXI} = T_{RED} = 850\ °C$ with a CO_2 concentration in the N_2-based oxidizing gas mixture of $20\ \%, 30\ \%$ and $40\ \%$, respectively, for $30\ min$. The other three redox cycles are carried out with the same variation of CO_2 during the oxidation step, but at different temperature level $T_{OXI} = T_{RED} = 750\ °C$. On the other hand, the operating conditions of the reduction step are maintained constant and equal to previous step, hence the reducing gas mixture sent is composed by $10\ \%\ H_2/N_2$ lasting $60\ min$. The global graphical results of TEST (III) are reported in *Figure 4.7.*

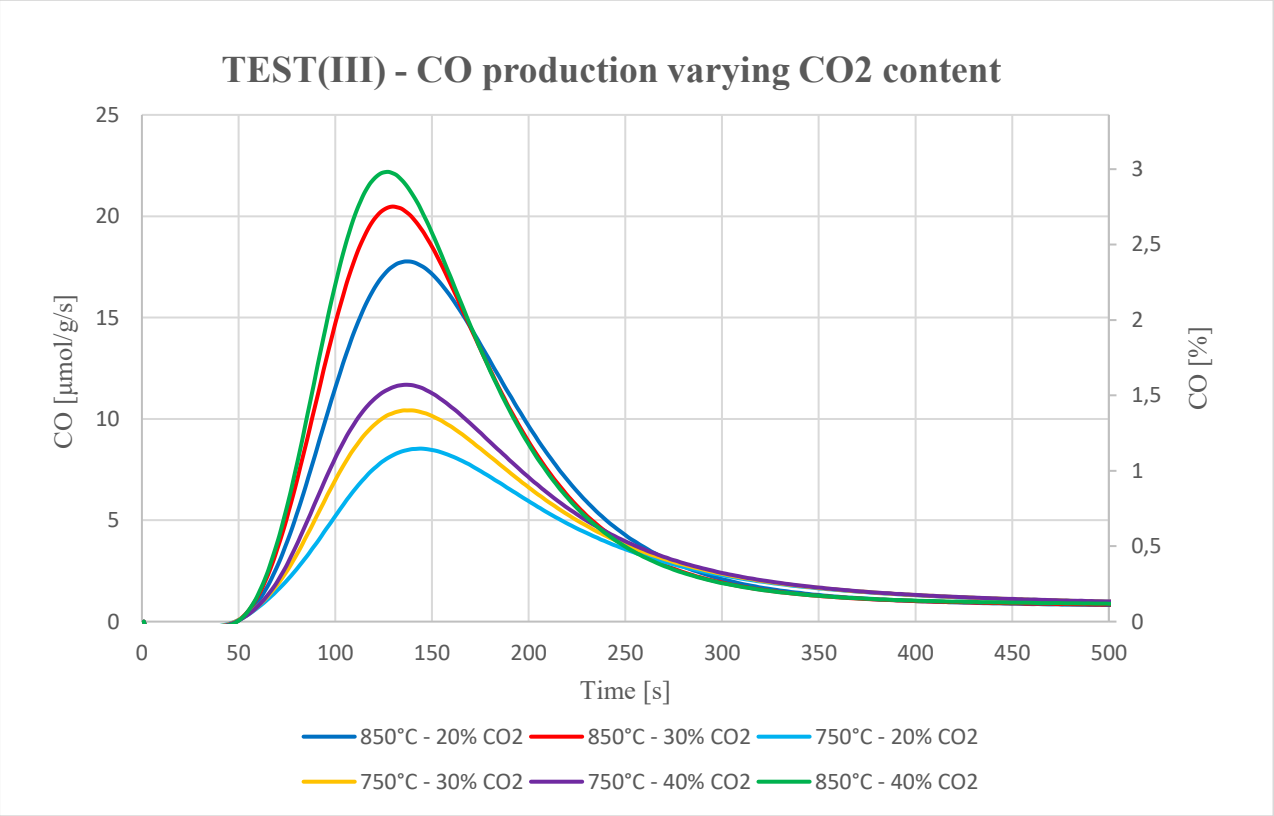

Figure 4.7: *CO Production of TEST (III) expressed in $[\mu mol/g \cdot s]$ and in $[\%]$ terms.*

As already demonstrated by the previous TEST (II), it is evident how the three cycles performed at $T = 850\ °C$ (green, red and dark blue curves) present higher CO peaks and faster production reaction compared to the other three cycles performed at $T = 750\ °C$ (violet, yellow and light blue curves). Nevertheless, the main goal of TEST (III) is to analyse the influence of different CO_2 concentration in the N_2-based oxidizing gas mixture. Concerning this aspect, as the CO_2 content increases, consequently the CO production significantly increments.

In fact, the maximum value of CO production is represented by the green curve (40 % CO_2/N_2 at $T = 850\ °C$) reaching values of the orders of 22 $[\mu mol/g \cdot s]$ corresponding to a CO volume percentage of about 3 %. Then, the CO production progressively decreases achieving values of about 20 $[\mu mol/g \cdot s]$ and 17 $[\mu mol/g \cdot s]$ corresponding to the red curve (30 % CO_2/N_2 at $T = 850\ °C$) and dark blue curve (20 % CO_2/N_2 at $T = 850\ °C$), respectively. The same trend is noticed for the other three curves at $T = 750\ °C$, but these oxidation curves present lower peaks reaching CO production values of the order of 10 $[\mu mol/g \cdot s]$. A first possible explanation of this trend is that, ideally, a higher amount of CO_2 in the oxidizing gas mixture entering in the microreactor promotes the re-oxidation of the SFNM-04 sample producing more CO because, in this way, it is favoured the process during which the oxygen vacancies are occupied by CO_2 molecules. Hence, higher is the CO_2 concentration during the oxidation step, higher will be the probability that these CO_2 molecules are able to occupy the oxygen vacancies generated during the reduction step.

Furthermore, from a kinetics reaction point of view, by increasing the CO_2 content, it is evident how the CO peaks of the oxidation curves tend to slightly shift towards left resulting a faster reaction kinetics and emphasizing that the oxidation step is more promising when the partial pressure of the oxidant agent increases. In fact, as explained in chapter 2, concerning the Thermodynamics of the CO_2-splitting reaction, an increase of CO_2 content in the oxidizing gas mixture causes an increase of the partial pressure and consequently the oxidation step is more favourable.

In the next *Table 5* are reported the main numerical results of TEST (III).

Table 5: *Results for each redox cycle of TEST (III): CO yield in* $[\mu mol/g]$*, maximum CO yield in* [%]*, CO_2 conversion rate in* [%].

N° Cycle	T_{OXI} [°C]	CO_2 ***Content [%]***	***CO yield*** $[\mu mol/g]$	***Max CO [%]***	CO_2 ***conversion [%]***
1	850	20	2183	2.39	11.94
2	850	30	2224	2.75	9.17
3	850	40	2341	2.98	7.46
4	750	20	1444	1.15	5.74
5	750	30	1634	1.40	4.67
6	750	40	1789	1.57	3.93

Considering the CO yield, it is evident the huge difference between the values of the first three rows evaluated at $T = 850\ °C$ and the values evaluated at $T = 750\ °C$ that are almost 25 % lower. The same for the maximum CO production rate and the CO_2 conversion that at $T = 850\ °C$ and fixed CO_2 content are about two times higher compared to the results at $T = 750\ °C$. Therefore, it is again demonstrated that the oxidation temperature plays a crucial role in terms of redox activity and reaction kinetics; this because a variation of only $\Delta T = 100\ °C$ significantly affects the redox performance of the SFNM-04 sample. On the other hand, considering only the CO_2 content variation, the difference of the results is less remarkable, almost negligible. For instance, considering the results of the first three rows, or those of the last three rows, both CO yield and maximum CO production present very similar values.

In conclusion, thanks to the results obtained by TEST (III), it is possible to assert that the oxidation temperature variation affects the redox ability and reaction kinetics of the SFNM-04 sample more than the CO_2 content variation. This aspect is valid especially for perovskite materials because the oxidation temperature must be high enough in order to be able to reduce eventual carbonates formation typically generated when using material composed by element like Strontium Sr. However, TEST (III) is only a preliminary analysis of the CO_2 content variation, in fact in the following TEST (IV) and TEST (V) is investigated the entire range of possible CO_2 percentage from 6 % up to 100 %.

4.1.4 – TEST (IV): 20 Isothermal Cycles with CO_2 Content (6 ÷ 100 %)

TEST (IV) is aimed to investigate the CO_2 content variation considering a wider range compared to the previous test, not again 20 ÷ 40 %, but instead 6 ÷ 100 %. It consists of:

- Ten isothermal redox cycles at $T_{OXI} = T_{RED} = 750\ °C$.
- Ten isothermal redox cycles at $T_{OXI} = T_{RED} = 850\ °C$.

More precisely, each cycle is composed by:

- A reducing step during which it is provided a gas reducing flow with a constant composition of 10 % H_2/N_2 for 60 min.
- An oxidation step with a gas oxidizing mixture having different CO_2 concentration ranging between 6 ÷ 100 % for 30 min.

The graphical results are depicted in *Figure 4.8* and show the first ten oxidation curves performed at $T_{OXI} = T_{RED} = 750\ °C$ in terms of CO production.

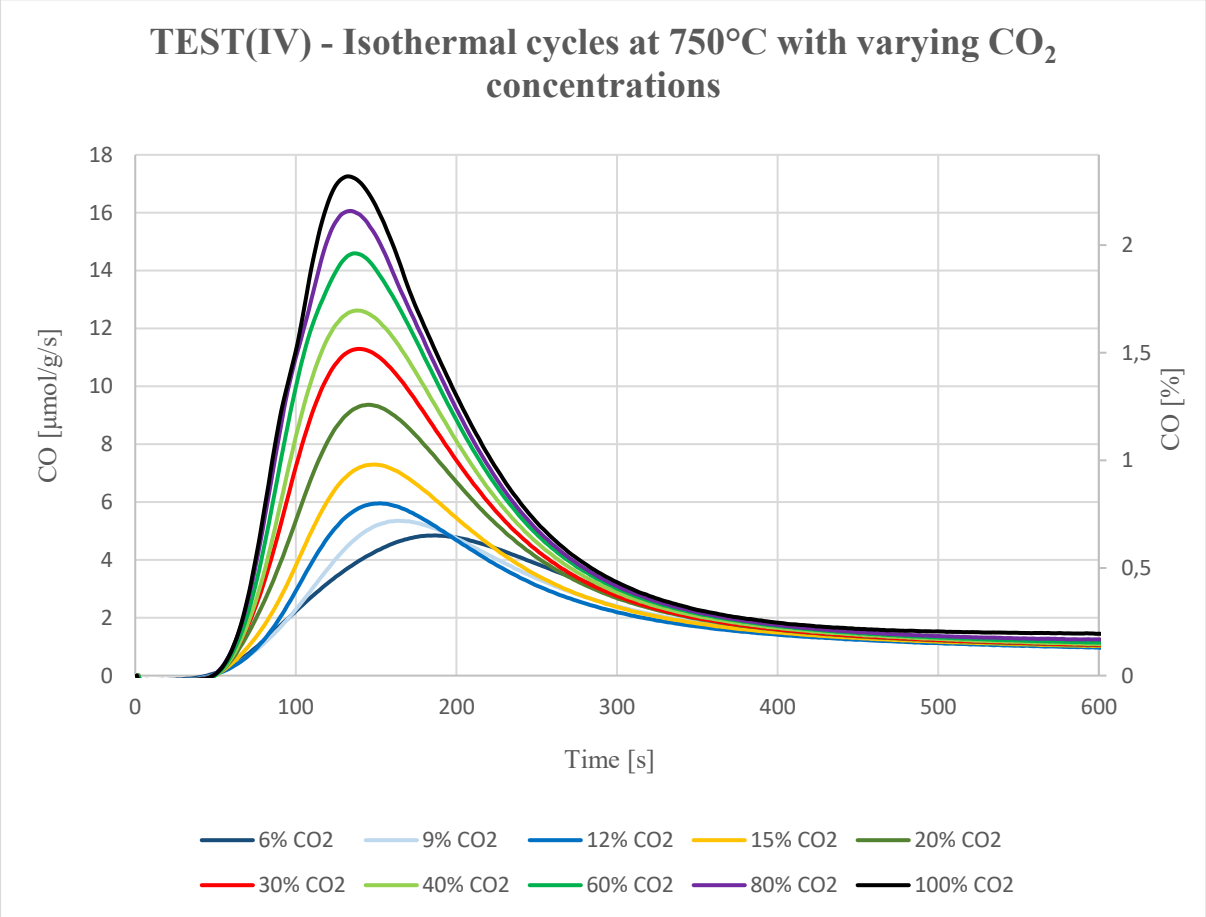

***Figure 4.8**: CO Production of TEST (IV) expressed in $[\mu mol/g \cdot s]$ and in [%] terms: 10 Isothermal Cycles at $T = 750\ °C$ by varying the CO_2 content (6 ÷ 100 %) during oxidation.*

It is evident that the trend of the oxidation curves is the same evaluated in the previous TEST (III), hence the increment of the CO_2 content of the gas oxidizing mixture allows to achieve higher CO yield. Moreover, the results obtained with a CO_2 concentration of $20\ \% - 30\ \% - 40\ \%$ (orange, red and light green curves, respectively) are almost identical to those obtained in TEST (III) with the same operating condition, indicating that the double perovskite material under investigation presents a good redox repeatability also after subjecting to a huge number of thermochemical CO_2-splitting work cycles. The most relevant numerical results obtained from the first ten cycles performed at $T_{OXI} = T_{RED} = 750\ °C$ are summarized in *Table 6.*

Table 6: *Results for each redox cycle of TEST (IV) performed at* $T = 750\ °C$*:* CO *yield in* $[\mu mol/g]$*, maximum* CO *yield in* [%]*,* CO_2 *conversion rate in* [%].

N° Cycle	***CO_2 Content [%]***	***CO yield*** $[\mu mol/g]$	***Max CO [%]***	***CO_2 conversion [%]***
1	6	1115	0.65	10.85
2	9	1118	0.72	7.99
3	12	1139	0.80	6.67
4	15	1194	0.98	6.54
5	20	1500	1.26	6.29
6	30	1723	1.52	5.06
7	40	1895	1.70	4.24
8	60	2111	1.96	3.27
9	80	2158	2.16	2.70
10	100	2270	2.32	2.32

Considering the black oxidation curve of *Figure 4.*8 evaluated with a CO_2 content of 100 %, the maximum CO yield produced is about 2270 $[\mu mol/g]$, with a CO peak located at around 17 $[\mu mol/g \cdot s]$ (in volume percentage terms about 2.32 %). This maximum value is slightly lower compared to the value obtained in the reference TEST (I) carried out at $T = 850\ °C$ with a gas oxidizing mixture composed by 20 % CO_2/N_2 (in this case the CO peak is located around to 18 $[\mu mol/g \cdot s]$).

This emphasizes that even if the CO_2 content of the gas mixture used during the oxidation step is increased from 20 % to 100 %, it is reached almost the same CO production rate indicating that the oxidation temperature is a variable that affects more than the CO_2 variation.

This aspect is further analysed in the next test that is the same of the previous one, with the only difference of the operating temperature: it is not more $T_{OXI} = T_{RED} = 750\ °C$, but now it is increased up to $T_{OXI} = T_{RED} = 850\ °C$. Observing the ten oxidation curves depicted in *Figure 4.9*, also in this configuration, an increase of the CO_2 content of the gas oxidizing mixture allows to an increase of the CO production rate.

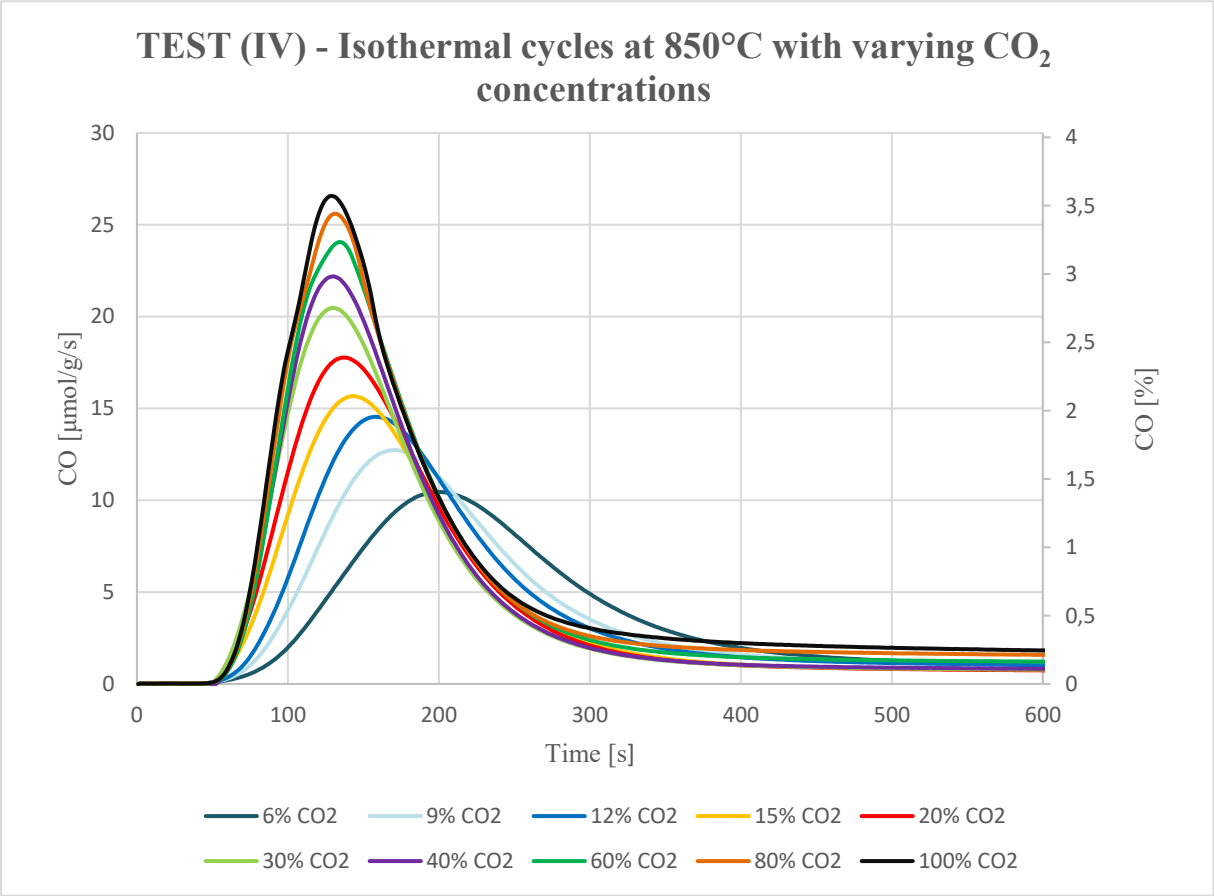

Figure 4.9: *CO Production of TEST (IV) expressed in $[\mu mol/g \cdot s]$ and in [%] terms:* 10 *Isothermal Cycles at $T = 850\ °C$ by varying the CO_2 content* $(6 \div 100\ \%)$ *during oxidation.*

From this graph it is noticed that the ten oxidation curves tend to shrink when the CO_2 content increase, indicating a more rapid reaction kinetics. Furthermore, it is evident that the differences between the curves in terms of CO peaks are wider for low CO_2 concentrations (from 6 % to 40 %) and almost trifling for high CO_2 concentrations (from 60 % to 100 %), revealing that the CO_2 content variation affects more the results for low concentration values compared to high concentration values.

In conclusion, the next *Table 7* summarizes the numerical results obtained by this second stage of TEST (IV) consisting of ten isothermal cycles at $T_{OXI} = T_{RED} = 850\ °C$.

Table 7: *Results for each redox cycle of TEST (IV) performed at* $T = 850\ °C$*:* CO *yield in* $[\mu mol/g]$*, maximum* CO *yield in* [%]*,* CO_2 *conversion rate in* [%].

N° Cycle	CO_2 *Content [%]*	CO *yield* $[\mu mol/g]$	*Max* CO *[%]*	CO_2 *conversion [%]*
1	6	1800	1.41	23.43
2	9	1937	1.71	19.01
3	12	2027	1.96	16.29
4	15	2090	2.11	14.04
5	20	2183	2.39	11.94
6	30	2224	2.75	9.17
7	40	2341	2.98	7.46
8	60	2622	3.23	5.39
9	80	2689	3.44	4.30
10	100	2778	3.57	3.57

With these operating conditions, the maximum CO yield produced, corresponding to the black oxidation curve of *Figure 4.18*, is about 2778 $[\mu mol/g]$, with a CO peak located at around 26 $[\mu mol/g \cdot s]$ (in volume percentage terms about 3.57 %). Therefore, this maximum value obtained with gas oxidizing mixture composed by 100 % CO_2 at $T = 850\ °C$ is significantly higher compared to the previous performed at $T = 750\ °C$ enhancing the predominate role of the oxidation temperature in terms of redox performance: an increase of $\Delta T = 100\ °C$ implies a variation of the CO production yield from 2270 $[\mu mol/g]$ to 2778 $[\mu mol/g]$ and an increase of the CO peak value from 17 $[\mu mol/g \cdot s]$ to about 26 $[\mu mol/g \cdot s]$. The same trend can be detected considering a reference-intermediate CO_2 concentration of 20 % CO_2 in a N_2- based gas oxidizing mixture corresponding to the red curve of *Figure 4.9* in the case of $T_{OXI} = T_{RED} = 850\ °C$ and to the orange curve of *Figure 4.8* in the case of $T_{OXI} = T_{RED} = 750\ °C$: in this configuration an increase of $\Delta T = 100\ °C$ allows to a variation CO production yield from 1500 $[\mu mol/g]$ to 2183 $[\mu mol/g]$ and an increase of the CO peak value from 9 $[\mu mol/g \cdot s]$ to about 18 $[\mu mol/g \cdot s]$.

Thence, this difference highlights again that the CO_2 content modification affects more the results for low concentration values compared to high concentration values, in fact in the case of 100 % CO_2 the CO peak value variation due to $\Delta T = 100\ °C$ is about 1.5 %, while in the case of 20 % CO_2/N_2 the CO peak value variation is about 2 %. Moreover, the SFNM-04 redox cyclic repeatability and integrity is again confirmed, in fact the results obtained at $T_{OXI} = T_{RED} = 850\ °C$ with 20 % CO_2/N_2 are almost identical to those obtained in TEST (I) performed with the same operating conditions.

Finally, concerning the CO_2 conversion labelled in the last column of *Table 7*, the amount of CO_2 converted decreases as its content in the oxidizing gas mixture increases following a logarithmic behaviour: a concentration of 6 % leads a CO_2 conversion of 23.43 % that is about height times higher than the CO_2 conversion obtained with a concentration of 100 % (about 3.57 %). This aspect can be detailed analysed considering the following *Figure 4.10* that shows the relationship between the CO_2 concentration variation and the maximum CO yield and the grams of Oxygen exchanged with respect to the grams of SFNM-04 during the oxidation step. It is composed by the x-axis corresponding to the different CO_2 concentrations, the left y-axis indicates the maximum CO yield (red points) and the right y-axis the grams of Oxygen exchanged with respect to the grams of SFNM-04 (blue points) used in each redox cycle of TEST (IV). The blue and red dashed curves are the trend lines based on a logarithmic law.

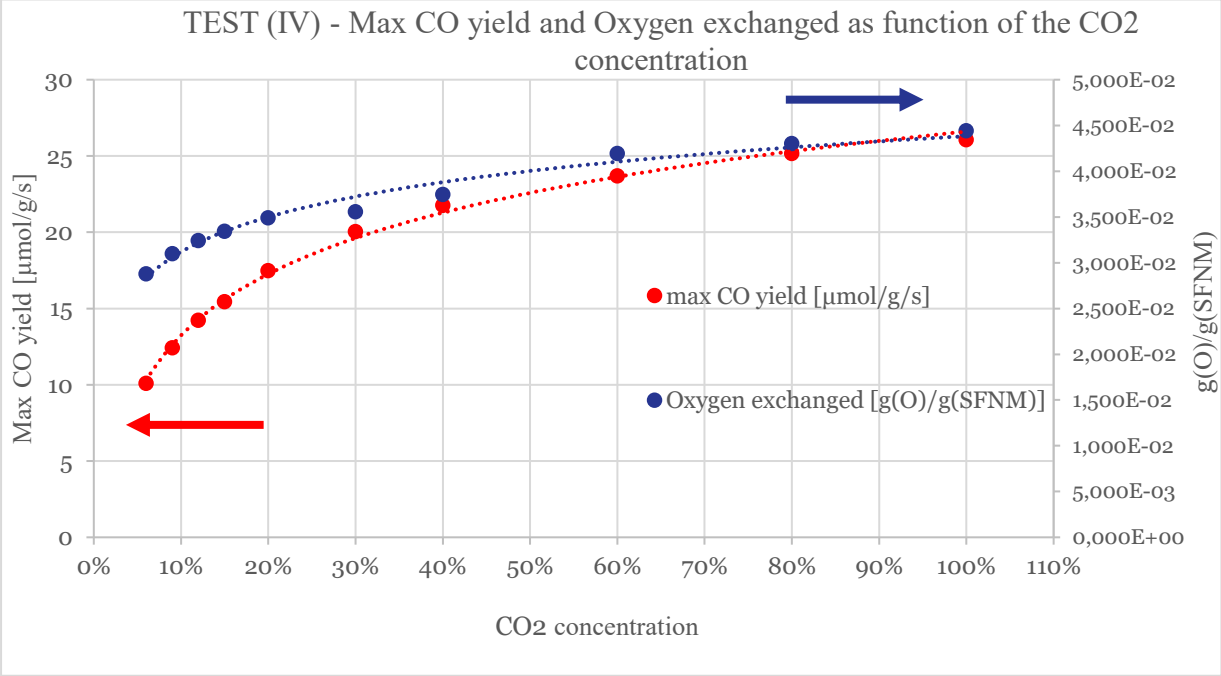

Figure 4.10: *Maximum CO yield (left-y axis) and Oxygen Exchanged (right-y axis) plotted as function of the CO_2 concentration in the oxidating flux at $T_{OXI} = T_{RED} = 850\ °C$.*

At first view, it is pointed out the results consistency of TEST (IV) because all the values evaluated at the specific operating conditions follow an expected logarithmic trend. In fact, by increasing the CO_2 concentration the maximum CO yield and the $g(O)/g(SFNM)$ increase because, ideally, higher is the CO_2 concentration during the oxidation step, higher will be the probability that these CO_2 molecules are able to occupy the oxygen vacancies generated during the reduction step and the term $g(O)/g(SFNM)$ is a parameter strictly related to the amount of oxygen vacancies inside the SFNM-04 lattice. *Table 8* summarizes the numerical results used to construct the plot of *Figure 4.10*. In conclusion, another relevant aspect visible on the graph is that the evaluated values (red and blue points) tend to reach a plateau with a progressive reduction of the gap between them as the CO_2 concentration increases. This concept opens another crucial issue: if the SFNM-04 sample re-oxidation had been complete, the global yield should not vary as the CO_2 concentration increased, instead the opposite behavior is observed in the *Figure 4.10* suggesting that, probably, the sample never reached a complete re-oxidation. Notwithstanding, this is a hypothesis difficult to verify because strongly depends on the reliability of the analyzer measured data.

Table 8: *Results for each redox cycle of TEST (IV) performed at* $T = 850\ °C$ *with varying the* CO_2 *concentration in the oxidating flux: Max* CO *yield (CO peak value) in* $[\mu mol/g]$*,* $g(O)/g(SFNM)$ *and* $g(CO)/g(SFNM)$*.*

N° Cycle	***CO_2 Content [%]***	***Max CO yield*** $[\mu mol/g]$	$g(O)/g(SFNM)$ $[g_O/g_{SFNM}] \cdot 10^{-2}$	$g(CO)/g(SFNM)$ $[g_{CO}/g_{SFNM}] \cdot 10^{-2}$
1	6	10.11	2.88	5.04
2	9	12.42	3.10	5.42
3	12	14.24	3.24	5.68
4	15	15.45	3.34	5.85
5	20	17.49	3.49	6.11
6	30	20.04	3.56	6.23
7	40	21.78	3.75	6.56
8	60	23.70	4.20	7.34
9	80	25.16	4.30	7.53
10	100	26.08	4.44	7.78

4.1.5– TEST (V): 10 Non-Isothermal Cycles with CO_2 Content (6 ÷ 100 %)

TEST (V) is the last test focused on the oxidation parameters; it is very similar to the previous TEST (IV) with the only difference of the non-isothermal conditions. In, fact the CO_2 content range from 6 % to 100 % is investigated by performing ten redox cycles at $T_{OXI} = 750\ °C$ and at $T_{RED} = 850\ °C$. More precisely, each of the ten cycles is composed by:

- A reducing step during which it is provided a gas reducing flow with a constant composition of 10 % H_2/N_2 for 60 min.
- An oxidation step with a gas oxidizing mixture having different CO_2 concentration ranging between 6 ÷ 100 % for 30 min.

The graphical results showing the ten oxidation curves in terms of CO production rate are depicted in *Figure 4.11*.

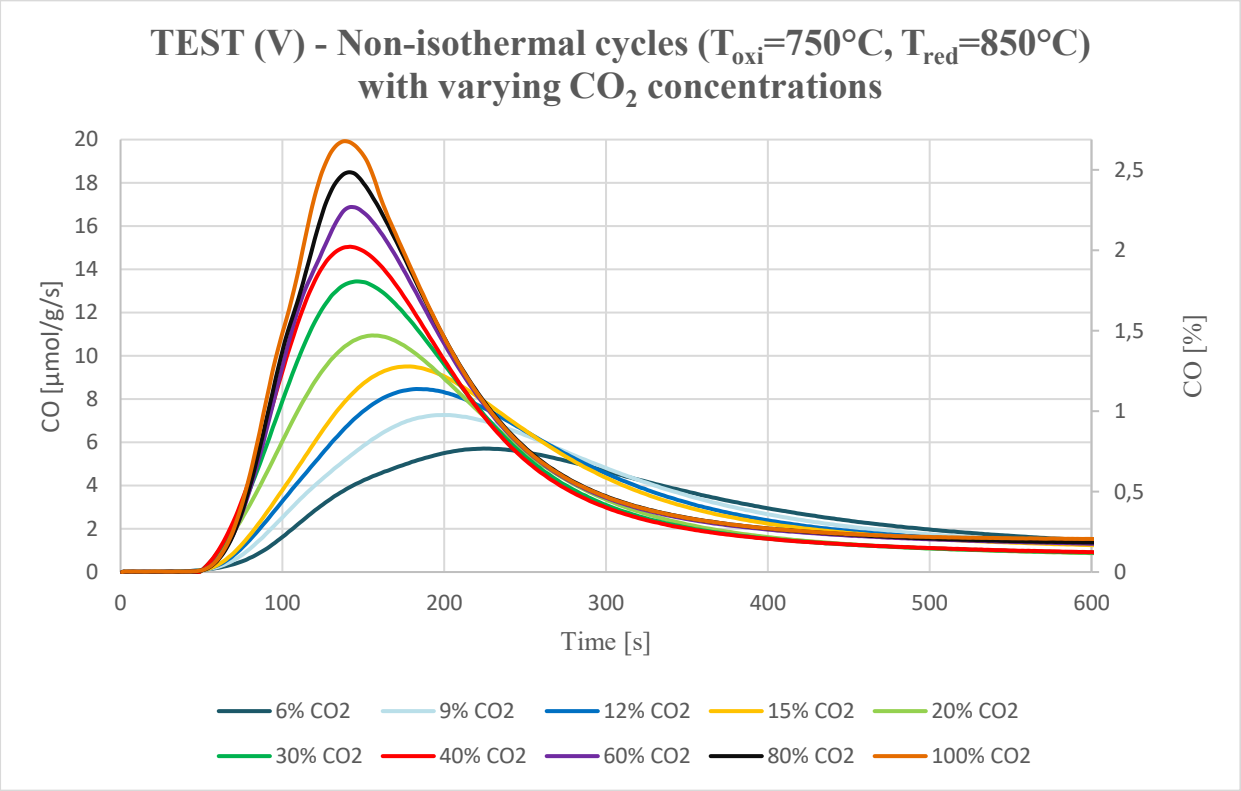

Figure 4.11: *CO Production of TEST (V) expressed in* $[\mu mol/g \cdot s]$ *and in* [%] *terms:* 10 *Non-Isothermal Cycles at* $T_{OXI} = 750\ °C$ *and* $T_{RED} = 850\ °C$ *by varying the* CO_2 *content* (6 ÷ 100 %) *during oxidation.*

As the previous test, as the CO_2 content increases the redox performance of the SFNM-04 sample improves, revealing a faster kinetics, a higher maximum CO production rate, and higher global yields.

More detailed. the CO production rate assume intermediate values between those obtained through the first stage of TEST (IV) (isothermal condition at $T_{OXI} = T_{RED} = 750\ °C$) and those obtained by the second stage of TEST (IV) (isothermal conditions at $T_{OXI} = T_{RED} = 850\ °C$). In fact, considering the orange curve of *Figure 4.11* corresponding to a CO_2 content of 100 %, the maximum CO peak reaches about 19.47 $[\mu mol/g \cdot s]$ and it is an intermediate value included between 17 $[\mu mol/g \cdot s]$ (CO peak value of the first stage of TEST (IV) with 100 % of CO_2) and 26 $[\mu mol/g \cdot s]$ (CO peak value of the second stage of TEST (IV) with 100 % of CO_2). The same is valid for all the other redox cycles. In agreement with these results, the increase of the reduction temperature implies the creation of a larger amount of oxygen vacancies during the reduction step and consequently a higher CO production rate because, during the oxidation step, the CO_2 molecules, finding more vacancies, occupy them in an easier way. Therefore, the CO production of the first stage of TEST (IV) can be improved without varying the oxidation parameters, but only the reduction ones. Nevertheless, the presence of a temperature swing between oxidation and reduction step may allow to a negative effect on the gas analyser reading process. Generally, it is preferable to operate in isothermal conditions to obtain more stable and clean instrument measurements. Furthermore, as before, the next *Figure 4.12* shows the dependency between the CO_2 concentration variation and the maximum CO yield and the grams of oxygen exchanged with respect to the grams of SFNM-04 during the oxidation step.

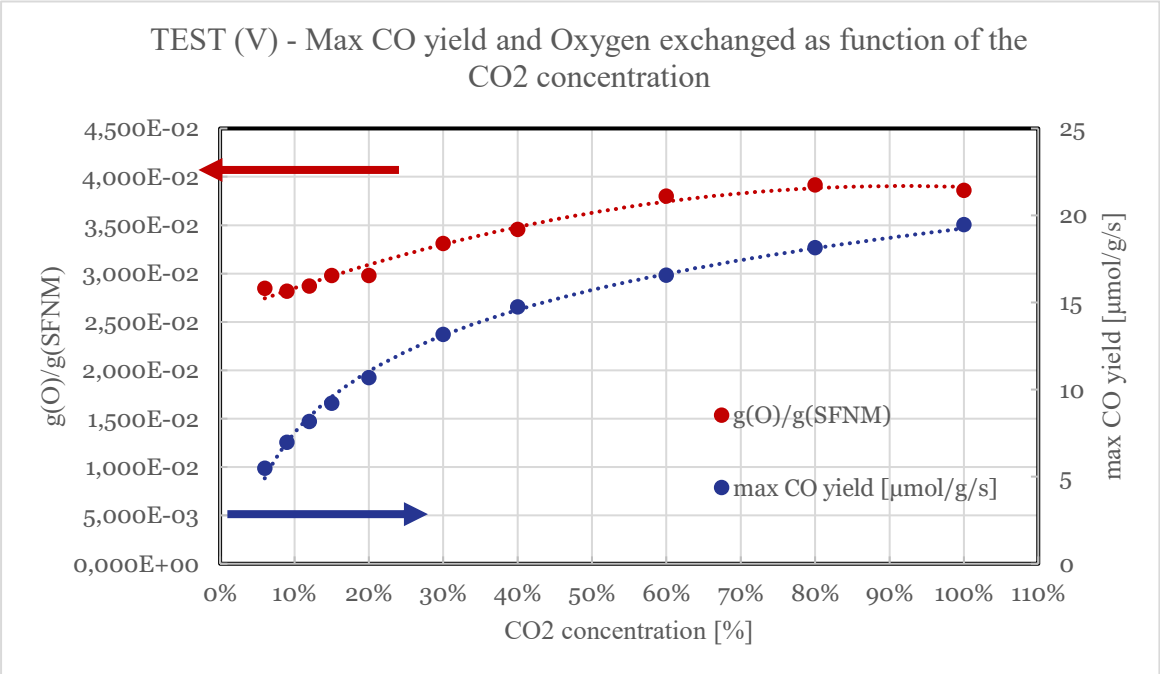

Figure 4.12: *Maximum CO yield (left-y axis) and Oxygen Exchanged (right-y axis) plotted as function of the CO_2 concentration in the oxidating flux at $T_{OXI} = 750\ °C$ and $T_{RED} = 850\ °C$.*

The expected logarithmic trend is almost equal to the previous one of *Figure 4.10*, confirming again the consistency of the results obtained. The parameters useful to plot the graph of *Figure 4.12* are listed below in *Table 9.*

Table 9: *Results for each redox cycle of TEST (IV) performed at* $T_{OXI} = 750\ °C$ *and* $T_{RED} = 850\ °C$ *with varying the* CO_2 *concentration in the oxidating flux:* CO *yield in* $[\mu mol/g]$*, Max* CO *yield (*CO *peak value) in* $[\mu mol/g]$*,* $g(O)/g(SFNM)$ *and* $g(CO)/g(SFNM)$*.*

N° Cycle	CO_2 *Content [%]*	*CO yield* $[\mu mol/g]$	*Max CO yield* $[\mu mol/g]$	$g(O)/g(SFNM)$ $[g_O/g_{SFNM}]$ $\cdot 10^{-2}$	$g(CO)/g(SFNM)$ $[g_{CO}/g_{SFNM}]$ $\cdot 10^{-2}$
1	6	1778	5.49	2.85	4.98
2	9	1760	6.98	2.82	4.93
3	12	1793	8.16	2.87	5.02
4	15	1862	9.22	2.98	5.21
5	20	1862	10.68	2.98	5.21
6	30	2070	13.17	3.31	5.80
7	40	2160	14.76	3.46	6.05
8	60	2375	16.58	3.80	6.65
9	80	2448	18.15	3.92	6.85
10	100	2413	19.47	3.86	6.76

TEST (V) concludes the investigation of SFNM-04 redox ability based on the oxidation parameters. Thanks to this first set of experimental tests, it demonstrated that the oxidation/reduction temperature and the CO_2 content variation play a crucial role on the CO production rate of the SFNM-04 used as oxygen carrier for two-step CO_2-splitting thermochemical process. Another very relevant concept significantly established is the redox cyclic repeatability of the double perovskite material under investigation. In fact, after the 46 redox cycles carried out from TEST (I) to TEST (V), the material response is not changed indicating a very excellent integrity.

In the next sections, from TEST (VI) to TEST (X), it is investigated the redox performance of SFNM-04 by changing the reduction parameters and the last test is focused on a variable that is kept constant until now: the duration of the redox reactions.

4.1.6 – TEST(VI): 5 Redox Cycles at different Reduction Temperatures

TEST (IV) investigates the SFNM-04 response during 5 redox cycles by varying the oxidation temperature. More precisely, the first and the last cycles are performed at $T_{RED} = 850\ °C$ to verify the data repeatability in CO production terms, while the other three oxidation steps respectively at $T_{RED} = 550\ °C - 650\ °C - 750°C$. Concerning the gas compositions, during the reduction step it is sent a gas reducing mixture with a constant content of $10\ \%\ H_2/N_2$ for $60\ min$, and during the oxidation step a gas oxidizing mixture with a constant composition of $20\ \%\ CO_2/N_2$ for $30\ min$. As usual, the first step consists of a pre-treatment in air at $T = 500\ °C$, then, while a $100\ \%\ N_2$ flow is flushing inside the microreactor, it is imposed a ramp with a temperature increase rate of $10\ °C/min$ in order to reach $T = 850\ °C$. The other following steps are listed below:

- Reduction step with a gas reducing mixture composed by $10\ \%\ H_2/N_2$ for $60\ min$ at $T_{RED} = 850\ °C$ (cycle 1), $T_{RED} = 750\ °C$ (cycle 2), $T_{RED} = 650\ °C$ (cycle 3), $T_{RED} = 750\ °C$ (cycle 4) and finally again at $T_{RED} = 850\ °C$ (cycle 5).
- Purging step in N_2 atmosphere for $10\ min$ (cycle 1,5), then heating up ramp to $T = 850\ °C$ (cycle $2, 3, 4$).
- Oxidation step with a gas mixture composed by $20\ \%\ CO_2/N_2$ for $30\ min$ perfomed at $T_{OXI} = 850\ °C$ (cycle 1,5).
- Cooling down phase in N_2 from $T = 850\ °C$ (cycle 1) to $T = 650\ °C$ (cycle 2), $T = 550\ °C$ (cycle 3).
- Purging step in N_2 atmosphere for $10\ min$ (cycle 4), ramp-down up to room-temperature in N_2 (cycle 5 – end of the test).

The graphical results of TEST (VI) are shown in *Figure 4.13* illustrating the CO peaks occurring during the oxidation reaction. The cyclic repeatability of SFNM-04 is confirmed because the first and last cycle (green and blue curves), performed with the same operating conditions, present an almost similar trend both graphically and numerically, even if the difference between them is more evident than those of TEST (II). Considering the redox performance, the expected results, already evaluated from the point of view of oxidation, are confirmed also in this configuration with a variation of a reduction parameter as the reduction temperature.

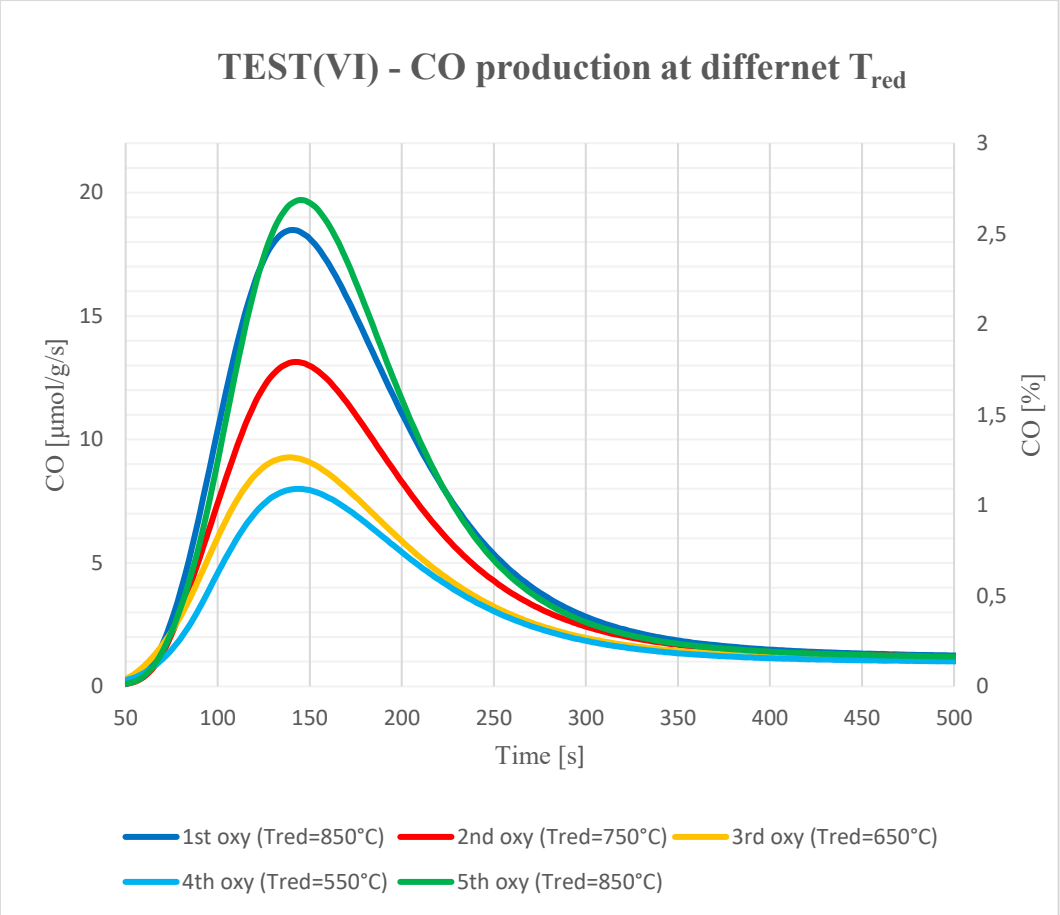

Figure 4.13: *CO Production of TEST (VI) at different Reduction Temperatures* $T_{RED} = 850\ °C - 550\ °C - 650 - 750 - 850\ °C$ *expressed in* $[\mu mol/g \cdot s]$ *and in* $[\%]$ *terms.*

Therefore, a higher reduction temperature allows to a higher CO production rate promoting the Oxygen vacancies creation process occurring exactly during the reduction step. A larger amount of Oxygen vacancies means that, during the oxidation step, the number of CO_2 molecules adsorbed increases and consequently the CO production rate raises up because the oxidation redox reaction is more favoured.

The trend of the oxidation curves is similar than that evaluated in TEST (II), hence by increasing the redox temperature, the SFNM-04 sample improves its redox performance. Nevertheless, since only the reduction temperature varies, while the oxidation one is maintained constant, the kinetic reactions seem to be not affected, in fact the CO peaks at different reduction temperatures occur in a similar time interval of about $t = 300\ s$. In the next *Table 10* are listed the numerical results of TEST (VI).

Comparing these values with those obtained in TEST (II), it is noticed a similar trend in terms of CO yield, maximum CO production and CO_2 conversion. In fact, the maximum CO peak correspondent to the oxidation curve at $T_{RED} = 850\ °C$ (green curve, cycle 5), is located at around at 19 $[\mu mol/g \cdot s]$, the same is valid for TEST (II). Considering the lowest temperature cycle performed at $T = 550\ °C$ (light blue oxidation curve, cycle 4), the CO production rate reaches about 1116 $[\mu mol/g]$, a value slightly higher compared to the oxidation curve at $T_{OXI} = 550\ °C$ of TEST (II) that reaches about 825 $[\mu mol/g]$. This little difference may be a possible demonstration that at low temperature levels, the effect of reduction temperature on the SFNM-04 redox activity is more pronounced with respect to the effect of the oxidation temperature. The same concept is valid for the CO_2 conversion at $T = 550\ °C$: considering TEST (VI) it is achieved a value of 5.38 % that at least two times higher compared to that of TEST (II) equal to 2.25 %.

Table 10: *Results for each redox cycle of TEST (VI):* CO *yield in* $[\mu mol/g]$*, maximum* CO *yield in* [%]*,* CO_2 *conversion rate in* [%]*,* $g(O)/g(SFNM)$ *and* $g(CO)/g(SFNM)$*.*

N° Cycle	T_{RED} $[°C]$	***CO yield*** $[\mu mol/g]$	***Max CO [%]***	CO_2 ***conversion [%]***	$g(O)/g(SFNM)$ $[g_O/g_{SFNM}] \cdot 10^{-2}$	$g(CO)/g(SFNM)$ $[g_{CO}/g_{SFNM}] \cdot 10^{-2}$
1	850	2304	2.48	12.42	3.69	6.45
2	750	1725	1.77	8.83	2.76	4.83
3	650	1277	1.25	6.23	2.04	3.57
4	550	1116	1.08	5.38	1.79	3.12
5	850	2360	2.69	13.43	3.78	6.61

In conclusion, regarding the last two columns that indicate the grams of oxygen and of CO with respect the grams of SFNM-04 sample, it is evident that by decreasing the reduction temperature, the amount of oxygen exchanged and the amount of CO produced diminish. As consequence, the CO production rate decreases due to a combined effect of the scarcity of oxygen vacancies and the limited exsolution evolution phenomenon of Fe and Ni cations that obstruct the SFNM-04 redox activity.

4.1.7 – TEST (VII): 18 Isothermal Cycles with H_2 Content ($5 \div 100$ %)

TEST (VII) is conceptually the dual of TEST (IV). It analyses the SFNM-04 response in terms of CO production rate by changing the H_2 content considering a range of $5 \div 100$ %. The lower limit of H_2 content is 5 % because it is the minimum amount that can be sent in the microreactor and that can be properly measured by the gas analyser. More precisely, TEST (VII) I subdivided into two stages:

- Nine isothermal redox cycles at $T_{OXI} = T_{RED} = 750\ °C$.
- Nine isothermal redox cycles at $T_{OXI} = T_{RED} = 850\ °C$.

As usual, the first step consists of an air pre-treatment of the sample at $T = 500\ °C$ to guarantee a full re-oxidation of the sample. Each of the eighteen cycle is composed by:

- An oxidation step during which it is provided a gas oxidizing flow with a constant reference composition of 20 % CO_2/N_2 for 30 min.
- A reducing step with a gas reducing mixture having different H_2 concentration ranging between $5 \div 100$ % for 60 min.

The graphical results of the first stage are depicted in *Figure 4.14* and show the first nine oxidation curves performed at $T_{OXI} = T_{RED} = 750\ °C$ in terms of CO production. As expected, as the H_2 content increases from 5 % to 100 %, the CO production rate tends to grow up. From a microscopic point of view, this behaviour can be explained in this way: a higher H_2 concentration makes more favourable the SFNM-04 sample reduction that release more oxygen molecules during the reduction step and, consequently, it is obtained a higher amount of oxygen vacancies that are occupied further by the CO_2 molecules during the oxidation step. At the same time, also the exsolution evolution is enhanced when the SFNM-04 sample performs the redox reactions in a considerable reducing environment. This is valid always, but as further discussed the main affecting parameter of the exsolution phenomenon is the reduction temperature.

To better understand the effect of H_2 content variation on the SFNM-04 redox performance, it is possible to make a graphical comparison between this first stage of TEST (VII) represented in *Figure 4.14*, and the first stage of TEST (IV) depicted in the previous *Figure 4.8* having the same isothermal operating conditions, but instead varying the reducing flow, it is varied the CO_2 content of the oxidizing gas mixture.

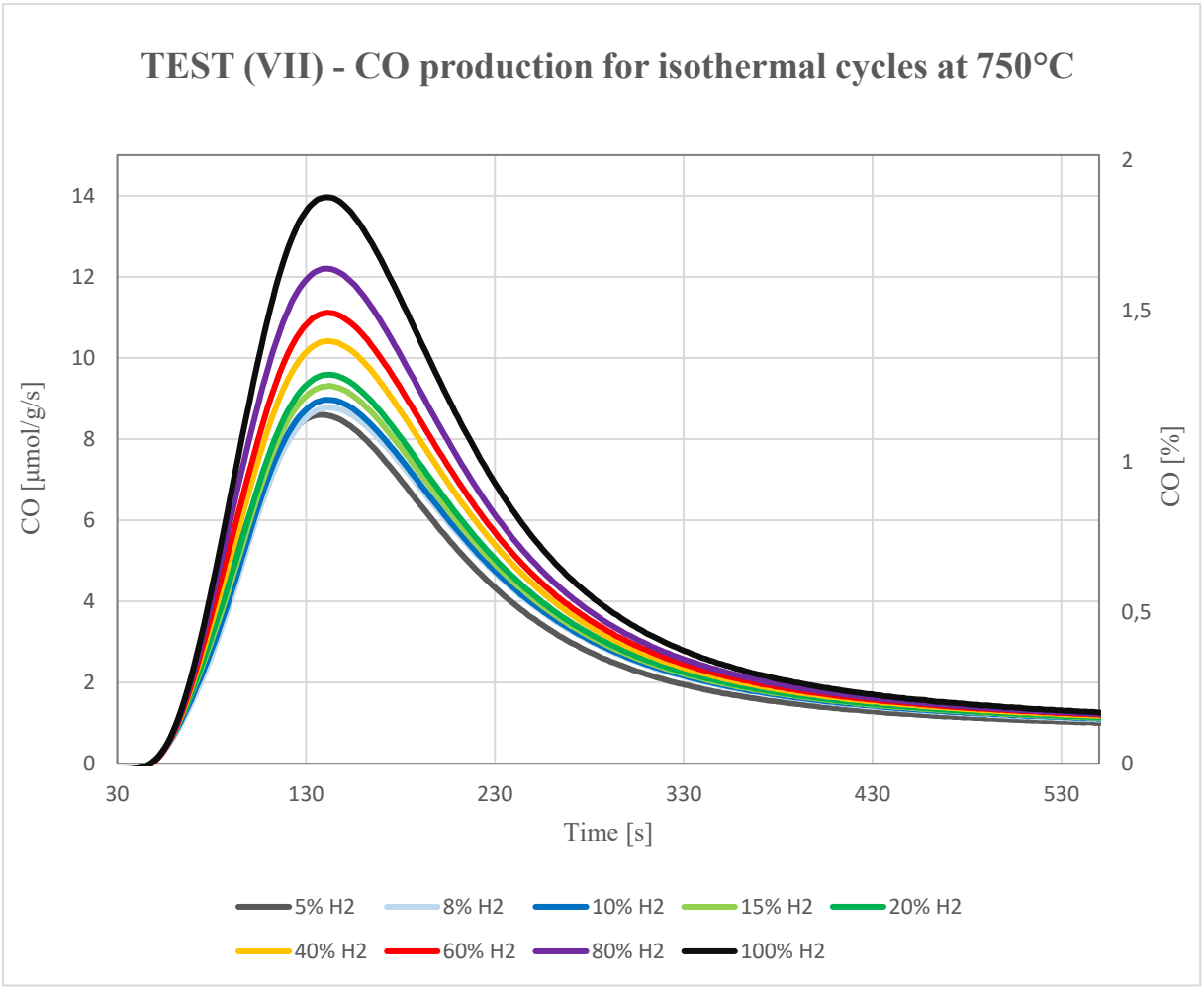

Figure 4.14: *CO Production of TEST (VII) expressed in $[\mu mol/g \cdot s]$ and in $[\%]$ terms: 9 Isothermal Cycles at $T = 750\,°C$ by varying the H_2 content $(5 \div 100\,\%)$ during reduction.*

At first view, it is evident that in this configuration the difference between the CO peaks tend to increase at higher H_2 concentration (from the green oxidation curve corresponding to $20\,\%\ H_2/N_2$ to the black one corresponding to $100\,\%$ of H_2). This was not noticed during TEST (IV), where the CO peaks difference between the ten different oxidation curves is more evident, but at the same more homogenously distributed.

Another visible graphical difference regards the reaction kinetics: the composition variation of the reducing gas by increasing/decreasing H_2 leads to oxidation curves having the CO peaks always around at the same time instant (in this configuration about $t = 150\ s$). On the other hand, observing *Figure 4.8*, the CO peaks of the oxidation curves tend to slightly shift leftwards when the CO_2 increases, resulting a faster reaction kinetics and emphasizing that the oxidation step is more promising when the partial pressure of the oxidant agent increases.

This marked difference of the influence on the reaction kinetics is confirmed by the numerical results of the first stage of TEST (VII) listed below in *Table 11*. In fact, the CO yield, the maximum CO and the CO_2 conversion present values very similar to the others with respect to those summarized in *Table 6.* even if the variability of the H_2 content.

Table 11: *Results for each redox cycle of TEST (VII) performed at* $T = 750\ °C$*:* CO *yield in* $[\mu mol/g]$*, maximum* CO *yield in* [%]*,* CO_2 *conversion rate in* [%].

N° Cycle	***H_2 Content [%]***	***CO yield*** $[\boldsymbol{\mu mol/g}]$	***Max CO [%]***	***CO_2 conversion [%]***
1	5	1396	1.16	5.78
2	8	1434	1.18	5.90
3	10	1458	1.21	6.03
4	15	1514	1.25	6.26
5	20	1558	1.29	6.44
6	40	1688	1.40	7.00
7	60	1790	1.49	7.47
8	80	1944	1.64	8.20
9	100	2190	1.88	9.38

Now, comparing these numerical results with those obtained during TEST (IV) and summarized previously in *Table 6*, the first huge difference is the CO peak range variability:

- by varying the H_2 content from 5 % to 100 % the CO peak range goes from 8.60 $[\mu mol/g \cdot s]$ to 13.96 $[\mu mol/g \cdot s]$ with a global difference of 5.36 $[\mu mol/g \cdot s]$.
- Differently, by varying the CO_2 content from 6 % to 100 % the CO peak range goes from 5.49 $[\mu mol/g \cdot s]$ to 19.47 $[\mu mol/g \cdot s]$, with a global difference of 13.98 $[\mu mol/g \cdot s]$.

This huge difference establishes that the amount of CO_2 in the gas oxidizing mixture directly affects the CO production because it occurs right during the oxidation step, thence, the amount of CO_2 used during the oxidation step presents a higher impact compared to the amount of H_2 used during the reduction step in terms of CO production rate.

In fact, the H_2 content indirectly affect the CO generation creating a lattice structure with a lower amount of oxygen vacancies and so less favourable to produce CO molecules during the re-oxidation step. Furthermore, the values of the CO_2 converted listed in the last column of *Table 11* confirm that as the H_2 content increase, higher will be the number of CO_2 molecules converted into CO ones because more oxygen vacancies are generated during the reduction step and, consequently, the CO production process occurring during the next re-oxidation step of the sample is promoted.

To conclude this numerical results comparison, another relevant aspect is the similarity of the CO global yield reached with 100 % of H_2 (about 2190 $[\mu mol/g]$ with a CO_2 conversion of 9.38 %) and the CO global yield reached in the reference TEST (I) whose numerical results are listed in *Table 3* (the average CO yield reached is about 2238 $[\mu mol/g]$ with an average CO_2 conversion of 11.9 %). This means that the CO production rate is very close to the value obtained in the isothermal TEST (I) performed at $T = 850\ °C$ with an oxidizing gas of 20 % CO_2/N_2 and a reducing gas with only 10 % H_2/N_2, indicating that even if the gas reducing mixture changes from 10 % to 100 %, the main impacting parameter remains the operating temperature of the process.

As done before during TEST (IV), in *Figure 4.15* is represented the trend of the CO peaks (blue points) and of the percentage of the CO_2 converted (red points) during the oxidation step as a function of the variation of the H_2 content carried out during the reduction step. Differently from the almost logarithmic trend observed in *Figure 4.10* by changing the CO_2 content, in this case the behaviour does not show a tendency to reach a plateau, but instead the trend lines tend to sharply increase from 20 % to 100 % of H_2. Thus, this trend confirms that the H_2 content indirectly affect the CO production because it does not induce an impact on the oxidation performance, and so on the maximum CO yield and on the CO_2 conversion rate.

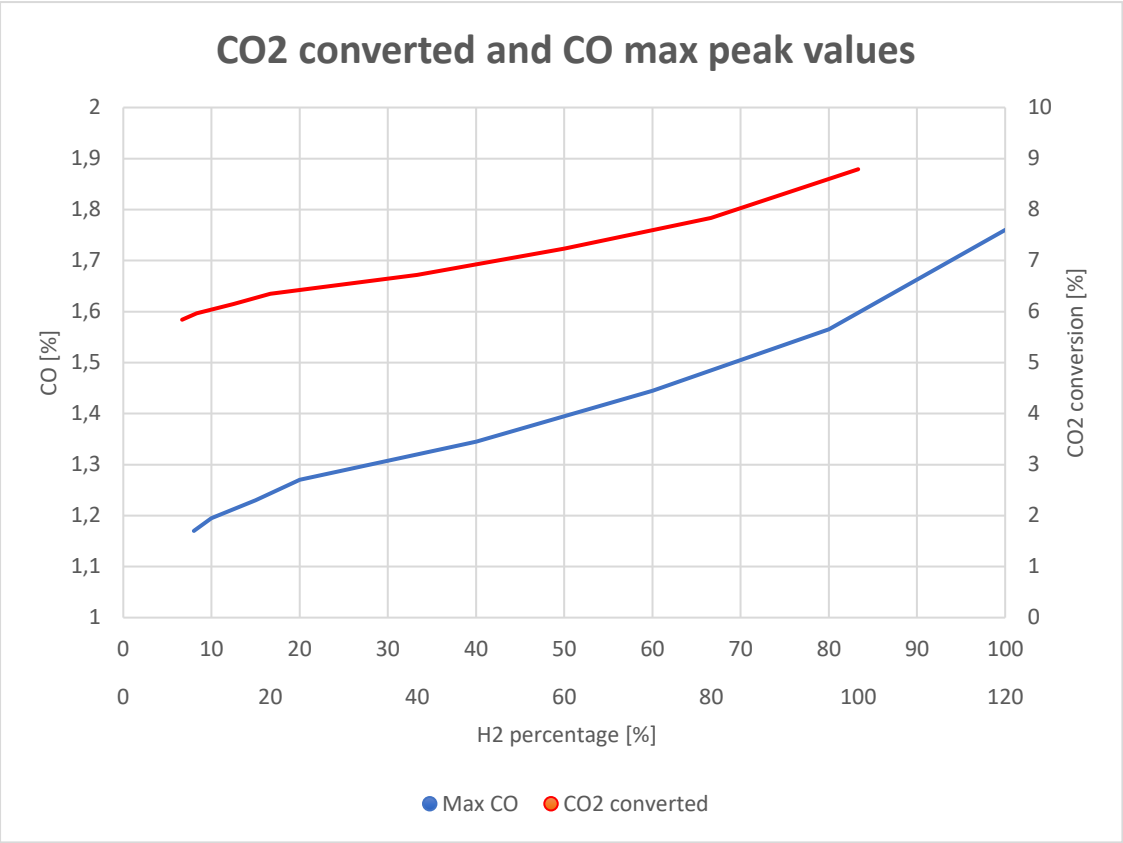

Figure 4.15: *Maximum CO yield (left-y axis) and CO_2 converted (right-y axis) plotted as function of the H_2 concentration in the reducing flux at $T_{OXI} = T_{RED} = 750\ °C$.*

This aspect can be observed also by the marked relative difference of blue and red points between the first part of the graph (until 20 %) and the second one (from 20 % to 100 %); the points are more detached in this part just why the H_2 content does not affect the re-oxidation of the sample, but they are responsible to the generation of oxygen vacancies during the reduction step. On the other hand, the CO_2 content variation directly affects the sample re-oxidation promoting the up-taking of oxygen molecules and a higher CO production, and as the oxidation step approaches completion, the CO peaks tend to similar values and, consequently, a plateau is reached following a logarithmic law. In other words, the H_2 content reduction parameter does not influence the oxidation competition, but it plays a relevant role in the process to reach high CO production rates.

Now, it is described the second stage of TEST (VII) that is the same of the previous one, with the only difference of the operating temperature: it is not more $T_{OXI} = T_{RED} = 750\ °C$, but now it is increased up to $T_{OXI} = T_{RED} = 850\ °C$. Observing the nine oxidation curves pictured in *Figure 4.16*, also in this configuration, an increase of the H_2 content of the gas reducing mixture allows to an increase of the CO production rate and an enhancement of the reaction kinetics.

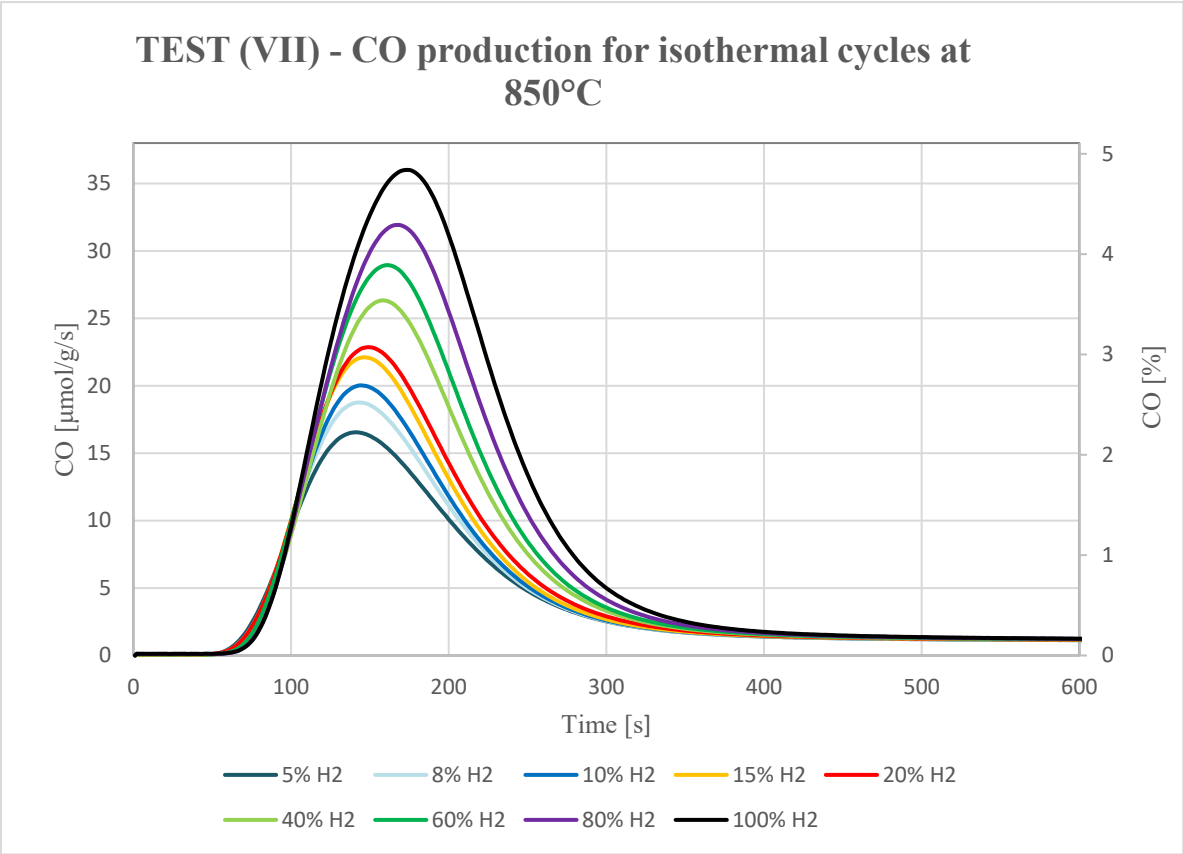

Figure 4.16: *CO Production of TEST (VII) expressed in $[\mu mol/g \cdot s]$ and in $[\%]$ terms: 9 Isothermal Cycles at $T = 850\ °C$ by varying the H_2 content $(5 \div 100\ \%)$ during reduction.*

The first evident graphical difference with respect to the previous first stage performed at $T = 750\ °C$ regards the reaction kinetics: the CO peaks does not occur around at the same time instant as before, but instead tend to slightly shift rightwards when the H_2 increases, suggesting a faster reaction kinetics. More precisely, the numerical results of this second stage of TEST (VII) are summarized below in *Table 12*.

Table 12: *Results for each redox cycle of TEST (VII) performed at* $T = 850\ °C$*:* CO *yield in* $[\mu mol/g]$*, maximum* CO *yield in* [%]*,* CO_2 *conversion rate in* [%].

N° Cycle	H_2 *Content [%]*	CO *yield* $[\mu mol/g]$	*Max* CO *[%]*	CO_2 *conversion [%]*
1	5	2068	2.22	11.12
2	8	2252	2.52	12.61
3	10	2364	2.69	13.46
4	15	2583	2.97	14.86
5	20	2714	3.07	15.36
6	40	3123	3.54	17.70
7	60	3469	3.89	19.45
8	80	3884	4.29	21.45
9	100	4524	4.84	24.20

Comparing these numerical results obtained at $T = 850\ °C$ with those obtained at $T = 750\ °C$, it is evident an enormous difference in terms of CO yield, maximum CO produced and the percentage of CO_2 converted. Concerning the global CO yield, with a reducing gas mixture composed by 100 % of H_2, it is reached the highest value among all tests performed until now, equal to 4524 $[\mu mol/g]$.

To better visualize the difference of the numerical results for just a temperature variation of $\Delta T = 100\ °C$, *Table 13* resumes the CO production rates and the CO peaks values in $[\mu mol/g \cdot s]$ terms of the first and second stage of TEST (VII). Furthermore, in the next *Table 14* are reported the CO production rates and peaks values also of the first and second stage of TEST (IV) to completely analyse the whole process, both in reduction and oxidation terms.

Table 13: *Comparison of CO yield in $[\mu mol/g]$ and maximum CO yield in $[\mu mol/g \cdot s]$ of the first stage performed at $T = 750\ °C$ and second stage at $T = 850\ °C$ of TEST (VII).*

		$T = 750\ °C$	$T = 750\ °C$	$T = 850\ °C$	$T = 850\ °C$
N° Cycle	H_2 **Content** [%]	***C*O yield** [µmol/g]	**Max *CO* yield** [µmol/g · **s**]	***C*O yield** [µmol/g]	**Max *CO* yield** [µmol/g · **s**]
1	5	1396	8.60	2068	16.55
2	8	1434	8.78	2252	18.76
3	10	1458	8.97	2364	20.03
4	15	1514	9.31	2583	22.11
5	20	1558	9.59	2714	22.86
6	40	1688	10.41	3123	26.33
7	60	1790	11.11	3469	28.95
8	80	1944	12.20	3884	31.93
9	100	2190	13.96	4524	36.01

Table 14: *Comparison of CO yield in $[\mu mol/g]$ and maximum CO yield in $[\mu mol/g \cdot s]$ of the first stage performed at $T = 750\ °C$ and second stage at $T = 850\ °C$ of TEST (IV).*

		$T = 750\ °C$	$T = 750\ °C$	$T = 850\ °C$	$T = 850\ °C$
N° Cycle	CO_2 **Content** [%]	***C*O yield** [µmol/g]	**Max *CO* yield** [µmol/g · **s**]	***C*O yield** [µmol/g]	**Max *CO* yield** [µmol/g · **s**]
1	6	1115	4.85	1800	10.11
2	9	1118	5.35	1937	12.42
3	12	1139	5.95	2027	14.24
4	15	1194	7.29	2090	15.45
5	20	1500	9.36	2183	17.49
6	30	1723	11.29	2224	20.04
7	40	1895	12.62	2341	21.78
8	60	2111	14.59	2622	23.70
9	80	2158	16.06	2689	25.16
10	100	2270	17.25	2778	26.08

At first view, considering the values obtained at $T = 850\ °C$, it is noticed a huge difference:

- by using a reducing gas flow composed by $100\ \%$ of H_2 during the reduction step and an oxidizing flow of $20\ \%\ CO_2/N_2$ during the oxidation step, it is reached a global CO yield of $4524\ [\mu mol/g]$ and maximum CO production of $36.01\ [\mu mol/g \cdot s]$.
- On the other hand, by using a reducing gas flow composed by $10\ \%\ H_2/N_2$ and an oxidizing gas flow with $100\ \%$ of CO_2, it is achieved a global CO yield of $2778\ [\mu mol/g]$ and a maximum CO peak of $26.08\ [\mu mol/g \cdot s]$,

Generally, observing the other numerical results, a difference of $1746\ [\mu mol/g]$ and $10\ [\mu mol/g \cdot s]$ is significant, suggesting that at a fixed temperature (in this case $T = 850\ °C$), increasing the H_2 content in the gas reducing flow allows to reach higher CO production rates with respect to increase the CO_2 content in the gas oxidizing flow. This large difference is remarkable also for the other values of concentrations. Differently, considering the values obtained at $T = 750\ °C$, the difference between increasing/decreasing H_2 and CO_2 is less marked, in fact the values are almost similar. Therefore, this aspect confirms again the predominant role of the reduction temperature on the redox performance of SFNM-04, more in general, establishes that, by improving the reduction phase and strongly reducing the SFNM sample, are obtained the highest CO production rates that overcome all the results obtained from all tests performed so far. Until now, the highest values are achieved by TEST (IV), but as previously discussed, the results of this TEST (VII) are in some cases even two times higher, suggesting that the variance of the oxidation parameters can lead to an improvement in terms of fuel production, but this improvement is limited if compared to this obtained by varying the reduction parameters. Thence, it is possible to assert that the optimization process to reach the highest possible CO production should be a trade-off, a combination between improvements related to the oxidation parameters and improvements related to the reduction ones.

In conclusion, the next *Figure 4.17* shows the CO peaks (blue points) and the amount in percentage terms of CO_2 converted (red points) as a function of the H_2 content variation of the gas reducing flow during the reduction step. As previously for the first stage, also in this second stage of TEST (VII) carried out at $T = 850\ °C$, it is observed an almost linear trend without the tendency to reach a plateau, but instead the trend lines increase monotonically. Comparing this figure below with the previous *Figure 4.15*, the higher increase rate is detected for low H_2 contents (from $5\ \%$ to $20\ \%$) with the blue and red points very close to each other, then the trend follows an almost linear behaviour where the blue and red points more detached.

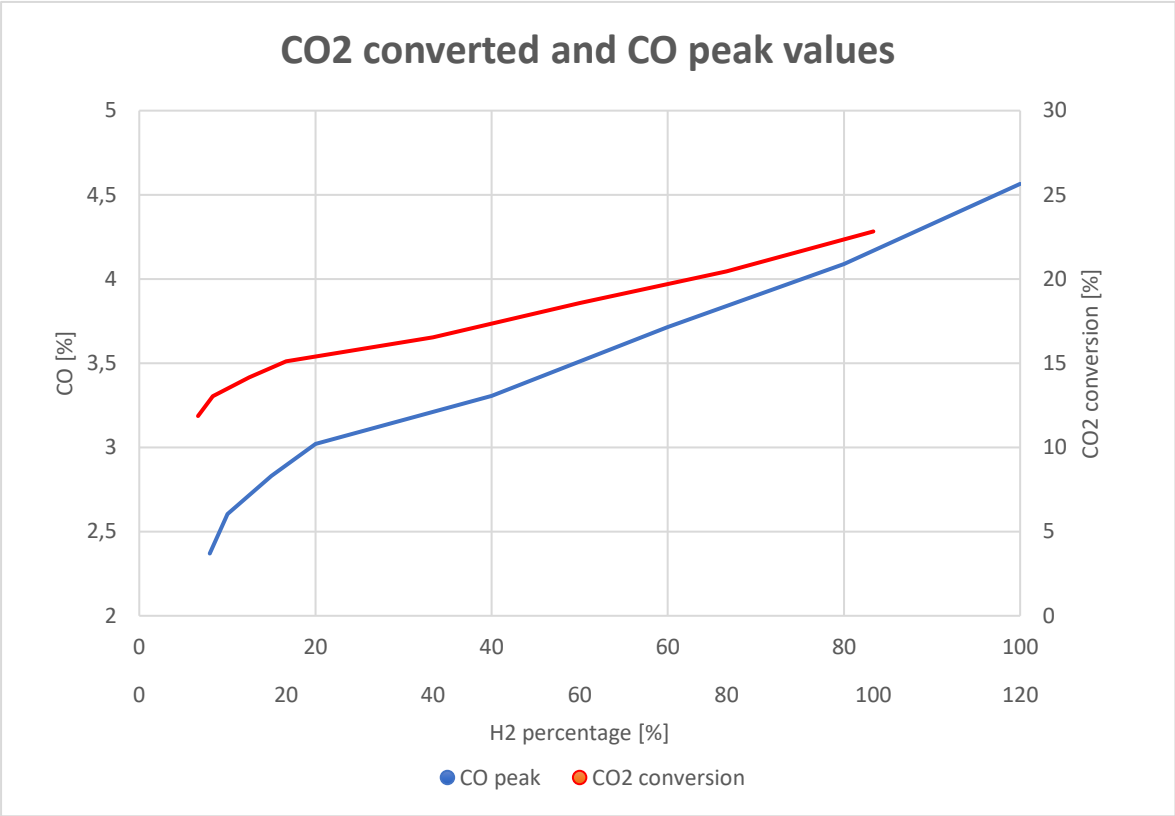

Figure 4.17: *Maximum CO yield (left-y axis) and CO_2 converted (right-y axis) plotted as function of the H_2 concentration in the reducing flux at $T_{OXI} = T_{RED} = 850\ °C$.*

The same identical trend is observed both for the CO peaks (blue points) and the amount in percentage terms of CO_2 converted (red points). In particularly, the CO_2 converted reaches a maximum of $24.20\ \%$ that is two times higher with respect to the value obtained from the previous isothermal test at $T = 750\ °C$ (about $9.38\ \%$).

In conclusion, as before discussed from an oxidation point of view, thanks to this last graph it is established that probably the SFNM-04 sample is not fully reduced. In fact, if the sample reduction had been complete, the CO global yield should not vary as a function of the H_2 concentration of the gas reducing mixture, but instead the opposite behaviour is observed in the *Figure 4.17* suggesting that, probably, the sample never reached a complete reduction. In other words, if the CO production increment is a consequence of the increase of H_2 content in the reducing gas during the reduction step, eventually, this means that the SFNM-04 is not fully reduced. Nevertheless, this is a hypothesis difficult to verify because strongly depends on the reliability of the data measured by the gas analyser system.

4.1.8 – TEST (VIII): 9 Non-Isothermal Cycles with H_2 Content (5 ÷ 100 %)

TEST (VII) is aimed to investigate the H_2 content range from 5 % to 100 % in non-isothermal conditions by performing nine redox cycles at $T_{OXI} = 750\ °C$ and at $T_{RED} = 850\ °C$. More precisely, each of the nine cycles is composed by:

- An oxidation step with a gas oxidizing mixture having a constant molar composition of 20 % CO_2/N_2 for 15 min.
- A reducing step during which it is provided a gas reducing flow with a variable H_2 composition ranging from 5 % to 100 % for 60 min.

Between the oxidation and reduction step, during the heating and cooling ramps useful to switch the operating temperature, it is provided a N_2 flow and, as usual, before starting with the first cycle it is performed an air pre-treatment at $T = 500\ °C$ to delete any eventual kind of contaminants. The air pre-treatment is also implemented to re-oxidize and to restore the SFNM-04 sample that is previously subjected to other thermochemical redox cycles that may affect the reliability of the data measured. The graphical results, namely the nine oxidation curves evaluated at different H_2content in terms of CO production, are represented in *Figure 4.18.*

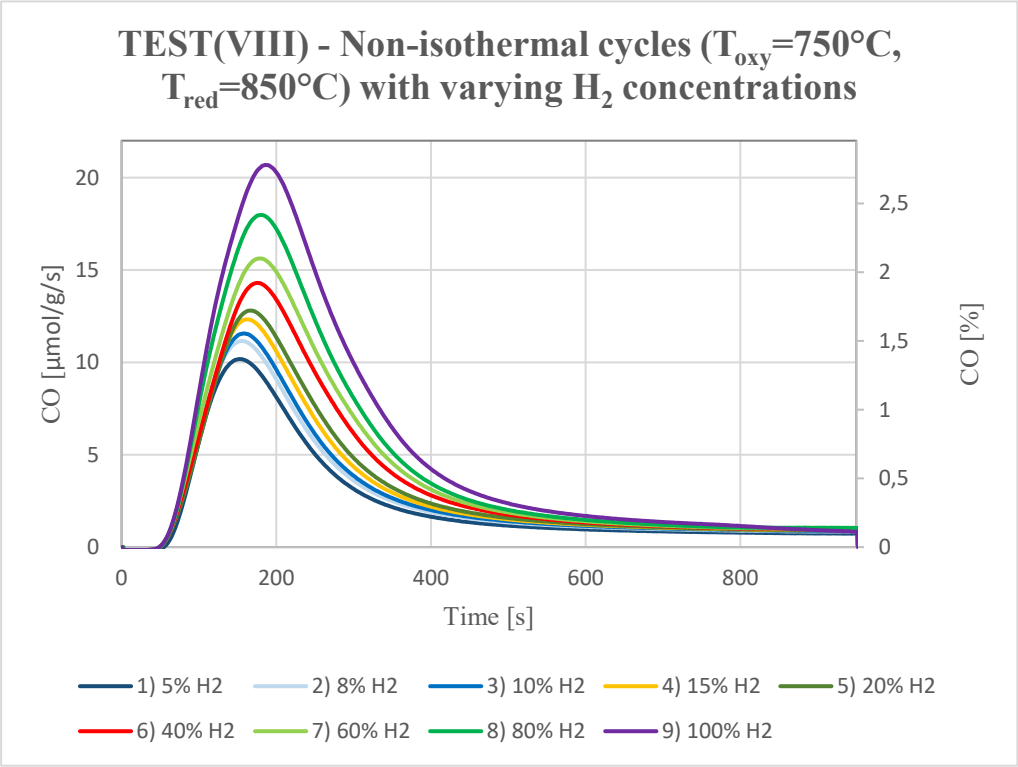

Figure 4.18: *CO Production of TEST (VIII) expressed in $[\mu mol/g \cdot s]$ and in [%] terms: 9 Non-Isothermal Cycles at $T_{OXI} = 750\ °C$ and $T_{RED} = 850\ °C$ by varying the H_2 content* (5 ÷ 100 %) *during oxidation.*

As expected, the CO production rate and its global yield increases as the H_2 content in the reducing gas mixture increases. This TEST (VIII) is conceptually the dual case of TEST (V) that investigates the non-isothermal conditions by varying the CO_2 content in the gas oxidizing mixture. The numerical results obtained from TEST (VIII) are summarized in the following *Table 15*.

Table 15: *Results for each redox cycle of TEST (VIII) performed at* $T_{OXI} = 750\ °C$ *and* $T_{RED} = 850\ °C$ *with varying the* CO_2 *concentration in the oxidating flux:* CO *yield in* $[\mu mol/g]$*, Max* CO *yield (*CO *peak value) in* [%] *and* $[\mu mol/g]$*,* CO_2 *conversion rate in* [%].

N° Cycle	***H_2 Content [%]***	***CO yield $[\mu mol/g]$***	***Max CO [%]***	***Max CO yield $[\mu mol/g \cdot s]$***	***CO_2 conversion [%]***
1	5	1739	1.37	10.18	6.84
2	8	1916	1.50	11.16	7.50
3	10	1995	1.55	11.56	7.77
4	15	2157	1.66	12.33	8.29
5	20	2286	1.72	12.80	8.60
6	40	2667	1.92	14.30	9.61
7	60	2982	2.10	15.63	10.50
8	80	3424	2.42	17.98	12.09
9	100	4034	2.78	20.69	13.90

Comparing these results with those obtained by the dual TEST (V) listed in *Table 9*, it is noticed that even if the maximum CO peaks reach similar values, the global CO yield presents value slightly higher for low H_2 content, while significantly higher for high H_2 content:

- Using a reducing gas flow composed by 100 % of H_2 during the reduction step and an oxidizing flow of 20 % CO_2/N_2 during the oxidation step in non-isothermal conditions ($T_{OXI} = 750\ °C$, $T_{RED} = 850\ °C$) , it is reached a global CO yield of 4034 $[\mu mol/g]$ and maximum CO production of 20.69 $[\mu mol/g \cdot s]$.
- On the other hand, by using a reducing gas flow composed by 10 % H_2/N_2 and an oxidizing gas flow with 100 % of CO_2 in non-isothermal conditions ($T_{OXI} = 750\ °C$,

$T_{RED} = 850\ °C$), it is achieved a global CO yield of 2413 $[\mu mol/g]$ and a maximum CO peak of 19.47 $[\mu mol/g \cdot s]$.

Therefore, even if the maximum CO peaks values are almost equal, the global CO yield in this configuration is about 1621 $[\mu mol/g]$ times higher to the case of TEST (V) indicating that the H_2 content variation has a more predominant role compared to the CO_2variation.

Concerning the reaction kinetics, it is detected a similarity in terms the CO peak range variability comparing with the results of TEST (V):

- by varying the H_2 content from 5 % to 100 % the CO peak range goes from 10.18 $[\mu mol/g \cdot s]$ to 20.69 $[\mu mol/g \cdot s]$ with a global difference of 10.51 $[\mu mol/g \cdot s]$.
- Differently, by varying the CO_2 content from 6 % to 100 % the CO peak range goes from 5.49 $[\mu mol/g \cdot s]$ to 19.47 $[\mu mol/g \cdot s]$, with a global difference of 13.98 $[\mu mol/g \cdot s]$.

Now, comparing these numerical results obtained in non-isothermal conditions with those obtained in isothermal conditions during the second stage TEST (VII) summarized in *Table 12*, it is evident that the non-isothermal conditions allow to lower CO production rate values. In fact, considering the extreme values correspondent to a H_2 content of 5 % and 100 %, respectively, it is noticed that:

- In non-isothermal conditions ($T_{OXI} = 750\ °C$, $T_{RED} = 850\ °C$, TEST (VIII)), with a H_2 content of 5 %, it is reached a global CO yield of 1739 $[\mu mol/g]$ and maximum CO production of 10.18 $[\mu mol/g \cdot s]$, while using 100 % of H_2 it is achieved a global CO yield of 4034 $[\mu mol/g]$ and maximum CO production of 20.69 $[\mu mol/g \cdot s]$
- In isothermal conditions ($T_{OXI} = T_{RED} = 850\ °C$, second stage of TEST (VII)), with a H_2 content of 5 % it is reached a global CO yield of 2068 $[\mu mol/g]$ and maximum CO production of 16.55 $[\mu mol/g \cdot s]$, while using 100 % of H_2 it is achieved a global CO yield of 4524 $[\mu mol/g]$ and maximum CO production of 36.01 $[\mu mol/g \cdot s]$

Thence, TEST (VIII) establishes again that it is better to operate in isothermal conditions with respect to the non-isothermal one. But at the same time, observing the results obtained during the second stage of TEST (IV) performed in isothermal conditions ($T_{OXI} = T_{RED} = 850\ °C$) with a CO_2 content of 100 %, it noticed that TEST (VIII) presents significantly higher values even if in this configuration the oxidation temperature is lower ($T_{OXI} = 750\ °C$) and there is a

lower CO_2 concentration in the gas oxidizing flow. More precisely, comparing these results listed in *Table 15* and those summarized in *Table 7*:

- during the second stage of TEST (IV) performed in isothermal conditions ($T_{OXI} = T_{RED} = 850\ °C$), with a CO_2 content of 100 % of the gas oxidizing flow during the oxidation step, and using a reducing gas flow composed by 10 % H_2/N_2 during the reduction step, it is reached a CO yield of 2778 [$\mu mol/g$] and a CO_2 conversion rate of 3.57 %.
- Differently, during TEST (VIII) performed in non-isothermal conditions ($T_{OXI} = 750\ °C$, $T_{RED} = 850\ °C$), with an oxidizing gas mixture composed by 20 % CO_2/N_2 and a reducing gas mixture of 100 % of H_2, it is achieved a global CO yield of 4034 [$\mu mol/g$] and a CO_2 conversion rate of 13.90 %.

Thence, this huge difference remarks that at lower oxidation temperature and with a lower CO_2 concentration, it is possible to significantly increase the fuel production by augmenting the reduction step, promoting the sample reduction and the creation of a larger amount of oxygen vacancies.

Moreover, considering the percentage of CO_2 converted, the highest value (23.43 %), concerning the oxidation parameters investigation, is obtained during the second stage of TEST (IV) with a gas oxidizing flow of 6 % CO_2/N_2 and 100 % of H_2 as reducing gas flow. Despite, as listed in *Table 12,* it is achieved a higher value of CO_2 converted (24.20 %) when it is used an oxidizing gas of 20 % CO_2/N_2 and a reducing gas flow of 100 % of H_2. Thence, it is established that high CO_2 conversion rate values can be obtained by enhancing the sample reduction phase as alternative to implement gas oxidizing flow with a low CO_2 concentration that allows to obtain high conversion values but, at the same time leads to a decrease of the CO production rates.

This TEST (VIII) is the last that investigates the SFNM-04 redox response by varying the H_2 concentration in the gas reducing flow during the reduction step. Generally, it is demonstrated that the H_2 content variations affect more the CO production compared to the CO_2 content variation. In fact, during these tests (from TEST (VI) to TEST (VIII)), wider CO peaks and consequently larger CO yield values are obtained, suggesting that the improvement of the sample reduction phase is crucial to obtain the highest possible fuel production values. Concerning the reaction kinetics, by changing the H_2 content, the oxidation curves start to rise at the same time, then continuing to increment until the CO peak is reached, and both the peak

value and the time duration strongly depends on the amount of oxygen vacancies generated in the SFNM-04 lattice.

At the contrary, by varying the CO_2 concentration in the gas oxidizing mixture, as the CO_2 increases the starting increase rate of the CO production is faster, in fact the peaks tend to shift leftwards meaning that the peak values are reached in less time and that the reaction kinetic is faster. Thence in conclusion, it is possible to assert that the oxidant gas composition mainly affects the reaction kinetic, and thus the velocity at which the CO is produced by CO_2 dissociation, while the reducing gas composition affects mainly the curves width, indicating that it significantly depends on the oxygen vacancies potentially available in the double perovskite lattice.

In the following TEST (IX) and TEST (X) it is investigated the SFNM-04 response by varying the reaction time durations.

4.2.9 – TEST (IX): 6 Isothermal Cycles at $T = 850\ °C$ with Different Reduction Reaction Times

TEST (IX) is composed by 6 isothermal redox cycles carried out at $T = 850\ °C$ during which it is varied the reduction reaction time t_{RED}. In all the previously tests the reduction step lasts 60 min, but now it ranges from 15 min to 120 min. More detailed, each of the six cycles is performed considering the reference operating conditions:

- Oxidation step with a gas mixture composed by 20 % CO_2/N_2 for 30 min.
- Reduction step with a gas mixture composed by 10 % H_2/N_2 for $15, 30, 45, 60, 90, 120\ min$.

The graphical results of TEST (IX) are depicted in *Figure 4.19* and show the six oxidation curves at different rection reduction time t_{RED}.

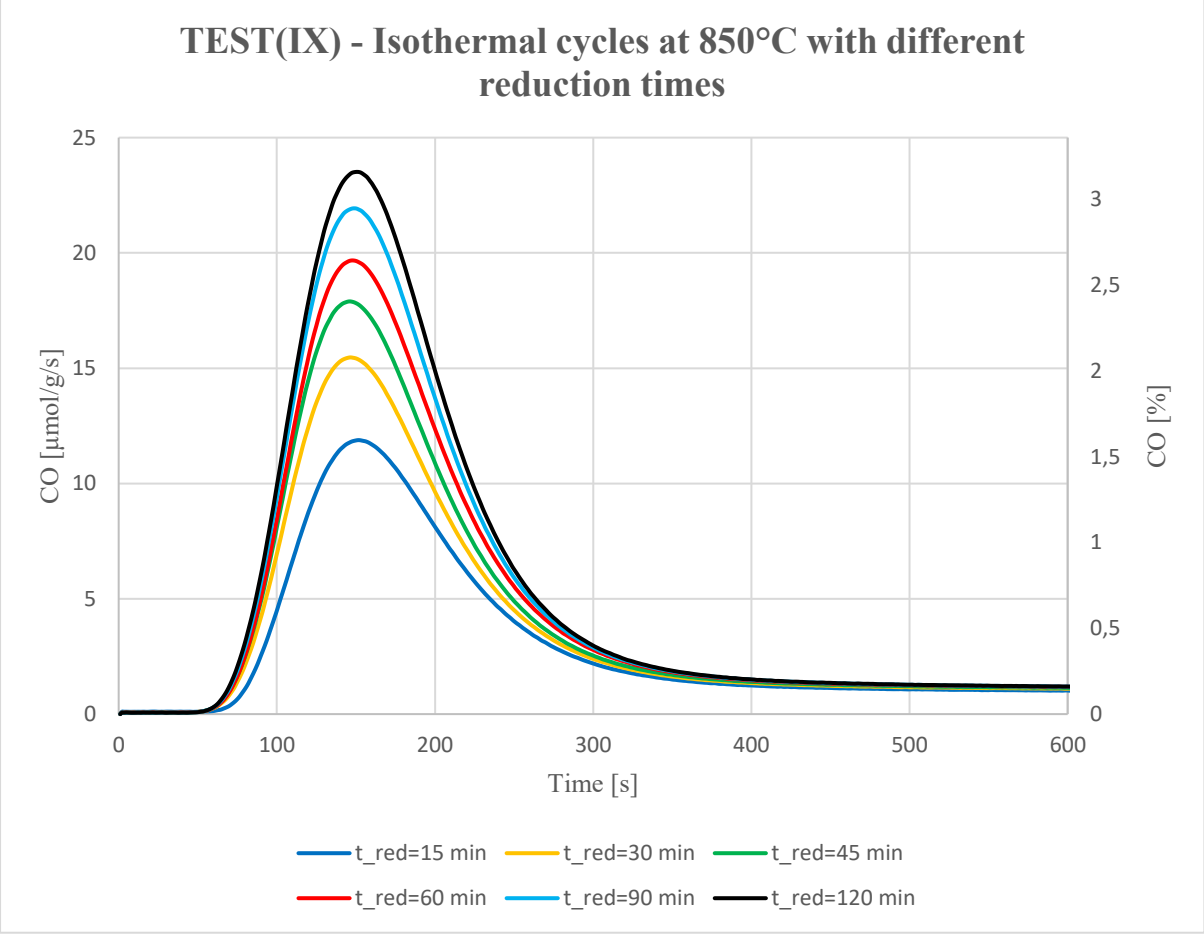

Figure 4.19: *CO Production of TEST (IX) expressed in* $[\mu mol/g \cdot s]$ *and in* [%] *terms:* 6 *Isothermal Cycles at* $T_{OXI} = T_{RED} = 850\ °C$ *by varying the reaction reduction time* t_{RED} *(*$15, 30, 45, 60, 90, 120\ min$*).*

During TEST (IX) the reference operating conditions are imposed in order to better investigate the role of the reaction reduction time. The general trend observed is the increase of the CO production rates as t_{RED} increases. These graphical results are expected, in fact, by maintaining constant the gas reducing composition, but by increasing the time during which this gas mixture flows inside the microreactor, the SFNM-04 sample is subjected to a more efficient reduction step. From a microscopical point of view, the redox reactions start on the sample surface and, if the time available for the reaction is larger, the gas mixture improves its potential and can react with the entire double perovskite structure, diffusing into the lattice generating a higher number of oxygen vacancies. Thence, the redox reduction reaction is not more stopped on the sample surface where the CO production is promoted mainly by the exsolution evolution phenomenon, but it continues taking place also in the bulk of the SFNM-04 sample, releasing a larger number of Oxygen ions and, consequently, creating a bigger amount of oxygen vacancies that can be occupied further during the re-oxidation step.

The numerical results, listed below in *Table 16*, confirm this trend.

Table 16: *Results for each redox cycle of TEST (IX) performed at* $T_{OXI} = T_{RED} = 850\ °C$ *with varying thereaction reduction time* t_{RED}*:* CO *yield in* $[\mu mol/g]$*, Max* CO *yield (*CO *peak value) in* $[\%]$*,* CO_2 *conversion rate in* $[\%]$.

N° Cycle	t_{RED} ***[min]***	***CO yield*** $[\mu mol/g]$	***Max CO [%]***	CO_2 ***conversion [%]***
1	15	1454	1.60	7.98
2	30	1864	2.08	10.39
3	45	2129	2.41	12.03
4	60	2356	2.64	13.22
5	90	2607	2.95	14.74
6	120	2793	3.16	15.80

As expected, the lowest value in terms of CO production is obtained with $t_{RED} = 15\ min$, with a global CO yield of 1454 $[\mu mol/g]$ that is about 62 % lower than the value obtained with the reference reaction reduction time $t_{RED} = 60\ min$. The highest CO yield value is obtained with $t_{RED} = 120\ min$ reaching 2793 $[\mu mol/g]$, that is about 19 % higher than the reference value of 2356 $[\mu mol/g]$ correspondent to $t_{RED} = 60\ min$.

The same behaviour is detected considering the CO peaks and the CO_2 conversion rate. Furthermore, in *Figure 4.20* are represented the CO peaks (blue points) and the amount in percentage terms of CO_2 converted (red points) as a function of the reaction reduction time.

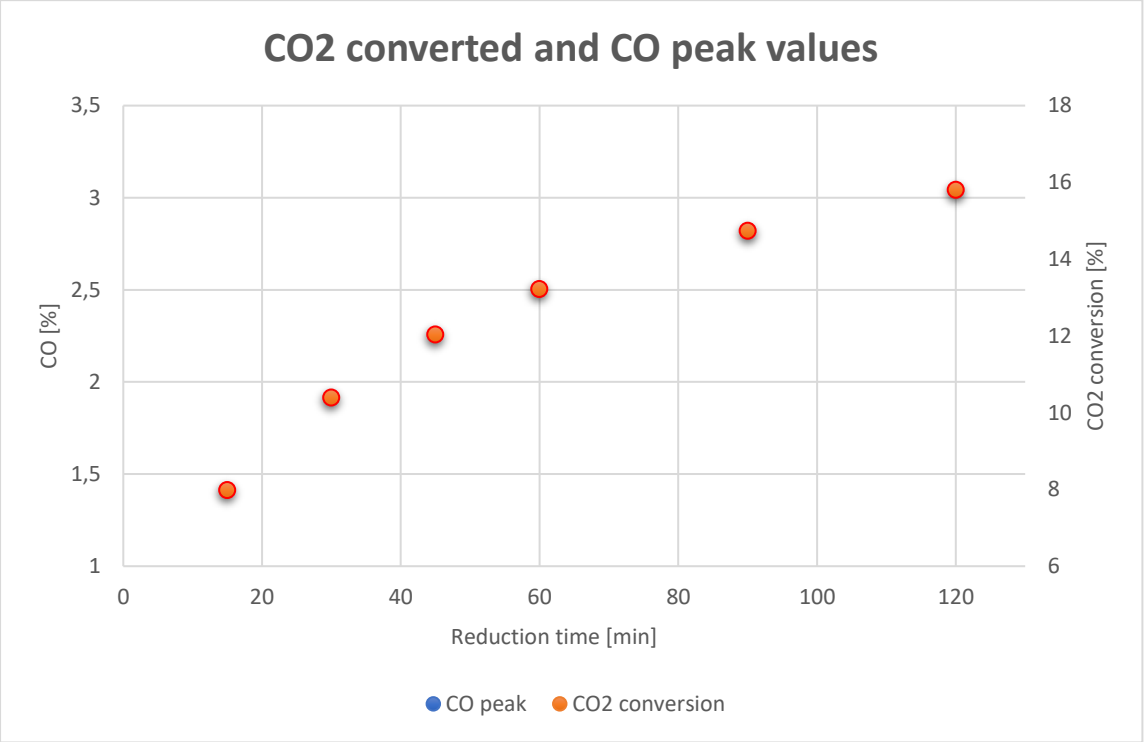

Figure 4.20: *Maximum CO yield (left-y axis) and CO_2 converted (right-y axis) plotted as function of the reaction reduction time t_{RED} at $T_{OXI} = T_{RED} = 850\ °C$.*

It is noticed an almost linear trend in the first part until the reference reaction reduction time $t_{RED} = 60\ min$, then the blue and red points seem to reach a plateau. It is evident that in the first part the relative distance between the points is lower compared to the second part after $t_{RED} = 60\ min$. Notwithstanding, this relative difference between the last values evaluated at $t_{RED} = 120\ min$ is still marked indicating that also with this high reaction time, the sample reduction phase seems to be not complete yet.

Finally, thanks to the results from TEST (IX), it is established how much the reduction time affects the CO production rate obtaining that longer is the reaction reduction time t_{RED}, larger will be the CO production rate due to the increase of the available amount of oxygen vacancies.

4.2.10 – TEST (X): 1 Isothermal cycle at $T = 850\ °C$ with Oxidation Reaction of 7 h

This last experimental test is focused on the investigation of the last oxidation parameter not analyzed yet, namely the reaction oxidation time t_{OXI}. In all previous tests, it is kept a constant value $t_{OXI} = 30\ min$, but now in this TEST (X) it is carried out with an oxidation step having a time duration of $t_{OXI} = 7\ h = 420\ min$. As before detected for the reaction reduction time, also in this case it is expected an increase of the SFNM-04 redox performance in terms of CO production because, during this very large time interval, the CO_2 molecules in the oxidation step can occupy the Oxygen vacancies not only on the sample surface, but deeper into the bulk of the double perovskite lattice. More precisely, the redox cycle is performed in isothermal environment at $T_{OXI} = 750\ °C$, $T_{RED} = 850\ °C$ considering the following operating conditions:

- Oxidation step with a gas oxidizing mixture composed by 20 % CO_2/N_2 for 7 h.
- Reduction step with a gas reducing mixture composed by 100 % H_2 for 120 min.

The oxidation curve obtained from TEST (X) is represented in *Figure 4.21*.

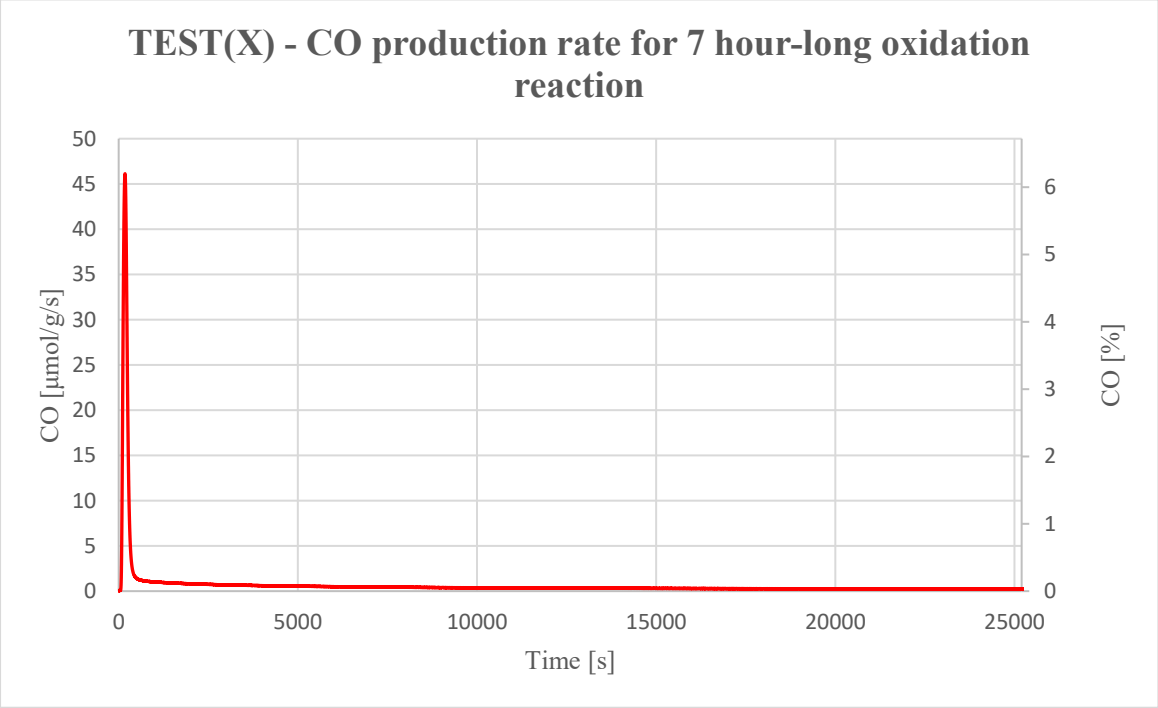

Figure 4.21: *CO Production of TEST (X) expressed in $[\mu mol/g \cdot s]$ and in [%] terms: 1 Isothermal Cycle at $T_{OXI} = T_{RED} = 850\ °C$ composed by an oxidation step with 20 % CO_2/N_2 lasting $t_{OXI} = 7\ h$ and a reduction step with 100 % H_2 lasting $t_{RED} = 120\ min$.*

At first view, it is evident that the x-axis representing the time interval of the oxidation step, presents not more as extreme upper value $t = 600 - 900\ s$ as in all previous tests, but now it is increased up to $t = 25000\ s$ because the oxidation step lasts $7\ h$. TEST (X) establishes the highest CO production rate value obtained so far, with a CO peak located at $46.13\ [\mu mol/g \cdot s]$ correspondent in percentage terms to $6.20\ \%$. The same for the CO_2 conversion rate that reaches about $31\ \%$ and it is the highest value among all tests. This is considered the optimal configuration because during this test are implemented the best possible operating conditions both from the oxidation and reduction point of view. In this way, by combining the best operating conditions of the reduction and oxidation step, the CO production rate is optimized.

Furthermore, to evaluate the global CO yield it is firstly necessary to investigate the CO production values in proximity of the oxidation curve tail. In fact, by elaborating the data of TEST (X), it is noticed that once the CO peak is reached at a time instant of about $t = 150\ s$, the measured data tend to stabilize on an almost constant value generating a flat tail trend that exhibists CO production values slightly higher compared to the values before the CO peak. At first instance, probably these obtained non-zero values after the CO peak are due to a reading inaccuracy of the gas analyser system, or eventually the Emerson X-Stream gas analyser continues to measure little traces of CO that could be confused with the amount of CO_2 present in the gas oxidizing mixture. These are probable hypothesis non completely confirmed, therefore in the next *Figure 4.22*, it is performed a comparison between the oxidation curve evaluated in TEST (X) and the oxidation curves obtained implementing a white test composed by a single redox cycle having an oxidation step of $30\ min$, with a gas oxidizing mixture composed by $20\ \%\ CO_2/N_2$. White test means that inside the microreactor there is no more the $200\ mg$ of the SFNM-04 sample, in fact it is evident that the blue curve correspondent to the white test does not present the CO peak. Hence, as shown by the upper magnification plot, in this way it is established that the CO peak of the blue oxidation curve correspondent to TEST (X) occurs just why inside the microreactor it is present the SFNM-04 sample. Concerning the CO production values in proximity of the tail (lower magnification plot), it is noticed that the blue oxidation curve stabilizes around $0.10\ [\mu mol/g \cdot s]$, differently, when the microreactor is charged by the SFMN-04 sample, the yellow oxidation curve steadies around $0.25\ [\mu mol/g \cdot s]$. Ideally, the tail values of the white test can be considered as the zero values read by the gas analyser, thence this small difference of about $0.15\ [\mu mol/g \cdot s]$ could mean that, when the SFNM-04 sample is inserted inside the microreactor, there is a minimum rate of CO production that perseveres for long time interval after the CO peak occurrence.

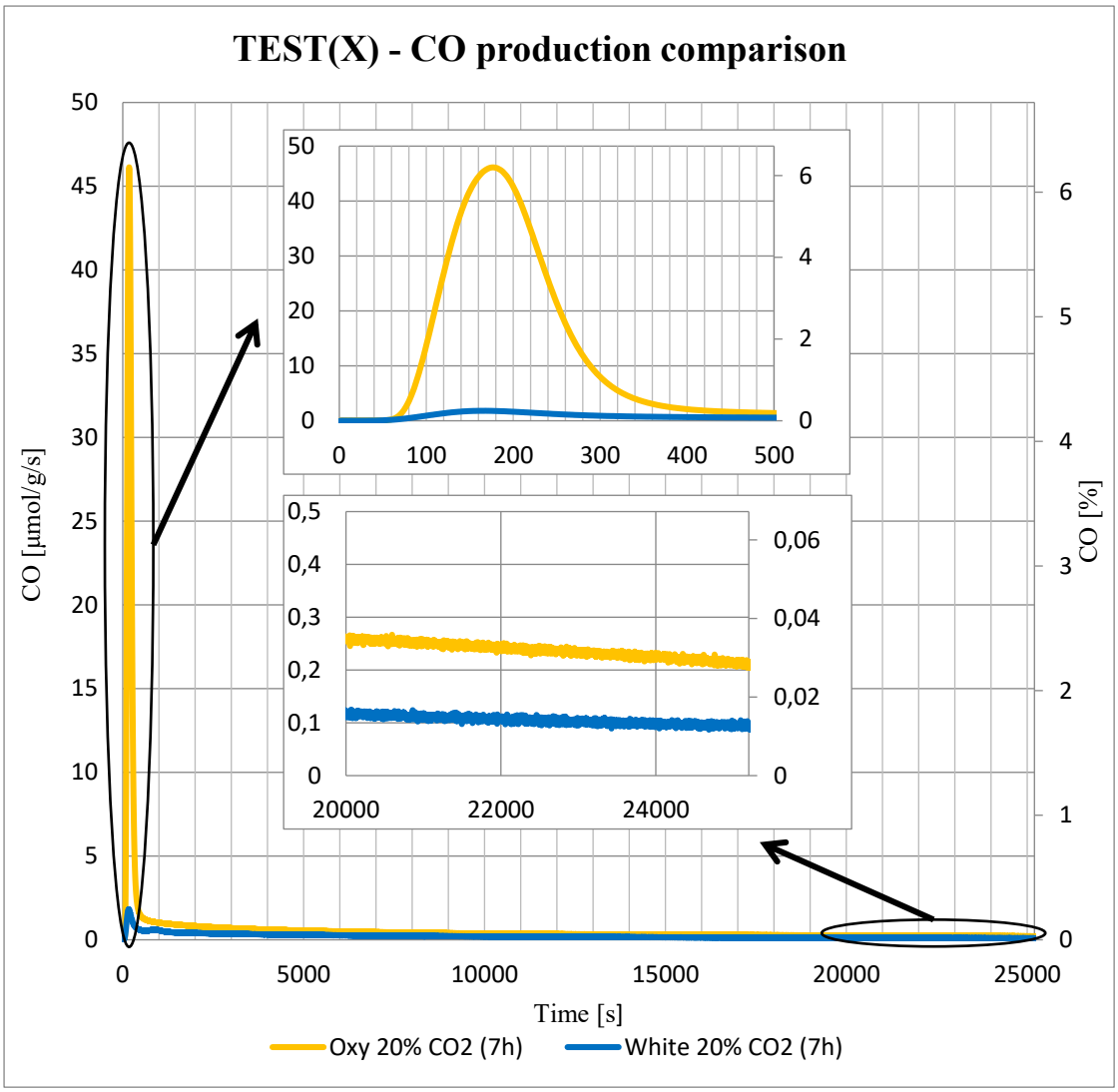

Figure 4.22: *CO Production of TEST (X) (yellow curve) compared with the CO Production of white test (blue curve) expressed in* $[\mu mol/g \cdot s]$ *and in* [%] *terms:* 1 *Isothermal Cycle at* $T_{OXI} = T_{RED} = 850\ °C$ *composed by an oxidation step with* 20 % CO_2/N_2 *lasting* $t_{OXI} = 7\ h$ *and a reduction step with* 100 % H_2 *lasting* $t_{RED} = 120\ min$.

Moreover, this constant difference between the two tails of about 0.15 $[\mu mol/g \cdot s]$ may be further explained by a non-ended reaction, or also it could be possible that the redox reaction continues to grow because an equilibrium condition is reached and it involves, even if low, a progressive production of *CO*.

Finally, as listed below in *Table 17*, the CO yield of TEST (X) is evaluated implementing not only the same integration method used until now and explained previously in *Figure 4.3 (a-b)*, but, due to the longer oxidation reaction time (not more the reference value $t_{OXI} = 30\ min$, but now $t_{OXI} = 7\ h$), are considered three different CO yield calculation methods:

1. Area 1: global CO yield evaluated by considering only the area below the CO peak and cutting the tail in the time instant in which the first derivative tends to be between a fixed tolerance having a maximum value of 0.05 % and a minimum value of -0.05 % as represented by *Figure 4.3 (a-b).*
2. Area 2: global CO yield calculated by considering the net difference between the yellow oxidation curve correspondent of TEST (X) and the blue oxidation curve correspondent to the white test.
3. Area 3: global CO yield considering all the values under the yellow oxidation curve.

Table 17: *Global CO yield of TEST (X) expressed in $[\mu mol/g \cdot s]$ terms and evaluated considering three different numerical integration methods.*

CO yield Area 1 $[\boldsymbol{\mu mol/g}]$	***CO yield Area 2*** $[\boldsymbol{\mu mol/g}]$	***CO yield Area 3*** $[\boldsymbol{\mu mol/g}]$
6344	11282	16778

It is evident a huge difference of global CO yield among the three different methods indicating that the integration method used to evaluate the CO production values under the oxidation curve in a specific time interval, is a crucial process that strongly affects the results. This concept is further discussed in the last section of chapter 5 where it is carried out a comparison with other looping materials tested in literature.

TEST (X) concludes the set of experimental tests and the main result obtained is that by combining the best possible operating conditions during both oxidation and reduction step, the CO production is maximized.

Chapter 5

5. Summary of the Results

5.1 – Results Considerations

The results obtained demonstrates that SFNM-04 material presents a very good replicability, stability and ability to be subjected to cyclic redox reactions in a two-step CO_2-splitting thermochemical process. The CO production rate of SFNM-04 is evaluated considering different operating conditions:

- Operating oxidation and reduction temperatures from $T = 550\ °C$ to $T = 850\ °C$.
- Gas mixture compositions from 6 % to 100 % of CO_2 during the oxidation step and from 5 % to 100 % of H_2 during the reduction step in a N_2-based gas mixture.
- Reduction and oxidation reaction time from 15 to 25 minutes.

The experimental analysis is performed in two different steps, the first one focused on the oxidation reaction parameters and the second one on the reduction reaction parameters. Considering the operating temperatures variation, the reference temperature imposed during the tests is $T = 850\ °C$ and, as soon as the temperature decreases until reaching the lowest value $T = 550\ °C$, the kinetic of the reaction becomes slower and, consequently, the CO production rate substantially decrease. From the oxidation reaction point of view, at $T_{ox} = 550\ °C$, the reaction kinetic results slower with a maximum CO production rate of about 3.4 $[\mu mol/g/s]$ corresponding to a CO production rate in percentage terms of 0.45 %, that is remarkably lower compared to the reference case at $T_{ox} = 850\ °C$ with a maximum production rate of about 18 $[\mu mol/g/s]$ (in percentage terms 2.4 %). From the reduction reaction point of view, a similar trend is obtained; at $T_{red} = 550\ °C$ the CO production rate is about 8 $[\mu mol/g/s]$ corresponding to a CO production rate in percentage terms of 1.1 %, while at $T_{red} = 850\ °C$ the CO production rate is about 19 $[\mu mol/g/s]$ (in percentage terms 2.5 %).

These data are extrapolated from TEST (II) and TEST (VI). Each oxidation curve at different oxidation/reduction temperature levels exhibits a fast-initial CO increase corresponding to the rapid oxygen vacancies ion incorporation followed by a sudden decrease. This behaviour demonstrates a strong temperature dependence of the CO rate profile, which becomes higher and wider at higher temperature due to the higher amount of available oxygen sites. Thus, the temperature variable affects the kinetic of the reaction and consequently the CO production rate because it allows to the activation various favourable mechanisms as the exsolution evolution that improves the CO_2 dissociation creating more oxygen vacancies inside the lattice, the main driver of the two-steps thermochemical process under investigation.

Now concerning the gas mixture compositions variation without considering the temperature effect in first approximation (hence in isothermal condition of both oxidation and reduction at $T = 850\ °C$), by increasing the CO_2 concentration during the oxidation step in a N_2-based gas mixture from 6 % to 100 %, the CO yield and so the CO production peak significantly increases; more detailed as reported in TEST (IV), with a CO_2 concentration of 6 % the maximum CO yield reached is about 10.11 [$\mu mol/g/s$], while with a CO_2 concentration of 100 % the maximum CO yield reached is about 26.08 [$\mu mol/g/s$]. As represented by *figure 4.9* that show the oxidation curves at different CO_2 concentration, the amount of CO_2 in the N_2-based gas mixture affects the kinetic of the reaction: with 100 % of CO_2 the mixture takes around 120 seconds to reach the CO peak that is almost half the time needed to reach the maximum CO rate for a mixture with 6 % of CO_2 (about 200 seconds). The same result is obtained by increasing the H_2 concentration during the reduction step in a N_2-based gas mixture from 5 % to 100 %, in fact as reported in TEST (VII), with a H_2 concentration of 5 % the maximum CO yield reached is about 16.55 [$\mu mol/g/s$], while with a H_2 concentration of 100 % the maximum CO yield reached is about 36.01 [$\mu mol/g/s$]. These results indicate that the H_2 content increase of the reducing gas allows to higher CO production rate values compared to CO_2 content increase of the oxidizing gas. Hence, the increase of H_2 concentration improves the reduction of the SFNM-04 sample meaning a higher amount of released oxygen, and thus a higher amount of oxygen vacancies generated within the lattice. At the same time, also the exsolution process is slightly enhanced when the sample reacts in a stronger reducing environment, even if the most relevant factor remains the reduction temperature.

The main difference with respect to the results obtained by varying the CO_2 concentration regards the influence on the reaction kinetics: by increasing/decreasing the H_2 content, the CO peak is always reached around the same time instant (between 140 and 180 seconds), at the contrary by increasing/decreasing the CO_2 content the influence on reaction kinetics is more remarkable. This difference is due because the used amount of CO_2 directly affects the CO production rate during the oxidation step with a greater impact compared to H_2 content, since the latter indirectly affects the CO production creating a lattice structure with less oxygen vacancies and less suitable to produce fuels during a re-oxidation step. Finally, according to *figure 4.10* and *figure 4.17* that show the peaks of CO production rate at various CO_2 and H_2 content respectively, it is evident that in the first case the peak values tend to reach a plateau, while in the second case the peak values tend to increase monotonically. This plateau is not visible because the variation of H_2 concentration has not an explicit impact on the oxidation step and thus on the maximum CO production achieved, but only an implicit impact related to the creation of oxygen vacancies but not on the completion of the sample re-oxidation that is significantly affected by the CO_2 content.

In conclusion, TEST (IX) and TEST (X) are useful to analyse the influence of the reduction and oxidation reaction time duration; starting from the reduction time Δt_{red} variation, the reference value is $\Delta t_{red} = 1\ h$ and during TEST (IX) it has been changed from 15 minutes to 2 hours. The obtained results demonstrate that longer is the reduction, higher will be the CO production rate: even if the H_2 content is fixed to 10 % in a N_2-based reducing gas mixture, if this gas mixture flows for only 15 minutes it has a lower reducing effectiveness on the SFNM-04 sample compared to that of the same mixture that is constantly delivered for 1 or 2 hours. In fact, a redox reaction starts on the sample surface mainly thanks to the SFNM catalytic properties related also to the exsolution phenomenon and continues into the bulk of the lattice structure where the gas mixture diffuses releasing or absorbing oxygen ions, depending on the type of the redox reaction. Hence, increasing the reaction time, the gas flow presents a higher potential to better react with the entire structure, firstly on the surface and then into the bulk of the SFNM sample. Similarly, as reported in TEST (X), an increase of the time during the oxidation reaction Δt_{ox} implies higher CO production rate but less remarkable compared to the increase of Δt_{red}.

All the experimental tests performed are aimed to find the optimal operating conditions that allows to the maximum CO production rate. These optimal operating conditions tested in TEST (X) are:

- Reduction reaction at $T_{red} = 850\ °C$ using a reducing gas flow composed by 100 % of H_2 with a reaction reduction time of $t_{RED} = 120\ min = 2\ h$.
- Oxidation reaction at $T_{ox} = 850\ °C$ using the reference concentration of 20 % of CO_2 in the N_2-based gas oxidizing mixture with a reaction oxidation time of $t_{OXI} = 7\ h$.

This optimal configuration permits to obtain the highest CO production rate value equal to 46.13 $[\mu mol/g/s]$ corresponding to CO production rate in percentage terms of 6.20 %. Accordingly, in this configuration is obtained the highest CO_2 conversion rate reaching 31 %, meaning that 31 % of CO_2 molecules of the input stream flow are converted into CO molecules at the outlet of the chemical looping reactor. More precisely, this optimal configuration is summarized in the next *Table 18*.

Table 18: *Optimal values achieved during TEST (X): global CO yield in $[\mu mol/g]$, Max CO yield (CO peak value) in* [%] *and* $[\mu mol/g]$, CO_2 *conversion rate in* [%].

CO yield $[\boldsymbol{\mu mol/g}]$	***Max CO [%]***	***Max CO yield*** $[\boldsymbol{\mu mol/g \cdot s}]$	$\boldsymbol{CO_2}$ ***conversion [%]***
6344	6.20	46.13	31.0

5.2 – Exsolution Phenomenon

Once the optimal operating conditions are obtained, by analysing the entire set of experimental tests, it is evident that the reduction conditions variation presents a more influent benefit in terms of CO production rate compared to the oxidation conditions variation. A probable explanation of this crucial aspect can be the exsolution phenomenon: it is one of the most interesting features of the SFNM-04 material related on its capability to grow, throughout the Hydrogen reducing step, giving birth to an exsolution evolution, with the consequential appearance of spread Iron-Nickel alloy nanoparticles on the surface outer layer that enhance the catalytic activity of the perovskite surface. More detailed, the exsolution allows to the reduction of Fe^{2+} and Ni^{3+} which moves towards the surface where a $FeNi_3$ alloy is generated. This crystal structure transformation and surface morphology evolution under reducing environment is depicted in in *Figure 5.1.*

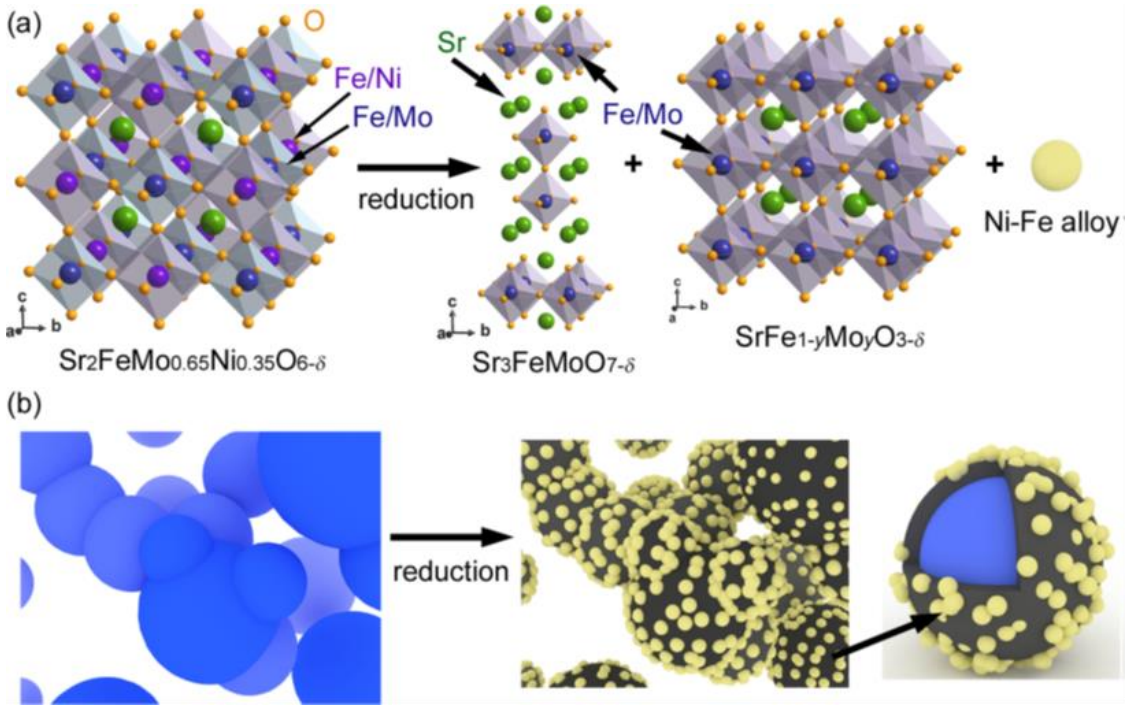

Figure 5.1: *Exsolution evolution illustration models (a) for structure transformation and (b) surface morphology evolution under reducing atmosphere [76].*

The exsolution evolution is the driver of two consequent effects that confirms the relevance of performing a reduction step with the best possible operating conditions: firstly, the exsolution of Fe^{2+} and Ni^{3+} ions generate a huge number of vacancies inside the lattice and then the $FeNi_3$ metal alloy acts as catalyst of the oxidation reaction promoting the CO_2 dissociation.

This phenomenon is studied by Du et al. [76] by analysing $Sr_2FeMo_{0.65}Ni_{0.35}O_{6-\delta}$, a double perovskite material with a Nickel content slightly lower compared to the SFNM-04 used in this assertation where the Ni content is not $x = 0{,}35$, but $x = 0{,}4$. As depicted in *Figure 5.*2, Du et al. [76] performs an XRD analysis on the SFNM-035 sample after a reduction step at $T = 850\ °C$ in pure H_2 for 10 hours.

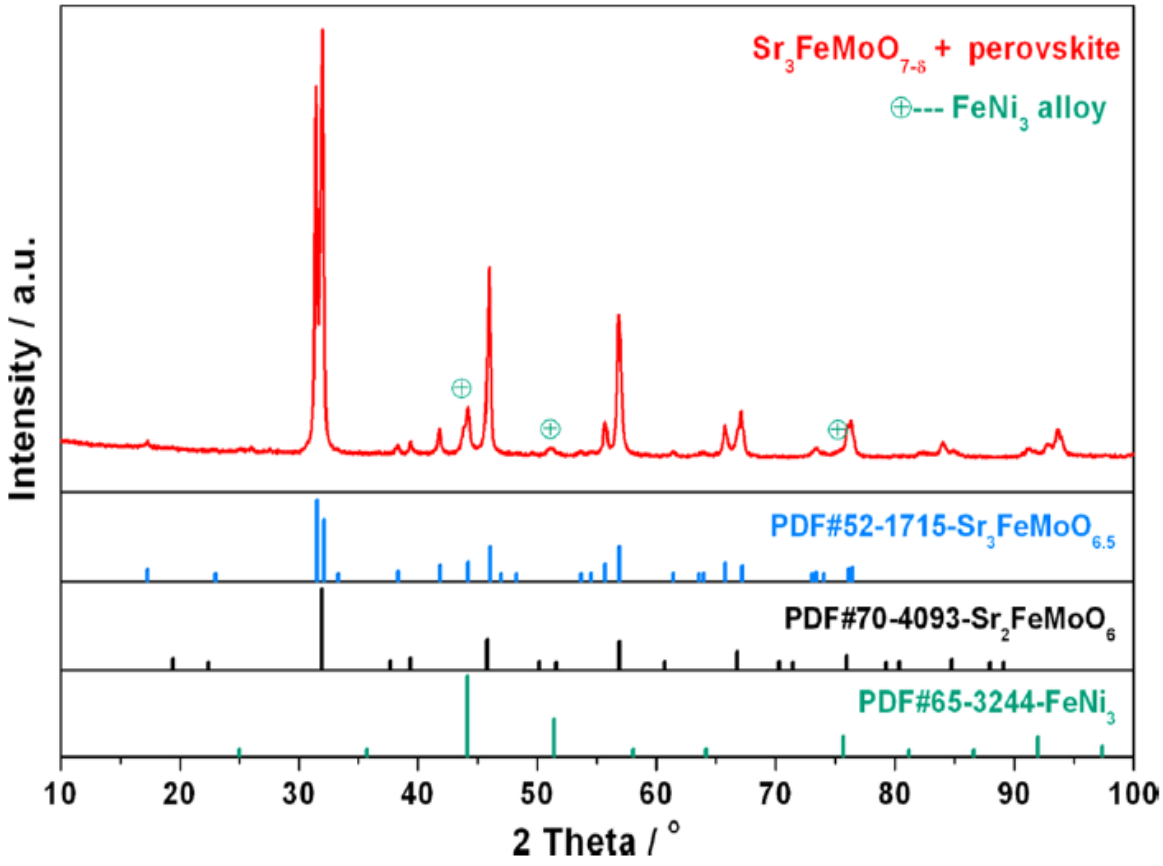

Figure 5.2: *XRD pattern of* $Sr_2FeMo_{0.65}Ni_{0.35}O_{6-\delta}$ *after reduction at* $T = 850\ °C$ *in pure* H_2 *for* 10 *hours [76].*

As expected, the reduction in H_2 converts the pure perovskite phase $Sr_3Fe_{1-y}Mo_yO_{3-\delta}$ $(y = 0{,}3)$ into mixed phase containing the Ruddlesden-Popper RP phase $Sr_3FeMoO_{7-\delta}$ and $FeNi_3$ metal alloy that can form a solid solution phase with a floating content of Fe and Ni mainly because these two elements are adjacent in the periodic table. In this way, the reduced products are $Fe - Ni$ alloy nanoparticles located on RP $Sr_3FeMoO_{7-\delta}$ and on $Sr_3Fe_{1-y}Mo_yO_{3-\delta}$ perovskite ceramics allowing to an increase of the structural stability in long-term operation conditions. This phase transformations mainly occurs on the SFNM particle surface, instead, at the bulk inside the lattice, the particles maintain the original perovskite structure because a decomposed phase in this inner region can impede further reduction steps.

In conclusion, it is possible to assert that the exsolution evolution plays a crucial role to improve the catalytic, electronic/ionic conduction properties of the SFNM looping material to obtain better performance and long-term stability and durability during two-steps thermochemical cycles.

Another possible exploitation of the exsolution phenomenon, strictly related to the material stability, is that the $FeNi_3$ metal alloy enhances the resistance to sulphide and coke poisoning. This poisoning embrittlement can occur during CO_2 splitting thermochemical cycles with the eventual creation of carbonates as Strontium Carbonate $SrCO_3$. As reported by Zhu et al. [77], an unexpected negative effect of Ni is found on $Sr_2Fe_{1.5-x}Mo_{0.5}Ni_xO$ $(x = 0, 0.005, 0.1, 0.2)$ material used as cathode for pure CO_2 electroreduction at $T = 800\ °C$; Although the $Fe - Ni$ cations in the B-site reduced to metal alloy nanoparticles promotes the CO_2 electroreduction, the presence of Ni favours the creation of $SrCO_3$ on the perovskite surface as a result of the weaker $Ni - O$ bond. A high concentration of this carbonate causes the carbon deposition phenomenon blocking the charge transfer and diffusion of the oxygen species on the cathode surface. In our case, the presence of carbonates negatively affects the re-oxidation of the SFNM-04 sample reducing the oxygen diffusion on the surface and consequently the CO production rate.

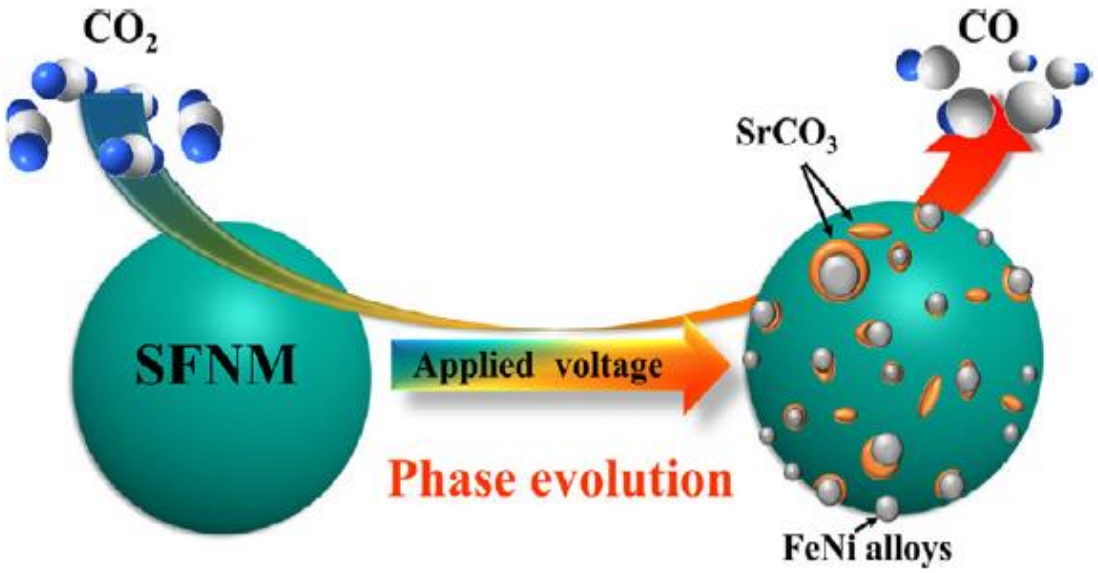

***Figure 5.3**: Phase Evolution of SFNM material with the consequence appearance of $FeNi_3$ metal alloy and $SrCO_3$ carbonates [77].*

More detailed as depicted in *Figure 5.3,* under a reducing environment the $Fe - Ni$ cations in the B-site are reduced to $FeNi_3$ metal alloy; at the same time, the Sr cations located on the A-site of the perovskite lattice structure are in excess from a stoichiometry point of view and react rapidly with CO_2 to generate $SrCO_3$. The driver of the process in our case considering the Renewable Chemical Looping Reforming is not the applied voltage as in a SOEC (Solid Oxide Electrolysis Cell), but the heat at high temperature provided by a renewable energy system such as a CSP plant, but the concept of carbonates formation remains the same.

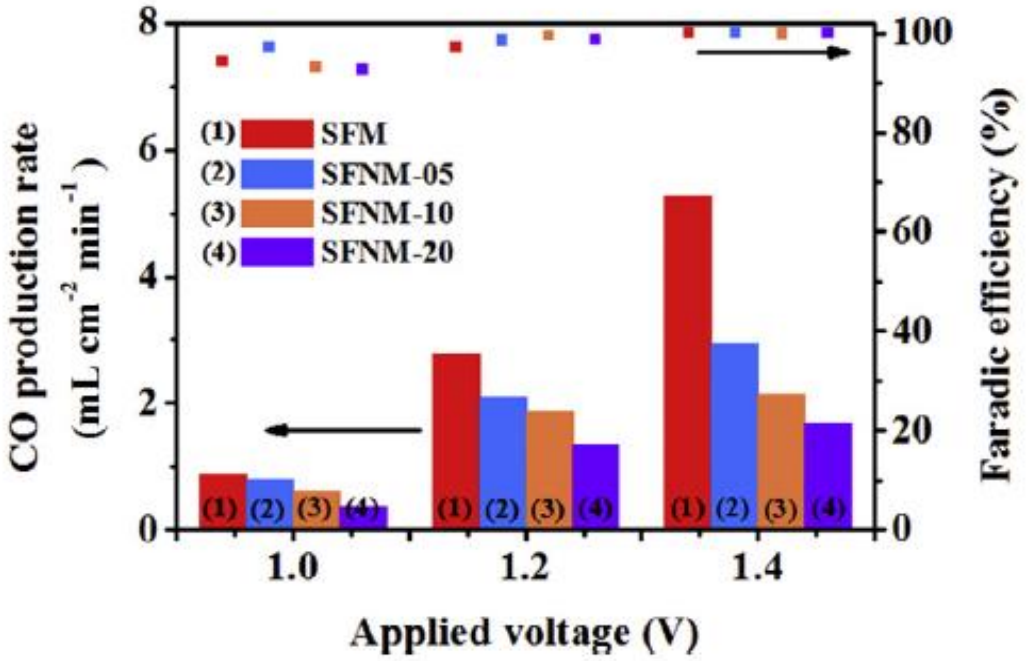

Figure 5.4: *CO production rate and Faradic Efficiency at different Applied Voltages and at different Ni doping content [77].*

In agreement to *Figure 5.4,* the electrochemical performance and so the CO production rate significantly decay with the increase of Ni doping amount; this negative effect is due to the slower kinetics of CO_2 electroreduction than that of the formation of $SrCO_3$. In other words, the excess of carbonates on the perovskite surface acts as an insulator occupying the catalytic active sites and simultaneously obstructs the charge transfer and the diffusion of oxygen ions. In the following figure SFM, SFNM-05, SFNM-10 and SFNM-20 indicate the double perovskite oxides material $Sr_2Fe_{1.5-x}Mo_{0.5}Ni_xO$ with different Ni doping content: $x = 0$ for SFM, $x = 0.05$ for SFNM-05, $x = 0.1$ for SFNM-10 and $x = 0.2$ for SFNM-20.

Through microreactor tests it is not possible to detect possible carbonates, but implementing a thermogravimetric analysis, a constant increase of the sample mass during the oxidation step may be a signal of the carbonate compounds formation. Summarizing, the Ni doping process in the SFM structure allows to the creation of many oxygen vacancies improving the reactivity, stability and cyclability of the sample, but simultaneously an excessive Ni doping can generate carbonates causing pore blocking. For this reason, the Ni doping process is crucial to obtain an optimal double perovskite material in terms of CO production rate and through thermogravimetric analysis it is possible to assess the proper Ni percentage that allows to the maximum CO production rate.

5.3 – Comparison of SFNM-04 with similar Looping Materials used in Literature

In this paragraph it is carried out a comparison between the SFNM-04 double perovskite tested in this dissertation with respect to similar looping materials used in other tests founded in literature. As discussed before, the perovskite oxide chemical structure is able to accommodate different chemical species allowing innumerable combinations of elements in stable solid solutions leaving a lot of space for improving existing materials.

The oxygen carriers for the two-step chemical looping CO_2 and H_2O splitting are the species of metal oxides which present at least two states of oxidation or one metallic and oxidized state. They can be technically classified into volatile and non-volatile oxygen carrier.

As discussed by Haeussler et al. [78], a large number of perovskite formulations have been studied, for both two-step CO_2 and H_2O splitting thermochemical cycles, because this kind of material can accommodate to a wide range of oxygen non-stoichiometry. Nevertheless, the ability to create a huge number of oxygen vacancies is typically correlated to a slow re-oxidation step, hindering a complete sample re-oxidation phase and resulting in low CO/H_2 production rates. Hence, a promising reduction capability can be found at the expense of lower reduction degree and vice-versa. In this way, the goal is to consider a trade-off between maximum fuel production yield and maximum achievable oxygen non-stoichiometry. The key to success of this optimal configuration derives from an optimization of the perovskite's composition. In the following *Table 19* are listed a huge number of perovskite material tested in literature: the first column represents the perovskite material investigated, the second column indicated the synthetization method used, the third column shows the experimental operating conditions, the fourth column the amount of oxygen exchanged in $[\mu mol/g]$, and the last column gives a value of CO or H_2 production rates in $[\mu mol/g]$. This table can be found in [78] and, more detailed, in this dissertation, it is possible to find the references associated to each row of the table. It is useful to remember that the redox performance of SFNM-04 evaluated in chapter 4 are focused only for the two-step CO_2-splitting reaction and not for the two-step H_2O-splitting reaction, but in this section are considered both the reactions to give a general comparison of the perovskite materials implemented for this kind of process.

Table 19: *Redox Perfomance Comparison of Current Perovskites Studied for thermochemical Cycles [78].*

Material	Synthesis Method	Experimental Conditions	Production (μmol/g)	
			O_2	H_2/CO
$La_{0.7}Sr_{0.3}Mn_{0.7}Cr_{0.3}O_3$	Modified Pechini	Reduction: 1350 °C under N_2 Oxidation: H_2O between 50 and 84%; 1000 °C during 60 min	~98	~107
$LaFe_{0.75}Co_{0.25}O_3$	Solid-state	Reduction: 1300 °C under Ar Oxidation: 50% CO_2 in Ar at 1000 °C	59	117
$LaCoO_3$	Solid-state	Reduction: 1300 °C under Ar Oxidation: 50% CO_2 in Ar at 1000 °C	369	123
$Ba_{0.5}Sr_{0.5}FeO_3$	Solid-state	Reduction: 1000 °C under Ar Oxidation: 50% CO_2 in Ar at 1000 °C	582	136
$La_{0.6}Sr_{0.4}Co_{0.2}Cr_{0.8}O_3$	Pechini	Reduction: 1200 °C under Ar Oxidation: 50% CO_2 in Ar at 800 °C	-	157
$La_{0.4}Ca_{0.6}Mn_{0.6}Al_{0.4}O_3$	Modified Pechini	Reduction: 1400 °C under Ar Oxidation: 40% H_2O in Ar at 1000 °C	231	429
$BaCe_{0.25}Mn_{0.75}O_3$	Modified Pechini	Reduction: 1350 °C under Ar Oxidation: 40% H_2O in Ar at 1000 °C	-	135
$La_{0.5}Sr_{0.5}MnO_3$	Solid-state	Reduction: 1400 °C under Ar Oxidation: H_2O at 1000 °C	298	195
$La_{0.35}Sr_{0.75}MnO_3$	Commercial powder	Reduction: 1400 °C under Ar Oxidation: H_2O at 1050 °C	166	124
$La_{0.5}Ca_{0.5}MnO_3$	Solid-state	Reduction: 1400 °C under Ar Oxidation: 50% CO_2 at 1050 °C	311	210
$La_{0.5}Ba_{0.5}MnO_3$	Solid-state	Reduction: 1400 °C under Ar Oxidation: 50% CO_2 at 1050 °C	203	185
$La_{0.5}Sr_{0.5}Mn_{0.4}Al_{0.6}O_3$	Pechini	Reduction: 1400 °C under Ar Oxidation: 50% CO_2 at 1050 °C	246	279
$La_{0.5}Sr_{0.5}Mn_{0.83}Mg_{0.17}O_3$	Solid-state	Reduction: 1400 °C under Ar Oxidation: 50% CO_2 at 1050 °C	214	209
$La_{0.5}Sr_{0.5}MnO_3$	Pechini	Reduction: 1400 °C under Ar Oxidation: 50% CO_2 at 1050 °C	256	256
$Y_{0.5}Sr_{0.5}MnO_3$	Pechini	Reduction: 1400 °C under Ar Oxidation: 50% CO_2 at 1050 °C	539	101
$La_{0.6}Sr_{0.4}Mn_{0.6}Al_{0.4}O_3$	Modified Pechini	Reduction: 1400 °C under Ar Oxidation: 40% CO_2 at 1000 °C	-	307
$La_{0.6}Ca_{0.4}Mn_{0.6}Al_{0.4}O_3$	Modified Pechini	Reduction: 1240 °C under Ar Oxidation: 50% CO_2 at 850 °C	165	230
$La_{0.6}Sr_{0.4}Mn_{0.6}Al_{0.4}O_3$	Modified Pechini	Reduction: 1240 °C under Ar Oxidation: 50% CO_2 at 850 °C	190	245
$La_{0.6}Ca_{0.4}Mn_{0.8}Ga_{0.2}O_3$	Modified Pechini	Reduction: 1300 °C Oxidation: H_2O at 900 °C	212	401
$La_{0.5}Sr_{0.5}Mn_{0.95}Sc_{0.05}O_3$	-	Reduction: 1400 °C under Ar Oxidation: 40% CO_2 at 1100 °C	417	545
$La_{0.6}Sr_{0.4}Mn_{0.8}Fe_{0.2}O_3$	Modified Pechini	Reduction: 1350 °C under N_2 Oxidation: CO_2 at 1000 °C	286	329
$La_{0.6}Sr_{0.4}CoO_3$	Modified Pechini	Reduction: 1300 °C Oxidation: 40% H_2O at 900 °C	718	514
$La_{0.6}Ca_{0.4}CoO_3$	Modified Pechini	Reduction: 1300 °C Oxidation: 40% H_2O at 900 °C	715	587
$Y_{0.5}Ca_{0.5}MnO_3$	Solid state	Reduction: 1400 °C Oxidation: CO_2 at 1100 °C	573	671

Furthermore, as discussed by Azharuddin et al [79], in *Table 20* are listed the redox performance of several perovskites used for both CDS (Carbon Dioxide Splitting) and WS (Water Splitting) reactions. The first column indicates the reduction temperature, the second column the oxidation temperature, the third column the amount of Oxygen exchanged during the redox reactions in $[\mu mol/g]$ terms, and the last one provides a numerical evaluation of the CO or H_2 production rates in $[\mu mol/g]$. The letter *a, b. c* on the values of the last column gives a briefly clarification of the experimental procedure implemented:

- (a) means that the experimental procedure is a TGA (Thermogravimetric Analysis) for CDS reaction.
- (b) indicates that is a TGA (Thermogravimetric Analysis) for WS reaction.
- (c) means that it is used a tube reactor for WS with an infrared furnace heating rate of $500\ °C/min$.

As detailed described in chapter 3, in our dissertation the SFNM-04 redox performance are evaluated by inserting a $200\ mg$ sample inside a tubular reactor made of alumina positioned inside a tubular furnace that guarantees an isothermal environment up to 1600 °C, therefore the experimental set-up is quite similar to the case (c). As before, in this work [79], for each row of the column it is indicated the correspondent reference. The terms YSM, LCM, LSM corresponds to Yttrium-Manganese, Lanthanum-Cobalt and Lanthanum-Manganese double perovskite materials, respectively.

Table 20: *YSM, LCM, LSM Perovskites Redox Performance Comparison [79].*

Oxide	T_{RED}(°C)	T_{OXI}(°C)	O_2 (µmol/g)	$CO(H_2)$ (µmol/g)
$Y_{0.5}Sr_{0.5}MnO_3$(YSM50)	1400	800	483	757[a]
$Y_{0.5}Sr_{0.5}MnO_3$(YSM50)	1300	800	389	624[a]
$Y_{0.5}Sr_{0.5}MnO_3$(YSM50)	1200	800	258	418[a]
$Y_{0.5}Ca_{0.5}MnO_3$(YCM50)	1400	1100	575	671[a]
$La_{0.5}Ca_{0.5}MnO_3$(LCM50)	1400	1100	315	525[a]
$La_{0.5}Sr_{0.5}MnO_3$(LSM50)	1400	1100	201	325[a]
$La_{0.5}Sr_{0.5}MnO_3$(LSM50)	1400	1000	298	298[b]
$La_{0.5}Sr_{0.5}MnO_3$(LSM50)	1400	873	236	224[a]
$La_{0.6}Sr_{0.4}MnO_3$(LSM40)	1400	700	205	397[c]
$La_{0.6}Sr_{0.}Al_{0.6}Mn0_{.4}O_3$	1350	1000	120	247[a]

Other useful perovskites redox performance comparison for the two-step chemical looping CO_2 and H_2O splitting reaction are discussed by Kubicek et al. [50] as represented by the following *Table 21*. In the column *gas/fuel* is indicated if the process investigated is the CDS or WS, then as before, the other columns show the operating temperature range and the CO/H_2 production yield per grams per cycle.

Table 21: *Redox Perfomance Comparison of Current Perovskites Studied for thermochemical Cycles [50].*

Composition	Gas/fuel	Temperature range/°C	Fuel yield μmol per g per cycle
$La_{0.9}Sr_{0.1}MnO_{3-\delta}$	H_2O/H_2	800–1400	10
$La_{0.8}Sr_{0.2}MnO_{3-\delta}$	H_2O/H_2	800–1400	33
$La_{0.7}Sr_{0.3}MnO_{3-\delta}$	H_2O/H_2	800–1400	65
$La_{0.6}Sr_{0.4}MnO_{3-\delta}$	H_2O/H_2	800–1400	102
$La_{0.65}Sr_{0.35}MnO_{3-\delta}$	CO_2/CO	1050–1400	198
$La_{0.5}Sr_{0.5}MnO_{3-\delta}$	CO_2/CO	1050–1400	215
$La_{0.35}Sr_{0.65}MnO_{3-\delta}$	CO_2/CO	1050–1400	151
$La_{0.2}Sr_{0.8}MnO_{3-\delta}$	CO_2/CO	1050–1400	117
$La_{0.5}Sr_{0.5}MnO_{3-\delta}$	CO_2/CO	1100–1400	325
$La_{0.65}Sr_{0.35}MnO_{3-\delta}$	H_2O/H_2	1050–1400	113
$La_{0.5}Sr_{0.5}MnO_{3-\delta}$	H_2O/H_2	1000–1400	160
$La_{0.5}Sr_{0.5}MnO_{3-\delta}$	H_2O/H_2	900–1400	133
$Y_{0.5}Sr_{0.5}MnO_{3-\delta}$	CO_2/CO	900–1400	757
$Y_{0.5}Sr_{0.5}MnO_{3-\delta}$	CO_2/CO	900–1300	624
$Y_{0.5}Sr_{0.5}MnO_{3-\delta}$	CO_2/CO	900–1200	418
$Y_{0.5}Sr_{0.5}MnO_{3-\delta}$	CO_2/CO	1050–1400	105
$Y_{0.5}Ca_{0.5}MnO_{3-\delta}$	CO_2/CO	1100–1400	671
$La_{0.5}Ca_{0.5}MnO_{3-\delta}$	CO_2/CO	1050–1400	168
$La_{0.5}Ca_{0.5}MnO_{3-\delta}$	CO_2/CO	1100–1400	525
$La_{0.65}Ca_{0.35}MnO_{3-\delta}$	CO_2/CO	1050–1400	188
$La_{0.65}Ba_{0.35}MnO_{3-\delta}$	CO_2/CO	1050–1400	159
$La_{0.5}Ba_{0.5}MnO_{3-\delta}$	CO_2/CO	1050–1400	149
$La_{0.6}Sr_{0.4}Mn_{0.6}Al_{0.4}O_{3-\delta}$	H_2O/H_2	1000–1350	307
$La_{0.4}Sr_{0.6}Mn_{0.6}Al_{0.4}O_{3-\delta}$	H_2O/H_2	1000–1350	277
$La_{0.6}Sr_{0.4}Mn_{0.4}Al_{0.6}O_{3-\delta}$	H_2O/H_2	1000–1350	220
$La_{0.6}Sr_{0.4}Mn_{0.6}Al_{0.4}O_{3-\delta}$	CO_2/CO	1000–1350	294
$La_{0.4}Sr_{0.6}Mn_{0.6}Al_{0.4}O_{3-\delta}$	CO_2/CO	1000–1350	286
$La_{0.6}Sr_{0.4}Mn_{0.4}Al_{0.6}O_{3-\delta}$	CO_2/CO	1000–1350	247
$La_{0.5}Sr_{0.5}Mn_{0.75}Al_{0.25}O_{3-\delta}$	CO_2/CO	1050–1400	186
$La_{0.6}Sr_{0.4}Mn_{0.6}Al_{0.4}O_{3-\delta}$	CO_2/CO	1050–1400	187
$La_{0.6}Sr_{0.4}Mn_{0.4}Al_{0.6}O_{3-\delta}$	CO_2/CO	1050–1400	180
$La_{0.5}Sr_{0.5}Mn_{0.85}Mg_{0.15}O_{3-\delta}$	CO_2/CO	1050–1400	183
$La_{0.6}Sr_{0.4}Mn_{0.83}Mg_{0.17}O_{3-\delta}$	CO_2/CO	1050–1400	207
$LaMn_{2/3}Mg_{1/3}O_{3-\delta}$	CO_2/CO	1050–1400	55
$La_{0.6}Sr_{0.4}Cr_{0.95}Co_{0.05}O_{3-\delta}$	CO_2/CO	800–1200	14
$La_{0.6}Sr_{0.4}Cr_{0.9}Co_{0.1}O_{3-\delta}$	CO_2/CO	800–1200	56
$La_{0.6}Sr_{0.4}Cr_{0.8}Co_{0.2}O_{3-\delta}$	CO_2/CO	800–1200	157
$La_{0.6}Sr_{0.4}Cr_{0.5}Co_{0.5}O_{3-\delta}$	CO_2/CO	800–1200	51
$La_{0.6}Sr_{0.4}Cr_{0.8}Co_{0.2}O_{3-\delta}$	H_2O/H_2	800–1200	50
$Ba_{0.5}Sr_{0.5}Co_{0.8}Fe_{0.2}O_{3-\delta}$	H_2O/H_2	800–1000	83
$La_{0.6}Sr_{0.4}Co_{0.8}Fe_{0.2}O_{3-\delta}$	H_2O/H_2	800–1200	51
$La_{0.6}Sr_{0.4}CoO_{3-\delta}$	H_2O/H_2	800–1300	107

Comparing the fuel yield production listed in the previous tables with the results obtained by the experimental tests described in chapter 4, it is noticed a remarkable difference:

- The maximum CO yield production reached in this dissertation is $6344\ [\mu mol/g]$ if the optimal operating conditions of TEST (X) are considered. Generally, considering the reference operating conditions of TEST (I), namely isothermal conditions at $T_{OXI} = T_{RED} = 850\ °C$ with a gas reducing mixture composed by $10\ \%\ H_2/N_2$ for $60\ min$ and a gas oxidizing mixture composed by $20\ \%\ CO_2/N_2$ for $90\ min$, it is reached an average CO yield of $2238\ [\mu mol/g]$ per cycle. The double perovskite material testes is SFNM-04, namely $Sr_2FeNi_{0.4}Mo_{0.6}O_{6-\delta}$;
- The CO/H_2 yield production considering *Table 19, 20, 21* ranging between $10 \div 757\ [\mu mol/g]$. The maximum value is achieved by YSM50 having the following chemical formula $Y_{0.5}Sr_{0.5}MnO_{3-\delta}$.

At first view, it seems that the SFMN-04 redox response in terms of CO yield investigated through our experimental results is significantly higher compared with the other perovskite materials listed in the previous tables, with a relative difference of about $1481 \div 2228\ [\mu mol/g]$. However, besides the eventual very promising SFNM-04 CO yield values, these numerical results depend on several different factors, as discussed below.

At first instance from an arithmetic point of view, to evaluate the CO production values below the oxidation curve it is necessary to adopt the same integration method to be able to compare the CO yield in $[\mu mol/g]$ per cycle for different perovskite materials. The integration method implemented in this dissertation is described in *Figure 4.3 (a-b)*: the CO yield is calculated considering only the area below the CO peak and cutting the tail in the time instant in which the first derivative tends to be between a fixed tolerance having a maximum value of $0.05\ \%$ and a minimum value of $-0.05\ \%$. After that, once the breaking point to calculate the CO yield is set (in our tests the oxidation curve is considered concluded and stabilized at about $t = 450 \div 600\ s$), it is possible to draw a straight line and evaluate the difference between the values of the CO production curve and the values of the straight line obtaining in this way a CO net production. Differently, by analysing all the references associated to the values listed in the previous tables, it is noticed a lack of information about the integration method implemented to achieves those CO yield values. Thence, a first possible explanation of the difference between the values obtained by our tests and the others found in literature can be the specific integration method used to evaluate the CO production values second by second during the oxidation step.

Furthermore, another eventual explication of the difference between the CO yield values regard the operating conditions considered during the thermochemical redox cycles. The results of the experimental tests described in chapter 4 considerably confirm that the CO yield strongly depends on the operating conditions like the oxidation/reduction operating temperature, the oxidizing/reducing gas mixture composition and its volumetric flow rate, the oxidation/reduction reaction time, the mass of the sample tested. Not only the operating conditions, but also the experimental set-up. In fact, as indicated for instance in *Table 20*, most of the tests are performed implementing a TGA (Thermogravimetric Analysis): the change of mass is recorded as function of time. Typically, the mass of the sample tested through TGA is significantly lower compared to the $200\ mg$ of SFNM-04 tested through the microreactor. Therefore, another possible explanation of the deviation between the results obtained can be the amount of grams of the perovskite sample tested and the different type of experimental methods. Consequently, another crucial parameter that affects the results is the residence time of the reducing/oxidizing flow inside the microreactor: by performing a TGA analysis the residence time is considerably lower compared to that by testing the material through a microreactor setup like in this work. Hence, this may explain why CO yield values obtained from our tests are higher compared to the others listed in the previous tables.

In conclusion, it is carried out a graphical comparison of the fuel production between our experimental tests and others found in literature. Firstly, in *Figure 5.5* are reported the CO_2 splitting rate curves discussed by Carrillo et al. [80] that investigate the chemical looping reforming coupled with CO_2-splitting of a double perovskite material decorated with exsolved metallic Co nanoparticles having this chemical formula $La_{0.6}Sr_{0.4}Cr_{0.8}Co_{0.2}O_{3-\delta}$. More precisely, in this work [80] it is established that the exsolution evolution method activate the methane partial oxidation increasing and promoting the syngas selectivity and fuel production rates. In fact, it is noticed that the CO production of exLSCC (namely exsolution promoted LSCC perovskite) represented in *Figure 5.5 (a)* is higher compared to LSCC without Co exsolved nanoparticles (*Figure 5.5 (b)*) and to Ceria (*Figure 5.5 (c)*). Even if in this configuration it is considered as reducing oxidizing mixture CH_4 and not H_2 as in our dissertation, it is useful to graphically compare these plots with a specific oxidation curve elaborated by our tests. In *Figure 5.6*, it represented the CO_2-splitting rate curve of SFNM-04 tested in the microreactor at $T = 850\ °C$, with a total volumetric flow rate of $200\ mL/min$: reduction step with a gas mixture composed by $10\ \%\ H_2/N_2$ for $60\ min$, oxidation step with a gas mixture composed by $20\ \%\ CO_2/N_2$ for $30\ min$.

Similarly, Carrillo et al. [80] perform chemical looping reforming tests in a high-temperature fixed-bed reactor in isothermal conditions at $T = 900\ °C$, with a total volumetric flow rate of 300 mL/min: during the reduction step it is provided a reducing gas mixture composed by 5 % CH_4/Ar for 5 min, while during the oxidation step an oxidizing gas mixture of 16 % CO_2/Ar for 5 min.

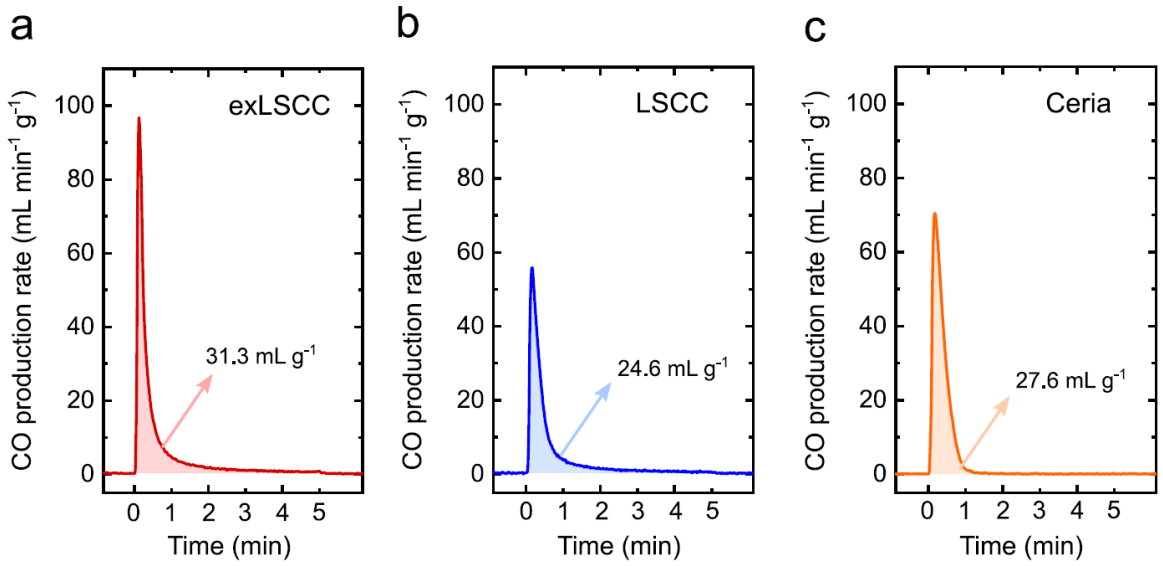

Figure 5.5: *CO_2-splitting rate curve for (a) exsolution-promoted LSCC (exLSCC), (b) LSCC without nanoparticle decoration, and (c) CeO_2. Reactions in isothermal conditions at $T = 900\ °C$, with a total volumetric flow rate of 300 mL/min: reduction step with 5 % CH_4/Ar for 5 min, oxidation step with 16 % CO_2/Ar for 5 min [80].*

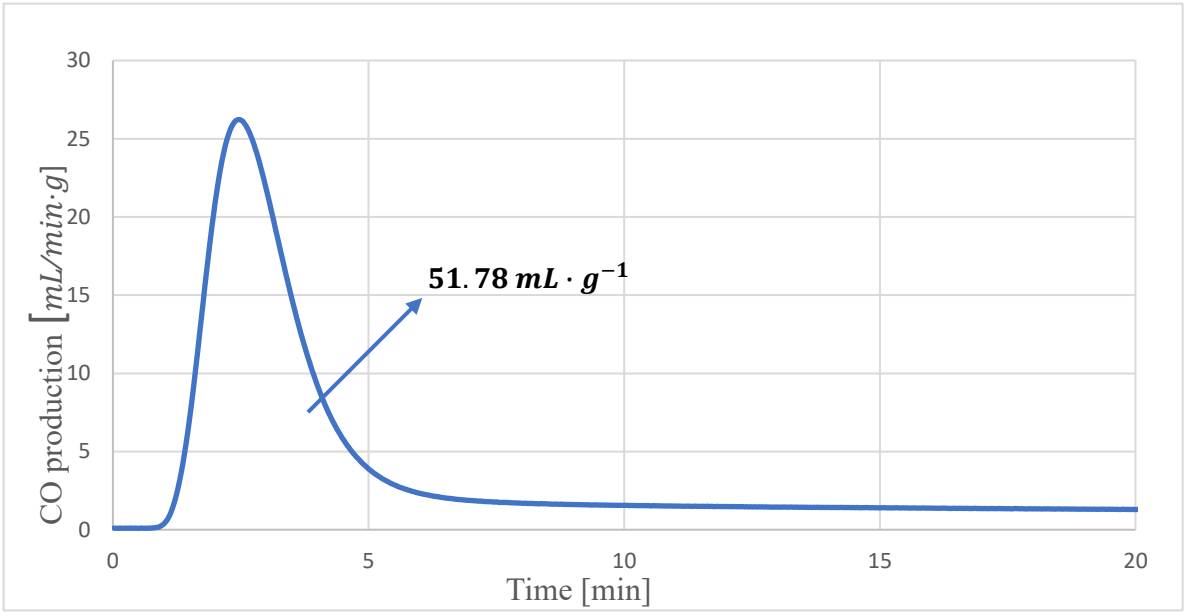

Figure 5.6: *CO_2-splitting rate curve for SFNM-04. Reactions in isothermal conditions at $T = 850\ °C$, with a total volumetric flow rate of 200 mL/min: reduction step with 10 % H_2/N_2 for 60 min, oxidation step with 20 % CO_2/H_2 for 30 min.*

The oxidation curve trend and its relative CO yield is comparable with that obtained in our test; hence this comparison demonstrates the consistency of our results. As discussed before, even if most of the operating conditions of the two tests compared are almost similar, the huge difference is the reduction/oxidation reaction time. In fact, in our test the reduction and oxidation step last $60\ min$ and $30\ min$, respectively. Differently, in the test proposed by Carrillo et al. [80], the reduction and oxidation step last only $5\ min$. This is visible by observing the x-axis indicating the time: in our test the CO peak occurs at time instant of about $t = 2.5\ min$, while in the other test it occurs at about $t = 0.5\ min$ Thence, this aspect remarks again that to compare the redox performance of different perovskite materials, it is necessary that all the operating conditions are almost similar. Nevertheless, the CO yield obtained by our test of $51.78\ [mL \cdot g^{-1}]$ is comparable with that obtained by Carrillo et al. [80] equal to $31.3\ [mL \cdot g^{-1}]$. Furthermore, also the CO peak values are almost comparable with a value of about $26\ [mL \cdot g^{-1} \cdot min^{-1}]$ and $60 \div 90\ [mL \cdot g^{-1} \cdot min^{-1}]$, respectively. The experimental set-up implemented by Carrillo et al. [80], described in the following *Figure 5.7*, is quite similar to that used in this dissertation explained previously in chapter 3, indicating that the chemical looping test bench used to evaluate the SFNM-04 redox performance is comparable with other experimental set-up for found in literature.

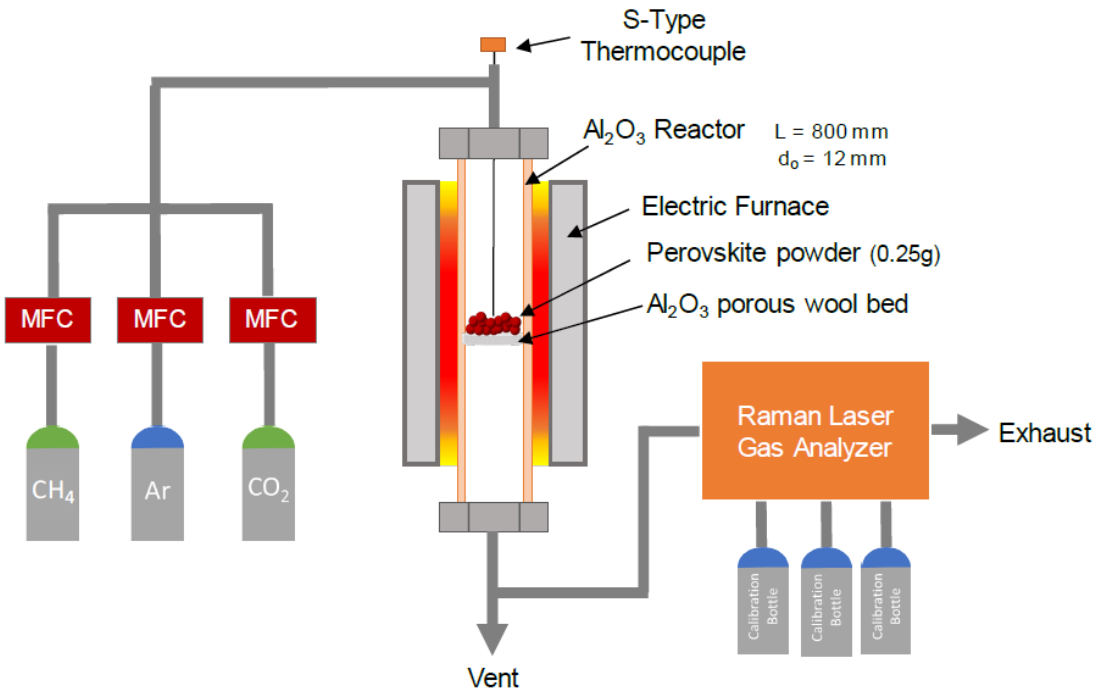

Figure 5.7: *Schematic of the experimental set-up used for testing the perovskite material under chemical looping methane reforming cycles [80].*

Another graphical comparison is presented below in *Figure 5.8* and *Figure 5.9*. The first one shows the CO production in $[ppm]$ terms of five redox cycles performed by D. Sastre et al [66]. In this work [66] it is investigated the role of Sr^{2+}doping using $La_{1-x}Sr_xFeO_3$ as perovskite for coupling Chemical Looping Methane Reforming (CLMR) with CO_2-splitting reactions using a fixed-bed, continuous-flow reactor operating isothermally at $T = 850°C$. A modified Pechini method is used for the synthesis of perovskites with composition $La_{1-x}Sr_xFeO_3$ with different Sr doping content x. More detailed:

- the name LF perovskite indicates a null Sr doping content ($x = 0$)
- L9S1F corresponds to a Sr doping content equal to $x = 0.1$
- L7S3F to $x = 0.3$
- L5S5F to $x = 0.5$
- L3S7F to $x = 0.7$
- L1S9F to $x = 0.9$
- SF to $x = 1$

In order to assess the effect of Sr^{2+}doping on CO production (more in general on syngas production), all the LSF samples are subjected to five redox cycles at $T = 850\ °C$, swinging the gas composition between $5\ \%\ CH_4$ and $5\ \%\ CO_2$ in Ar atmosphere. This LSF redox performance test is compared with the reference TEST (I) for SFNM-04. TEST (I) is composed by 5 redox cycles performed in isothermal conditions at $T = 850\ °C$, with a total volumetric flow rate of $200\ mL/min$. During the reduction step it is provided a gas reducing mixture composed by $10\ \%\ H_2/N_2$ for $60\ min$, while during the oxidation step a gas oxidizing mixture composed by $20\ \%\ CO_2/N_2$ for $90\ min$. Also in this case it is evident the different reduction/oxidation reaction time, and the different composition of the reducing/oxidizing gas, suggesting that typically the methane partial oxidation can be performed in shorter methane pulses when utilizing LSF (or exLSCC as before) as a reacting media because most of the syngas production occurs in about $2\ min$. This can be a possible expalination of why our time intervals of reduction/oxidation step are significantly longer compared to the others found in literature. Anyway, the same operating temperature at which the process occurs indicates that the temperature range used in our dissertation is properly detected in agreement with those used in literature for perovskite applications.

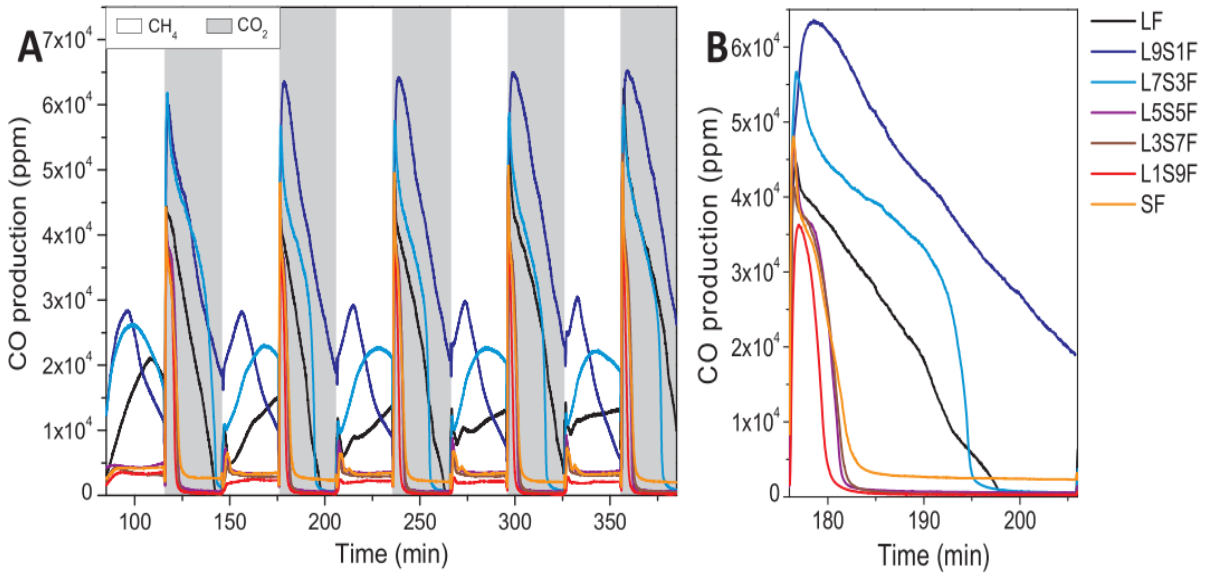

Figure 5.8: *(A) CO production for the LSF perovskite samples in [ppm]: 5 redox cycles at* $T = 850°C$ *alternating* $5\%\ CH_4$ *during the reduction step and* $5\%\ CO_2$ *during the oxidation step in Ar environment. (B) Zoom-detail of the second cycle of oxidation in* $5\ \%\ CO_2$ *stream [66].*

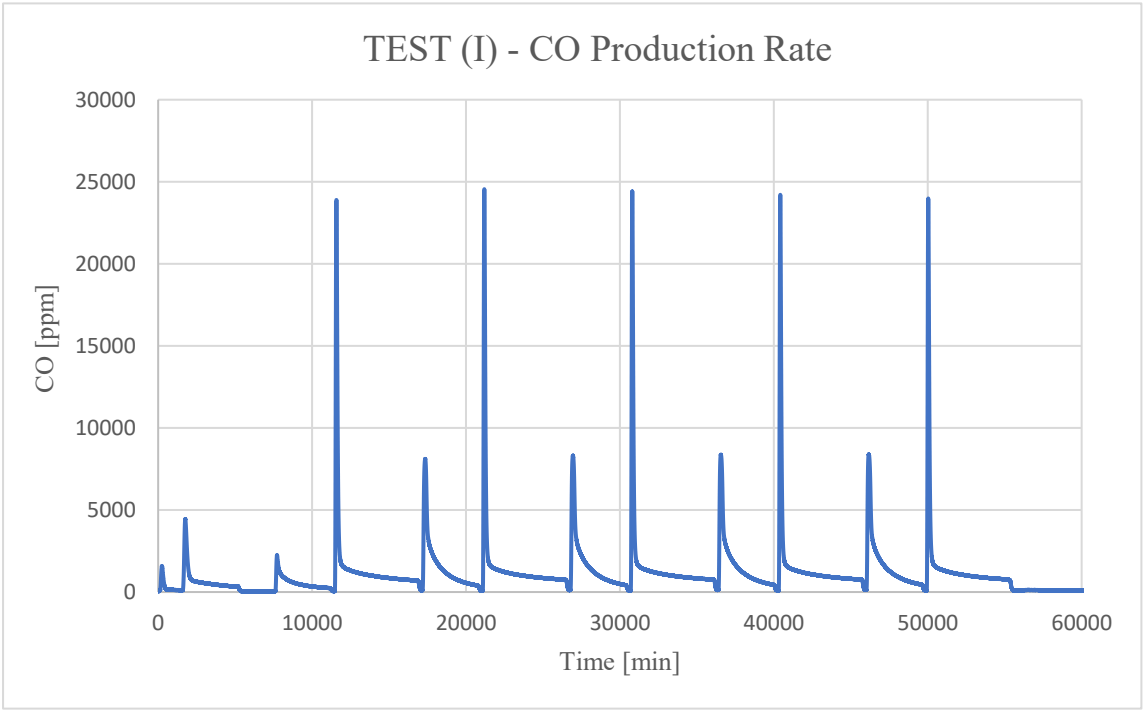

Figure 5.9: *CO production of TEST (I) for the SFNM-04 perovskite sample in [ppm]: 5 redox cycles at* $T = 850°C$ *alternating* $10\%\ H_2$ *during the reduction step and* $20\%\ CO_2$ *during the oxidation step in* N_2 *environment.*

It is noticed that the trend of the five oxidation curves follow the same behaviour in both cases. More precisely, observing *Figure 5.8*, the CO peaks reach an average value of about $6 \cdot 10^4$ $[ppm]$, while considering our TEST (I) in *Figure 5.9*, it is reached an average value of about $2.5 \cdot 10^4$ $[ppm]$. Moreover, concerning the CO yield, in the following *Figure 5.10* are shown the amount of CO produced from CO_2 dissociation over the reduced LSF perovskites plotted as a function of the number of cycles [66]. Considering SF, L1S9F, L3S7F, L5S5F, it is reached an average CO yield of about 2 $[mmol/g] = 2000$ $[\mu mol/g]$, while in agreement to the numerical results of TEST (I) listed in *Table 3*, it is achieved an average CO yield of about 2238 $[\mu mol/g]$. Hence, thanks to this comparison, it again confirmed the consistency of our results.

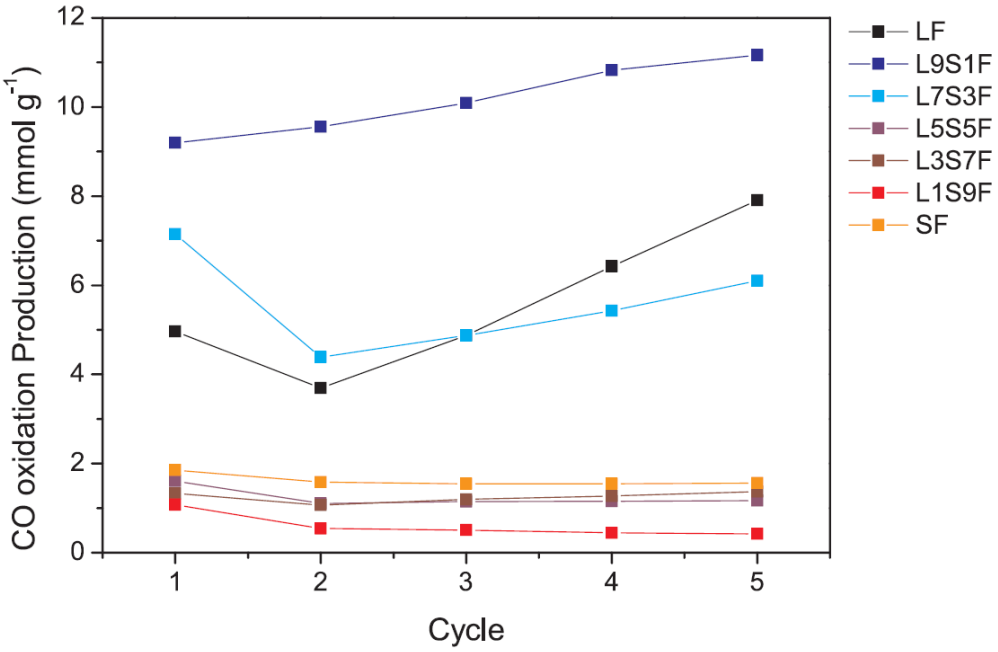

Figure 5.10: *CO yield values during re-oxidation steps for each cycle [66].*

In conclusion, after the numerical and graphical comparison, it is possible to assert that redox performance of SFNM-04 evaluated in this work are comparable with those obtained with different perovskite material tested in literature. Notwithstanding, as discussed before, to perform a completely correct comparison, it is necessary that all the variables able to affect the results should be almost equal, both from an arithmetical point of view considering the same integration method and from a thermodynamical point of view imposing the same operating conditions and experimental set-ups.

To conclude, all perovskite materials used for CDS/WS chemical looping thermochemical cycles presented above testify that the high number of possible perovskite formulation leaves space for the finding of suitable materials for this kind of processes.

Chapter 6

6. Conclusion

The aim of this dissertation is the evaluation of the redox performance in terms of carbon monoxide production during CO_2 splitting chemical looping thermochemical cycles, implementing as oxygen carrier the double perovskite material SFNM-04, namely $Sr_2FeMo_{0.6}Ni_{0.4}O_{6-\delta}$. This project is carried out out at CO_2 *Circle Lab* inside the Environment Park located at Parco Dora, Turin, Italy in collaboration with University of Udine and Massachusetts Institute of Technology (M.I.T.), Boston, USA. It is a preliminary study useful to determine the reproducibility of redox cycles for SFNM-04 perovskite. As explained, the perovskite structure is very stable and is able to accommodate a huge concentration of oxygen vacancies, which can allow highly productive redox cycles. On the other side, the ability of perovskite oxides to accommodate different chemical elements allows innumerable combinations of elements in stable solid solutions leaving a lot of space for improving existing materials. One of the most interesting feature of this double perovskite material is the exsolution evolution phenomenon occurrence during the reduction step. This phenomenon is related on its capability to grow, throughout the hydrogen reducing step, giving birth to an exsolution evolution, with the consequential appearance of spread Iron-Nickel alloy nanoparticles on the surface outer layer that enhance the catalytic activity of the perovskite surface. The exsolution allows to the reduction of Fe^{2+} and Ni^{3+} which moves towards the surface where a $FeNi_3$ alloy is generated. The main utility of this metallic alloy is to catalyse the oxidation reaction in order to generate a high number of oxygen vacancies inside the material lattice, the main driver of the chemical looping process.

A large number of experimental tests are carried out to evaluate the redox performance of the SFNM-04 double perovskite material. In particular, the CO production rate generated by the CO_2 splitting reaction is evaluated by varying the operating conditions of the thermochemical cycles as follows:

- Operating oxidation and reduction temperatures from $T = 550\ °C$ to $T = 850\ °C$.
- Gas mixture compositions from 6 % to 100 % of CO_2 during the oxidation step and from 5 % to 100 % of H_2 during the reduction step in a N_2-based gas mixture.
- Reduction and oxidation reaction time from 15 to 25 minutes.

The results obtained established an elevated CO production rate implementing SFNM-04 as oxygen carrier, and thanks to the comparison with other looping materials tested in literature performed in section 5.3, it is also demonstrated the consistency of these results.

Despite these very positive aspects, it is extensively questioned if the oxidation and reduction reactions are fully completed, or not. To find a possible solution of this issue, several experimental tests are performed by extending the reaction times and increasing the CO_2 and H_2 during the oxidation and reduction step, respectively. Furthermore, white tests are also carried out to compare the results with those obtained with the SFNM-04 sample. In detail, the comparison is mainly focused on the final portion of the oxidation curves, namely the curve tails, and a slight difference is found, suggesting that when the sample is used the results are higher with respect to the zero-value correspondent to the white test values. This difference, although small, is obtained also by extending the oxidation reaction until 7 hours. At first, instance, this difference can be ideally explained considering a higher difficulty to reach innermost vacancies in the lattice and, thence, the reaction takes more time, alternatively it could be due to the achievement of the reaction equilibrium. Notwithstanding, this issue related to the oxidation curve tails, can be due to the influence of different factors and mechanisms, that are not directly visible or measured by the gas analyser system, and for this reason, they are difficult to identify. One of the most possible option is the formation of carbonates ($SrCO_3$) and molybdates ($SrMoO_4$) that negatively affects the redox performance of SFNM-04: their formation is enhanced by the presence of Ni generated by the exsolution evolution. In fact, Ni acts a catalyst promoting the formation of $SrCO_3$ by hindering the CO_2 dissociation and it is also responsible for the stabilization of the insulating phase $SrMoO_4$. Consequentially, future experimental tests on this SFNM-04 sample can be focused on this aspect related to the complete/uncomplete oxidation/reduction reaction. In this perspective, thermogravimetric TGA, X-ray diffraction XRD and SEM (Scanning Electron Microscopy) analysis can be performed. For instance, a post-mortem XRD analysis can be extensively useful to detect eventual detrimental phases and to identify the causes of the abovementioned issue.

Nevertheless, SFNM-04 material as oxygen carrier for two-step CO_2 splitting chemical looping thermochemical cycle is established as a promising alternative to the most used oxygen carriers, such as metal oxides and ceria. The main attractiveness is due to the lower temperature level required during the reduction step that can make more easily the integration of the chemical looping method with a CSP. The main goal of this novel CCUS technology is to produce synthetic fuels, as the syngas ($CO + H_2$) and hydrogen in order to give a concrete contribute to the energy transition and decarbonization path. As discussed in the first chapter, the TRL value of renewable chemical looping is currently at level 3-4. In fact, this work has been carried out to experimentally prove the basic concept of this technology. To go further to the next levels, it will be necessary to validate the technology in the laboratory by finding the best possible material that provides better yields than those that today's metal oxides can provide. Once a promising material for these processes, capable of producing certain syngas yields, is determined, the next step sees a detailed thermodynamic study. In this way it is possible to simulate a stream and determine the flows and the ideal conditions of operation in order to find, in theory, a flow as pure as possible containing a maximum concentration of carbon monoxide. Then the idea is to be able to mix the CO produced with H_2 to have a syngas mixed according to the needs of future uses.

To conclude, all perovskite materials used for CDS/WS chemical looping thermochemical cycles presented in this work testify that the high number of possible perovskite formulation leaves space for the finding of suitable materials for this kind of processes. Thence, this dissertation can be helpful to make more rapidly the technology validation process of other future promising perovskite materials.

References

[1] I. E. Agency, “Net Zero by 2050 - A Roadmap for the Global Energy Sector,” May 2021.

[2] "IPCC, Foreword, Preface, Dedication and In Memoriam, Clim. Chang.," Chang. 2014 Mitig. Clim. Chang. Contrib. Work. Gr. III to Fifth Assess. Rep. Intergov. Panel Clim. Chang. (2014) 1454.

[3] IEA, "Global Energy & CO2 Status Report 2018. 2019".

[4] "IPCC, 2018: Global Warming of 1.5°C. An IPCC Special Report on the impacts of global warming of 1.5°C above pre-industrial levels and related global greenhouse gas emission pathways, in the context of strengthening the global response to the threat of cli".

[5] IPCC, "IPCC special report on global warming of 1.5oC, 2019.".

[6] i. p. w. I. Un Climate Change Conference UK 2021, "COP 26 Explained".

[7] "IEA, IRENA, UNSD, World Bank, WHO. 2020. Tracking SDG 7: The Energy Progress Report. World Bank, Washington DC. c World Bank. License: Creative Commons Attribution—NonCommercial 3.0 IGO (CC BY-NC 3.0 IGO). 2020.".

[8] "IEAGHG, “Information Sheets for CCS”, 2013/16, November 2013.".

[9] IEA, "Special Report on Carbon Capture Utilisation and Storage".

[10] "SJ Davis, RH Socolow, Environ. Res. Lett. 9 (2014) 084018".

[11] "Mai Bui, Claire S. Adjiman, André Bardow, Edward J. Anthony, Andy Boston, Solomon Brown, Paul S. Fennell, Sabine Fuss, Amparo Galindo, Leigh A. Hackett, Jason P. Hallett, Howard J. Herzorg, George Jackson, Jasmin Kemper, Samuel Krevor, Geoffrey C. Maitlan".

[12] "IPCC, 2005: IPCC Special Report on Carbon Dioxide Capture and Storage. Prepared by Working Group III of the Intergovernmental Panel on Climate Change [Metz, B., O. Davidson, H. C. de Coninck, M. Loos, and L. A. Meyer (eds.)]. Cambridge University Press, C".

[13] "http://bellona.org/ccs/technology/capture/post-combustion.html".

[14] "ENEA, V. Calabrò, A. Iulianelli, S. Liguori, A. Basile, A. Gugliuzza, A. Saraceno, “Stato dell’arte sui processi di rimozione della CO_2 mediante tecnologie a membrana”, 2011.".

[15] "ENEA, M. G. De Angelis, M. Giacinti Baschetti, M. Minelli, L. Olivieri, P. Deiana, C. Bassano, “Sintesi, caratterizzazione e prova di membrana per la separazione della CO_2 e la purificazione del Synthetic Natural Gas (SNG)”, 2014.".

[16] "Dennis Y. C. Leung, Giorgio Caramanna, M. Mercedes Maroto-Valer, “An overview of current status of carbon dioxide capture and storage technologies”. In Renewable and Sustainable Energy Reviews, vol. 39, pp. 426-443, 2014.".

[17] T. Hasegawa, "Numerical Study of Ammonia/O2-Fired Semiclosed Cycle Gas Turbine for Oxy-Fuel IGCC Power Generation With CO2 Capture".

[18] "ProbsteinRF,HicksRE.Syntheticfuels.Mineola,NY,U.S.A.:DoverPublica-".

[19] "TakeshitaT, YamajiK. Important roles ofFischer–Tropsch synfuels in the global energy future. Energy Policy 20 08;36:2773-84".

[20] "Rostrup-Nielsen JR. Syngas in perspective. Catal Today 2002;71:243–7.".

[21] "Ghoniem AF.Needs,re sources and climate change:c leanand efficient conversion technologies. Prog Energy Combust Sci 2011;37:15–51.".

[22] "Steinfeld A. Solar thermochemical productionofhydrogen—a review. Sol Energy 2005;78:603–15.".

[23] "Koumi Ngoh S, Njomo D. An overview of hydrogen gas production from solar energy. Renewable Sustainable Energy Rev 2012;16:6782–92.".

[24] "Meier A., Sattler C. Solar fuels from concentrated sunlight. SolarPACES: IEA Solar PACES implementing agreement; 2009.".

[25] "A.J. Traynor, R.J. Jensen, Direct Solar Reduction of CO2 to Fuel: First Prototype Results, Ind. Eng. Chem. Res. 41 (2002) 1935–1939. doi:10.1021/ie010871x.".

[26] "Ronald W. Breault, “Handbook of Chemical Looping Technology”, 2019.".

[27] "A. Edrisi, Z. Mansoori, B. Dabir, “Using three chemical looping reactors in ammonia production process – A novel plant configuration for a green production”. In International Journal of Hydrogen Energy, vol. 39, pp. 8271-8282, 2014.".

[28] "Liang Zeng, Fanxing Li, Ray Kim, Samuel Bayham, Omar McGiveron, Andrew Tong, Daniel Connell, Siwei Luo, Deepak Sridhar, Fei Wang, Zhenchao Sun, Liang-Shih Fan, “Coal direct chemical looping retrofit to pulverized coal power plants for in-situ CO_2 captu".

[29] "Anders Lyngfelt, “Chemical-looping combustion of solid fuels – Status of development”. In Applied Energy, vol. 113, pp. 1869-1873, 2014.".

[30] "Ronald W. Breault, “Handbook of Chemical Looping Technology”, 2019.".

[31] M. C. Christos Agrafiotis, "A review on solar thermal syngas production via redox pair-based water/carbon dioxide splitting thermochemical cycles".*Renewable and Sustainable Energy Reviews 42 (2015) 254–285.*

[32] "P.T. Krenzke, J.H. Davidson, Thermodynamic analysis of syngas production via the solar thermochemical cerium oxide redox cycle with methane-driven reduction, Energy and Fuels. 28 (2014) 4088–4095. doi:10.1021/ef500610n.".

[33] "M. Welte, K. Warren, J.R. Scheffe, A. Steinfeld, Combined Ceria Reduction and Methane Reforming in a Solar-Driven Particle-Transport Reactor, Ind. Eng. Chem. Res. 56 (2017) 10300–10308. doi:10.1021/acs.iecr.7b02738.".

[34] "Perkins C, Weimer AW. Solar-thermal production of renewable hydrogen. AIChE J 2009;55:286–93.".

[35] "Steinfeld A. Solar thermochemical production of hydrogen—a review. Sol Energy 2005;78:603–15.".

[36] "Rager T,GolczewskiJ.Solar-thermal zinc oxide reduction assisted by a second redox pair. Z Phys Chem 2005;219:235–46.".

[37] "Palumbo R,LedeJ,BoutinO,RicartE,SteinfeldA,MöllerS,etal.The production ofZnfromZnOinahigh-temperaturesolardecomposition quenchprocess—I. Thescientific frameworkfortheprocess.ChemEngSci 1998;53:2503–17.".

[38] "Peter G. Loutzenhiser, Anton Meier, Aldo Steinfeld, “Review of Two-Step H_2 O/CO_2 – Splitting Solar Thermochemical Cycle Based on Zn/ZnO Redox Reactions”. In Materials, vol. 3, pp. 4922-4938, 2010.".

[39] "Bilgen E, Bilgen C. Solar hydrogen production using two-step thermochemical cycles .Int J Hydrogen Energy1982;7:637–44".

[40] "Ma LJ, Chen LS, Chen SY. Study on the cycle decomposition of CO2 over NiCr0.08Fe1.92O4 and the microstructure of products. Materi Chem Phys 2007;105:122–6.".

[41] "T. Nakamura, “Hydrogen production from water utilizing solar heat at high temperature”. In Solar Energy, vol. 19, pp. 467-475, 1977.".

[42] "S. Abanades, G. Flamant, “Thermochemical hydrogen production from a two-step solar-driven water-splitting cycle based on cerium oxides”. In Solar Energy, vol.80, pp.1611-1623, 2006.".

[43] "WC. Chueh, SM. Haile, “Ceria as a thermochemical reaction medium for selectively generating syngas or methane from H2O and CO2”. In ChemSusChem, vol.2, pp.735-739, 2009.".

[44] "A. E. Farooqui, A. Manfredi Pica, P. Marocco, D. Ferrero, A. Lanzini, S. Fiorilli, J. Llorca, M. Santarelli, “Assessment of kinetic model for ceria oxidation for chemical-looping CO2 dissociation”. In Chemical Engineering Journal, vol. 346, pp.171-181, 20".

[45] "Haile SM. Fuel cell materials and components. Acta Mater 2003;51:5981-6000".

[46] "Olga Savinskaya, Alexnder P. Nemudry, “Oxygen transport properties of nanostructured SrFe_(1-x) Mo_x O_(2.5+3/2x) (0<x<0.1) perovskites”. In Accounts of Chemical Research, 47, 11, pp.3340-3348, 2011.".

[47] "Christopher L. Munich, Samuel Blaser, Marie C. Hoes, Aldo Steinfeld, “Comparing the solar-to-fuel energy conversion efficiency of ceria and perovskite based thermochemical redox cycles for splitting H2O and CO2”. In International Journal of Hydrogen Energ".

[48] "Anita Haeussler, Stephane Abanades, Julien Jouannaux, Anne Julbe, “Non-stoichiometric redox active perovskite materials for solar thermochemical fuel production: A review”. In Catalysts, 8(12), 611, 2018.".

[49] "Mingchen Tang, Long Xu, Maohong Fan, “Progress in oxygen carrier development of methane-based chemical-looping reforming: A review”. In Applied Energy, vol.151, pp.143-156, 2015.".

[50] Markus Kubicek, "Perovskite oxides - a review on a versatile material class for solar-to-fuel conversion process".*Journal of Materials Chemicstry A.*

[51] "Raymond E. Schaak, Thomas E. Mallouk, “Perovskite by design: A toolbox of solid-state reactions”. In Chemistry of Materials, 14, 4, pp.1455-1471, 2002.".

[52] "Marta Boaro, Andrea Felli, “PRIN17 Project Direct Biopower”, 2020.".

[53] Martin Hoffmann, Variation of mahnetic properties of Sr2FeMoO6.

[54] R. A. C. E. Pavone M, Oxide ion transport in Sr2Fe1.5Mo0.5O6-d, a mixed ion-electron conductor: new insights from first principles modeling..

[55] Yanru Yang, A Promising Composite Anode for Solid Oxide Fuel Cells: Sr2FeMo0.65Ni0.35O6-δ-Gd0.1Ce0.9O2-δ.

[56] Liu Q, A novel electrode material for symmetrical SOFCs. Adv Mater 2010;22:5478e82..

[57] Zhu, Hydrogen Oxidation Mechanisms on Perovskite Solid Oxide Fuel Cell Anodes.

[58] R. Josè Juan Alvarado-Flores, Synthesis, characterization and kinetic study of the Sr2FeMoO6-d double perovskite: New findings on the calcination of one of its precursors..

[59] Zhihong Du, Hailei Zhao, Sha Yi, Qing Xia, Yue Gong, Yang Zhang, Xing Cheng, Yan Li, Lin Gu, Konrad Swierczek, “High-performance anode material Sr_2 FeMo_0.65 Ni_0.35 O_(6-δ) with in situ exsolved nanoparticle catalyst”. In ACS Nano, 10, 9, pp.8660-.

[60] Shiqing Hu, Lixiao Zhang, Huanying Liu, Wenping Li, Zhongwei Cao, Lili Cai, Yue Zhu, Xuefeng Zhu, Weishen Yang, “Detrimental phase evolution triggered by Ni in perovskite-type cathodes for CO_2 electroreduction”. In Journal of Energy Chemistry, vol.36,.

[61] Rosa M. Cuellar-Franca, Adisa Azapagic, “Carbon capture, storage and utilization technologies: A critical analysis and comparison of their life cycle environmental impacts”. In Journal of CO2 Utilization, vol. 9, pp. 82-102, 2015..

[62] Kobayashi K, Room temperature magnetoresistance in an oxide material with an ordered double-perovskite..

[63] Wang K, Influence of the modulating interfacial state on Sr2FeMoO6 powder magnetoresistance properties..

[64] Hu Y, Synthesis and crystal structure of double perovskite compound Sr2FeMoO6..

[65] Zhihong Du, High-Performance Anode Material Sr2FeMo0.65Ni0.35O6−δ with In Situ Exsolved Nanoparticle Catalyst.

[66] Daniel Sastre, Chemical insights on the activity of La1-xSrxFeO3 perovskites for chemical looping reforming of methane coupled with CO2-splitting.

[67] Peipei Ding1, Review on Ruddlesden–Popper perovskites as cathode for solid oxide fuel cells.

[68] Hongbo Xiao, Ruddlesden−Popper Perovskite Oxides for Photocatalysis-Based Water Splitting and Wastewater Treatment.

[69] A. Pohar, I. Plazl, “Process intensification through microreactor application”. In Chemical and Biochemical Engineering Quarterly, 23(4), pp.537-544, 2009..

[70] Carbolite GeroLtd. “Carbolite Gero 3000°C, furnace brochure catalogue”..

[71] Invensys Eurotherm, “iTools Help Manual”, 2010..

[72] API SRL, “Manuale API-MIoT Poli_To”, 2020..

[73] Xiao Liu, Sitian Cheng, Hong Liu, Sha Hu, Daqiang Zhang, Huansheng Ning, “A survey on gas sensing technology”. In Sensors, 12(7), pp.9635-9665, 2012..

[74] S. B. Twiss, D. M. Teague, J. W. Bozek, M. V. Sink, “Application of infrared spectroscopy to exhaust gas analysis”. In Journal of the Air Pollution Control Association, 5:2, pp.75-83, 2012..

[75] XSTREAM, “Gas analyzers Z-Stream enhanced series – Instruction Manual”, 2017..

[76] Zhihong Du, Hailei Zhao, Sha Yi, Qing Xia, Yue Gong, Yang Zhang, Xing Cheng, Yan Li, Lin Gu, Konrad Swierczek, “High-performance anode material Sr_2 FeMo_0.65 Ni_0.35 O_(6-δ) with in situ exsolved nanoparticle catalyst”. In ACS Nano, 10, 9, pp.8660-.

[77] Shiqing Hu, Lixiao Zhang, Huanying Liu, Wenping Li, Zhongwei Cao, Lili Cai, Yue Zhu, Xuefeng Zhu, Weishen Yang, “Detrimental phase evolution triggered by Ni in perovskite-type cathodes for CO_2 electroreduction”. In Journal of Energy Chemistry, vol.36,.

[78] S. A. J. J. A. J. Anita Haeussler, Non-Stoichiometric Redox Active Perovskite Materials for Solar Thermochemical Fuel Production: A Review.

[79] A. E. Farooqui, Solar fuels via two-steo thermochemical redox cycles for power and fuel production.

[80] Alfonso J. Carrillo, La0.6Sr0.4Cr0.8Co0.2O3 Perovskite Decorated with Exsolved Co Nanoparticles for Stable CO2 Splitting and Syngas Production.

[81] "Magnus Ryden, Anders Lyngfelt, Tobias Mattisson, De Chen, Anders Holmen, Erlend Bjorgum, “Novel oxygen-carrier materials for chemical-looping combustion and chemical-looping reforming; La_x Sr_(1-x) Fe_y Co_(1-y) O_(3-δ) perovskite and mixed-metal".

[82] Mingyue Hou, Wang Sun, Pengfa Li, Jie Feng, Guoquan Yang, Jinshuo Qiao, Zhenhua Wang, David Rooney, Jinsheng Feng, Kening Sun, “Investigation into the effect of molybdenum-site substitution on the performance of Sr_2 Fe_1.5 Mo_0.5 O_(6-δ) for interm.

[83] Sun, Anode performance of LST-xCeO2 for solid oxide fuel cells.